OUKA
Osaka University Knowledge Archive

Title	Coupled Nonlinear Response of FOWT System Consisting of Main Floater, Mooring Buoy and Tether
Author(s)	馬, 冲
Citation	大阪大学, 2015, 博士論文
Version Type	VoR
URL	https://doi.org/10.18910/53995
rights	
Note	

Osaka University Knowledge Archive : OUKA

https://ir.library.osaka-u.ac.jp/

Osaka University

Doctoral Dissertation

Coupled Nonlinear Response of FOWT System Consisting of Main Floater, Mooring Buoy and Tether

(浮体、ブイおよび係留索からなる洋上風力発電の連成非線形応答に関する研究)

MA, CHONG

(馬　沖)

July 2015

Graduate School of Engineering,

Osaka University

Contents

List of Figures

List of Tables

1 INTRODUCTION

1.1 Background

As one kind of renewable energy, wind power, especially offshore wind energy, is attracting more and more attention all around the world. During decades' development, the on-land wind power has proven that wind energy can be selected to substitute the traditional fossil-fuel energy. However, some disadvantages of on-land wind power are also obvious and to compensate these weaknesses, offshore wind power system is proposed.

Compared with on-land wind turbine, offshore wind power has several key benefits:

- Offshore wind power does not require any land.

  Traditional wind turbine not only needs considerable amount of land but also causes serious noise pollution. So besides the place of wind farm, the surrounding area is also not appropriate for human habitation.

- Offshore wind is typically much stronger than wind on land.

  Unlike wind that hits land, offshore breezes can be strong even in the middle of the afternoon making it much easier to match the power demands of the population.

Europe is the world leader in offshore wind power, with the first offshore wind farm being installed in Denmark in 1991. In 2008, offshore wind power contributed 0.8 gigawatt (GW) of the total 28 GW of wind power capacity constructed that year. By October 2009, 26 offshore wind farms had been constructed in Europe with an average rated capacity of 76 MW. At the end of 2012, 1,662 turbines at 55 offshore wind farms across 10 European countries were generating electricity enough to power almost five million households [1]. Figure 1-1 shows the annual and cumulative installations of offshore wind in Europe [1].

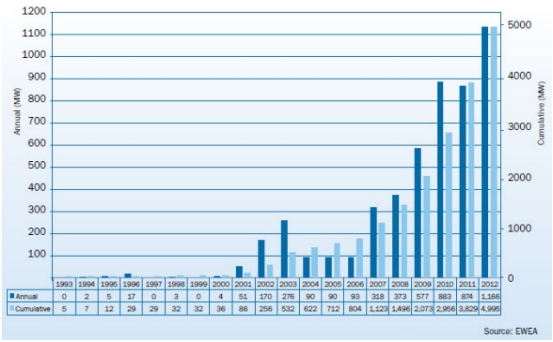

Figure 1-1 Annual and cumulative installations of offshore wind in Europe

At the end of 2011, there were 53 European offshore wind farms in waters off Belgium, Denmark, Finland, Germany, Ireland, the Netherlands, Norway, Sweden and the United Kingdom, with an operating capacity of 3,813 MW, while 5,603 MW is under construction [2]. More than 100 GW (or 100, 000 MW) of offshore projects are proposed or under development in Europe. The European Wind Energy Association has set a target of 40 GW installed by 2020 and 150 GW by 2030 [3].

As of July 2013, the 175-turbine London Array in the United Kingdom is the largest offshore wind farm in the world with a capacity of 630 MW, followed by Greater Gabbard (504 MW), also in the United Kingdom, Anholt (400 MW) in Denmark, and BARD Offshore 1 (400 MW) in Germany. There are many large offshore wind farms under construction including Gwynt y Môr (576 MW), Borkum West II (400 MW), and West of Duddon Sands (389 MW) [4]. Table 1-1 presents the largest offshore wind farms in the world until 2014 [4]. The overview of London Array, which is the largest offshore wind farm, is shown in Figure 1-2.

Table 1-1 World's largest offshore wind farms

Wind farm	Capacity (MW)	Country	Turbines and model	Commissioned
London Array	630	United Kingdom	175 × Siemens SWT-3.6	2012
Greater Gabbard	504	United Kingdom	140 × Siemens SWT-3.6	2012
Anholt	400	Denmark	111 × Siemens SWT-3.6-120	2013
BARD Offshore 1	400	Germany	80 x BARD 5.0 turbines	2013
Walney	367	United Kingdom	102 × Siemens SWT-3.6	2012
Thorntonbank	325	Belgium	54 × Senvion 6 MW	2013
Sheringham Shoal	317	United Kingdom	88 × Siemens 3.6	2013
Thanet	300	United Kingdom	100 × Vestas V90-3MW	2010
Meerwind Süd/Ost	288	Germany	80 × Siemens SWT-3.6-120	2014
Lincs	270	United Kingdom	75 × Siemens 3.6	2013
Horns Rev II	209	Denmark	91 × Siemens 2.3-93	2009

Figure 1-2 Overview of London Array

However, all the wind farms mentioned above utilizes the bottom-fixed type of platform (mostly monopole, e.g. London Array) which means the available water depth has to be limited to 30 meters. According to the research of NREL [5], worldwide deep-water wind resources are extremely abundant in subsea areas with depths up to 600 meters, which are thought to best facilitate transmission of the generated electric power to shore communities.

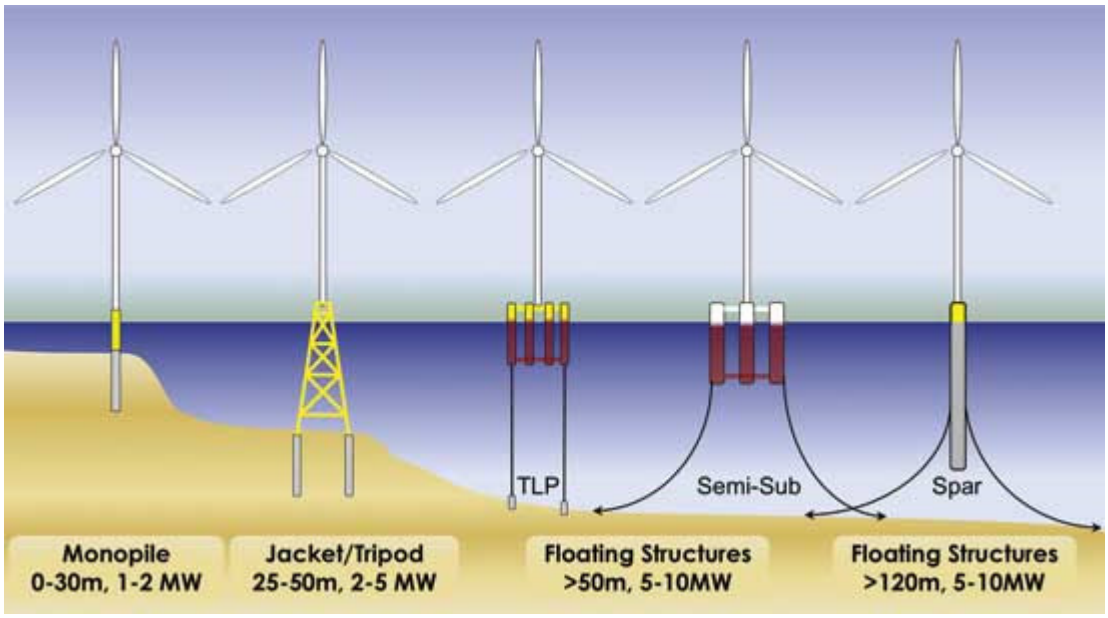

Figure 1-3 Different kinds of offshore wind turbine

For Japan, the country's energy landscape is shifting dramatically in the wake of Fukushima crisis, the world's worst nuclear disaster since Chernobyl in 1986. A so-called feed-in tariff (FIT) program that guarantees higher price above the market rates for clean energy to accelerate investment in renewable energy is already started. Citing Germany and China as examples, it is wind, not solar will grow the most under FIT schemes.

Japan Wind Power Association estimates Japan's potential for wind is 144,000 megawatts for onshore and 608,000 for offshore [6]. Comparing with the 49,000 megawatts of nuclear power, it is possible for Japan to replace the nuclear power by wind energy. Land-Based wind-energy development is limited by Japan's mountains, making offshore developments more viable. However, more than 80% of the offshore wind energy potential in Japan are located at deep water (See Figure 1.4) and this poses challenges to offshore wind turbines that are attached to the bottom of the sea which require a stable floating platform [7].

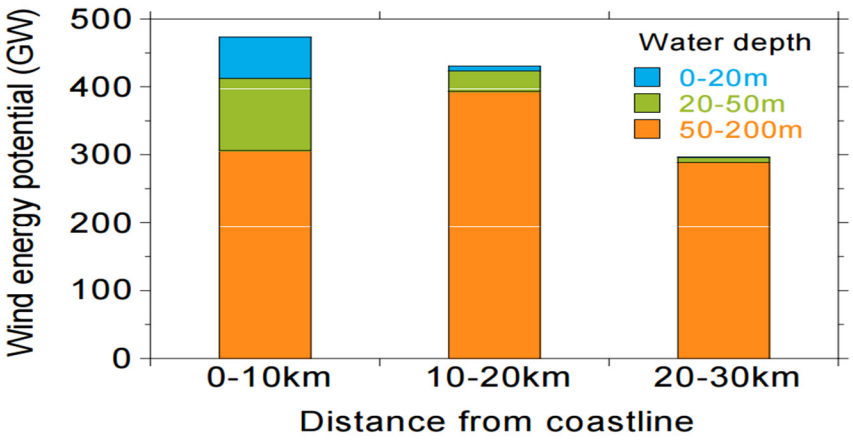

Figure 1-4 Offshore wind energy potential in Japan [7]

1.2 Research Objectives

Compared with the conventional method of deploying fixed versions of the machines, floating turbine technology is still in its infancy. At the present, most design for floating offshore wind turbine (FOWT) are proposed based on the design experience of oil platform which includes SPAR, TLP, semi-submersible and barge types (several typical concepts of FOWT are introduced in Chapter 2). However, due to the different property or functionality between FOWT and oil platform, it is necessary to optimize the design especially for FOWT in aspects of fabrication, construction, installation and maintenance costs. At the beginning of this research, a new design of FOWT consists of semi-submersible floater and single-point-mooring (SPM) is proposed. By this new concept, the lower installation cost of the floater and mooring, acceptable stability and weather-vane property can be expected. To verify the design, model test with scale ratio 1/100 was conducted.

Many researches have been conducted for simulation of the response of FOWT system. The simulation can be classified into two categories, frequency-domain analysis and time-domain analysis. For frequency-domain model, the computational time is much less compared with the time-domain model. So it will be much convenient to utilize the frequency-domain model to obtain the response amplitude operators (RAOs) which is important when designing the floater. A typical frequency-domain model was built by Bulder [8] to obtain the RAOs for the six rigid-body modes which is designed for a 5-MW turbine. Lee [9] also conducted a similar simulation to analyze a TLP design and Spar-Buoy design for 1.5-MW turbine. The research team from NREL and MIT analyzed multiple TLP designs and a shallow drafted barge design for a 5-MW wind turbine [10] [11].

However, the frequency-domain model has the limitation that it cannot be used to analyze the nonlinear behavior such as the nonlinear structural stiffness or dynamics, nonlinear aerodynamics, nonlinear hydrodynamics and nonlinear coupling influence between mooring-floater and floater-turbine. To overcome these limitations, time-domain analysis was proposed even though it may take much more computational time.

Table 1-2 The verified codes in OC4 [12]

Code	Developer	Mooring Model
FAST	NREL	QS
FAST v8	NREL	QS
CHARM3D+FAST	TAMU+NREL	FE/Dyn
OPASS+FAST	CENER+NREL	LM/Dyn
UOU+FAST	UOU+NREL	QS

Bladed	GH	QS
Bladed Advanced Hydro Beta	GH	QS
OrcaFlex	Orcina	LM/Dyn
HAWC2	DTU	FE/Dyn
hydro-GAST	NTUA	FE/Dyn
Simo+Riflex+AeroDyn	MARINTEK+NREL	FE/Dyn
Riflex-Coupled	MARINTEK	FE/Dyn
3Dfloat	IFE+UMB	FE/Dyn
SWT	SAMTEC	FE/Dyn
DeepLinesWT	PRINCIPIA-IFPEN	FE/Dyn
SIMPACK+HydroDyn	SIMPACK	QS
CAsT	University of Tokyo	QS
Wavec2Wire	WavEC	QS
WAMSIM	DHI	QS

QS: quasi-static; Dyn: dynamic; LM:lumped mass: FE: finite element

Offshore Code Comparison Collaboration Continuation (OC4) project which operates under the International Energy Agency Wind Task 30 has been started to verify the popular time domain simulation tools [12]. Table 1-2 shows the verified codes and the corresponding developers. Among these codes, FAST which is developed by NREL is the one of the most advanced codes to analyze the response of wind turbine system. Based on blade-element/momentum (BEM), generalized dynamic wake (GDW) and dynamic stall theory, the simulation results of aerodynamics can offer a very good correlation with model tests. However, to save the computational time-consuming, the response of flexible structure is obtained by the mode theory which is not enough when the structural nonlinearity is of interest. From the view of hydrodynamics, the WAMIT which is based the potential theory has been utilized in most codes and shows an acceptable feasibility. However, as it is not an open source and the objects in fluid are always assumed as rigid body, it is not easy to adopt the WAMIT in the simulation of FOWT when considering the structural flexibility.

CHARM3D+FAST is a coupled tool proposed by the cooperation between TAMU and NREL [13]. The rigid platform and dynamic FE mooring is modeled in CHARM3D and the wind turbine & wind tower is handled by FAST. The hydrodynamics of CHARM3D basted on WAMIT is mature in which the linear and nonlinear (e.g. mean dirft, Newman's approximation, instantaneous water level et al.) fluid influence can be considered.

Simo+Riflex+AeroDyn [14] is developed mainly by MARINTEK. The aerodynamic force is referred to the AeroDyn which is an independent module in FAST. The

structural model in Simo+Riflex+AeroDyn is the most advanced in Table 1-2 as all of the wind tower, platform and mooring are built as FE model. The hydrodynamics in Simo+Riflex+AeroDyn is basically based on first order panel model with considering the mean drift forces due to the first order solution.

The CAsT [15] is developed by the team the University of Tokyo. Linear beam element is utilized to build the wind tower and platform. Mooring is calculated according to lumped mass method. Hydrodynamic load is calculated by the Morison equation. For the Aerodynamic load, they developed their own BEM simulation model.

In the most of the tools mentioned above, the mooring part is usually modeled by a linear spring or catenary theory. They are classified to quasi-static model and apparently insufficient to discuss the coupled dynamic behavior between FOWT and mooring structures. In the other tools, a lumped mass approach is used at best. However, this approach is still insufficient when there is a tension variation and large deflection in the mooring, which is the case with tension leg mooring.

The objectives of this research are to establish a numerical tool to simulate coupled response of FOWT with mooring not only for the conventional design but also for the new design, and then to clarify the coupled behavior which is frequently seen in the FOWT systems. The new concept of FOWT can have multiple floating bodies or unique mooring system which may affect a lot on the response of FOWT. The numerical tool is mainly used to evaluate the motion and structural responses of platform and mooring under wave or combined steady-wind & wave condition. The simulation results can be utilized for design or optimization of the design parameters of FOWT in the first phase. It is observed in the model test [16] [17] [18] that, when the wind speed is constant, aerodynamic force can be regarded as static thrust which has little influence on the dynamic response of platform or mooring. Therefore, how to calculate the fluid force and couple the multiple body and mooring become much more important in this research. Especially for the tension leg mooring system, the nonlinear stiffness influence and coupling methodology with the platform have to be handled carefully. In order to simplify the simulation, the aerodynamics is simply substituted by the static thrust on the nacelle which can be measured in the model test beforehand. This simplification could however not be applied for the design of drivetrains. Aerodynamic-coupled analysis is necessary to this end.

In this research, a simulation tool for FOWT, DYNABEAM in both frequency and time domains is developed. As the FOWT always consists of slender columns, the structural flexibility is taken into account by utilizing structural finite element method. In the frequency domain simulation, all nonlinear influences are neglected and the RAOs of FOWT can be solved in a relatively short time. The floater and mooring system are modeled together.

In the time domain model, in order to consider the nonlinear influence of mooring system, the floater and mooring system are separately modeled. In most time domain researches, the floater and the mooring system are coupled in different time-step by transferring the force and the displacement on the joint which is called as weakly coupling. For conventional catenary mooring system, the weakly coupling may work after verifying the convergence. But for the tension leg system, the weakly coupling cannot work well as the restoring stiffness of mooring is too high in some direction and even a small error in the displacement results in a huge error in the restoring force which causes the divergence problem. In DYNABEAM, the strongly coupling technique is utilized and the divergence problem of TLP system can be solved.

To more accurately predict the behavior of mooring system, the geometrical nonlinearity of the mooring system is considered. The hydrodynamic force is calculated based on the linear potential theory. However, the quadratic viscous force, memory function, transient wave elevation and quadratic influence of water particle velocity are accounted for.

After establishing the DYNABEAM model, a series of frequency domain analyses are performed for different type of FOWTs and based on the simulation results, the OU-Design for FOWT is proposed.

A series of scaled model tests for two conventional designs, TLP type and Spar type FOWTs are utilized to verify the feasibility of time-domain DYNABEAM. It shows that, DYNABEAM can achieve reasonable simulation results for both tension-leg and catenary type of mooring system.

To confirm the feasibility of OU-Design, a scaled model test and the corresponding simulation results are performed. The simulation is validated against the results of test again. An acceptable correlation between simulation and model test is achieved. To explain the nonlinear response of the model test, a contact model is introduced into simulation.

The buoy-tether system may be found in other applications. Another design, named as TLSPAR, for FOWT which consists of SPAR type of floater and single-point-mooring system has been proposed by Osaka Prefecture University. In the scaled model tests, the TLSPAR exhibits a significant sub-harmonic response of FOWT. A theoretical model according to the Mathieu instability theory is derived to clarify the mechanism of such kind of sub-harmonic response. The DYNABEAM is also used to reproduce the same behavior. The nonlinear influence of mooring turned to be the cause of the onset of the sub-harmonic response. To confirm the sub-harmonic response experimentally, a scaled model for single-point-mooring buoy (SPMB) system is further designed and a new series of model tests are carried. The sub-harmonic response

of SPMB is confirmed to occur in the expected frequency region which has been predicted by the theoretical analysis and simulation by DYNABEAM. Then, the difference of the mechanism between the TLSPAR and SPMB is discussed based on the simulation.

The proposed numerical model based on potential theory should naturally have its limitation in applicability to severe sea load cases. It is expected to extend the method to severer sea cases where the green-water, bottom emergence, slamming may occur. Its prediction is of interest to the designers and engineers. Finally, the hydrodynamic model in DYNABEAM is substituted by the smoothed-particle hydrodynamic (SPH) model to capture the coupled response under severer wave conditions. The simulation results based on the SPH model is finally compared with the model test results of SPMB.

1.3 The Organization of the Thesis

In Chapter 2, the some typical designs for FOWT which have been installed in the real scale are introduced firstly. Then, based on the linear frequency-domain DYNABEAM, the behavior of four types of FOWT including Semi-Sub, Spar, TLP and Barge are simulated under same wave condition. The RAOs among these four designs are compared and discussed. Then, the new concept of FOWT, OU-design, is proposed.

In Chapter 3, the frequency domain model and time domain model which are utilized in DYNABEAM are discussed. The linear wave potential theory is introduced. Besides, the nonlinear hydrodynamic influences consisting of quadratic viscous force, memory function, quadratic velocity influences and transient wave elevation are demonstrated. The linear stiffness for floater and linear and nonlinear stiffness for mooring are presented as well. The simulation results of mooring model are verified by the static catenary theory. The strongly coupling technique between the floater and mooring system is emphasized finally.

The validation work for nonlinear time domain DYNABEAM is presented in Chapter 4. Two conventional designs (TLP and SPAR) from Osaka Prefecture University are used to verify the simulation results. Not only the 6DOFs of motions but also the structural bending load and mooring tension which are measured during the model tests are compared with the simulation results.

The introduction for the scaled model test of OU-design is presented in Chapter 5. The RAOs for the motions of the main floater and buoy are compared between the model test results and simulation. The influence of mooring and wind thrust is investigated. Special contact model is adopted to interpret the large influence of wind thrust on the pitch motion of the main floater. The RAOs for the motions of the main floater and buoy are compared between the model test results and simulation.

In Chapter 6, the nonlinear influence of tether tension on the floater motion is discussed concentratedly for SPM system. The natural mode and associated natural frequency for SPM is derived theoretically. Then, the mechanism of the sub-harmonic motion is clarified according to the Mathieu instability theory. Time domain DYNABEAM is utilized for reproducing the sub-harmonic motion which is observed in the model test of TLSPAR and SPMB. The comparison between the simulation and model test is presented for both 3DOF motion and tether tension and a good correlation is proven. Stability diagram for this SPM system is proposed based on the theoretical analysis and validated by the simulation and model test. Finally, the discussion on how to mitigate the sub-harmonic motion and how to obtain a permanent sub-harmonic motion is given.

In Chapter 7, the SPH is brought in the time domain DYNABEAM model to solve the nonlinear problem when the wave condition becomes severe. The utilized SPH is remarked in brief and the coupling process between SPH and DYNABEAM is introduced. The simulation results are compared with the SPMB model tests results finally.

Chapter 8 concludes the thesis with a summary of the main findings. The possible improvements in the future are proposed.

2 DEVELOPMENT OF NEW CONCEPT OF FOWT

2.1 Overview of Different FOWT Designs

Before proposing a new concept for FOWT system, some typical design concepts with high recognition are introduced in this section.

2.1.1 Traditional type

Most proposed designs referred to the design experience of oil&gas platform which we classify them as traditional type.

Figure 2-1 Fukushima-mirai

Fuskushima floating offshore wind farm demonstration project (Fukushima-Forward) plans to install one 2MW FOWT in first phase and two FOWT with world largest 7MW wind turbine in second phase [19]. The first phase had been completed in 2013 and the photo of installed FOWT, Fukushima-mirai, is shown in Figure 2-1. Fukushima-mirai utilized semi-sub type of floater which consists of one center column, three side columns, three braces, the main deck beams and the pontoon beams which support the wind turbine. The compact semi-sub floater has advantages for construction and installation due to its shallow draft. The draft of the floater can be controlled by using

the ballast tank located at the bottom of the side columns. 6 pieces of catenary are used to locate the FOWT.

Figure 2-2 GOTO-FOWT

Another wind turbine project funded by Japanese Ministry of the Environment proposed a spar type of FOWT, GOTO-FOWT (see Figure 2-2), with 2MW capacity. This is the first grid-connected FOWT in japan. The mooring system consists of three catenary moorings. It has been proven that, this spar type design has a good stability even under extreme environmental conditions [20].

Hywind (see Figure 2-3) is the world's first operational deep-water floating large-capacity wind turbine which is located in the North Sea off Norway [21]. The 2.3-MW turbine was constructed by Siemens Wind Power and mounted on a floating tower with a 100-metre deep draft. With spar type of floater, Hywind also shows a well stability with undergoing 11 meter wave amplitude. However, due to utilizing catenary mooring system which consumes much under-water space, it is difficult to install multiple Hywind intensively. It is the usual problem for catenary mooring system.

Figure 2-3 Hywind

To overcome the space-consuming problem of catenary, TLP type of FOWT was proposed. Blue H Technologies [22] designed a FOWT with TLP floater (Figure 2-4) and installed a scaled model (3/4 scale ratio) with 80kW capacity in south of Italy, 2008. This is the first TLP type of FOWT installed in the real sea.

Figure 2-4 Blue H TLP

2.1.2 Multiple wind turbines combined type

To absorb wind energy with more efficiency, combined type of FOWT was proposed which consists of one main floater but multiple wind turbines.

Figure 2-5 Wind Lens, Kyushu

Figure 2-5 shows the one type of combined FOWT designed by Kyushu University. On December 4th, 2011, the University launched a 1 yeat test with a scaled model of an 18 meter diameter floating platform with two 3kw turbines 600 meters from shore in Hakata Bay. The pilot also includes solar panels [23].

Figure 2-6 WindSea

Another combined design was proposed in Norway as WindSea (Figure 2-6). Three wind turbines are installed in one main floater. In order to prevent the mutual interference among the turbines, the tower is designed with an inclination. However, the improved efficiency of the inclination and its influence on the structure stability is still under research.

Figure 2-7 Hexicon

A company from Sweden proposed a bold concept for the FOWT as shown in Figure 2-7. Not only normal size of wind turbines but also small scale of turbines are installed in one main floater in order to make the best of the carrying capacity of the floater. As it is rather complicated, the relevant research is still immature.

2.1.3 New concept

Some new concepts for FOWT with considering the unique property of FOWT are proposed in recent years.

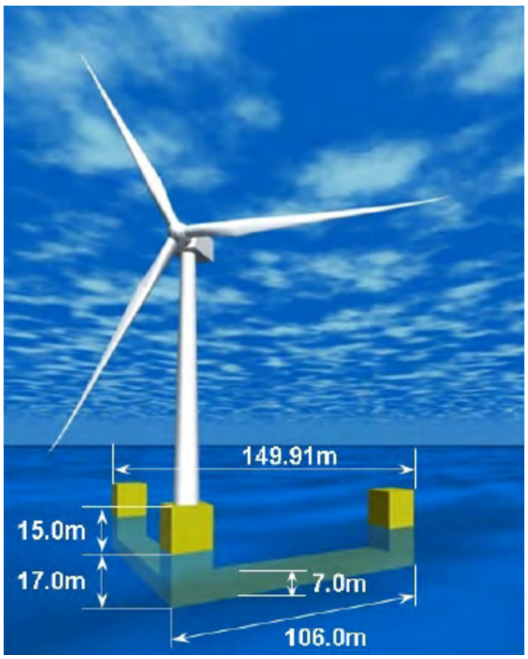

Figure 2-8 MHI-FOWT

As mentioned previously, Fukushima-Forward project plan to install a FOWT with 7 MW capacity in its second phase which plans to be completed in 2015. Figure 2-8 shows the adopted design which is proposed by MHI [19]. The floater is designed with V shape with two large column to provide sufficient buoyancy. The floating motion can be reduced by turbine control and Operation & Maintenance program. Catenary mooring system is utilized as well. Several researches were conducted and the feasibility of this design was proven [24]. As less materials is needed comparing with the traditional floater, the expense of this concept is expected smaller than usual designs.

The Principle Power of USA proposed a design named as WindFloat (Figure 2-9). It is also an asymmetric design with patented water entrapment plates at the base of each column [25]. The plates improve the motion performance of the system significantly due to damping and entrained water effects. The mooring system employs conventional components such as chain and polyester lines to minimize cost and complexity. The first scale 2MW WindFloat was launched into the water in October 2011.

Figure 2-9 WindFloat

Figure 2-10 Sway

Compared with the previous design, the SWAY (Figure 2-10) is the most revolutionary concept for FOWT which consists of spar type of floater and single-tension-leg mooring system. The floater is designed to rotate around the single-tension-leg freely so that the yaw control in the wind turbine is not necessary. Besides, compared with the catenary, the tension leg provides more restoring force which results in a better stability. Scaled model test with 1/6 ratio was conducted in the real sea.

2.2 Comparison among Different FOWT Designs

2.2.1 Model

In this section, four typical types of 5 MW class FOWT including Semi-sub, TLP, SPAR and Barge are selected and the corresponding simulations are conducted. Figure 2 11 shows the exteriors of these four FOWTs without turbine. The wind turbine system consists of three blades upwind HAWT (Horizontal Axis Wind Turbine). The weight of the nacelle including rotor, hub, and generator weighs as much as 400tonf. The height of the tower is 80m. The scantlings of the tower are taken from Kim et al. Table 2 1 shows the principal particulars of the wind turbine. Table 2-2 compares the main dimensions of the four concepts.

Various wave conditions are considered in the analysis. The circular frequency of the waves ranges from 0.05 rad/s to 1.5 rad/s with an interval of 0.05rad/s. On the other hand, the heading angle of the waves is fixed to 90deg, or longitudinal wave which is the most critical especially for the barge type. State of waves is shown in Figure 2-12. In this Figure, waves proceed in the direction of the arrow.

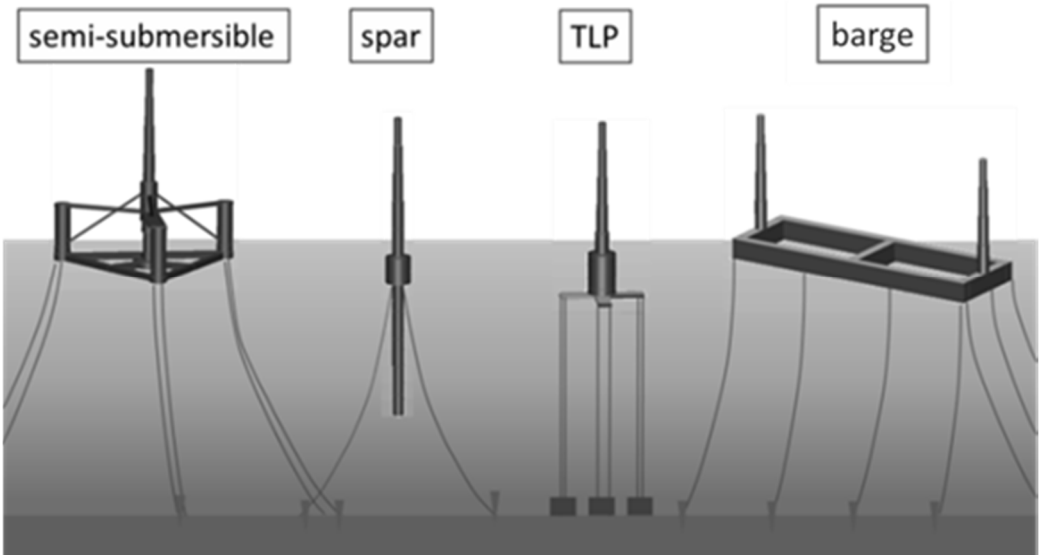

Figure 2-11 Exteriors of semi-submersible, SPAR, TLP and barge

Table 2-1 Principal particulars of the wind turbine

Item	Value	Unit
Capacity	5	MW
Number of blades	3	-
Blade diameter	120	m
Height of the hub	80	m
Blade mass	20	tons/a blade
Rotor mass	60	tons
Nacelle mass	290	tons
Tower mass	468	tons
Total mass	838	tons
Tower diameter(Min)	5	m
Tower diameter(Max)	8	m

Table 2-2 main dimension of semi-submersible, SPAR, TLP and barge

	semi-submersible	SPAR	TLP	barge	unit
Platform Mass (including ballast)	17510	10352	3068	14492	tons
Draft	18	125	38	4	m
Column diameter	12	8	20	-	m
Total initial tension	-	-	16285	-	tonf
# of mooring line	6	4	8	14	-

Static wind loads are evaluated and applied to the same structure model. Considering the safety factor, the maximum wind loads on the rotor and the tower are estimated to be 2000kN. The load is assumed to be working to the hub.

Motions, bending stress at the base of the tower and angle of inclination are firstly referenced to check the feasibility. The inclination influences the generation efficiency. Considering that the yield stress of steel is approximately 240MPa, the allowable stress for the dynamic component is set 120MPa.

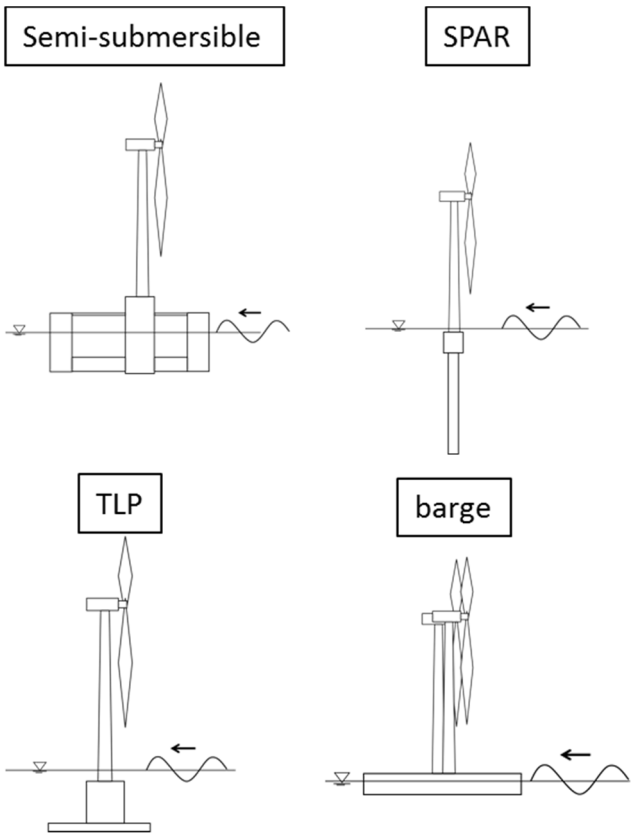

Figure 2-12 State of waves

2.2.2 Results

Figure 2-13 compares the surge RAOs (Response Amplitude Operators) of the four types of structures. The TLP type shows the largest response at around 0.2rad/s when its natural frequency in surge motion is met by the frequency of the incident wave. However, the resonance frequency may be considered out of frequency range where the wave energy concentrates. Therefore, the resonance of TLP in surge may be neglected for design consideration. In the case of the semi-submersible and the SPAR types, the amplitude of the response is almost the same level, and these types show a better performance compared with that of other types of foundations whereas the barge type shows the largest.

Figure 2-14 compares the heave RAOs. The response of the TLP type is the smallest of all because the vertical motions are restrained by tendons. Next to the TLP type, the responses of the semi-submersible and the SPAR types are smaller. The structure which has the largest response is, again, the barge type. This is because the barge type has the largest water-plane area and it is easily subjected to larger vertical forces. Comparing with the semi-submersible and the SPAR types, since the water-plane area of the semi-submersible is much larger than that of the SPAR type, the natural frequency of the

semi-submersible type is larger. However, both frequencies are lower than 0.5 rad/s and in the frequency ranges above 0.5rad/s, heave motions are, in general, small.

Figure 2-15 compares the pitch RAOs. From the Figure, it can be found that the response of the barge type is extremely large. As discussed in heave RAOs, the barge type has the largest water-plane area, and thus is subjected to the large buoyancy fluctuations, which makes the barge type easily disturbed by the waves. Comparing among the semi-submersible type, the SPAR type and the TLP type, the response of the SPAR type is the largest. Because the meta-centric height from center of gravity (GM) is the smallest for the SPAR type, it has the smallest restoring moment coefficient. Therefore it has the lowest natural frequency in pitch motion. The natural frequencies of the semi-submersible type and the TLP type are larger.

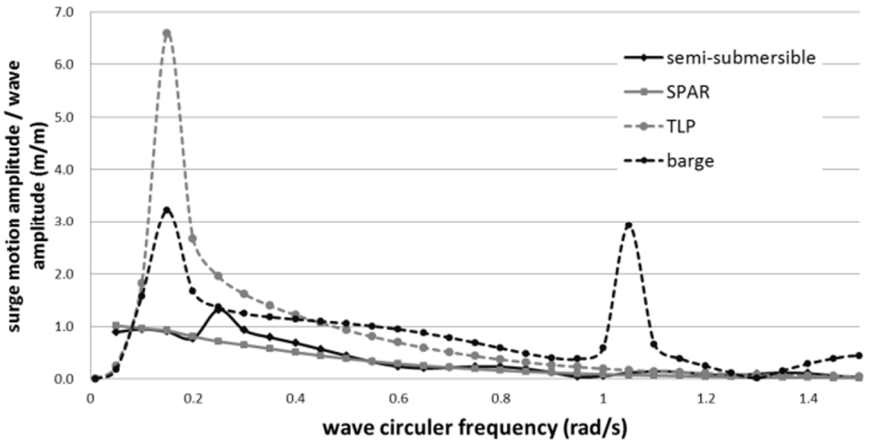

Figure 2-13 RAOs for Surge

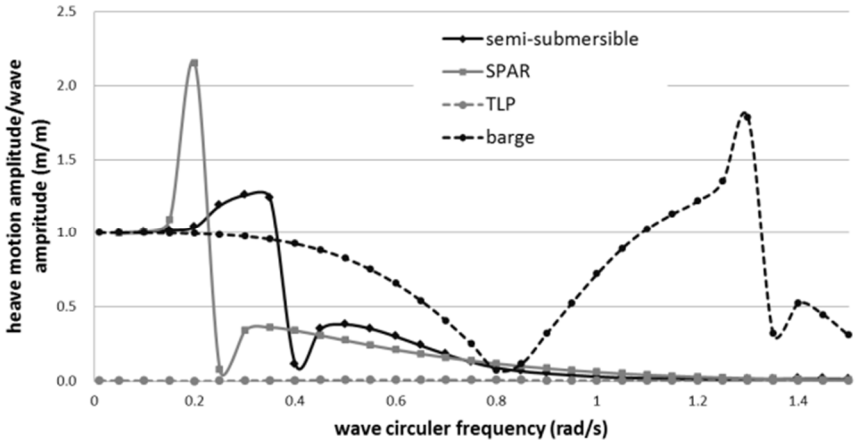

Figure 2-14 RAOs for Heave

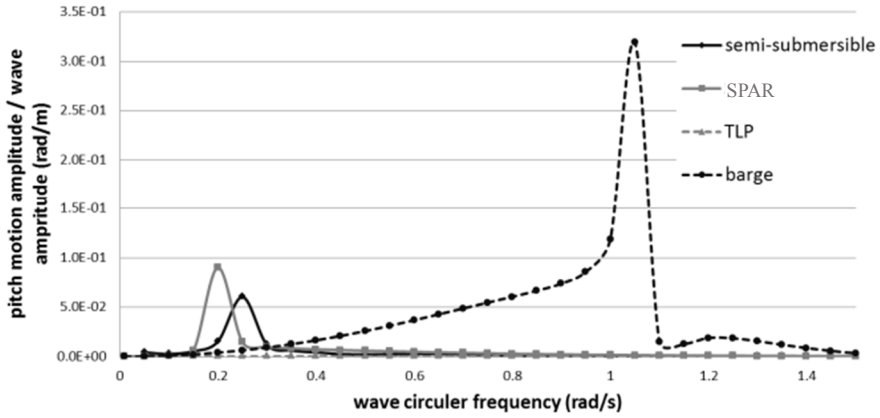

Figure 2-15 RAOs for Pitch

Figure 2-16 compares RAOs of the bending stress at the base of the tower. The bending moment is mainly affected by the inertia force of the nacelle and tower. In this regard, the pitch acceleration is relevant to the bending moment at the base. In the frequency range less than 0.5 rad/s, the response of the SPAR is the largest due to the low natural frequency of pitch motion as discussed. In the range more than 0.5 rad/s, that of the barge is the largest due to large pitch motion as shown in Figure 2-15. On the other hand, the responses of the semi-submersible type and the TLP type are smaller.

Figure 2-17 compares the horizontal acceleration RAOs at the nacelle. It is confirmed that the peaks and troughs of the curves in Figure 2-15 resemble those in Figure 2-17. In addition, it is to be noted that the effect of gravity on the element after displacement is added up. In this case, the horizontal force given by a product of gravity acceleration and pitch angle is exerted to the nacelle. In the case of the semi-sub, the aforesaid resonance of elastic oscillation is appeared as the peak. From the above, inertial force on the top of the tower, effect of gravity by inclination and resonance of elastic oscillation can be reasons why the bending stress becomes large.

Table 2-3 shows the comparisons of the heel angle under wind thrust, the restoring moment coefficient and bending stress at the base of tower due to the wind thrust. The SPAR is easily influenced by the wind load because it has the smallest restoring moment coefficient.

The heel angle of the barge type is comparable to that of the semi-sub in spite of the fact that the barge type has the largest restoring moment coefficient. It is because the barge has two rotors and is subjected to the twice the wind loads. Even then, the heel angle is 0.78 deg. The angle of the TLP type is much smaller than that of the semi-sub type. In sum, the heel angle to the wind load of the SPAR type, the semi-sub type, the barge type, and the TLP type are larger in order. The bending stress of the SPAR is the

largest among the others although they have the same tower and rotor. It is mainly attributed to the inclined gravity effect in addition to the direct wind thrust on the rotor.

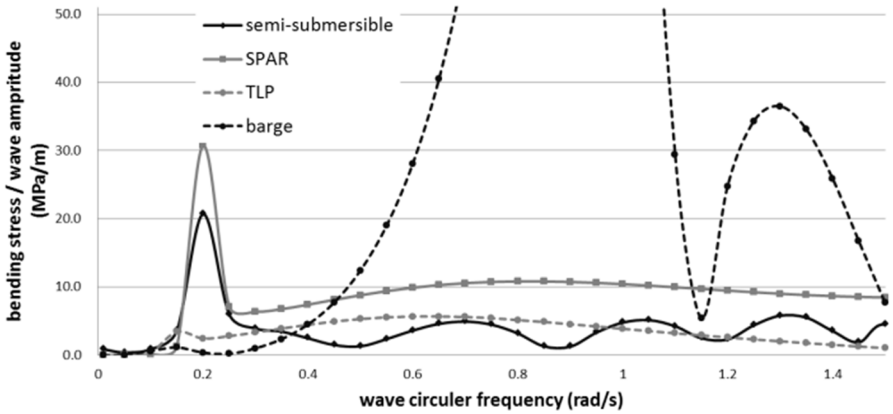

Figure 2-16 Bending Stress RAO

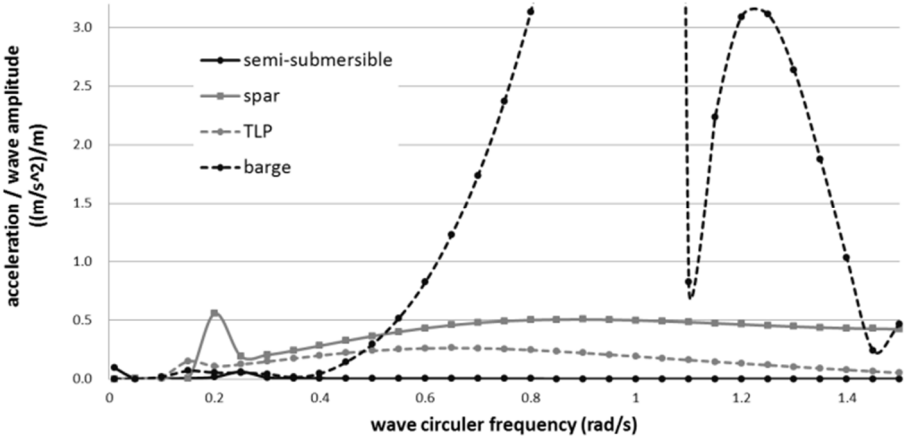

Figure 2-17 Nacelle Horizontal Acceleration RAO

Table 2-3 Comparisons of the parameters under wind thrust

	semi-submersible	SPAR	TLP	barge	unit
Inclination under wind	3.02	9.21	0.49	0.78	deg
Restoring moment coefficient	5.90 x10^9	2.44 x10^9	6.88 x10^{10}	1.80 x10^{10}	Nm
Bending stress	71.8	101.6	66.7	63.0	MPa

2.3 The OU-Design for FOWT

In this section, a new design for FOWT is introduced which is called OU-Design [26] [27]. According to the discussion in section 2.2, the pontoon type is firstly abandoned. TLP type may be one good choice, but considering the high installation cost for the tension leg, it was given up as well. Similar type as SWAY (see Figure 2-10) may be a good idea. But SWAY also has some demerit as follows:

- Spar type of floater needs high water draft to obtain the sufficient restoring moment which means that Spar type of FOWT can only be installed in deep sea.
- Due to the large draft, lots of construction and installation works have to be done far away from the quay where the water is deep enough. Besides, the complex installation must be done in short time.
- Due to the long slender structure, the inner stress is another serious problem which may cause the structural failure.
- The reliability of yaw bearing for the single-point-mooring system should be studied more as well.

At the end, we selected the semi-sub type of main floater to support the wind turbine and single-point-mooring system to locate the FOWT. The following advantage can be desired by introducing the semi-sub type of main floater.

- As the draft is relatively small compared with the SPAR, the semi-sub type of main floater can be constructed easily in dockyard.
- Wind turbine can be installed immediately after the construction of main floater. After towing the whole system to the site directly, the installation of main floater is completed.

The prototype of OU-Design is shown in Figure 2-18. The most distinct feature is introducing the SPM system to maintain the main floater which has been mainly adopted for FPSOs. The merit of SPM system can be concluded:

- Less anchors are necessary
- Installing mooring on the buoy with a relatively small dimension is obviously much easier than installing the mooring directly on the main floater.
- The connection work between the buoy and the main floater is also easy as it is conducted above the water.
- Small footprint is required compared with the catenary mooring system.

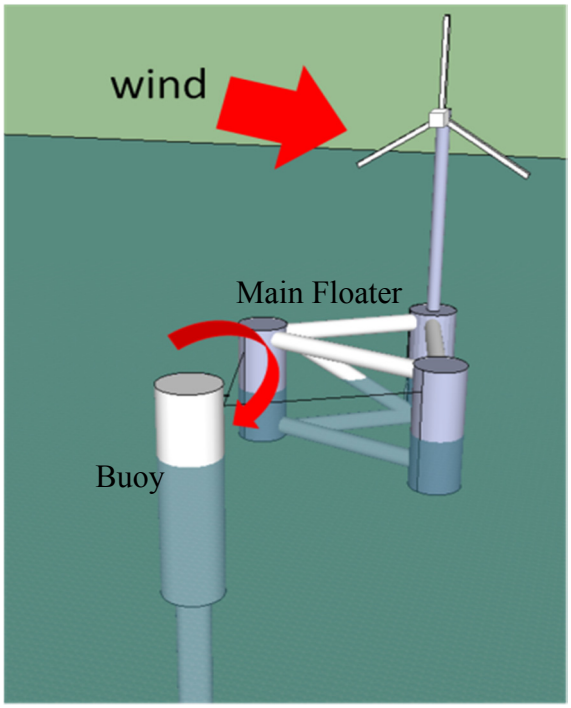

Figure 2-18 the prototype of OU-Design

Even though more motion freedom for the main floater may be induced as the result of its introduction, OU-Design, once appropriately designed, may give advantages including the property of weathervane. Due to the weathervane, the main floater with nacelle and rotor can freely rotate around the buoy which is moored to the seabed. Therefore, the yaw control system which is applied for optimizing the face of the rotor in most conventional design is not necessary. The simple mechanism may be advantageous in terms of installation cost, too.

2.3.1 Environmental conditions and specifications

The design environmental condition is given in Table 2-4.

Table 2-4 Environmental condition

Work Condition	Wind Velocity [m/s]	Wind thrust [kN]	Wave height [m]	Wave Period [sec]
Rated	12	1100	3.0	7.0
Cut-Out	25	1200	7.0	10.0

The wind turbine is assumed to have a generic 5MW wind turbine. The principal particulars of the turbine are presented in Table 2-5. It is similar to NREL 5MW wind turbine [17].

Table 2-5 Principal particulars of the wind turbine

Item	Value	Unit
Capacity	5	MW
Number of blades	3	-
Blade diameter	120	m
Height of the hub	80	m
Blade mass	20	tons/a blade
Rotor mass	60	tons
Nacelle mass	290	tons
Tower mass	468	tons
Total mass	838	tons
Tower diameter(Min)	5	m
Tower diameter(Max)	8	m

2.3.2 Design parameters

In determining the size and arrangement of the main floater, the followings are regarded as parameters.

・draft

・diameter of column

・height and width of lower hull

・column space

The following items must be considered in determining these parameters.

・Total weight balances with the buoyancy.

・GM is positive.

・The heel angle should be well below 5 degree to the wind thrust load of 1200kN (incl. thrust and drag of tower)

・Natural periods of heave, pitch and roll are more than 20s to have a good performance in waves.

・The water depth could be arbitrary, however, 50m-150m is the target of the present system.

A set of the parameters which satisfy the above is finally chosen after trials and errors (see Figure 2-19) even though an optimization is not necessarily done with regards to the cost and performance. An appropriate buoy and a tendon which give a sufficient restoring force are also selected.

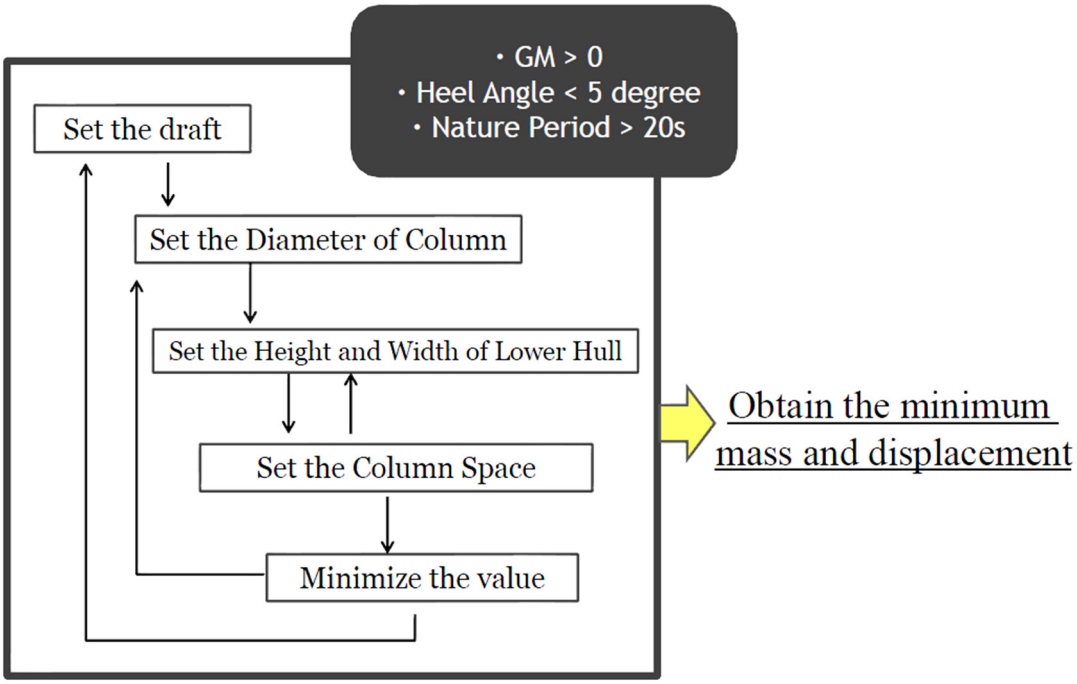

Figure 2-19 Design Flowchart

2.3.3 Weather vane

In order to confirm the function of weathervaning, a series of experiments were done with certain offset angles between wind direction and main floater (Figure 2-20). A position marker was attached on one of the columns as shown in Figure 2-21.

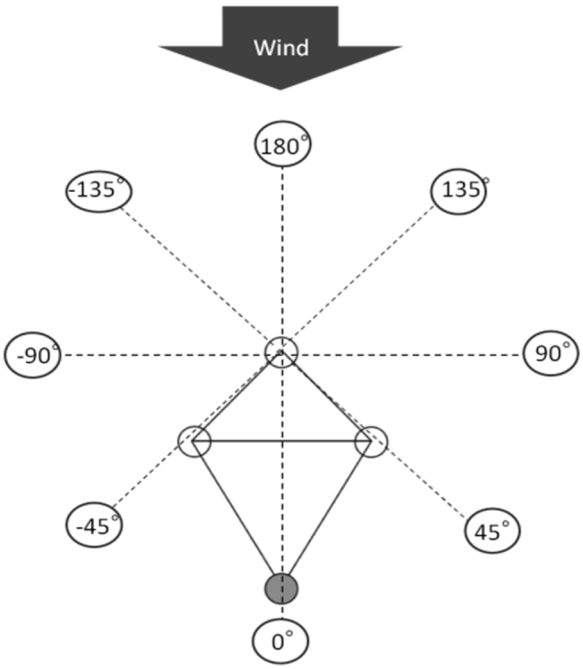

Figure 2-20 Initial position of the body for weather-vane test

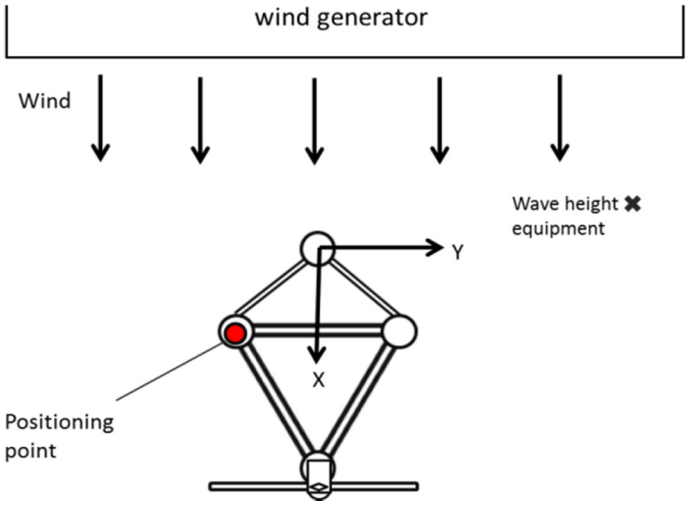

Figure 2-21 X-Y coordinate system on weather-vane test

Figure 2-22 shows the example of trajectory of LED in terms of x-y coordinates of Figure 2-21 where the cross marks means the starting points and black circle corresponds to the ending points. The appearance can be seen from Figure 2-23.

From these tests it is confirmed that in all initial positions from -180 degree to 180 degree weathervane is possible. However, in the cases of the initial position -180, -135, 135, 180 degree first turbine began to anti-clockwise rotation. Then, at 90 degrees, the turbine does not rotate because drag due to wind goes to zero and at smaller angle than 90 degrees starts rotating in the clock-wise. In order to put to practical use, some

ingenuity for this phenomenon will be required. In addition, it should be noted that in the initial position -180 and 180 degree, the structure always rotated counterclockwise as viewed from above around the buoyancy tank.

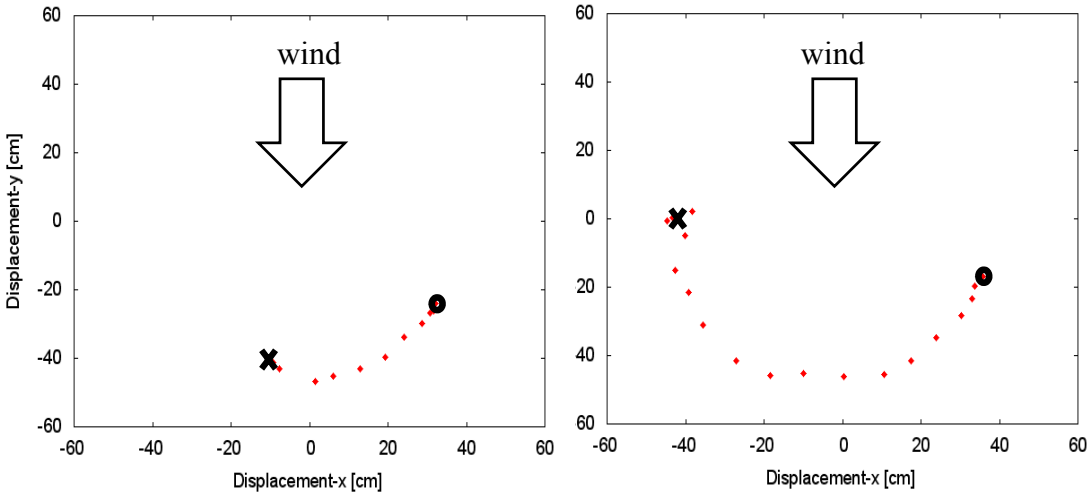

Figure 2-22 Trajectory for the case with an offset angle at -45 and -135degs. Circles plotted at an interval of 5s.

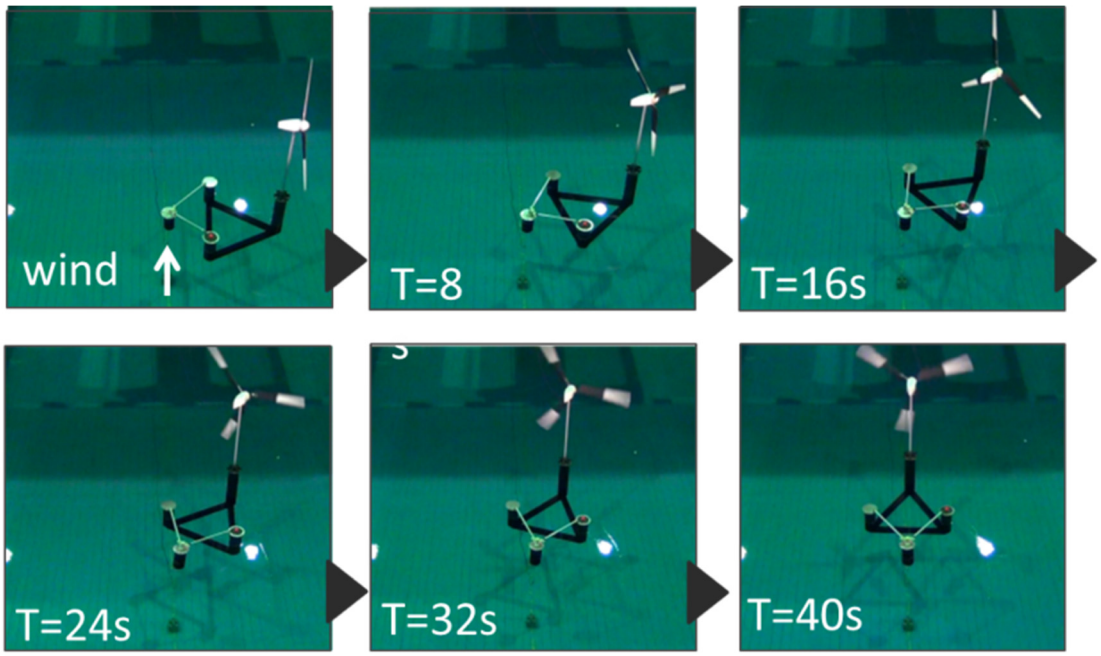

Figure 2-23 Appearance of weathervane test

2.4 Conclusions

In this chapter, several FOWT projects are introduced firstly. Four kinds of FOWT consisting of semi-sub, SPAR, TLP and barge in terms of 6DOF motions, structural load, nacelle acceleration and static inclination under wind are investigated based on the results of frequency-domain simulation. Based on the comparison, a new concept of FOWT named as OU-Design is proposed. By this new design, the construction and installation process can be simplified. In addition, the weathervane property due to the utilization of SPM was proven by the model test.

More results of model tests for OU-Design are introduced in Chapter 5 by comparing with simulation results.

3 NUMERICAL SIMULATION THEORY

In this chapter, the theory utilized in DYNABEAM simulation tool is introduced for both linear frequency domain and nonlinear time domain models.

3.1 The Linear Frequency Domain Model

3.1.1 Hydrodynamics

Linear wave potential theory is basically adopted with the assumptions that the fluid be inviscid and incompressive with irrotational motion. For offshore platform, there is no influence caused by forward speed. To obtain the hydrodynamic coefficients, 3D panel method based on Green function is employed [28] [29].

The potential around the platform under regular wave with angular frequency ω can be written as

$$\phi = \phi_0 + \phi_d + \sum_{j=1}^{6} -i\omega a_j \phi_j \qquad \textbf{(3-1)}$$

where, the time-dependent term $e^{-i\omega t}$ is dropped. ϕ_0 and ϕ_d mean the incident wave potential and diffraction potential. ϕ_j represents the radiation potential to the motion mode j with unit velocity. a_j is an complex value which includes the amplitude and phase for mode j.

As the potential ϕ must satisfy the Laplace equation and boundary conditions, the following equations can be derived:

$$\frac{\partial^2 \phi}{\partial x^2} + \frac{\partial^2 \phi}{\partial y^2} + \frac{\partial^2 \phi}{\partial z^2} = 0 \quad \text{Laplace, in the fluid domain} \qquad \textbf{(3-2)}$$

$$-\omega^2 \phi + g \frac{\partial \phi}{\partial z} = 0 \quad \text{free surface, on } z=0 \qquad \textbf{(3-3)}$$

$$\frac{\partial \phi}{\partial z} = 0 \qquad \text{on } z=-h, \text{ sea bottom} \qquad \textbf{(3-4)}$$

$$\frac{\partial \phi_0}{\partial n} + \frac{\partial \phi_d}{\partial n} = 0 \qquad \text{diffraction ,on the mean position of platform surface} \qquad \textbf{(3-5)}$$

$$\frac{\partial \phi_i}{\partial n} = n_i \qquad \text{radiation, on the mean position of platform surface} \qquad \textbf{(3-6)}$$

where, n is the unit normal vector to the platform which defined as positive when pointing into the fluid domain.

The wave-exciting force, added mass and damping coefficient can be finally calculated once the source strength is determined based on Eq. (3-2) to (3-6) [29]. To obtain these hydrodynamic coefficients, one numerical tool (SDM) [28] based on source-distributed-method is utilized. It should be noted that, the hydrodynamic interaction between the floater and mooring system is not accounted for in the present DYNABEAM by introducing the assumption that the mooring system has relatively small body dimension compared with the distance between the mooring system and the floater. By comparing the simulation results with the model test data (Chapter 4 and 5), the reasonability of this simplification is proven.

3.1.2 Model establishing

a) Element subdivision

The structure of platform is divided into finite elements as shown in Figure 3-1:

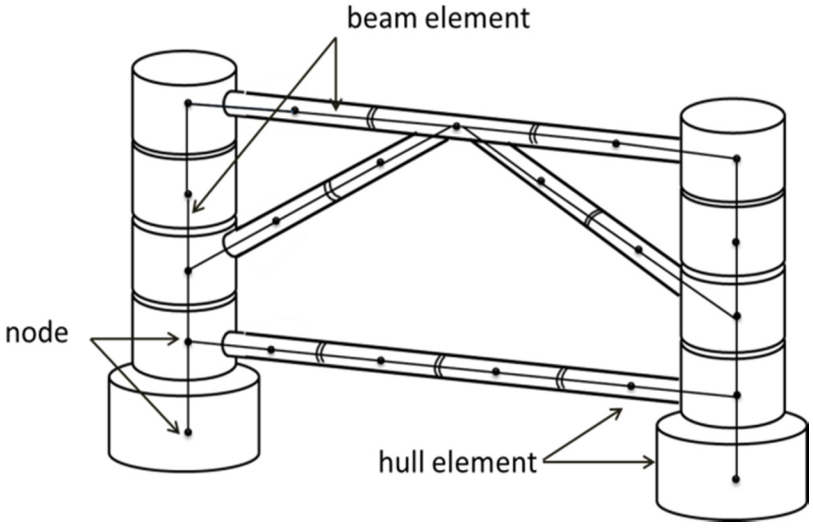

Figure 3-1 Two Kinds of Analysis Element

The hull element is used for estimating external forces (including inertia force for convenience). During simulation, all the external forces are integrated along the surface or the volume of the element to derive a concentrated force and moment in the node which representing all the external forces acting on the element.

Beam element is defined as straight column whose ends are located on the node of hull element. Based on the stiffness matrix, the beam element provides another viewpoint to evaluate the external force in both ends. Due to the assumption of small displacement, the stiffness matrix is considered as constant.

Finally, the equation of motion will be derived because the force for both kinds of element should be equivalent.

b) Coordinate system

In the formulation of the equations of motion, five kinds of coordinate systems are used as shown in Figure 3-2.

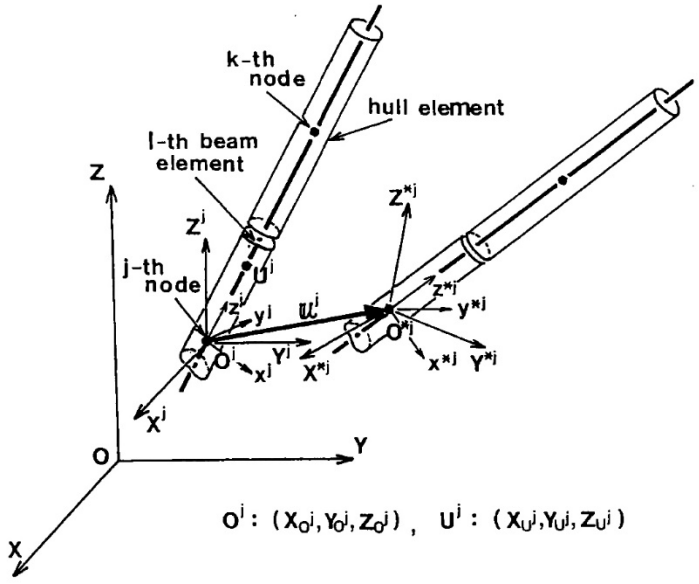

Figure 3-2 Coordinate Systems

- *XYZ* is a space-fixed global coordinate system, where the origin is located at the distance *d* below the still-water surface. The *XY*-plane is parallel to the still-water surface and the *Z*-axis is positive upwards. In this coordinate system, an incident wave and wave potential are expressed as follows:

$$\eta = a\,cos\{k(X\cos(\chi) + Y\sin(\chi)) - \omega t\}, \qquad Z \le d \qquad \textbf{(3-7)}$$

$$\Phi = \frac{ga}{\omega}\frac{\cosh\{k(Z-d+h)\}}{\cosh(kh)} sin\{k(X\cos(\chi) + Y\sin(\chi)) - \omega t\}, \qquad Z \le d \qquad \textbf{(3-8)}$$

where

η: surface elevation; Φ: velocity potential

a: wave amplitude; k: circular wave number

χ: angle of incident wave; ω: circular frequency

t: time; g: acceleration of gravity

h: water depth; d:draft

- O^j-$X^jY^jZ^j$ is element-wise space-fixed coordinate system whose origin O^j is taken at the pre-displacement position of j-th node and the axes are parallel to the global ones. This coordinate system is mainly used to deal with the buoyancy force. Meanwhile, it also acts as an intermediate system to transform the external force into O^{*j}-$X^{*j}Y^{*j}Z^{*j}$.
- o^j-$x^jy^jz^j$ is also element-wise space-fixed coordinate system. But its z-axis is taken at the pre-displacement position of the longitudinal axis of the element and the x-axis is defined so that the x^jz^j-plane may become vertical in the space. This system is also used as an intermediate system.
- O^{*j} -X^{*j} Y^{*j} Z^{*j} is element-fixed coordinate system. It initially coincides with O^j -X^j Y^j Z^j and move with the element. The equation of motion is derived from the equivalence of force in this system.
- o^{*j} -x^{*j} y^{*j} z^{*j} is also so-called element-fixed coordinate systems. But it coincides with o^j -x^j y^j z^j which is different with O^{*j} -X^{*j} Y^{*j} Z^{*j}. It is mainly used to calculate the inertia force, hydrodynamic force and the stiffness matrix of beam element.

Position vectors X, X^j, x^j, X^{*j} and x^{*j} are defined in the coordinate system implied by each symbolic nomenclature. In the same manner, the translational displacement vectors are defined as $\boldsymbol{U^j} = \{U^j\ V^j\ W^j\}^T$ and $\boldsymbol{u^j} = \{u^j\ v^j\ w^j\}^T$ corresponding to X^j and x^j, respectively and the rotational displacement vectors are defined as $\boldsymbol{\Theta^j} = \{\Phi^j\ \Theta^j\ \Psi^j\}^T$ and $\boldsymbol{\theta^j} = \{\varphi^j\ \theta^j\ \psi^j\}^T$ which are positive if they are clockwise about each axis of the corresponding coordinate system. The force vectors F^j, f^j, F^{*j}, f^{*j} are defined corresponding to X^j, x^j, X^{*j}, x^{*j} respectively and the moment vectors M^j, m^j, M^{*j}, m^{*j} are defined as to be clockwise about each axis of the corresponding coordinate system.

The transformation matrix C_S^j between the coordinate system O^j-$X^jY^jZ^j$ and o^j-$x^jy^jz^j$ is defined as follows.

$$x^j = C_S^j\ X^j \qquad \textbf{(3-9)}$$

where,

$$C_s^{\ j} = \begin{pmatrix} a_x & b_x & c_x \\ a_y & b_y & c_y \\ a_z & b_z & c_z \end{pmatrix} = \begin{pmatrix} \dfrac{\Delta_x \Delta_z}{\Delta} & \dfrac{\Delta_y \Delta_z}{\Delta} & -\Delta \\ -\dfrac{\Delta_y}{\Delta} & \dfrac{\Delta_x}{\Delta} & 0 \\ \Delta_x & \Delta_y & \Delta_z \end{pmatrix}$$

$$\Delta_x = \frac{(X_u^{\ j} - X_0^{\ j})}{L_0}, \Delta_y = \frac{(Y_u^{\ j} - Y_0^{\ j})}{L_0}, \Delta_z = \frac{(Z_u^{\ j} - Z_0^{\ j})}{L_0}$$

$$\Delta = \sqrt{\Delta_x^{\ 2} + \Delta_y^{\ 2}}, L_0 = \sqrt{(X_u^{\ j} - X_0^{\ j})^2 + (Y_u^{\ j} - Y_0^{\ j})^2 + (Z_u^{\ j} - Z_0^{\ j})^2}$$

C_s^j can also be utilized to transform the coordinate system O^{*j}-$X^{*j}Y^{*j}Z^{*j}$ and o^{*j}-$x^{*j}y^{*j}z^{*j}$ as

$$x^{*j} = C_S^j \, X^{*j} \qquad \textbf{(3-10)}$$

Moreover, the transformation of the displacement, force and moment are obtained as follows,

$$\begin{aligned} u^j &= C_S^j \, U^j \quad , \quad \theta^j = C_S^j \, \Theta^j \\ f^j &= C_S^j \, F^j \quad , \quad m^j = C_S^j \, M^j \\ f^{*j} &= C_S^j \, F^{*j} \quad , \quad m^{*j} = C_S^j \, M^{*j} \end{aligned} \qquad \textbf{(3-11)}$$

On the other hand, the transformation matrices between the space-fixed coordinate systems and the element-fixed ones contain the displacements temporarily and are expressed as follows,

$$X^{*j} = A_S^j \left(X^j - \ U^j \right) \qquad \textbf{(3-12)}$$

$$x^{*j} = a_S^j \left(x^j - \ u^j \right) \qquad \textbf{(3-13)}$$

where,

$$A_s^{\ j} = \begin{pmatrix} 1 & \Psi^j & -\Theta^j \\ -\Psi^j & 1 & \Phi^j \\ \Theta^j & -\Phi^j & 1 \end{pmatrix} \qquad a_s^{\ j} = \begin{pmatrix} 1 & \psi^j & -\theta^j \\ -\psi^j & 1 & \phi^j \\ \theta^j & -\phi^j & 1 \end{pmatrix}$$

The relations of the force and moment vectors in the two kinds of coordinate system

are expressed as

$$\begin{aligned} F^{*j} &= A_S^j F^j \quad , \quad M^{*j} = A_S^j M^j \\ f^{*j} &= a_S^j f^j \quad , \quad m^{*j} = a_S^j m^j \end{aligned} \tag{3-14}$$

c) External forces of hull element

External forces of hull element include gravity force, inertia force, hydrostatic force, hydrodynamic force. To keep the mathematical unitarily for different force, all of these forces should be described at the same coordinate system at last. For convenience of calculation, the coordinate system O^{*j}-$X^{*j}Y^{*j}Z^{*j}$ is selected.

- Gravity Force

The gravity force vector of *j*-*t*h hull element is expressed in O^{*j}-$X^{*j}Y^{*j}Z^{*j}$ using A_S^j as follows,

$$F_G^{*j} = A_S^j \{0 \;\; 0 \;\; -M^j g\}^T = \begin{Bmatrix} 0 \\ 0 \\ -M^j g \end{Bmatrix} - \begin{bmatrix} 0 & -M^j g & 0 \\ M^j g & 0 & 0 \\ 0 & 0 & 0 \end{bmatrix} \Theta^j \tag{3-15}$$

$$\begin{aligned} M_G^{*j} &= C_S^{jT} \left(\begin{Bmatrix} 0 \\ 0 \\ l_z^j \end{Bmatrix} \times C_S^j F_G^{*j} \right) \\ &= M^j g l_z^j \begin{Bmatrix} -b_z \\ a_z \\ 0 \end{Bmatrix} + M^j g l_z^j \begin{bmatrix} c_z & 0 & 0 \\ 0 & c_z & 0 \\ -a_z & -b_z & 0 \end{bmatrix} \Theta^j \end{aligned} \tag{3-16}$$

where, l_z^j is the distance between the node and the center of gravity of the element. a_z, b_z, c_z are defined in transformation matrix C_S^j.

- Inertia Force

The inertia force and moment are expressed as follows,

$$f_{Ig}^{*j} = -\begin{bmatrix} M^j & 0 & 0 \\ 0 & M^j & 0 \\ 0 & 0 & M^j \end{bmatrix} \ddot{u}_g^j \tag{3-17}$$

$$m_{Ig}^{*j} = -\begin{bmatrix} I_\varphi^j & 0 & 0 \\ 0 & I_\theta^j & 0 \\ 0 & 0 & I_\psi^j \end{bmatrix} \ddot{\theta}_g^j \tag{3-18}$$

The subscript g means this vector is defined at the center of gravity of the element. I_φ^j, I_θ^j, I_ψ^j are the moments of inertia of the element.

Then, transforming f_{Ig}^{*j} and m_{Ig}^{*j} to f_I^{*j} and m_I^{*j} whose acting point is the node of the hull element.

$$f_I^{*j} = f_{Ig}^{*j} \quad \textbf{(3-19)}$$

$$m_I^{*j} = m_{Ig}^{*j} + \begin{Bmatrix} 0 \\ 0 \\ l_z^j \end{Bmatrix} \times f_I^{*j} \quad \textbf{(3-20)}$$

$$\ddot{u}_g^j = \ddot{u}^j - \begin{Bmatrix} 0 \\ 0 \\ l_z^j \end{Bmatrix} \times \ddot{\theta}^j \quad \textbf{(3-21)}$$

$$\ddot{\theta}_g^j = \ddot{\theta}^j \quad \textbf{(3-22)}$$

where $\ddot{u}^j$ and $\ddot{\theta}^j$ are acceleration vectors at the node.
Thus the force and moment in O^{*j}-$X^{*j}Y^{*j}Z^{*j}$ are obtained by using C_s^j as follows,

$$F_I^{*j} = -C_S^{jT} \begin{bmatrix} M^j & 0 & 0 \\ 0 & M^j & 0 \\ 0 & 0 & M^j \end{bmatrix} C_S^j \ddot{U}^j - C_S^{jT} \begin{bmatrix} 0 & M^j l_z^j & 0 \\ -M^j l_z^j & 0 & 0 \\ 0 & 0 & 0 \end{bmatrix} C_S^j \ddot{\Theta}^j \quad \textbf{(3-23)}$$

$$M_I^{*j} = -C_S^{jT} \begin{bmatrix} 0 & -M^j l_z^j & 0 \\ M^j l_z^j & 0 & 0 \\ 0 & 0 & 0 \end{bmatrix} C_S^j \ddot{U}^j - C_S^{jT} \begin{bmatrix} I_\varphi^j + M^j {l_z^j}^2 & 0 & 0 \\ 0 & I_\theta^j + M^j {l_z^j}^2 & 0 \\ 0 & 0 & I_\psi^j \end{bmatrix} C_S^j \ddot{\Theta}^j \quad \textbf{(3-24)}$$

- Hydrostatic Force

The hydrostatic force is caused by the buoyancy due to static water pressure. As the definition of the wave surface elevation, the static water pressure can be estimated as

$$p_s = \rho g(d - Z), \qquad Z \le d + \eta \quad \textbf{(3-25)}$$

If the element is partially immersed, the region of integration varies with time due to the relative motion between the element and the water surface elevation. For simplifying the process of integration, the force is calculated under coordinate system o^{*j}-$x^{*j}y^{*j}z^{*j}$. And then transform the force f^{*j} into F^{*j} using transformation matrix C_s^j. The specific procedure is shown below:

$$\mathrm{X} = C_S^{jT} \left(a_S^{jT} x^{*j} + u^j \right) + X_0^j \quad \textbf{(3-26)}$$

The component *Z* is written as,

$$\begin{aligned} \mathrm{Z} = c_x\left(x^{*j} - y^{*j}\psi^j + z^{*j}\theta^j + u^j\right) + c_y\left(y^{*j} - z^{*j}\varphi^j + x^{*j}\psi^j + v^j\right) \\ +c_z\left(z^{*j} - x^{*j}\theta^j + y^{+j}\varphi^j + w^j\right) + Z_0^j \end{aligned} \quad \textbf{(3-27)}$$

In the pre-displacement condition, the free surface is expressed by *Z=d.*

Therefore, the following equation is formed on the center axis of the element$\left(x^{*j} = y^{*j} = 0\right)$

$$c_z z^{*j} = d - Z_0^j \quad \textbf{(3-28)}$$

The above equation can be used for judging by substituting l_2^j or l_1^j into z^{*j} whether the element is fully-immersed or not, where l_2^j or l_1^j is the distance between node and upper or lower end of the hull element.

$z_u^{*j} = l_2^j$ (fully-immersed element)

$$z_u^{*j} = \frac{d - Z_0^j}{c_z} - \frac{\eta}{c_z} - \frac{c_x u^j + c_y v^j + c_z w^j}{c_z} - \frac{\left(d - Z_0^j\right)\left(c_y\varphi^j - c_z\theta^j\right)}{{c_z}^2} \quad \textbf{(3-29)}$$

(partially-immersed element)

On the other hand, the static water pressure is expressed in o^{*j}-$x^{*j}y^{*j}z^{*j}$ using Eq.(2.18) as follows.

$$\begin{aligned} p_s = \rho g\,\{d - Z_0^j - \left(c_z + c_y\psi^j - c_z\theta^j\right)x^{*j} - \left(c_y + c_z\varphi^j - c_x\psi^j\right)y^{*j} \\ - \left(c_z + c_x\theta^j - c_y\varphi^j\right)y^{*j} - c_x u^j - c_y v^j - c_z w^j\} \end{aligned} \quad \textbf{(3-30)}$$

Integrating p_s over the immersed surface, the buoyancy due to static water pressure is approximately estimated under assumption that incident wave are regular waves with small amplitude and the length of wave is long enough compared with sectional of structural members.

$$\begin{aligned} f_S^{*j} &= \iint p_S n\ ds^{*j} \\ &= \iiint_V -\nabla^{*j} p_S dv^{*j} \\ &\approx \int_{-l_1^j}^{z_u^{*j}} -\rho g A^j \begin{Bmatrix} -c_x - c_y\psi^j + c_z\theta^j \\ -c_y - c_z\varphi^j + c_x\psi^j \\ -c_z - c_x\theta^j + c_y\varphi^j \end{Bmatrix} dz^{*j} \end{aligned} \quad \textbf{(3-31)}$$

where,

$$\nabla^{*j} \equiv \left\{ \frac{\partial}{\partial x^{*j}} \quad \frac{\partial}{\partial y^{*j}} \quad \frac{\partial}{\partial z^{*j}} \right\}^T$$

n is the normal vector of submerged surface (positive direction is into the submerged surface). $\iint ds^{*j}$ and $\iiint_V dv^{*j}$ are integrations over area and volume. A^j is the sectional area of the element.

Consequently, the force due to static water pressure is estimated in O^{*j}-$X^{*j}Y^{*j}Z^{*j}$ as follows,

For fully-immersed element,

$$\begin{aligned} F_S^{*j} &= \begin{Bmatrix} 0 \\ 0 \\ \rho g A^j \left(l_2^j + l_1^j \right) \end{Bmatrix} \\ &\quad -\rho g A^j \left(l_2^j + l_1^j \right) C_S^{jT} \begin{bmatrix} 0 & c_z & -c_y \\ -c_z & 0 & c_x \\ c_y & -c_x & 0 \end{bmatrix} C_S^j \Theta^j \end{aligned} \qquad \textbf{(3-32)}$$

For partially-immersed element,

$$\begin{aligned} F_S^{*j} &= \begin{Bmatrix} 0 \\ 0 \\ \rho g A^j \left(\dfrac{d - Z_0^j}{c_z} + l_1^j \right) \end{Bmatrix} \\ &\quad -\rho g A^j \left(\frac{d - Z_0^j}{c_z} + l_1^j \right) C_S^{jT} \begin{bmatrix} 0 & c_z & -c_y \\ -c_z & 0 & c_x \\ c_y & -c_x & 0 \end{bmatrix} C_S^j \Theta^j \\ &\quad -\frac{\rho g A^j}{c_z} C_S^{jT} \begin{bmatrix} c_x^2 & c_x c_y & c_x c_z \\ c_x c_y & c_y^2 & c_y c_z \\ c_x c_z & c_y c_z & c_z^2 \end{bmatrix} C_S^j U^j \\ &\quad -\frac{\rho g A^j \left(d - Z_0^j \right)}{{c_z}^2} C_S^{jT} \begin{bmatrix} -c_x c_y & c_x^2 & 0 \\ -c_y^2 & c_x c_y & 0 \\ -c_y c_z & c_x c_z & 0 \end{bmatrix} C_S^j \Theta^j \end{aligned} \qquad \textbf{(3-33)}$$

The moment due to buoyancy is estimated as follows,

$$m_S^{*j} = \iiint_V \begin{Bmatrix} \mathrm{x}^{*j} \\ \mathrm{y}^{*j} \\ \mathrm{z}^{*j} \end{Bmatrix} \times \left(-\nabla^{*j} p_S \right) dv^{*j} \qquad \textbf{(3-34)}$$

For fully-immersed element,

$$\begin{aligned} M_S^{*j} &= \rho g A^j \frac{l_2^{j2} - l_1^{j2}}{2} \begin{Bmatrix} b_z \\ -a_z \\ 0 \end{Bmatrix} \\ &\quad -\rho g A^j \frac{l_2^{j2} - l_1^{j2}}{2} C_S^{jT} \begin{bmatrix} c_z & 0 & -c_x \\ 0 & c_z & -c_y \\ 0 & 0 & 0 \end{bmatrix} C_S^j \Theta^j \end{aligned} \qquad \textbf{(3-35)}$$

For partially-immersed element,

$$
\begin{aligned}
M_S^{*j} = \rho g A^j \frac{\left(\frac{d - Z_0^j}{c_z}\right)^2 - l_1^{j2}}{2} \begin{Bmatrix} b_z \\ -a_z \\ 0 \end{Bmatrix} \\
-\rho g A^j \frac{\left(\frac{d - Z_0^j}{c_z}\right)^2 - l_1^{j2}}{2} C_S^{jT} \begin{bmatrix} c_z & 0 & -c_x \\ 0 & c_z & -c_y \\ 0 & 0 & 0 \end{bmatrix} C_S^j \Theta^j \\
-\rho g A^j \frac{d - Z_0^j}{{c_z}^2} C_S^{jT} \begin{bmatrix} -c_x c_y & -c_y^2 & -c_y c_z \\ c_x^2 & c_x c_y & c_x c_z \\ 0 & 0 & 0 \end{bmatrix} C_S^j U^j \\
-\rho g A^j \frac{\left(d - Z_0^j\right)^2}{{c_z}^2} C_S^{jT} \begin{bmatrix} c_y^2 & -c_x c_y & 0 \\ -c_x c_y & c_x^2 & 0 \\ 0 & 0 & 0 \end{bmatrix} C_S^j \Theta^j \\
-\frac{\rho g \pi {R^j}^4}{4 c_z} C_S^{jT} \begin{bmatrix} c_x^2 & 0 & -c_x c_z \\ 0 & c_z^2 & -c_y c_z \\ -c_x c_z & -c_y c_z & c_x^2 + c_y^2 \end{bmatrix} C_S^j \Theta^j
\end{aligned}
\qquad \textbf{(3-36)}
$$

Note that the coupling influences of heave-pitch and heave-roll are neglected as all it provides high order influence on the hydrostatic restoring moment. However, this coupling is important when analyzing the instability of platform when the natural frequency meets some criteria. This part will be discussed in Chapter 6 as a Mathieu instability problem.

- Hydrodynamic force

The hydrodynamic coefficient calculated based on the linear potential theory (see 3.1.1) is employed to obtain the hydrodynamic force. Then the hydrodynamic force can be written as:

$$F_D^{*j} = F_k^{*j} - M_a^j \ddot{U}^j - C_D^j \dot{U}^j \qquad \textbf{(3-37)}$$

where, F_k^{*j}, M_a^j, C_D^j are the wave excitation force, added mass and damping coefficient for element j correspondingly.

d) Stiffness matrix of beam element

From the viewpoint of beam element, the external force acting on the node can be also calculated by stiffness matrix of beam element. It is assumed that the displacement of beam element is small and the linearized displacement-strain relationship is accurate enough. Then the external force due to the structure stiffness can be calculated as:

$$\begin{Bmatrix} f_B^{*j} \\ m_B^{*j} \\ f_B^{*k} \\ m_B^{*k} \end{Bmatrix} = -\begin{bmatrix} K_{jj}^l & K_{jk}^l \\ K_{kj}^l & K_{kk}^l \end{bmatrix} \begin{Bmatrix} u^j \\ \theta^j \\ u^k \\ \theta^k \end{Bmatrix} \quad \textbf{(3-38)}$$

where script *j*, *k* means the number of node,

$$K_{jj}^l = \begin{bmatrix} 12EI_\theta/l^3 & 0 & 0 & 0 & 6EI_\theta/l^2 & 0 \\ & 12EI_\varphi/l^3 & 0 & -6EI_\varphi/l^2 & 0 & 0 \\ & & EA/l & 0 & 0 & 0 \\ & & & 4EI_\varphi/l & 0 & 0 \\ & (sym.) & & & 4EI_\theta/l & 0 \\ & & & & & -GJ_\psi/l \end{bmatrix} \quad \textbf{(3-39)}$$

$$K_{jk}^l = \begin{bmatrix} -12EI_\theta/l^3 & 0 & 0 & 0 & 6EI_\theta/l^2 & 0 \\ 0 & -12EI_\varphi/l^3 & 0 & -6EI_\varphi/l^2 & 0 & 0 \\ 0 & 0 & -EA/l & 0 & 0 & 0 \\ 0 & 6EI_\varphi/l^2 & 0 & 2EI_\varphi/l & 0 & 0 \\ -6EI_\theta/l^2 & 0 & 0 & 0 & 2EI_\theta/l & 0 \\ 0 & 0 & 0 & 0 & 0 & -GJ_\psi/l \end{bmatrix} \quad \textbf{(3-40)}$$

$$K_{kj}^l = K_{jk}^l \quad \textbf{(3-41)}$$

$$K_{kk}^l = \begin{bmatrix} 12EI_\theta/l^3 & 0 & 0 & 0 & -6EI_\theta/l^2 & 0 \\ & 12EI_\varphi/l^3 & 0 & -6EI_\varphi/l^2 & 0 & 0 \\ & & EA/l & 0 & 0 & 0 \\ & & & 4EI_\varphi/l & 0 & 0 \\ & (sym.) & & & 4EI_\theta/l & 0 \\ & & & & & GJ_\psi/l \end{bmatrix} \quad \textbf{(3-42)}$$

where EA is axial rigidity, EI_φ and EI_θ are bending rigidities, GJ_ψ is torsional rigidity and l is the length of the beam element.

Then, transfer the above force from coordinate system o^{*j}-$x^{*j}y^{*j}z^{*j}$ to coordinate system O^{*j}-$X^{*j}Y^{*j}Z^{*j}$:

$$\begin{Bmatrix} F_B^{*j} \\ M_B^{*j} \\ F_B^{*k} \\ M_B^{*k} \end{Bmatrix} = -\begin{bmatrix} C^{jT}K_{jj}^l C^l & C^{jT}K_{jk}^l C^l \\ C^{jT}K_{kj}^l C^l & C^{jT}K_{kk}^l C^l \end{bmatrix} \begin{Bmatrix} \delta^j \\ \\ \delta^k \end{Bmatrix} \quad \textbf{(3-43)}$$

where C^j is the coordinate transformation matrix which is defined as that in hull element.

e) Mooring force

Although the nonlinear mooring part will be analyzed separately with floating structure

part, the basic linear tension leg system is still attached in floating structure part to make the program more efficient when simplifying the mooring system as spring model.

For the tension leg system, attention must be paid to the high pretension in tendon when the restoring force due to the tendon is estimated. It is convenient to use a coordinate system fixed to the tendon which is called tendon-fixed coordinate system. Therefore, the mooring force can be obtained easily as linear spring force.

The longitudinal displacement of the mooring point of tendon generates tension variation, while the lateral displacement causes the directional change of the tendon-fixed coordinate system. The mooring force is estimated as the sum of pretension T_p^j and tension variation due to the longitudinal displacement w^j. Therefore, the mooring force vector f_T^{*j} in the tendon-fixed coordinate system is expressed as follows.

$$f_T^{*j} = \left\{ \begin{array}{ccc} 0 & 0 & -T_p^j - \dfrac{EA_l^j}{L^j} w^j \end{array} \right\}^T \qquad \textbf{(3-44)}$$

where EA_l^j and L^j are the axial rigidity and the initial length of tendon, respectively.

The transformation matrix C_L^{jT} from tendon-fixed coordinate system into space-fixed coordinate system is defined as

$$C_L^{jT} = \begin{bmatrix} 1 & 0 & u^j/L^j \\ 0 & 1 & v^j/L^j \\ -u^j/L^j & -v^j/L^j & 1 \end{bmatrix} \qquad \textbf{(3-45)}$$

where u^j and v^j are the components of lateral displacement.
The transfer the mooring force vector in the tendon-fixed coordinate system to hull element fixed coordinate system:

$$\begin{aligned} F_T^{*j} &= C_S^{jT} a_S^j C_L^{jT} f_T^{*j} \\ &= C_S^{jT} \begin{Bmatrix} 0 \\ 0 \\ -T_p^j \end{Bmatrix} - C_S^{jT} \begin{bmatrix} \dfrac{T_p^j}{L^j} & 0 & 0 \\ 0 & \dfrac{T_p^j}{L^j} & 0 \\ 0 & 0 & \dfrac{EA_l^j}{L^j} \end{bmatrix} C_S^j U^j - C_S^{jT} \begin{bmatrix} 0 & -T_p^j & 0 \\ T_p^j & 0 & 0 \\ 0 & 0 & 0 \end{bmatrix} C_S^j \Theta^j \end{aligned} \qquad \textbf{(3-46)}$$

f) Equation of motion

Assembling the forces and moments evaluated at all nodes, the equations of motion of a whole structure are formulated as follows,

$$(M + M_a)\ddot{\delta} + C_D\dot{\delta} + (K_r + K_B + K_T)\delta = F_K^*(t) + F_0^* \qquad \textbf{(3-47)}$$

where, M is the mass matrix; M_a is the added mass matrix

C_D is the hydrodynamic damping matrix;

K_r is the restoring matrix due to hull element

K_B is restoring matrix due to beam element

K_T is restoring matrix due to mooring element

$F_K^*(t)$ is the time dependent wave exciting force vector

F_0^* is the time constant force vector following: $F_0^* = F_{S0}^* + F_{G0}^* + F_{T0}^*$, which is zero if the system is initially balanced.

F_{S0}^* is the constant component of hydrostatic force

F_{G0}^* is the constant component of gravity force

F_{T0}^* is the constant component of mooring force

Due to the degree of freedom is six, the size of all the above matrices is 6N×6N and the size of force vector is 6N, where N is the number of free nodes. Solving Eq. (3-47) in frequency is easy as the external force $F_K^*(t)$ satisfies sinusoidal function.

3.2 The Nonlinear Time Domain Model

In this section, nonlinearity considered in DYNABEAM is discussed. Then the time domain solving procedure is demonstrated. The coupling technique is finally introduced.

3.2.1 Geometric nonlinear structural stiffness

In previous section, all the nonlinearities in beam stiffness are neglected with the assumption that the displacement of beam is small enough. This assumption may be sufficient for the analysis of floater with large scale. However, for the mooring system, due to the long length but small stiffness, the nonlinear influence of large displacement may occur by which the bifurcation or increased stiffness can be detected. The geometric nonlinearity incudes:

- Nonlinear influence of coordinate system transformation
- Nonlinear displacement –strain relationship

a) Nonlinear influence of coordinate system transformation

When the displacement of element becomes large, the stiffness matrix must be transformed from, while in sub-section 3.1.2 this transformation matrix is not considered. To simplify the problem, the utilized coordinate systems described in sub-section 3.1.2 are reduced from 4 to 2 which is enough for mooring model. The coordinate systems are defined as below,

The state vector of an element is defined by a vector which has as components the displacements and rotation of nodes at the both ends of the element

$$\{\delta\}_{12\times1} = ({}_1u_x, {}_1u_y, {}_1u_z, {}_1t_x, {}_1t_y, {}_1t_z, {}_2u_x, {}_1u_y, {}_1u_z, {}_1t_x, {}_1t_y, {}_1t_z) \qquad \textbf{(3-48)}$$

where u and t show displacement and rotation of nodes, and the left subscript indicate node.

The transformation matrix between space-fixed coordinate system and element-fixed coordinate system is no longer linear owing to the large displacement. According to the definition of the C_{sj} in section 3.1.2, the transformation matrix can be obtained as,

$$[A_s]=\begin{pmatrix} \frac{\Delta_x\Delta_z}{\Delta} & \frac{\Delta_y\Delta_z}{\Delta} & -\Delta \\ -\frac{\Delta_y}{\Delta} & \frac{\Delta_x}{\Delta} & 0 \\ \Delta_x & \Delta_y & \Delta_z \end{pmatrix} \qquad \textbf{(3-49)}$$

where

$$\Delta_x=\frac{({}_2u_x-{}_1u_x)}{L},\Delta_y=\frac{({}_1u_y-{}_1u_y)}{L},\Delta_z=\frac{({}_2u_z-{}_1u_z)}{L}$$
$$\Delta=\sqrt{\Delta_x{}^2+\Delta_y{}^2},L_0=\sqrt{({}_2u_x-{}_1u_x)^2+({}_1u_y-{}_1u_y)^2+({}_2u_z-{}_1u_z)^2} \qquad \textbf{(3-50)}$$

Note that coordinates X, Y, Z represent the transient position of relevant point

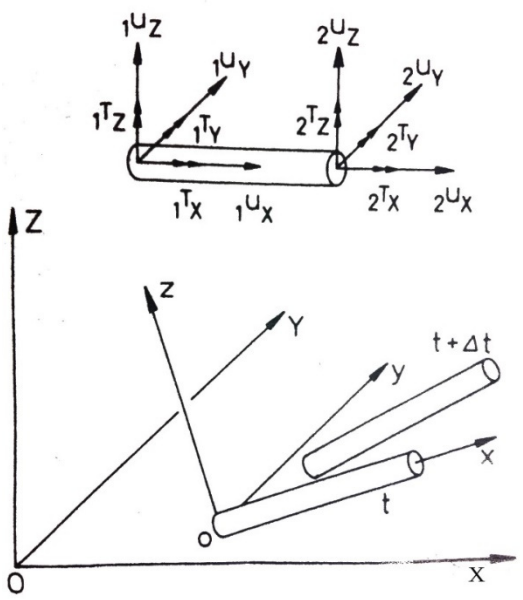

Figure 3-3 Coordinate System

These two coordinate systems include:

- Space-fixed coordinate system *O-XYZ*
- Element-fixed coordinate system *o-xyz*

The stiffness matrix $[K]^E$ derived in element system has to be transformed to space-fixed system before calculating the internal force:

$$[K]^G=[A_s]^T[K]^E[A_s] \qquad \textbf{(3-51)}$$

b) Nonlinear displacement –strain relationship

To obtain the displacement of any point in the axis of element, the hermite cubics interpolation function is selected [30].

Defining *V(x)* and *W(x)* as the deflection of the beam axis in the *y* and *z* directions, and *U(x)* as the displacement in the x direction,

$$\begin{Bmatrix} U(x) \\ V(x) \\ W(x) \end{Bmatrix} = \begin{Bmatrix} {}_1u_x\phi_1(x) + {}_2u_x\phi_2(x) \\ {}_1u_y\phi_3(x) + {}_1u_y\phi_4(x) + {}_1t_z\phi_5(x) - {}_1t_z\phi_6(x) \\ {}_1u_z\phi_3(x) + {}_1u_z\phi_4(x) - {}_1t_y\phi_5(x) + {}_1t_y\phi_6(x) \end{Bmatrix} = [C_n]_{3\times12}\{\delta\}_{12\times1} \qquad \textbf{(3-52)}$$

where,

$$\phi_1(x) = 1 - \frac{x}{L}$$

$$\phi_2(x) = \frac{x}{L}$$

$$\phi_3(x) = 1 - \frac{3x^2}{L^2} + \frac{2x^3}{L^3}$$

$$\phi_4(x) = \frac{3x^2}{L^2} - \frac{2x^3}{L^3}$$

$$\phi_5(x) = x - \frac{2x^2}{L} + \frac{x^3}{L^2}$$

$$\phi_6(x) = \frac{x^2}{L} - \frac{x^3}{L^2}$$

Based on the Green-Lagrange strain theory,

$$\varepsilon_x = \frac{\partial U(x)}{\partial x} + \frac{1}{2}\left\{\left(\frac{\partial U(x)}{\partial x}\right)^2 + \left(\frac{\partial V(x)}{\partial x}\right)^2 + \left(\frac{\partial W(x)}{\partial x}\right)^2\right\} \qquad \textbf{(3-53)}$$

When the displacement is large enough, the nonlinear strain should not be neglected. Here, the nonlinear part of strain is defined as

$$g_x = \frac{1}{2}\left\{\left(\frac{\partial U(x)}{\partial x}\right)^2 + \left(\frac{\partial V(x)}{\partial x}\right)^2 + \left(\frac{\partial W(x)}{\partial x}\right)^2\right\}$$

$$= \frac{1}{2}\left(\frac{\partial U(x)}{\partial x}, \frac{\partial V(x)}{\partial x}, \frac{\partial W(x)}{\partial x}\right)^T \cdot \left(\frac{\partial U(x)}{\partial x}, \frac{\partial V(x)}{\partial x}, \frac{\partial W(x)}{\partial x}\right) \qquad \textbf{(3-54)}$$

$$= \frac{1}{2}\{\delta\}^T [B_n]^T [B_n]\{\delta\}$$

where $[B_n] = \frac{\partial [C_n]}{\partial x}$

According to the principle of virtual work, the nonlinear part of stiffness matrix can be derived as following (assuming the cross-section is rigid so that the influence of strain in non-x direction can be neglected [31]):

$$\{d\delta\}^T \{F_n\} = \int (\sigma_x \delta g_x) dxdydz = \{d\delta\}^T \int (\sigma_x [B_n]^T [B_n]) dxdydz \{\delta\} \quad \textbf{(3-55)}$$

Then the additional external force is

$$\{F_n\} = \int (\sigma_x [B_n]^T [B_n]) dxdydz \{\delta\} \quad \textbf{(3-56)}$$

At last, the nonlinear part of stiffness matrix is obtained as,

$$[K_n] = \int (\sigma_x [B_n]^T [B_n]) dxdydz \quad \textbf{(3-57)}$$

The above matrix should be added to the linear part of stiffness matrix which has been discussed in section 3.1.2.

It is known that, $\frac{\partial V(x)}{\partial x}$ and $\frac{\partial W(x)}{\partial x}$ in Eq. (3-54) dominates geometric nonlinearity when the displacement is large so that the $\frac{\partial U(x)}{\partial x}$ is eliminated. If we substitutes σ_x by average axial force *T* which is usually performed when analyzing the buckling behavior, the nonlinear stiffness matrix can be written as:

$$[K_n]_{12\times 12} = \begin{bmatrix} K_{n,jj} & K_{n,jk} \\ K_{n,kj} & K_{n,kk} \end{bmatrix} \quad \textbf{(3-58)}$$

$$K_{n,jj}=\frac{T}{L}\begin{bmatrix} 0 & 0 & 0 & 0 & 0 & 0 \\ & 6/5 & 0 & 0 & 0 & L/10 \\ & & 6/5 & 0 & -L/10 & 0 \\ & & & 0 & 0 & 0 \\ & Sym. & & & 2L^2/15 & 0 \\ & & & & & 2L^2/15 \end{bmatrix}$$

$$K_{n,jk}=\frac{T}{L}\begin{bmatrix} 0 & 0 & 0 & 0 & 0 & 0 \\ 0 & -6/5 & 0 & 0 & 0 & L/10 \\ 0 & 0 & -6/5 & 0 & -L/10 & 0 \\ 0 & 0 & 0 & 0 & 0 & 0 \\ 0 & 0 & L/10 & 0 & -L^2/30 & 0 \\ 0 & -L/10 & 0 & 0 & 0 & -L^2/30 \end{bmatrix} \quad \textbf{(3-59)}$$

$$K_{n,kj}=K_{n,jk}$$

$$K_{n,kk}=\frac{T}{L}\begin{bmatrix} 0 & 0 & 0 & 0 & 0 & 0 \\ & 6/5 & 0 & 0 & 0 & -L/10 \\ & & 6/5 & 0 & L/10 & 0 \\ & & & 0 & 0 & 0 \\ & Sym. & & & 2L^2/15 & 0 \\ & & & & & 2L^2/15 \end{bmatrix}$$

T: average axial force

c) Time-domain solving methodology

Implicit Newmark-beta [32] is utilized when solving the time-domain equation of motion and the solving process is shown below:

The equation of motion can be written as Eq. (3-60) in which time equals to *t*. It is assumed that the exact values for $\ddot{\delta}_t, \dot{\delta}_t, \delta_t$ are already solved

$$M\ddot{\delta}_t + C\dot{\delta}_t + Q_t = F_t \quad \textbf{(3-60)}$$

where, Q_t is the inner force which is nonlinear function of displacement.

To solve this nonlinear equation in next time step, Newton-Raphson (see Appendix A) is employed. The equation of motion in next time step $t+\Delta t$ can be written in an iteration manner:

$$M\ddot{\delta}_{t+\Delta t}^{(k)} + C\dot{\delta}_{t+\Delta t}^{(k)} + K_{t+\Delta t}^{(k-1)}\Delta\delta^{(k)} = F_{t+\Delta t} - Q_{t+\Delta t}^{(k-1)} \qquad \textbf{(3-61)}$$

where *k* is the iteration number.

$$\begin{aligned}
\ddot{\delta}_{t+\Delta t}^{(k)} &= \ddot{\delta}_{t+\Delta t}^{(k-1)} + \Delta\ddot{\delta}^{(k)} \\
\dot{\delta}_{t+\Delta t}^{(k)} &= \dot{\delta}_{t+\Delta t}^{(k-1)} + \Delta\dot{\delta}^{(k)} \\
\delta_{t+\Delta t}^{(k)} &= \delta_{t+\Delta t}^{(k-1)} + \Delta\delta^{(k)}
\end{aligned} \qquad \textbf{(3-62)}$$

All the values with superscript *k-1* are solved in Eq. (3-63) and (3-64) with initial assumption that:

$$K_{t+\Delta t}^{(0)} = K_t;\ \ Q_{t+\Delta t}^{(0)} = Q_t;\ \ \ddot{\delta}_{t+\Delta t}^{(0)} = \ddot{\delta}_t;\ \ \dot{\delta}_{t+\Delta t}^{(0)} = \dot{\delta}_t;\ \ \delta_{t+\Delta t}^{(0)} = \delta_t$$

At the end, three unknown values, $\Delta\ddot{\delta}^{(k)}$, $\Delta\dot{\delta}^{(k)}$, $\Delta\delta^{(k)}$ are left and the Eq. (3-63) becomes linear. According to Newton-Raphson method, it is known that after certain iteration for Eq. (3-63), $\ddot{\delta}_{t+\Delta t}, \dot{\delta}_{t+\Delta t}, \delta_{t+\Delta t}$ can be solved with high accuracy when Max($\Delta\ddot{\delta}^{(k)}$, $\Delta\dot{\delta}^{(k)}$, $\Delta\delta^{(k)}$) < tolerance.

Next problem is to find the relationship between the acceleration, velocity and displacement. The assumption based on Newmark-beta method is frequently used which provides linear increased or average acceleration in certain time step.

According to the assumption of Newmark-beta method, the value of $\ddot{\delta}, \dot{\delta}, \delta$ in next time step can be written as:

$$\begin{aligned}
\dot{\delta}_{t+\Delta t} &= \dot{\delta}_t + \Delta t\{\gamma\ddot{\delta}_{t+\Delta t} + (1-\gamma)\ddot{\delta}_t\} \\
\delta_{t+\Delta t} &= \delta_t + \Delta t\dot{\delta}_t + \Delta t^2\{\beta\ddot{\delta}_{t+\Delta t} + (\frac{1}{2} - \beta)\ddot{\delta}_t\}
\end{aligned} \qquad \textbf{(3-63)}$$

Set γ=0.5 and β=0.25 which yields the constant average acceleration.

Eq. (3-63) may be rewritten in an incremental displacement based form:

$$\begin{aligned}\dot{\delta}_{t+\Delta t} &= \frac{\gamma}{\beta\Delta t}\Delta\delta + (1-\frac{\gamma}{\beta})\dot{\delta}_t + (1-\frac{\gamma}{2\beta})\Delta t\ddot{\delta}_t \\ \ddot{\delta}_{t+\Delta t} &= \frac{1}{\beta}\{\frac{1}{\Delta t^2}\Delta\delta - \frac{1}{\Delta t}\dot{\delta}_t - (\frac{1}{2}-\beta)\ddot{\delta}_t\}\end{aligned} \qquad \textbf{(3-64)}$$

Substituting Eq. (3-64) into Eq. (3-61), the initial-iteration equation for time $t+\Delta t$ is obtained:

$$(\frac{1}{\beta\Delta t^2}M + \frac{\gamma}{\beta\Delta t}C + K_{t+\Delta t}^{(0)})\Delta\delta^{(1)} = F_{t+\Delta t} - Q_{t+\Delta t}^{(0)} + H_t \qquad \textbf{(3-65)}$$

where, H_t is a constant value which depends on the previous velocity and acceleration as shown below:

$$H_t = \frac{1}{\beta}M\{\frac{1}{\Delta t}\dot{\delta}_t + (\frac{1}{2}-\beta)\ddot{\delta}_t\} - C\{(1-\frac{\gamma}{\beta})\dot{\delta}_t + (1-\frac{\gamma}{2\beta})\Delta t\ddot{\delta}_t\}$$

By solving Eq. (3-65), the displacement, velocity and acceleration $\delta_{t+\Delta t}^{(1)}$ ($\delta_{t+\Delta t}^{(1)} = \delta_t + \Delta\delta^{(1)}$) are obtained. Then $\dot{\delta}_{t+\Delta t}^{(1)}, \ddot{\delta}_{t+\Delta t}^{(1)}$ can be obtained based on Eq. (3-63). Substituting $\delta_{t+\Delta t}^{(1)}$ into nonlinear inner force Q and nonlinear stiffness K, the $Q_{t+\Delta t}^{(1)}$ and $K_{t+\Delta t}^{(1)}$ are solved which will be substituted into Eq. (3-65) to get the new incremental displacement $\Delta\delta^{(2)}$. Then incremental velocity and acceleration will be:

$$\begin{aligned}\Delta\dot{\delta}^{(2)} &= \frac{\gamma}{\beta\Delta t}\Delta\delta^{(2)} \\ \Delta\ddot{\delta}^{(2)} &= \frac{1}{\beta\Delta t^2}\Delta\delta^{(2)}\end{aligned} \qquad \textbf{(3-66)}$$

According to Eq. (3-62), the new displacement, velocity and acceleration $\delta_{t+\Delta t}^{(2)}, \dot{\delta}_{t+\Delta t}^{(2)}, \ddot{\delta}_{t+\Delta t}^{(2)}$ can be obtained which will be employed for next iteration. By this process, the values $\ddot{\delta}_{t+\Delta t}$, $\dot{\delta}_{t+\Delta t}$, $\delta_{t+\Delta t}$ can be solved once the convergent criteria is satisfied (see last page).

d) Solving inner force

According to the previous items (a)(b), it is known that the inner force Q and stiffness K satisfy nonlinear function of displacement δ. The stiffness can be written as:

$$K_t = [A_s(\delta_t)]^T \{[K_l] + [K_n(\delta_t)]\}[A_s(\delta_t)] \quad \textbf{(3-67)}$$

Due to the large displacement, the inner force cannot be easily written as $Q_t = K_t \delta_t$ even though the nonlinear stiffness can be solved exactly. Instead, inner force has to be solved in accumulating manner as Eq. (3-68).

$$Q_t = Q_{t-\Delta t} + K_t(\delta_t - \delta_{t-\Delta t}) \quad \textbf{(3-68)}$$

Note in Eq. (3-68), the stiffness K at time step t is utilized implicitly in order to get a good convergence. However, the real value for stiffness K should be between $K_{t-\Delta t}$ and K_t. That means the inner force Q has some accumulated error even if the nonlinear equation of motion Eq. (3-60) can be solved exactly which may cause the diverging problem after long simulation time.

To solve this problem, for bar element, the inner force is solved directly as:

$$\begin{aligned} Q_t &= E\{-I_{3\times 3}, I_{3\times 3}\}\{\delta\}(L_t - L_0) \\ L_t &= \sqrt{({}_2u_{x,t} - {}_1u_{x,t})^2 + ({}_1u_{y,t} - {}_1u_{y,t})^2 + ({}_2u_{z,t} - {}_1u_{z,t})^2} \\ L_t &= \sqrt{({}_2u_{x,0} - {}_1u_{x,0})^2 + ({}_1u_{y,0} - {}_1u_{y,0})^2 + ({}_2u_{z,0} - {}_1u_{z,0})^2}) \end{aligned} \quad \textbf{(3-69)}$$

e) Validation of nonlinear model for truss

To verify the validity of program, the simulation result based on bar element is compared with the classic static catenary theory. The detail of catenary theory is introduced in Appendix B.

The data of analysis model is given as following:

Table 3-1 Parameters of simulation model

Length	300	m

Young's Modulus	2.06×10^{11}	N/m^2
Section Area	6.28×10^{-2}	m^2
Poisson's Ratio	0.3	
Density	7.8×10^{3}	Kg/m^3
Diameter	0.318	m

The structure damping is given based on Rayleigh damping theory as given in Eq. (3-70)

$$C_s = \gamma_m M + \gamma_k K \qquad \textbf{(3-70)}$$

where,

C_s is the Rayleigh damping coefficient.

γ_m is the mass proportional Rayleigh damping coefficient.

γ_k is the stiffness proportional Rayleigh damping coefficient.

M is the system structural mass matrix.

K is the initial structural stiffness matrix.

- Case 1

The model is fully submerged and both ends are horizontally fixed during simulation.

Because the buoyancy is not enough to balance with the gravity, the horizontal model will sink downward.

Rayleigh damping: γ_m=0.0, γ_k=0.0

Number of Finite Element: 61

In Figure 3-4, the MS means that the result is obtained from FE model theory which is described in this chapter and Catenary or Cat indicates that the result is predicted by static catenary theory.

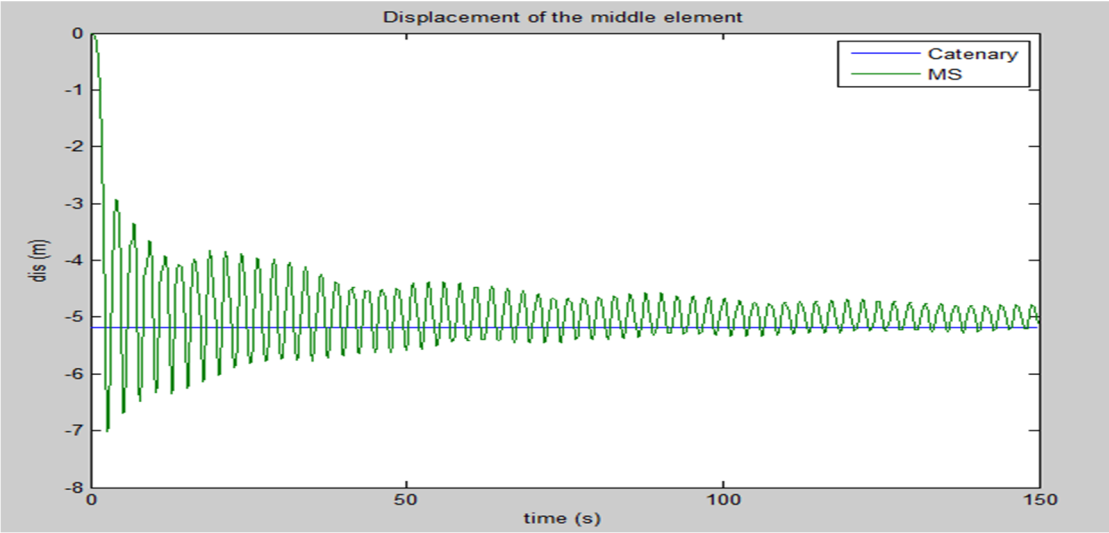

Figure 3-4 Time History of midspan node displacement

Figure 3-4 gives the time history of midspan node displacement calculated by Nonlinear DYNABEAM. In this figure, the green line represents the displacement of midspan node in *z* direction. The blue line is the balance position predicted by catenary theory. Because of lacking structure damping, the vibration of structure will be vanished slowly owning to the fluid damping.

The reason why the balance position obtained from the MS is smaller than catenary is that the freedom of MS is smaller than catenary. If the element number increases, the distinction will be decreased. This phenomenon will be discussed in Case 3 because the reduction will be seen more apparently when the sinking becomes more significant.

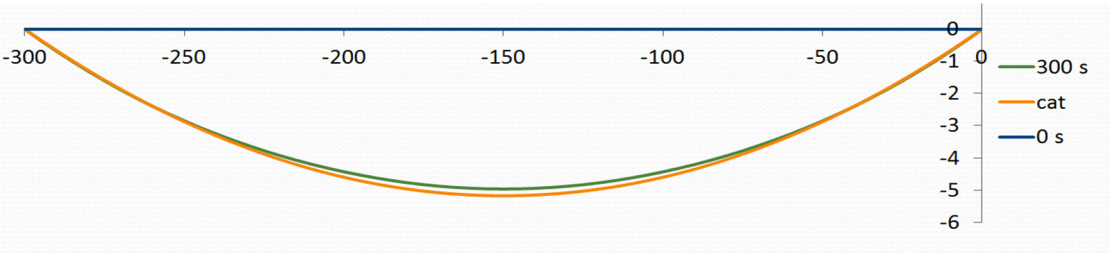

300s: the shape of the model after 300s
0s: the initial shape of the model
cat: the equilibrium shape of the model predicted by catenary theory

Figure 3-5 Comparison of the equilibrium state

Figure 3-5 shows the shape of model predicted by Nonlinear DYNABEAM and catenary theory.

- Case 2

The model is the same as that in Case 1 except for the structural damping. For Case 2, the Rayleigh damping is set as: γ_m=0.1, γ_k=0.1

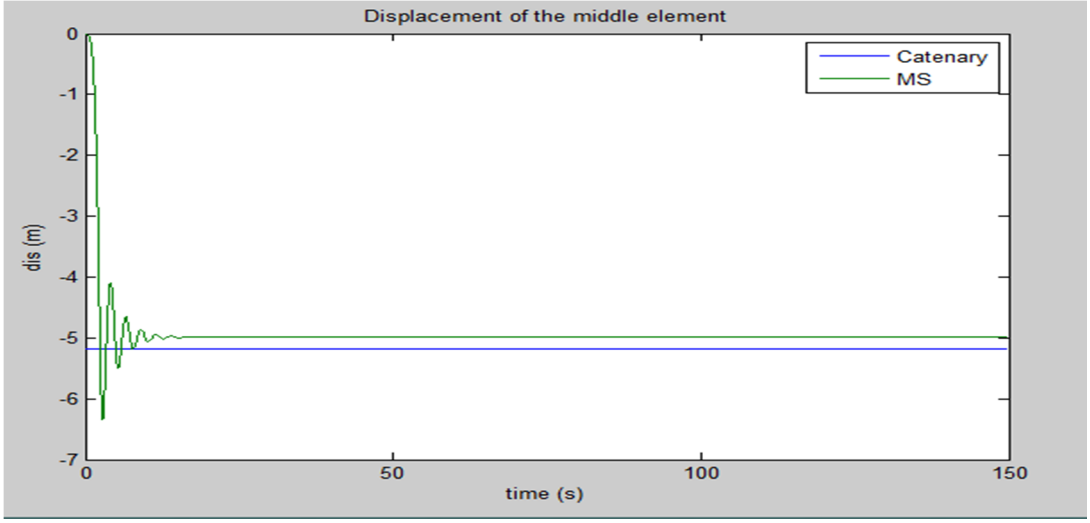

Figure 3-6 Time History of midspan node displacement

Figure 3-6 gives the time history of midspan node displacement. Comparing with Figure 3-4, it can be found that by considering the structure damping, the vibration will vanish more quickly than Case 1. However the balance position is still the same as Case 1 and smaller than the result predicted by catenary theory.

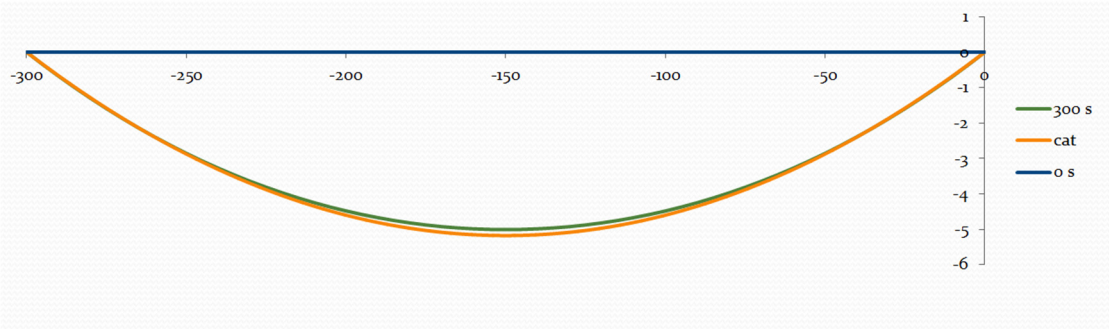

Figure 3-7 Comparison of the equilibrium state

Figure 3-7 shows the shape of model predicted by Nonlinear DYNABEAM and catenary theory.

- Case 3

The dimension of model for Case 3 is the same as that for Case 1&2. However, to obtain a significant sinkage, instead of fixing, both ends are moved horizontally towards the center of mooring by 10 m.

The Rayleigh damping: γ_m=0.1, γ_k=0.1

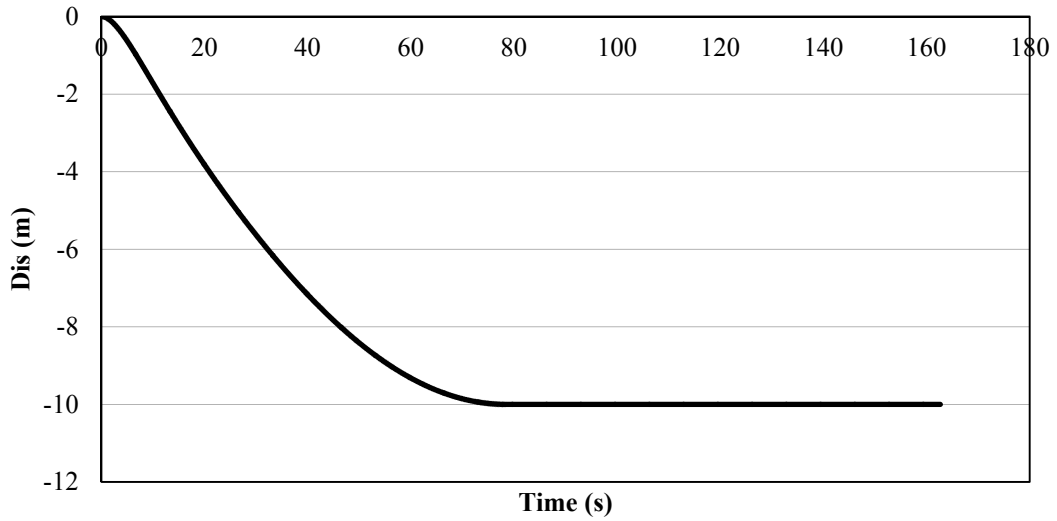

Figure 3-8 Time History of Horizontal Displacement for one end

Figure 3-8 shows the time history of horizontal displacement for one end. The motion of the other end is opposite with this end.

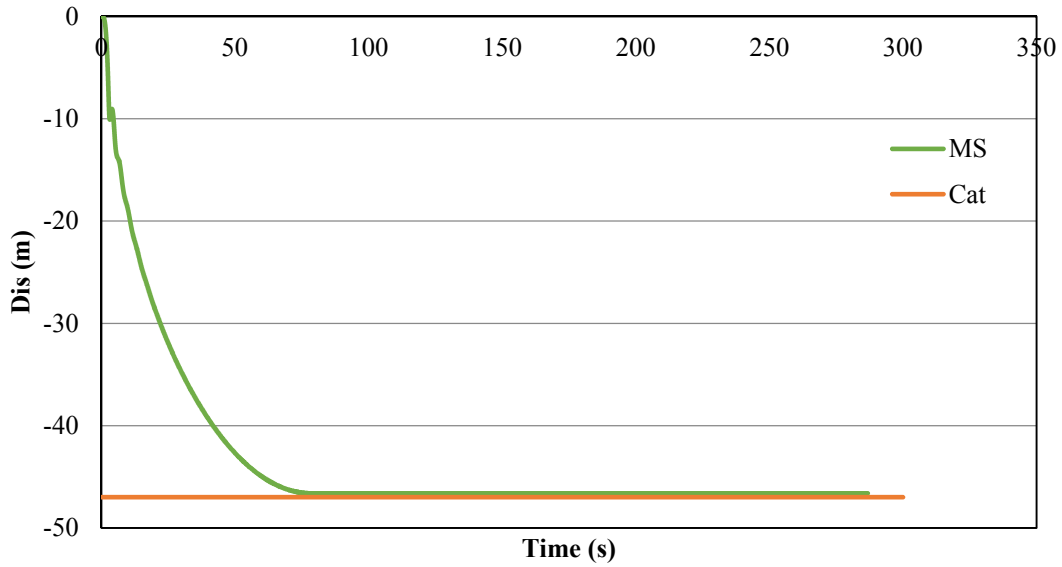

Figure 3-9 Time History of midspan node displacement

Figure 3-9 shows the time history of midspan node displacement.

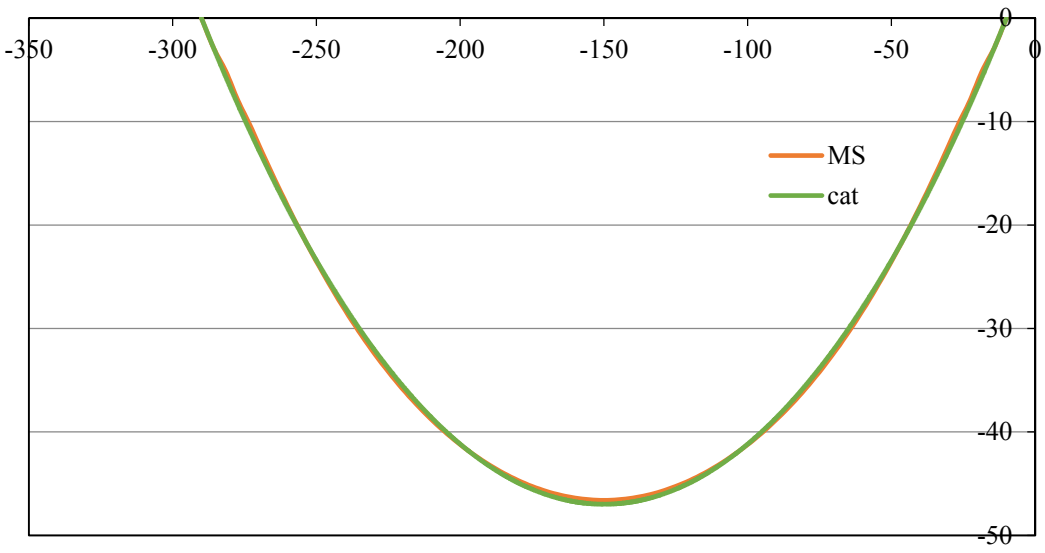

Figure 3-10 Comparison of the equilibrium state

Figure 3-10 shows the shape of model predicted by Nonlinear DYNABEAM and catenary theory.

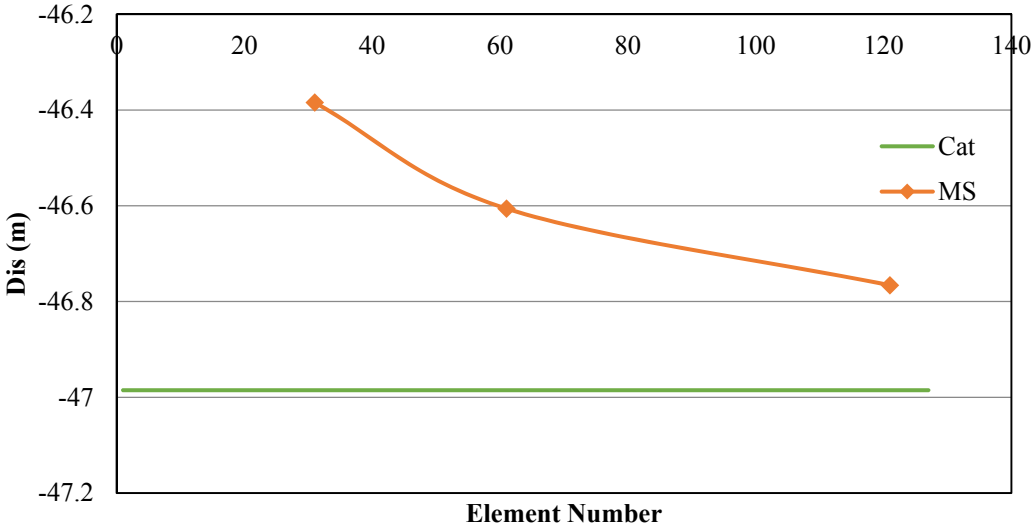

Figure 3-11 Comparison of the Displacement for Different Element Number

From Figure 3-9 and Figure 3-10, we can figure out that even though the sinkage is larger, the distinction between FE model and catenary theory is rather small. However, to explain this small deviation, the number of elements is increased. Figure 3 11 shows the different result for different element number. Through Figure 3-11, we can find that the accuracy of the nonlinear DYNABEAM increases when the model is subdivided into more elements which accord with the usual finite element theory.

f) Validation of nonlinear model for beam

For beam, the nonlinearity can be obviously observed when the buckling occurs. The buckling behavior is caused mainly by the interaction between the axial compressive load and internal moment.

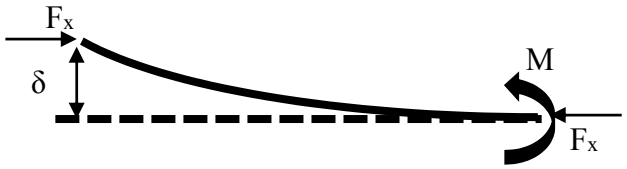

Figure 3-12 Interaction of axial compressive load and internal moment

Considering a cantilever as shown in Figure 3-12, if the initial deflection exists on one end of beam δ, the axial-load induced internal moment *M* can be written as:

$$M = F_x \cdot \delta \qquad \textbf{(3-71)}$$

Due to the presence of initial deflection, the internal moment is induced by the axial load. In addition, as the axial load approaches the critical buckling load, the deflection rapidly increases in an unstable manner. In the linear stiffness, this unstable behavior cannot be simulated. But by introducing the green strains as described in (b) and considering the coordinate transformation associated with the deformed states as described in 3.1.2, the unstable buckling behavior can be simulated. Here, a simulation case is demonstrated based on the linear and nonlinear stiffnesses for cantilever. The cantilever is orientated horizontally and the gravity load is not considered. To have a deflection, a lateral load is added on the left end of the beam (see Figure 3-13). The main parameters for the cantilever is given in Table 3-2.

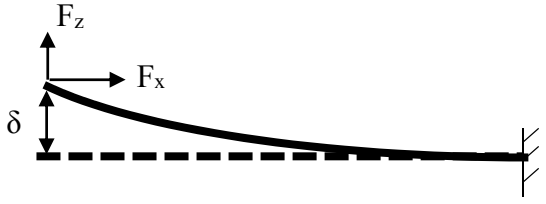

Figure 3-13 Simulation Case

Table 3-2 **Parameters of the simulated cantilever**

Length	500	m
Diameter	0.2	m
Moment of Inertia	7.85×10^{-5}	m^4
Density	7.80×10^{3}	Kg/m^3
Young's Modulus	2.06×10^{11}	Pa
Buckling Load (1st order)	1.60×10^{4}	N
Beam Element Number	10	
Lateral Load F_z	100	N
Initial Deflection δ	2.58×10^{-1}	m

- Static analysis

Firstly, the static analysis without the inertia force is conducted. To validate the accuracy the simulation, the same model is calculated in Abaqus (Abaqus is a commercial nonlinear structural FEM software) with considering the large deformation. Several cases with different axial compressive load F_x are simulated. The range of F_x is selected from 1000N to 15000N (Buckling Load).

Figure 3-14 shows the comparison of static displacement along with x-axis on the end of beam. The data marked "Abaqus" shows the results obtained by Abaqus. The "DYNA_NONLINEAR" and "DYNA_LINEAR" represent the calculation results of DYNABEAM with and without nonlinear stiffness. Even though the absolute value is relatively small compared with the length of the beam, an obvious discrepancy can be seen between the DYNA_NONLINEAR and DYNA_LINEAR. Through comparing the results of Abaqus and DYNA_NONLINEAR, we can find that, the good correlation is achieved when the axial compressive load is smaller than 14000N. When the axial compressive load is close to 16000N, which is the critical value for the beam buckling, the results obtained by Abaqus turns to be larger than that of DYNA_NONLINEAR even though the theory utilized in DYNA_NONLINEAR (see sub-section 3.2.1a and 3.2.1b) seems almost identical with that in Abaqus. The reason for the discrepancy of results between Abaqus and DYNA_NONLINEAR is that, in order to solve the inner force, the linearized incremental method (see Eq. (3-68)) is adopted which may result in some accumulated error when the displacement becomes sufficiently large. More reasonable model for obtaining the inner force is to calculate the inner force according to Green-Lagrange strain theory directly (see Eq. (3-53)). This correction work should be conducted in the future.

Figure 3-15 shows a similar comparison for the displacement along z-axis. The results predicted by the DYNA_LINEAR is constant as the axial compressive load has no influence on the deflection in linear stiffness. The predicted accuracy of DYNA_NONLINEAR is still acceptable when the axial compressive load is smaller than 15000.

Note that, we assume the axial compressive load cannot be so close to the critical buckling load in the real design. Also, for the dynamic problem, even when the transient axial compressive load is larger than the critical buckling load, the buckling may not occur as most external force is occupied by the inertia.

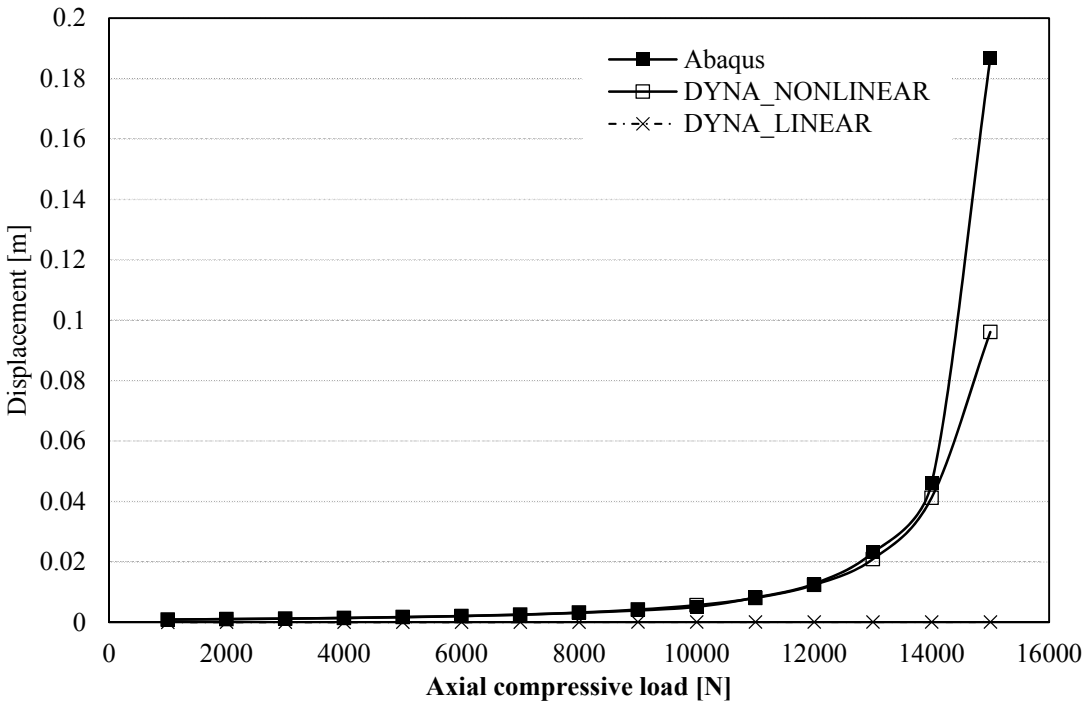

Figure 3-14 Comparison of displacement in x direction

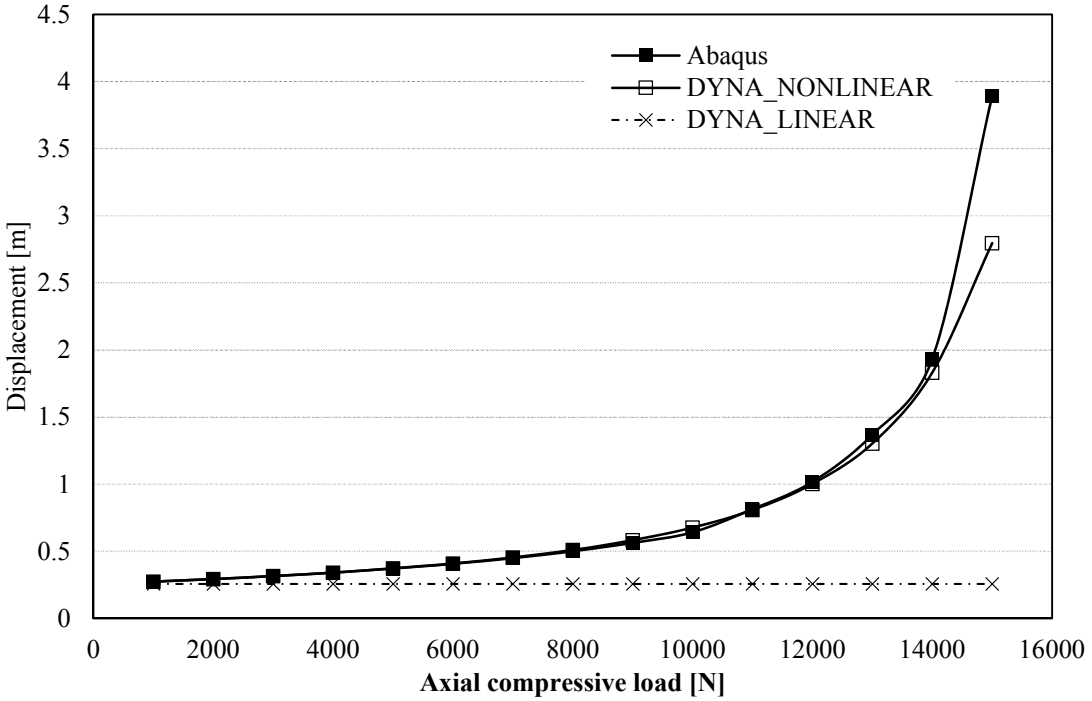

Figure 3-15 Comparison of displacement in z direction

- Dynamic analysis

For the dynamic simulation, the axial compressive load F_x, and lateral load F_z, are added linearly from 0 second to 4 second. After 4 second, both loads will be released suddenly. To confirm influence of the nonlinear stiffness, two different axial compressive loads are selected. The lateral load is set as 100N.

Figure 3-16 and Figure 3-17 show the comparison with axial compressive load as 1 x10^4 N. It is observed that, a good correlation is achieved between Abaqus and DYNA_NONLINEAR. For the displacement along *x* axis, the discrepancy between DYNA_LINEAR and DYNA_NONLINEAR seems large. But considering the absolute value, this discrepancy can be neglected. For the displacement along *z*, the discrepancy between linear model and nonlinear model is relatively small. It is also found that, even the axial compressive load is set as 1 x10^4 N, the deflection (smaller than 0.20m) is much smaller than the prediction value of static nonlinear analysis (0.67m). It is even smaller than the deflection (0.26m) predicted based on the linear stiffness. This smaller deflection can be interpreted by the inertia force.

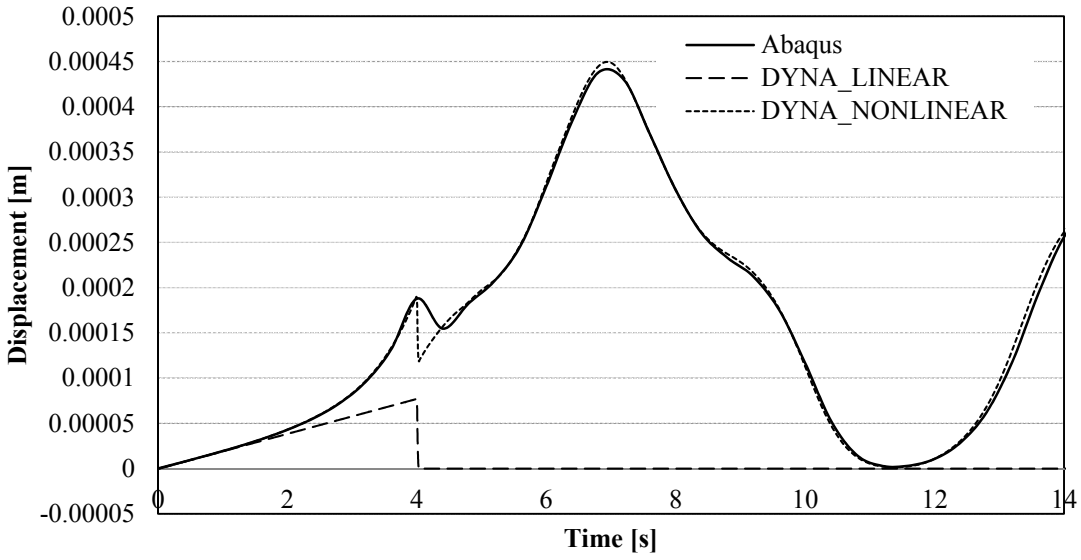

Figure 3-16 Comparison of x displacement in time domain (F_x=1 x10^4 N)

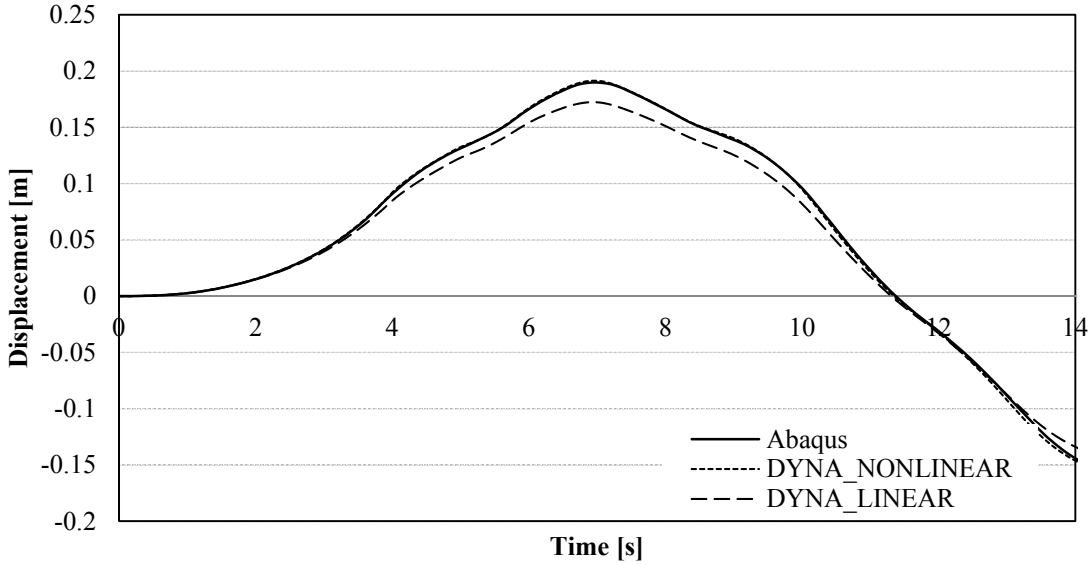

Figure 3-17 Comparison of z displacement in time domain (F_z=1 x10^4 N)

For getting a large deflection and observing a clear nonlinear stiffness influence, the axial compressive load is increased from 1 x10^4 N to 1 x10^5 N which is almost 6.3 times of the critical buckling load. Figure 3-18 and Figure 3-19 present the corresponding comparison of displacement in x and z directions. According to Figure 3-19, it is found that, the nonlinear stiffness can result in a large deflection which is same with the conclusion of static analyses. By comparing the results of nonlinear model with that of Abaqus, the reasonability of the nonlinear model is proven.

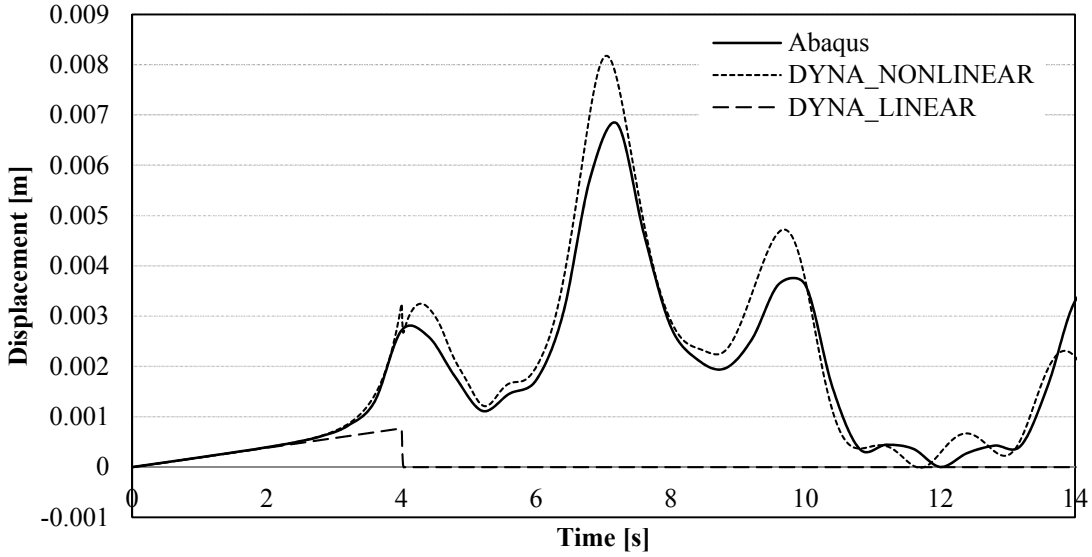

Figure 3-18 Comparison of x displacement in time domain (F_x=1 x10^5 N)

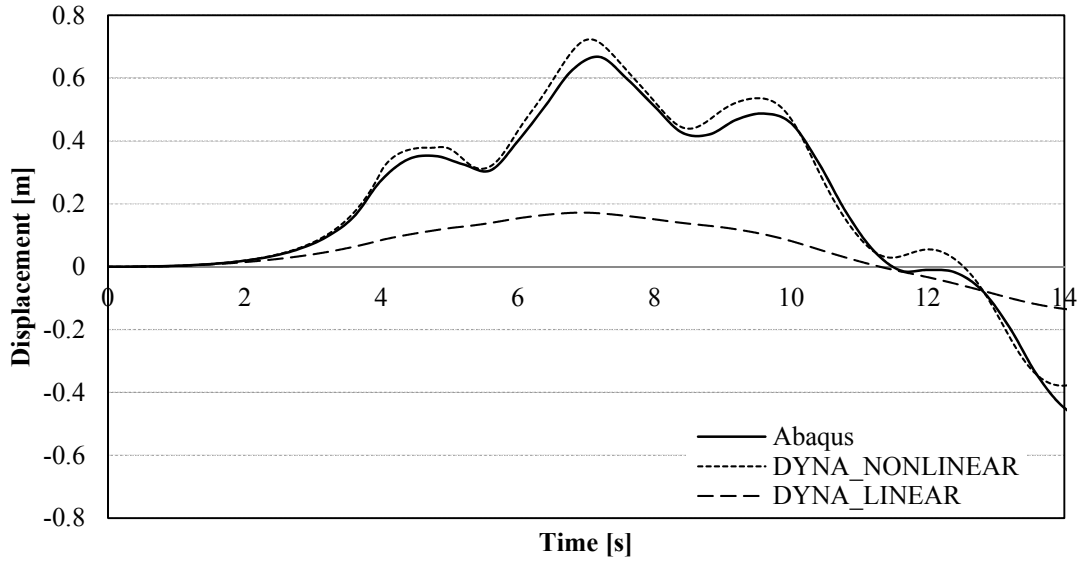

Figure 3-19 Comparison of z displacement in time domain (F_z=1 x10^5 N)

The comparisons of the deformation between Abaqus model and nonlinear model are shown from Figure 3-20 to Figure 3-25 when time equals to 3s, 5s, 7s, 9s, 11s and 13s. The accuracy of deformation predicted by the DYNA_NONLINEAR is also acceptable compared with the results of Abaqus.

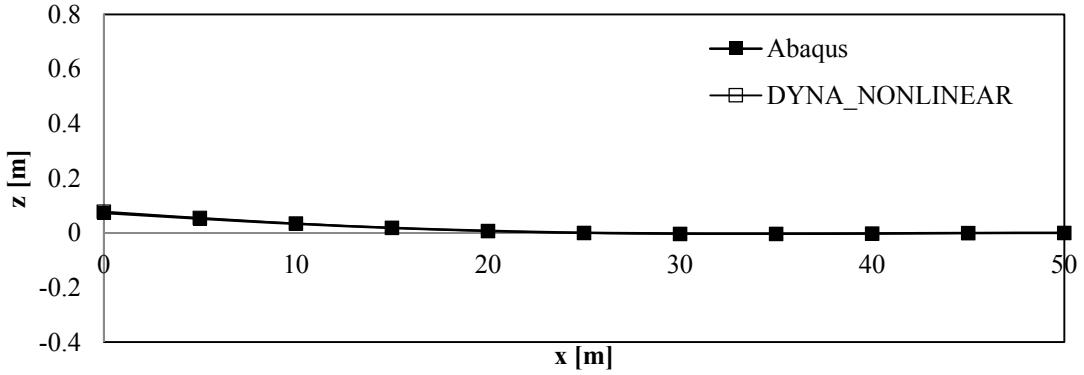

Figure 3-20 Deformation of beam (time=3s, F_z=1 x10^5 N)

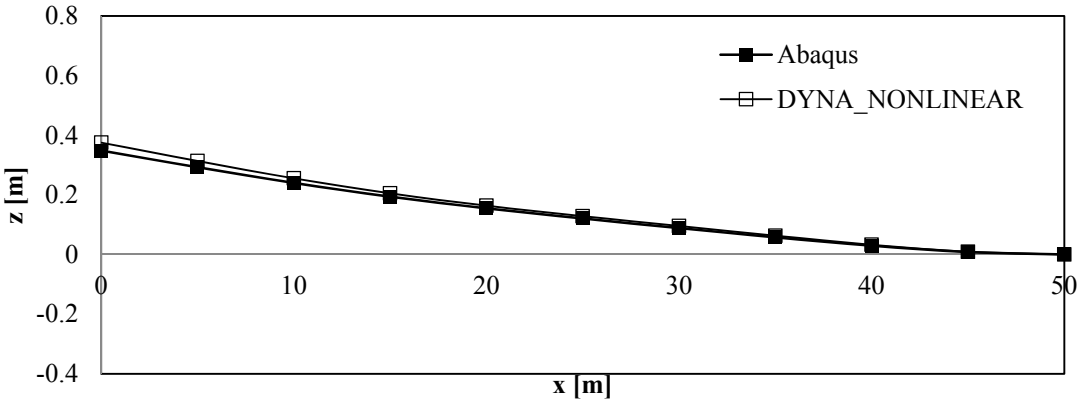

Figure 3-21 Deformation of beam (time=5s, F_z=1 x10^5 N)

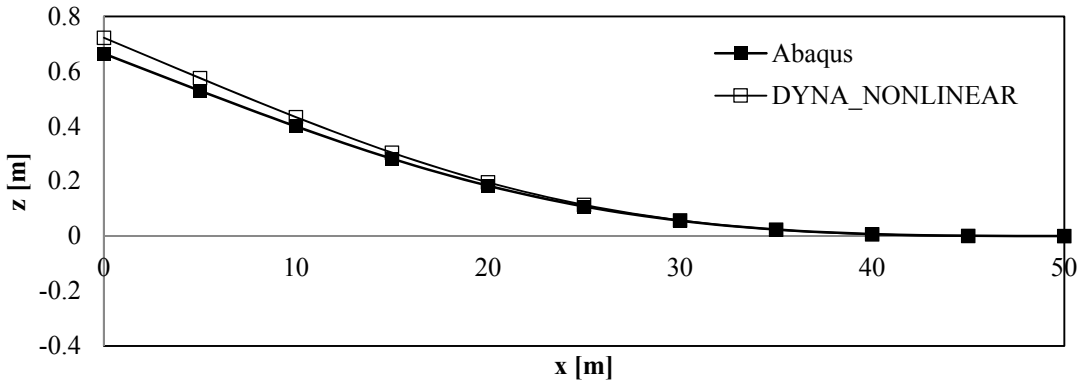

Figure 3-22 Deformation of beam (time=7s, F_z=1 x10^5 N)

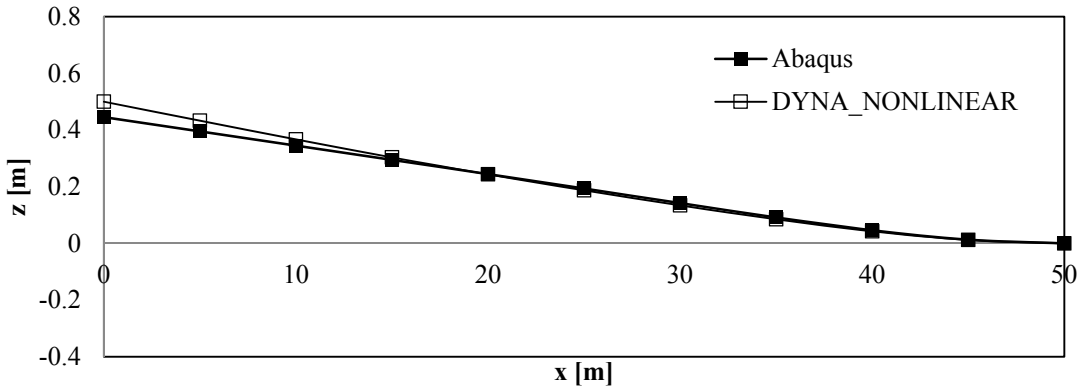

Figure 3-23 Deformation of beam (time=9s, F_z=1 x10^5 N)

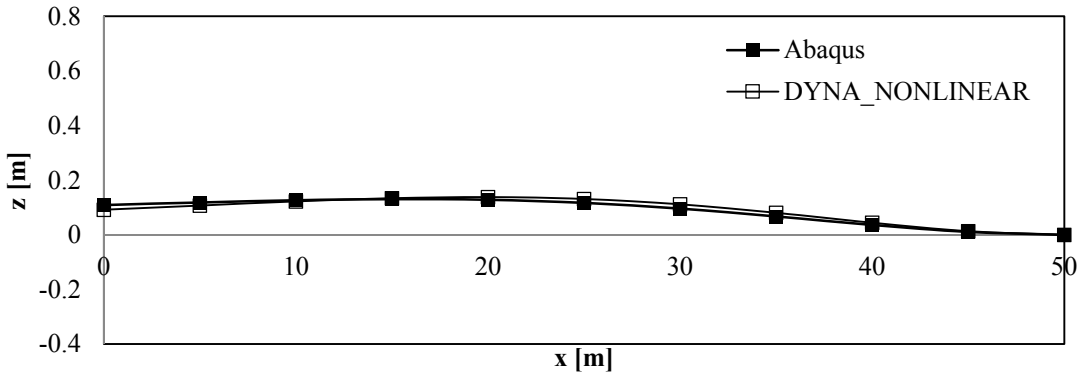

Figure 3-24 Deformation of beam (time=11s, F_z=1 x10^5 N)

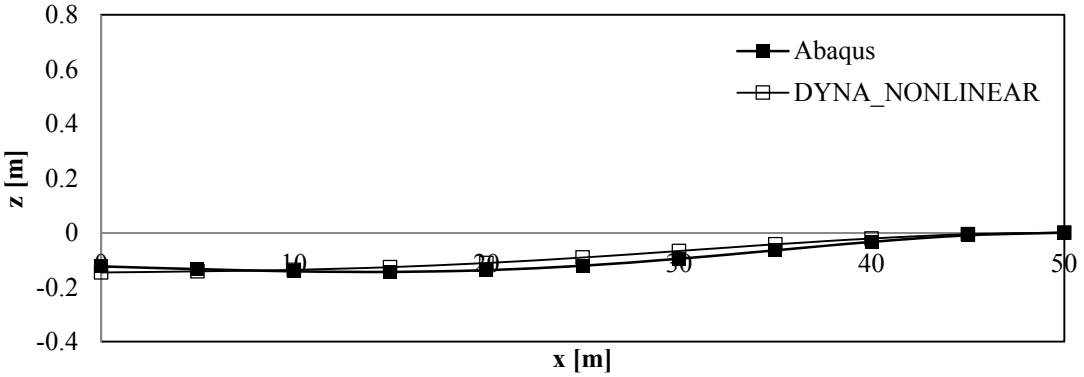

Figure 3-25 Deformation of beam (time=13s, F_z=1 x10^5 N)

3.2.2 Hydrodynamics

a) Memory function

When extending the research interest from regular wave to irregular wave or considering the nonlinear response of floater under even regular wave (see Chapter 6), the added mass and damping coefficient in Eq. (3-47) which depend on the wave frequency have to be modified. In some cases, the transient effects can be too important to be neglected. Faltinsen [33] points that, for the cases when the severe coupling between sloshing in ship tank and ship motion and slamming on a catamaran in wave occurs, the transient effects become crucial. To solve the above problems, a memory function must be taken into account in the equation of motion.

Cummins [34] and Ogilvie [35] demonstrated how to modify the equation of motion based on steady-state assumption to include the transient effects. It has been proven [35] that the existence of the free surface causes the physical system to have a 'memory' which means that, what happens at one instant of time affects the system for all later times. Equation (3-72) is the modified equation of motion which is based on Coummins [34] in order to include the time-domain effects.

$$\left(M + M_a(\infty)\right)\ddot{\delta} + C_D\dot{\delta} + \left(K_r + K_B + K_T\right)\delta + \int_0^t h(\tau)\dot{\delta}(t-\tau)dt = F_K^*(t) + F_0^* \qquad \textbf{(3-72)}$$

Compared with the Eq. (3-47) which is based on steady-state assumption, the added mass and damping coefficient corresponding infinite wave frequency are selected. The integral term is referred to as a convolution integral. The response is given as a convolution integral over the past history of the exciting force with the impulse response function appearing as the kernel [34]. $h(\tau)$ is the memory function which can be calculated based on either the added mass or the damping coefficients. In this research, the retardation function based on damping coefficient $h(\tau)$ is utilized as it is easier to obtain a good accuracy according to Faltinsen [33]. Then, the retardation function can be written as:

$$h(\tau) = \frac{2}{\pi}\int_0^\infty B(\omega)\cos(\omega t)d\omega \qquad \textbf{(3-73)}$$

b) Quadratic viscous drag force

The hydrodynamic theory described previously is based on the potential theory which assumes the fluid is inviscid and continuous. It is known that the inertia force contributes dominant influence on the response of the floater with large diameter relative to fluid and floater oscillation amplitude [36]. But for high wave cases, the viscous drag force affects the response of the floater more and the dominance of viscous drag force is of greater significance for pipelines, risers and tubular lattice structures for which the significant flow separation occurs. Further, drag forces play an important role in analyzing the dynamics of structures in the range of cancellation periods, i.e. when inertia forces fully compensate each other. Finally, viscous damping is the decisive parameter limiting oscillation amplitudes of hydrodynamically transparent structures at resonance conditions [36].

In order to include the influence of viscous drag force, for floater, the quadratic viscous drag force (see Eq. (3-74)) is added into the equation of motion according to the Morison's formula. For underwater mooring, the potential theory is substituted by Morison's formula Eq. (3-75).

$$F_{Dr} = C_{Dr}\frac{\rho}{2}A\left|\dot{u}_f - \dot{\delta}\right|(\dot{u}_f - \dot{\delta}) \qquad \textbf{(3-74)}$$

where, $\dot{u}_f$ is fluid particle velocity; C_{Dr} is the drag coefficient;

A is the projected area which is perpendicular to the direction of relative velocity.

$$F = \rho V\ddot{u}_f + C_a\rho V(\ddot{u}_f - \ddot{\delta}) + F_{Dr} \qquad \textbf{(3-75)}$$

V is the volume of water displacement

C_a is the added mass coefficient

c) 2nd order wave potential force

The higher order wave potential force is increased by many aspects when the wave height becomes high. In this research three kinds of 2nd order wave potential force are included in time-domain DYNABEAM.

- 2nd order force due to the fluid velocity

According to Bernoulli equation, fluid velocity can give a 2nd order influence on the water force as shown in Eq. (3-76)

$$F_v = \frac{\rho}{2}\iint((\frac{\partial\phi}{\partial x})^2 + (\frac{\partial\phi}{\partial y})^2 + (\frac{\partial\phi}{\partial z})^2)\mathbf{n}ds \qquad \textbf{(3-76)}$$

In time-domain DYNABEAM, the above integration is done along the mean submerged surface without considering the wave elevation. $\mathbf{n}$ is the unit normal vector directing into the fluid from the mean body surface. Wave potential ϕ includes the influence of incident wave, diffraction wave and radiation wave which can be obtained based on Eq. (3-1).

- 2nd order Froude-Krylov due to second order incident wave potential

According to the stokes second-order wave theory, the 2nd order Froude-Krylov force can be written as:

$$F_{2fk} = \frac{\rho g k a^2}{2\sinh(2kh)}\iint(\frac{3\cosh(2k(Z-d+h))}{\sinh^2(kh)}\cos(2(kX-\omega t))+1)\mathbf{n}ds \qquad \textbf{(3-77)}$$

where, the origin of Z locates on the bottom of the floater with water draft as d which is identical with the previous definition. The second-order component which is caused by the influence of the quadratic velocity in the original stokes wave theory is eliminated in Eq. (3-77) as it has been already included in Eq. (3-76).

In time-domain DYNABEAM, the above integration is done along the mean submerged surface without considering the wave elevation.

- 2nd order force due to wave free surface

Integrating the water pressure based on the instantaneous wetted hull can result to high order wave exciting force. Consider up to 2nd order, the pressure caused by the wave free surface can be write as:

$$F_{su} = -\frac{\rho g}{2}\oint\{\frac{1}{g}\frac{\partial\phi}{\partial t}\Big|_{Z=0} - (U(3)+\Theta(1)Y-\Theta(2)X)\}^2\mathbf{n}dl$$

In time-domain DYNABEAM, the above integration is done along the mean waterline.

- 2^{nd} order force due to motion of the floater

In radiations problem, the floater movies and the transient wave potential along the floater surface should be corrected according to the transient displacement of the floater in a spatial differential manner which can be regarded as a kind of 2^{nd} order force as shown below:

$$F_{sp} = \iint \{U + \Theta \times (X, Y, Z)^T\} \bullet \nabla(\frac{\partial \phi}{\partial t}) \mathbf{n} ds$$

In time-domain DYNABEAM, the above integration is done along the mean submerged surface without considering the wave elevation.

Add up all the terms introduced in sub-section 3.2.2(c) , in addition to the second order time variable force with circular frequency 2ω, the second order static drift force can be solved as well, which is called near-field method.

3.2.3 Coupling methodology

The two numerical models for floater and mooring are coupled together to account for the mutual interactions. The coupling is required since the tension variation in the tether affects much the motion of the floating body, i.e. for tension leg mooring system, the motion of the floater is strongly constrained by the tether. There are in general two strategies in the coupling procedure. One is known as weakly coupling while the other is known as strongly coupling.

The weakly coupling (Figure 3-26) means the simple displacement-force coupling in different time step. During the weakly coupling, the two numerical models (here, floater and mooring) can be kept relatively independent and only modifying the interface of two models is necessary. Therefore, the weakly coupling is much easier to be adopted, especially when the numerical model is complicated. At present, the weakly coupling is widely utilized in the offshore engineering simulation with catenary mooring system as the catenary mooring system provides low restoring stiffness.

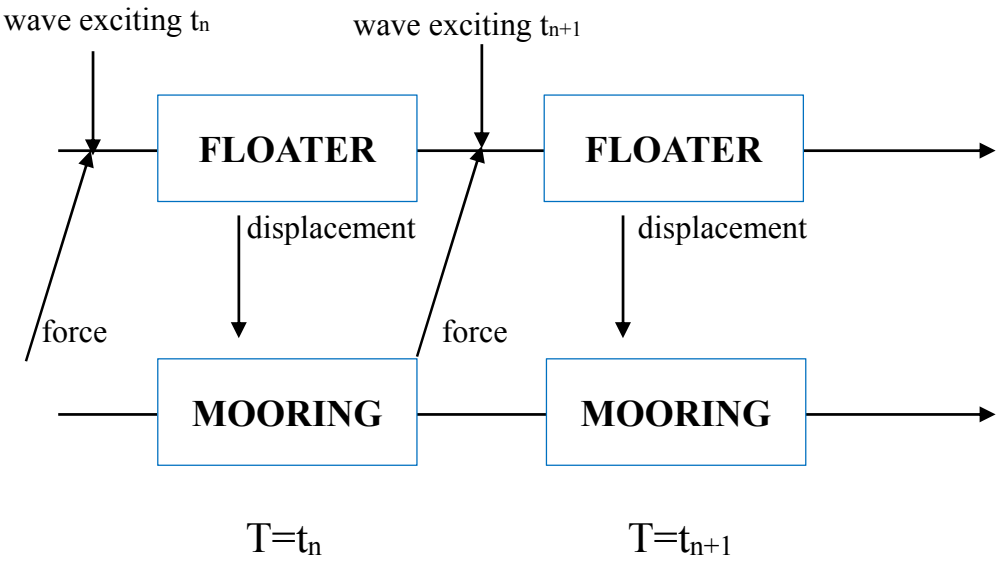

Figure 3-26 weak coupling procedure

However, as the weakly coupling does not solve the two numerical models simultaneously, it cannot give the exact solutions unless the convergence is confirmed at each time step. Especially, when the stiffness of numerical models is high, the solution of weakly coupling will be easy to diverge. As the mooring model has high stiffness, the weakly coupling is insufficient in this research. Instead, the strongly coupling is utilized here by coupling the two numerical models in matrix form. Unlike weakly coupling, strongly coupling can solve all the exact displacement and force for floater and mooring simultaneously. But the strongly coupling is more difficult to conduct as it needs modifying the numerical models much more than the weakly coupling. The main process of strongly coupling utilized in this research is discussed as following.

Generally, the equations of motion for both floater and mooring can be derived as given in the following form:

$$\begin{aligned} \boldsymbol{M}_f\ddot{X}_f + \boldsymbol{C}_f\dot{X}_f + \boldsymbol{K}_f X_f &= F_f + F^* \\ \boldsymbol{M}_m\ddot{X}_m + \boldsymbol{C}_m\dot{X}_m + \boldsymbol{K}_m X_m &= F_m - F^* \end{aligned} \qquad \textbf{(3-78)}$$

where the subscripts *f* and *m* mean the relevant matrix or vector for floater or mooring, respectively. *F** is the connection force between the floater and the mooring. After transformation according to Newmark-beta method, the whole equation for two numerical models can be shown in matrix manner as Figure 3-27.

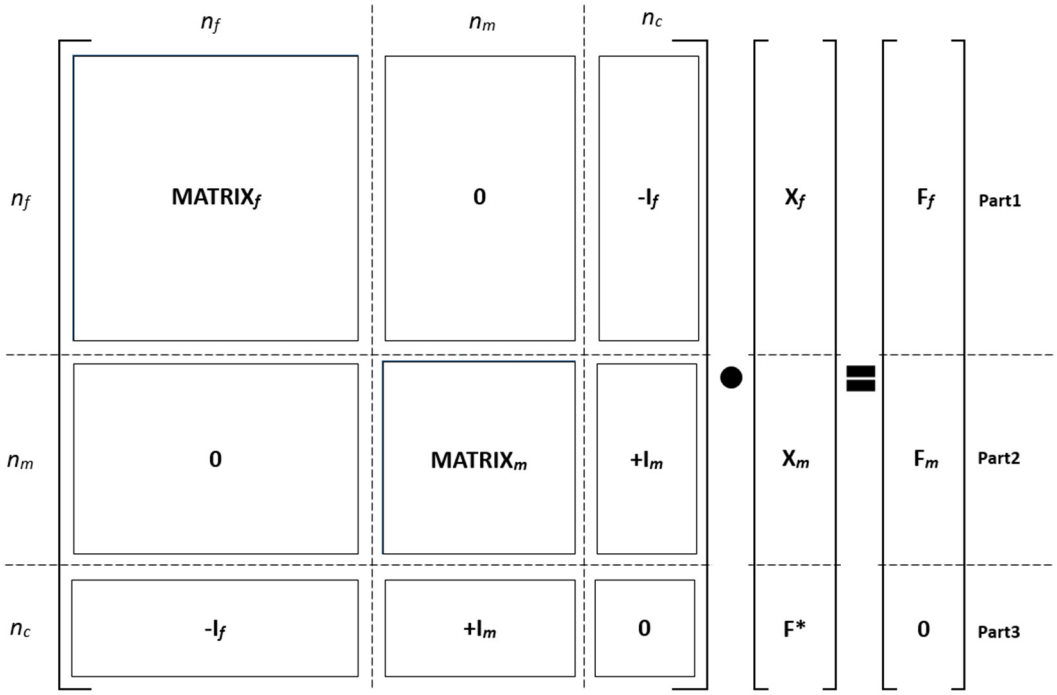

Figure 3-27 coupling matrix and vector for the whole equation of motion

where Parts 1 and 2 are derived based on Eq. (3-78). Part 3 can be obtained according to the boundary condition in the joint of floater and mooring. ***MATRIX*** represents the transformed matrix according Newmark-beta method. ***I*** means the coupling matrix which has the identical value on the coupling DOF (other values are zero). Finally, the size of the whole matrix is $n_f+n_m+n_c$, where n_f, n_m, n_c are the number of DOF for floater, mooring and the coupling joint respectively.

For example, the both simulations based on floater-mooring weakly coupling methodology and floater-mooring strongly coupling methodology are conducted. Same tethered-buoy model (SPM model) as discussed in Chapter 6 is employed and the simulation results for mooring tether tension in time domain are compared between both coupling models. The wave period is set as 0.5s and wave amplitude is set as 1cm.

To show the influence of the mooring stiffness, in addition to the real stiffness (EA= 6.28 x10^3 N) used in the model test, the case with low mooring stiffness (10% of real stiffness) is also simulated. Figure 3-28 shows the comparison of mooring tension with real mooring stiffness. It is found that, the strongly coupling simulation works well. While, for weakly coupling simulation, a severe convergence problem occurs and the simulation fails after 0.015s.

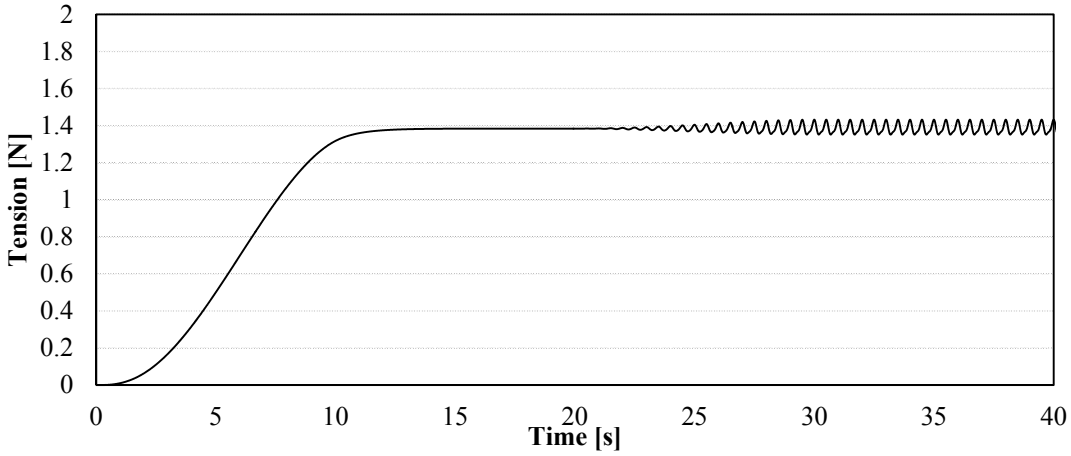

(a) Strongly coupling

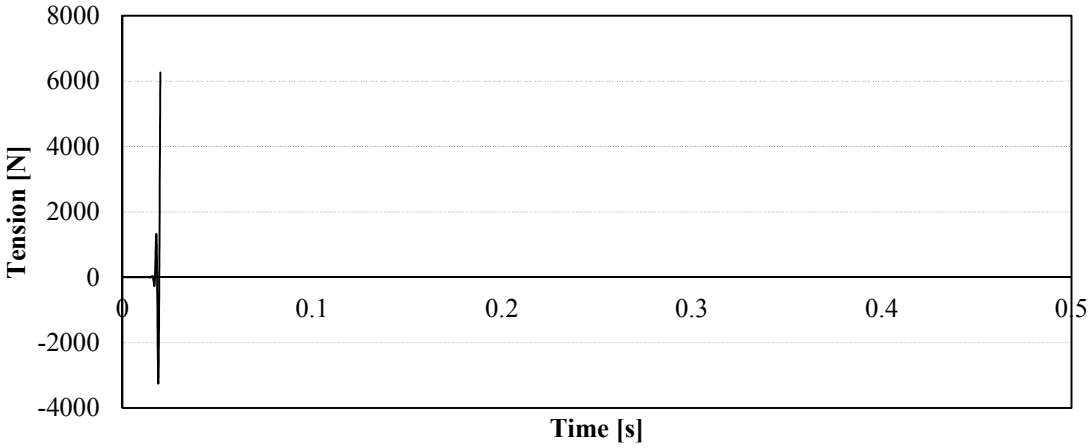

(b) Weakly coupling

Figure 3-28 Comparison of mooring tension with real mooring stiffness

Figure 3-29 and Figure 3-30 show the comparison of mooring tension with 10% real mooring stiffness. It is seen that, good results can be still obtained based on strongly coupling model. For weakly coupling model, the convergence problem is mitigated due to the low stiffness. However, after long enough time (here, 90s), the computation process based on weakly coupling becomes unstable which is not observed in the strongly coupling simulation.

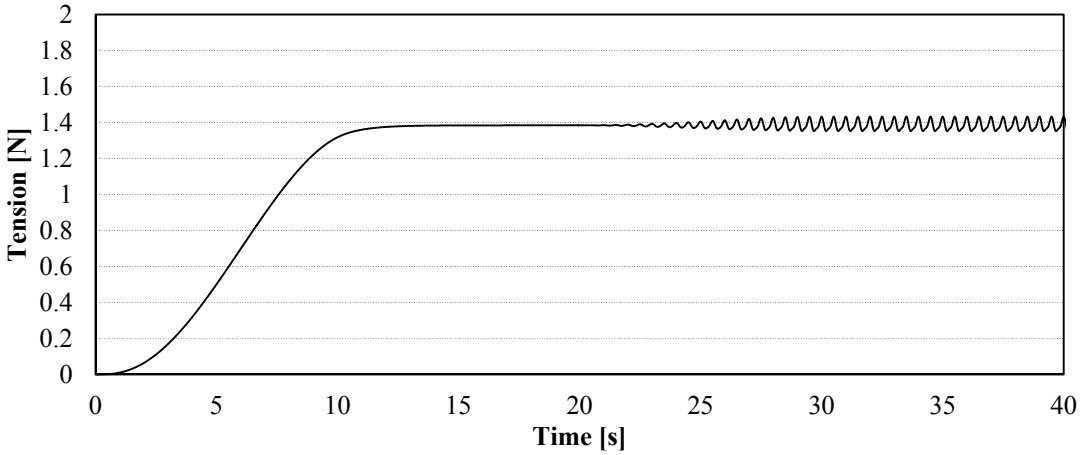

(a) Strongly coupling

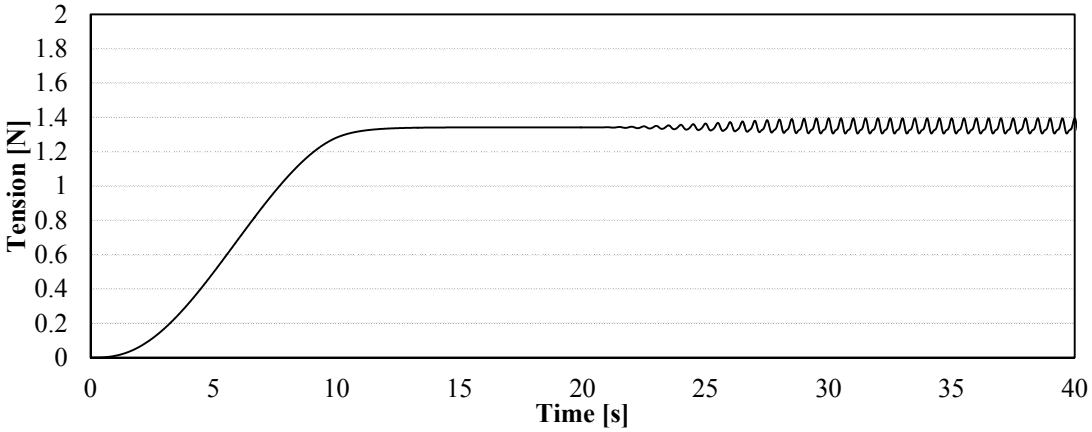

(b) Weakly coupling

Figure 3-29 Comparison of mooring tension with 10% real mooring stiffness (0s~40s)

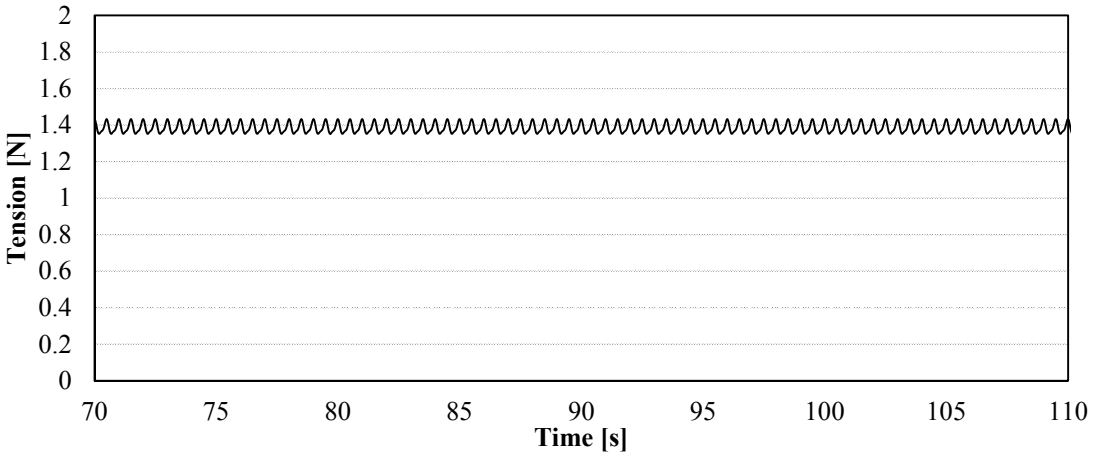

(a) Strongly coupling

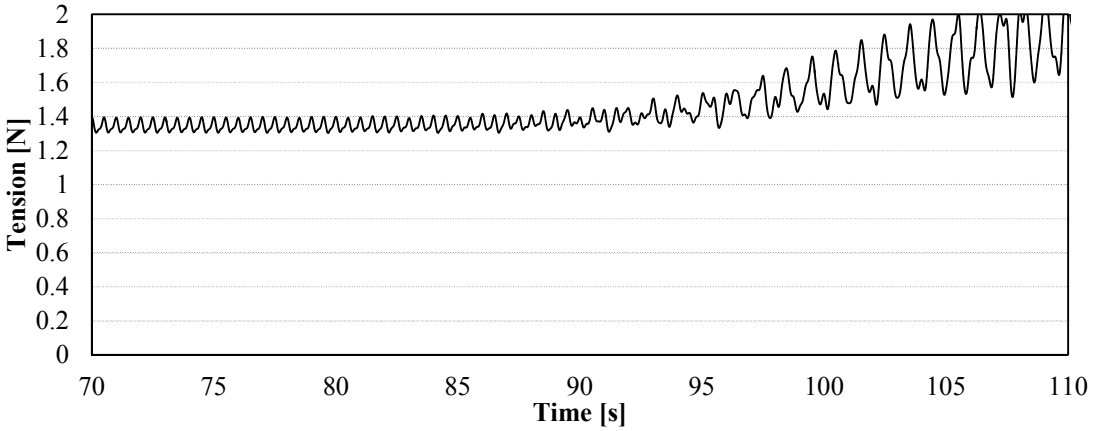

(b) Weakly coupling

Figure 3-30 Comparison of mooring tension with 10% real mooring stiffness (70s~110s)

3.2.4 Calculation flow

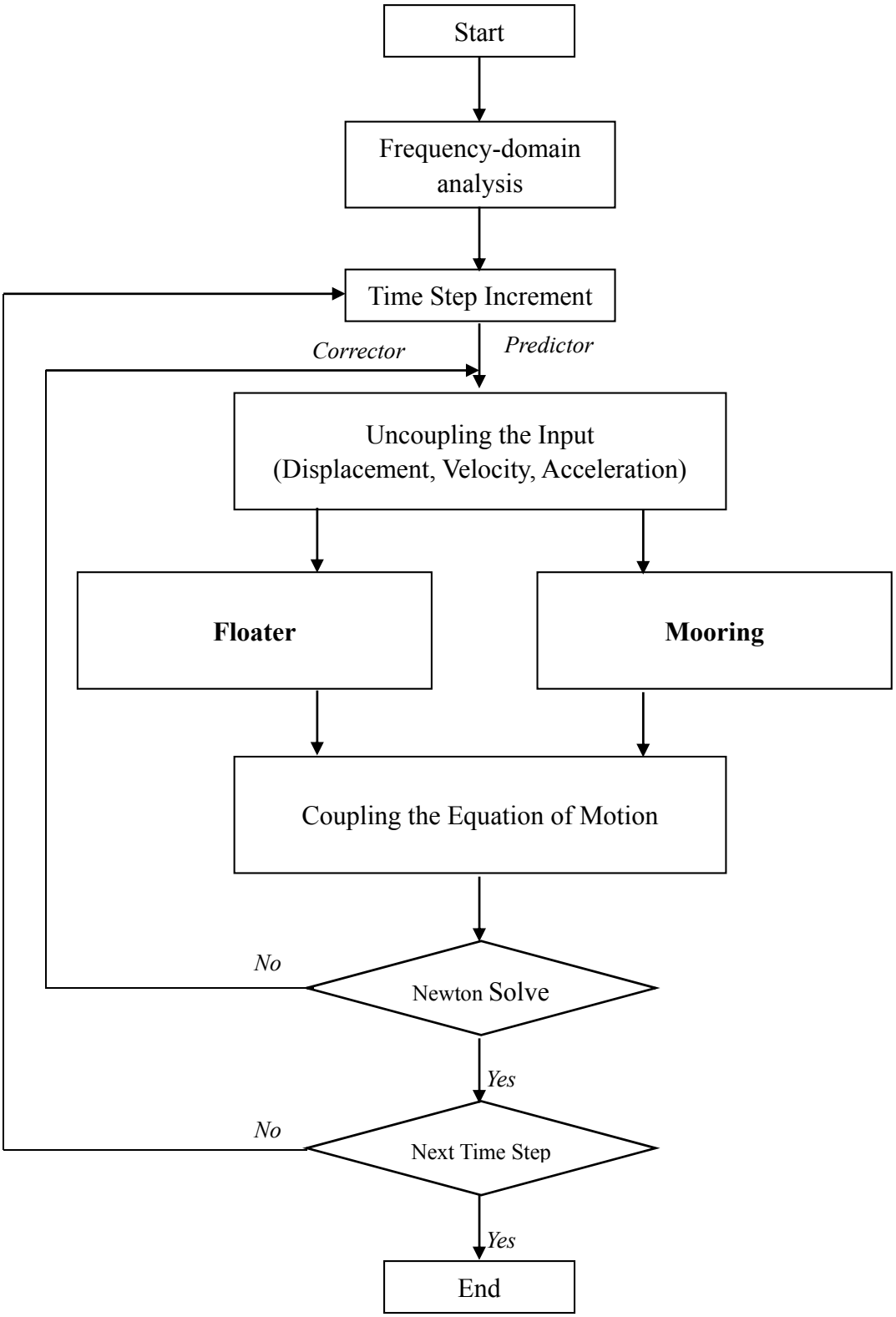

Figure 3-31 Calculation flowchart

Finally, the calculation flowchart of DYNABEAM in time-domain can be drawn as Figure 3-31. As shown in Figure 3-31, the frequency domain analysis is initially conducted for obtaining the hydrodynamic coefficients, mass and stiffness matrix for main floater. The displacement, velocity and acceleration are also initialized in this step for both floater and mooring in coupled form. Then the time domain integration starts. Then coupled displacement, velocity and acceleration are uncoupled firstly for floater and mooring. Then the hydrodynamics introduced in sub-suction 3.2.2 is calculated for floater. Meanwhile, for mooring, the nonlinear stiffness matrix and viscous drag force are calculated. After the solving process for floater and mooring, the equations of motion for floater and mooring are strongly coupled as described in sub-section 3.2.3. The Newton-Raphson method with the Newmark-beta assumption is employed for solving the displacement, velocity and acceleration for next time step. Necessary iteration is conducted when conducting Newton-Raphson solving process. After obtaining the displacement, velocity and acceleration for next time step with sufficient accuracy, these values are substituted for solving next, next time step. The loop is continued until the desired simulation time is reached.

4 VALIDATION OF DYNABEAM

In this chapter, two scaled model tests for FOWT of different designs are demonstrated and results of the scaled model tests are compared with the time-domain DYNABEAM simulation results to validate the accuracy of the simulation. Finally, it is proven that the DYNABEAM simulation tool can handle the different types of FOWT (TLP and SPAR) well in terms of floater motion, mooring tension and structural load.

4.1 Scaled Model Tests

Two kinds of conventional platform, TLP and SPAR supporting the same size of wind turbine are utilized in the model experiments which are carried out as part of joint work between Osaka Prefecture University, Yokohama National University, Nihon University and Osaka University [37]. Figure 4-1 and Figure 4-2 show the photos of the two scaled models with scale ratio 1/100. It is assumed that the floating structure supports a general 5MW wind turbine which is similar to NREL 5ML wind turbine. Regular waves and steady wind are selected for the environment condition. The performance of the FOWT is then checked under only-wave condition and combined wind and wave condition.

The TLP type consists of a tower and three long/slender lower hulls in order to avoid the upset under severe combined loads [38]. The SPAR type has a knob-like structure with larger diameter on the column to have sufficient restoring moment for the limited water depth. The knob-like structure gives a higher and sufficient metacentric height to the FOWT. The basic dimensions for both types of FOWT are shown in Table 4-1

Table 4-1 Basic parameter for scaled models

	Displacement (cm^3)	Height (with wind tower) (cm)	Draft (cm)	Length (lower hull) (cm)
TLP	5800.17	117.5	25	65
SPAR	9408.3	201.8	109.30	/

The relation between wind thrust load on the turbine and the steady wind speed at the generator has been measured a priori (Figure 4-3). Note that the wind speed does not mean the value at the rotor. As the wind speed was set as 2.8 m/s during the wind and wave test, this constant wind thrust 0.965 N was used to evaluate the influence of the wind in the simulation. Under the wind condition, the rotor rotated approximately at 3.2Hz in the model scale. The wind speed seems a little high as it is within the region over the rated-speed. However, it was intentioned to perform the similar tank tests with control under the same wind condition even though discussion about the results under control is out of the scope of the present paper.

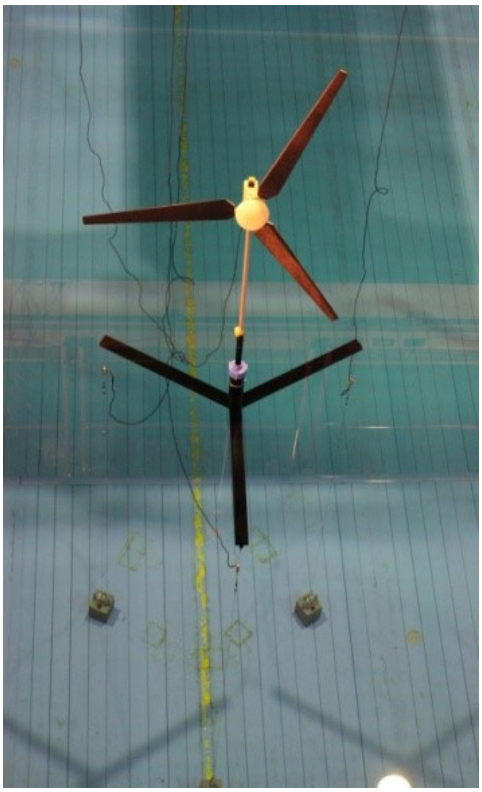

Figure 4-1 Scaled model of TLP type of FOWT

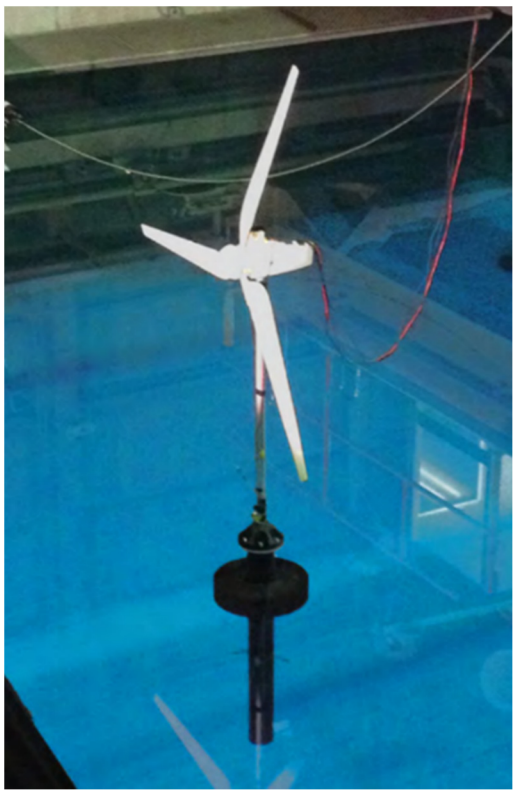

Figure 4-2 Scaled model of SPAR type of FOWT

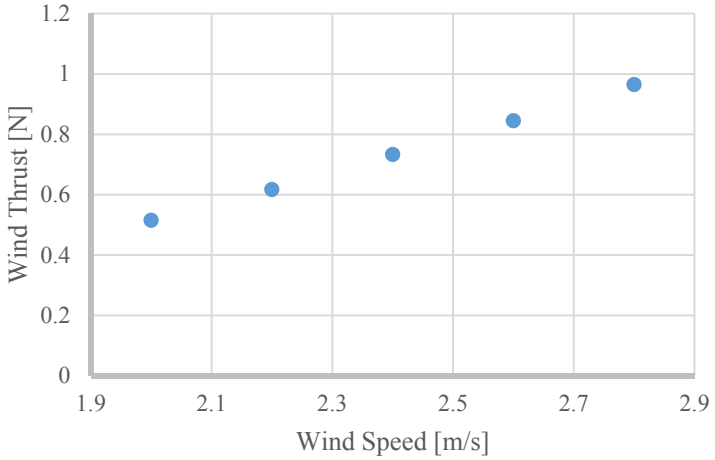

Figure 4-3 Relationship between wind speed and wind thrust

For both TLP and SPAR types of FOWT, the same wind turbine and same environment condition (e.g. wave parameter, water depth) were applied. The wave circular frequency was ranged from 3 to 12.5 rad/s. The wave height was targeted at 0.03m. The direction of the regular waves and steady wind was 0deg to the platform. The water depth was selected as 3m. 3D camera was equipped to measure the 6 DOF motion of platform. In addition, the bending moment and mooring tension were also collected. Figure 4-4 and Figure 4-5 show the experiment arrangement and coordinate system where the location of the load gauge and load cell could be seen. The detailed discussions about the design of the model and experiment could be found in Kozen [37].

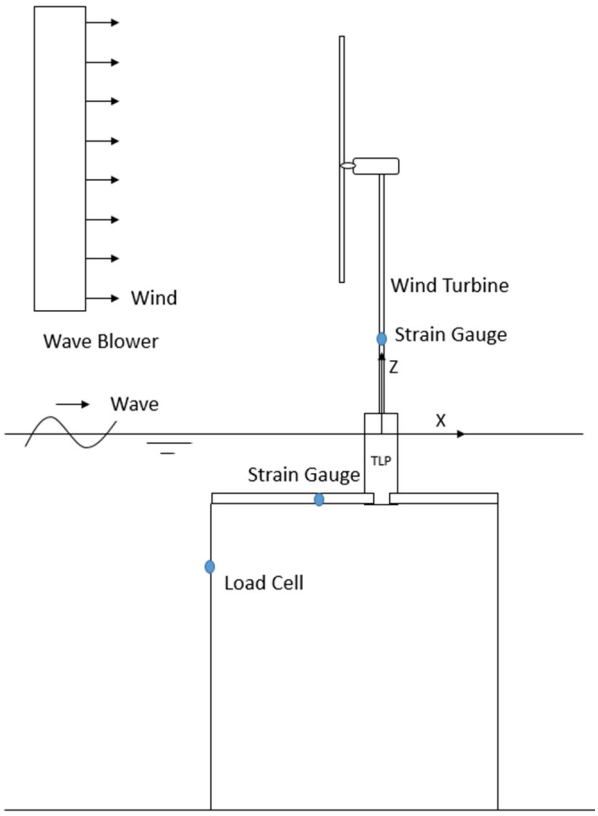

(a) Side view

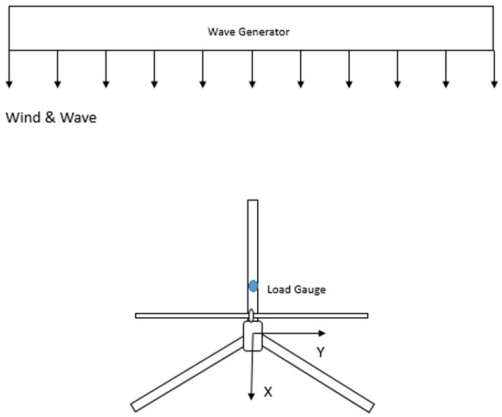

(b) Top view

Figure 4-4 The experiment arrangement and coordinate system for TLP type of FOWT

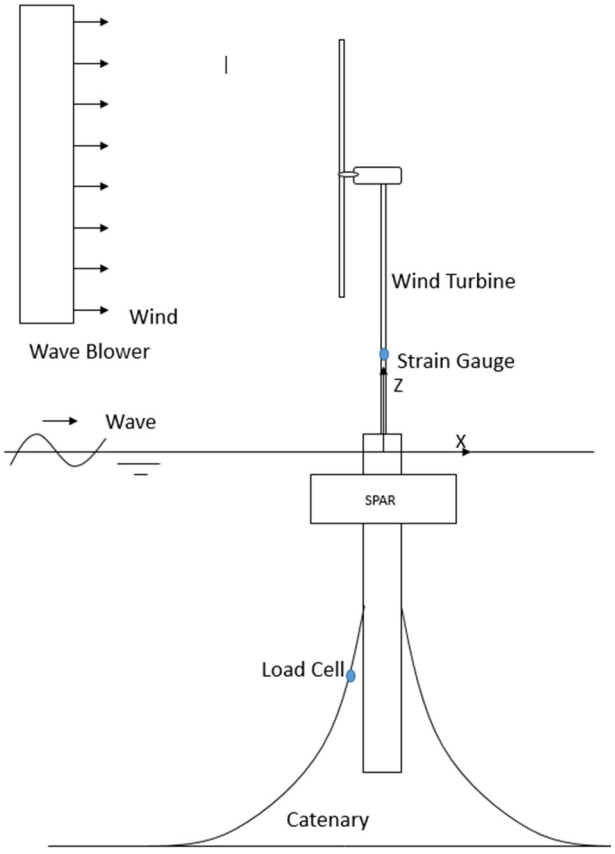

(a) Side view

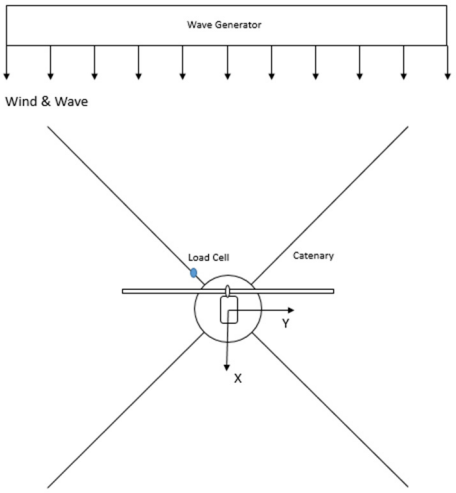

(b) Top view

Figure 4-5 The experiment arrangement and coordinate system for SPAR type of FOWT

4.2 Results and Discussions

The simulation results which include the nodal displacements, the mooring load and the bending moment are discussed in this section by comparing with the experimental results. The rigid body motions are estimated based on the nodal displacements. Two series of environment condition, only-wave condition and wind-wave condition are included.

For the convenience of comparison, results of TLP and SPAR in terms of RAOs are firstly discussed. The RAOs are obtained by taking only the linear component of the response using Fast Fourier Transform (FFT). Then, time domain results are discussed. Finally, the effect of the flexibility of the platform on the response is discussed.

4.2.1 Response amplitude operators (RAOs)

Comparisons of the TLP motion between the simulation results and experimental results are shown in Figure 4-6, Figure 4-7 and Figure 4-8. The horizontal axis represents the wave circular frequency in model scale. The vertical axis corresponds to the RAOs which are obtained by taking the ratio between amplitude of response and wave amplitude or wave slope. The data marked by “Simu” and “Exp” mean the results obtained by simulation and experiment. It could be found that a good agreement is, in general, achieved except for the pitch motion in the low frequency region. The increase tendency of surge and pitch when wave angular velocity omega decreases could be interpreted by taking into account the natural frequency for surge is about 1.03 rad/s which was measured by free-decay tests. Comparing with the surge, the heave and pitch motions are much smaller as is normal for the TLP as it is constrained in vertical direction.

Besides, it could be observed that the influence of the steady wind on the motion of the TLP is rather limited. Figure 4-9 gives the comparison for the mooring tension where we can find that the accuracy of the simulation is acceptable. A small influence of wind thrust could be reflected by both experiment and simulation. According to Figure 4-9, the mooring tension takes the maximum at wave circular frequency 6 rad/s when the wave length is approximately twice of the length of TLP. The length of TLP is about 0.9 m.

Figure 4-10 and Figure 4-11 show the characteristics of the bending moment on the lower hull of TLP and the wind tower (see Figure 4-4 for the position of the strain gauge). It could be seen that, the influence of the wind could be neglected and for both of the bending moments, the peak value occurs when the wave length gets the double value of TLP length.

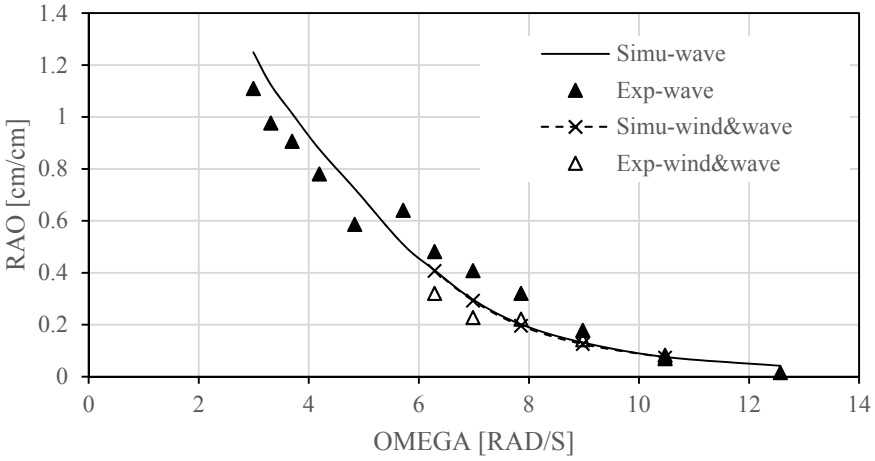

Figure 4-6 Surge motion of TLP

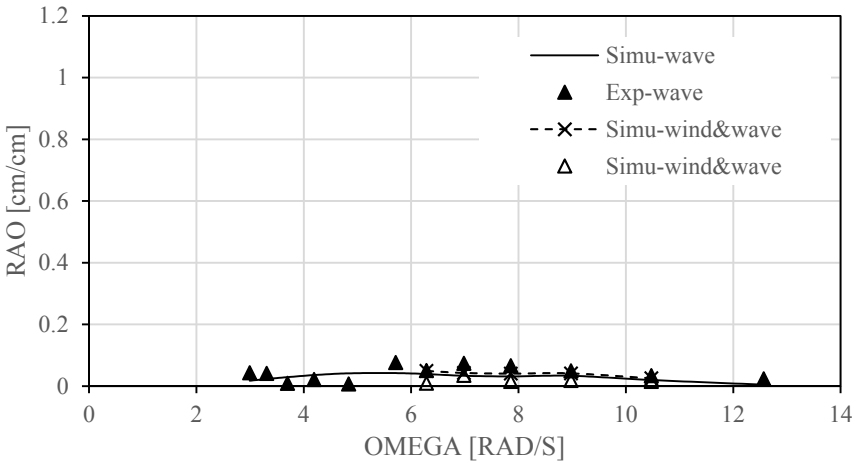

Figure 4-7 Heave motion of TLP

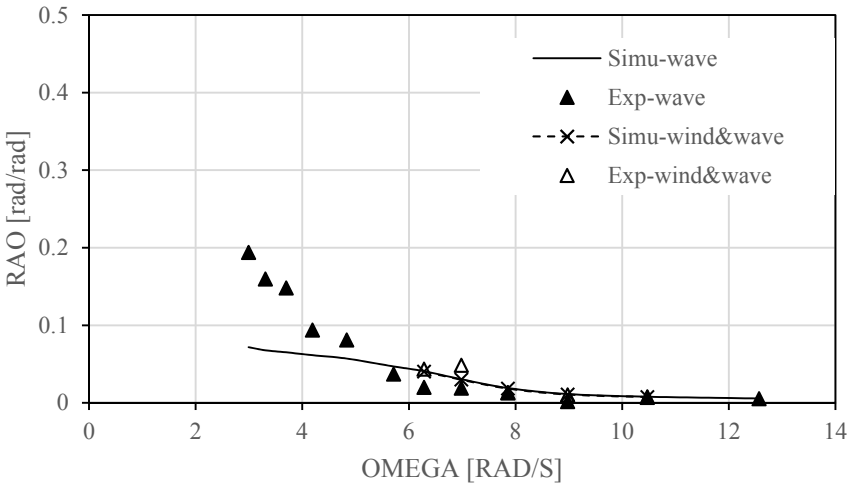

Figure 4-8 Pitch motion of TLP

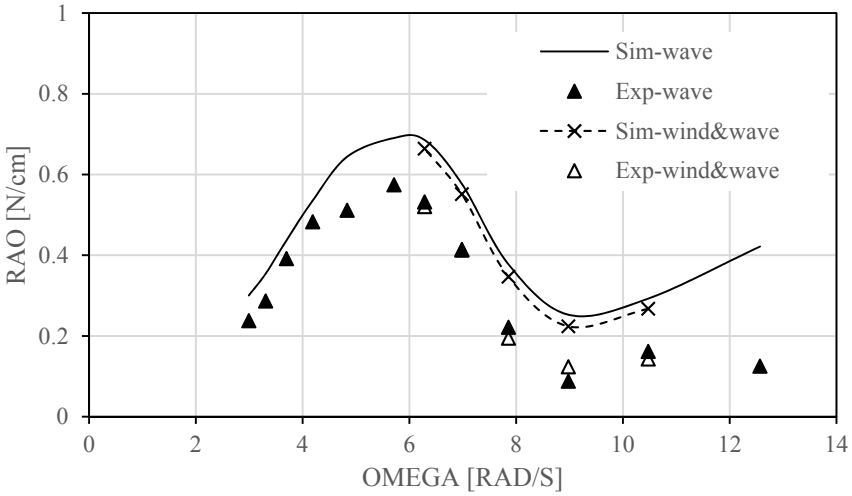

Figure 4-9 Mooring tension of TLP

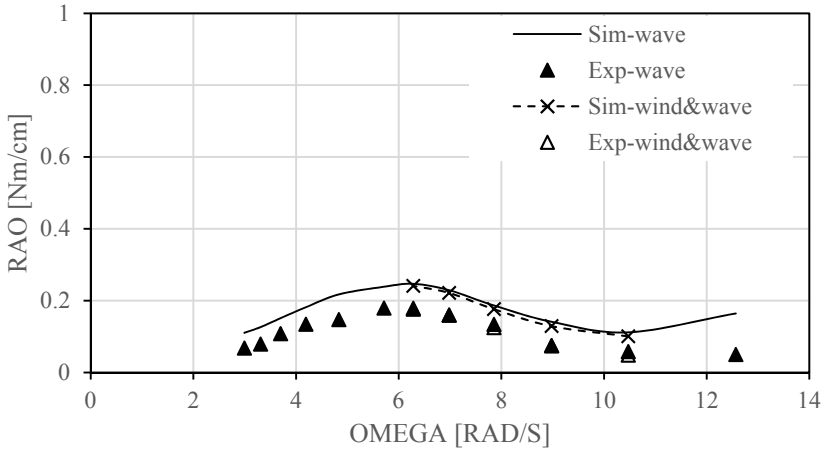

Figure 4-10 Bending moment on the lower hull of TLP

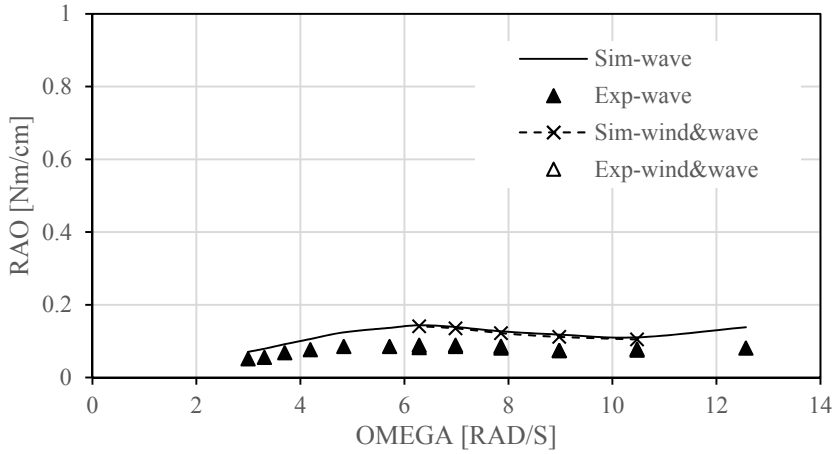

Figure 4-11 Bending moment on the tower of TLP

The motion of SPAR is presented in Figure 4-12, Figure 4-13 and Figure 4-14. The simulation can keep enough accuracy as well. As the natural period of the surge, heave and pitch for the SPAR is located on 8.4s, 3.8s and 5.3s (0.75 rad/s, 1.65 rad/s and 1.21 rad/s in angular velocity correspondingly), the motion of SPAR would increase with the decreasing of wave circular frequency. The influence of wind thrust on the SPAR motion is still limited.

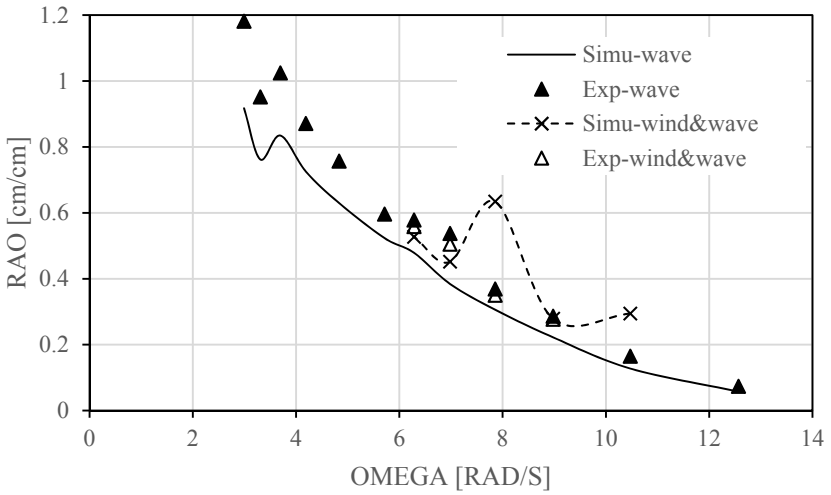

Figure 4-12 Surge motion of SPAR

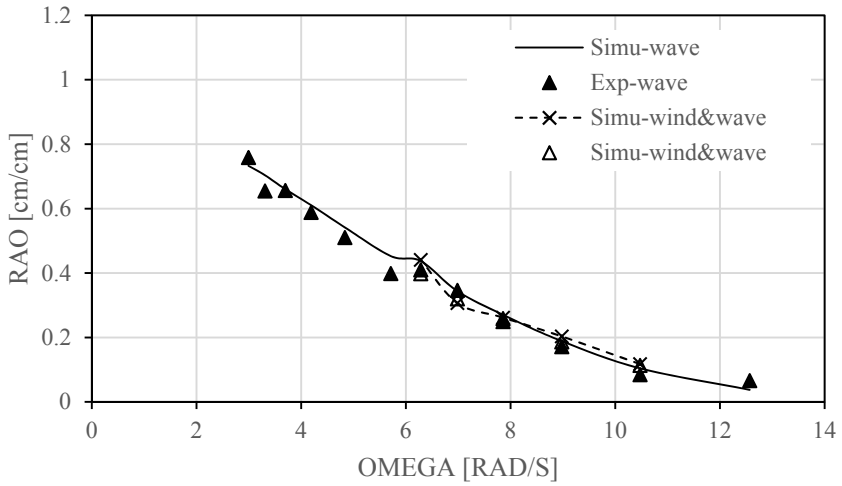

Figure 4-13 Heave motion of SPAR

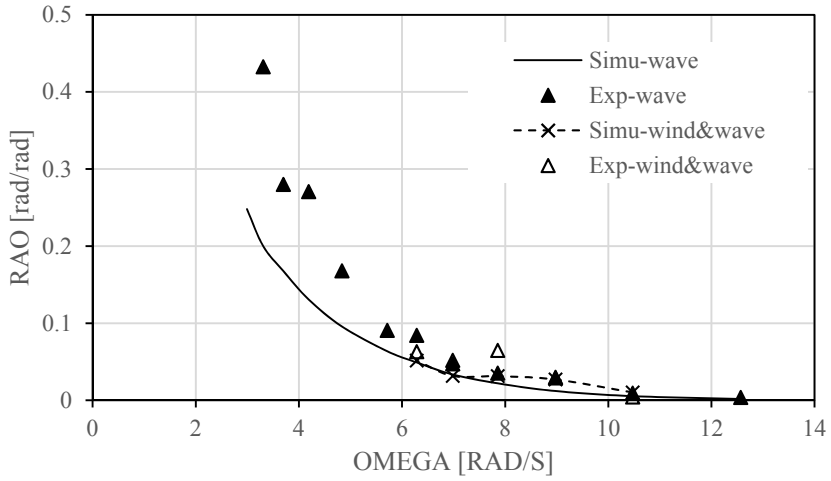

Figure 4-14 Pitch motion of SPAR

The comparison for the catenary tension is shown in Figure 4-15. By checking the experiment data, the results of wind-wave condition are relatively smaller than the only-wave condition. The simulation can also reflect this tendency. The bending moment of the wind tower was captured during the experiments (See. Figure 4-5), the comparison of bending moment between simulation and experiment is presented in the Figure 4-16. A good correlation can be achieved as well.

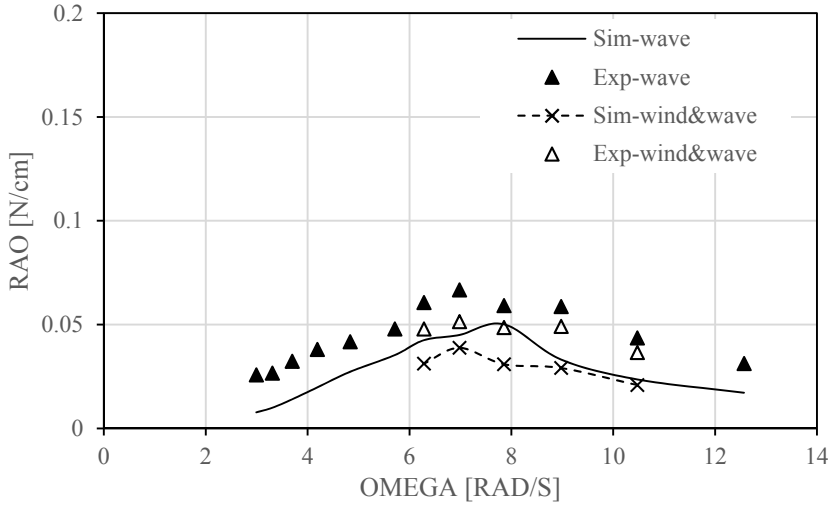

Figure 4-15 Catenary force of SPAR

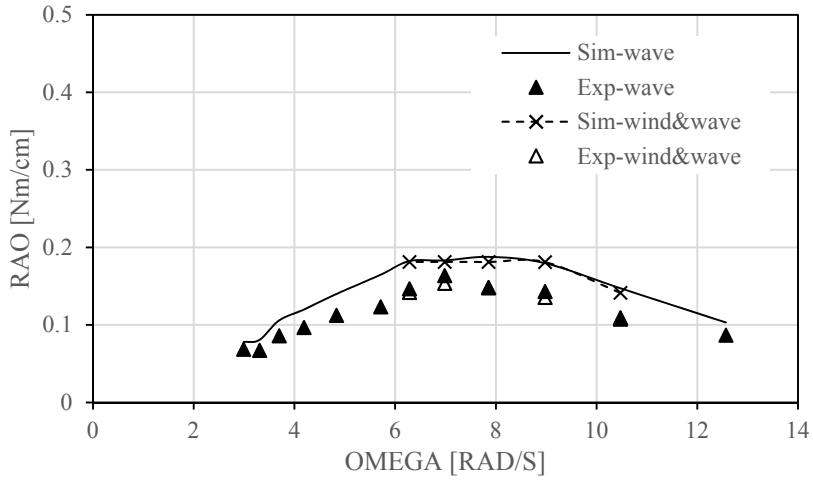

Figure 4-16 Bending moment on the tower of SPAR

4.2.2 Case results

To examine the accuracy of the simulation in a more detailed manner, some cases under only-wave have been selected for both of the TLP and SPAR type of FOWT. The relevant simulation results for the load are presented in this subsection [39].

For TLP, the only-wave case with wave circular frequency 5.7 rad/s is chosen since the corresponding structure response becomes the largest. The comparison for mooring tension and bending moment on the lower hull has been shown in the Figure 4-17 and Figure 4-19. To check the nonlinearity of the system, the time domain results are transferred to frequency domain in Figure 4-18 and Figure 4-20.

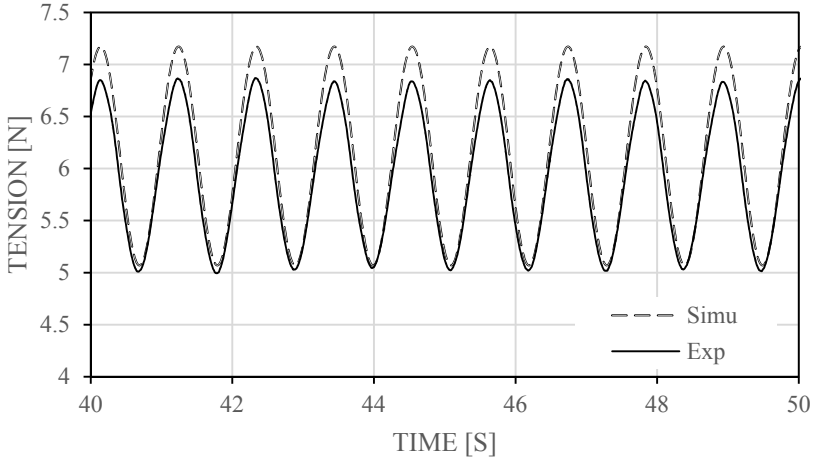

Figure 4-17 Mooring tension in time domain, TLP

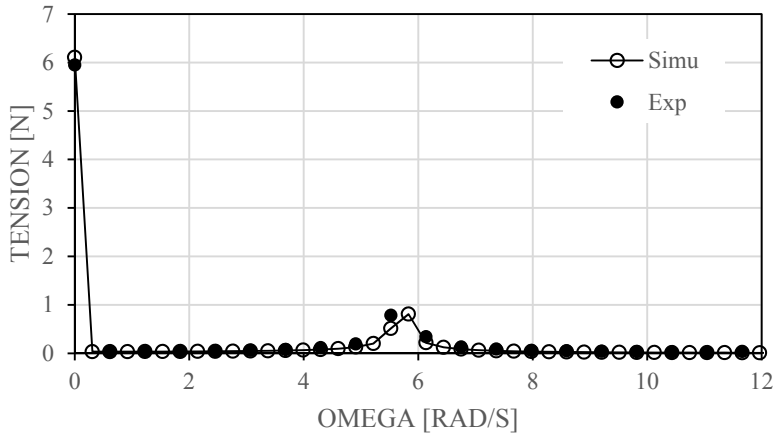

Figure 4-18 Mooring tension in frequency domain, TLP

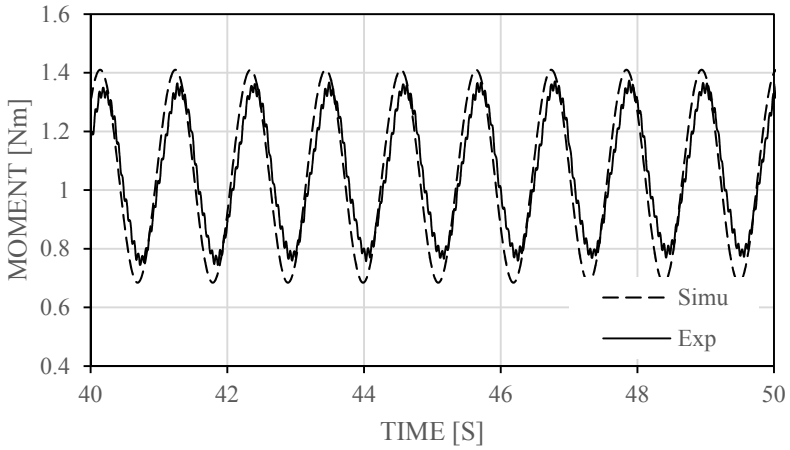

Figure 4-19 Bending moment on the lower hull in time domain, TLP

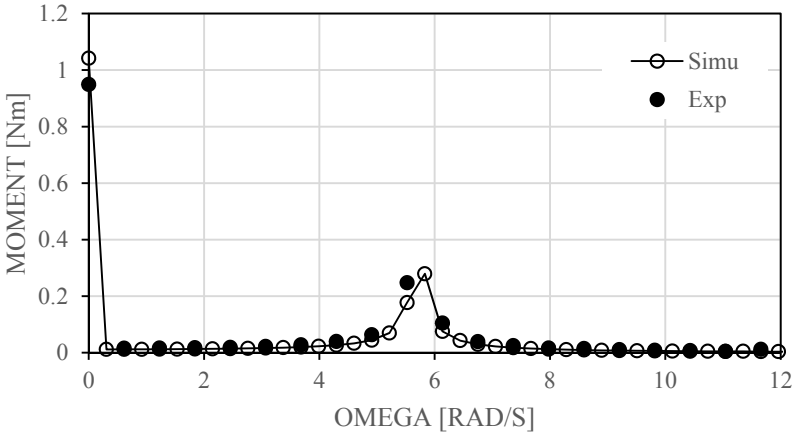

Figure 4-20 Bending moment on the lower hull in frequency domain, TLP

For SPAR, the results of catenary tension and bending moment on the tower for the only-wave case with omega 6.9 rad/s are shown from Figure 4-21 to Figure 4-24. A good correlation can be confirmed.

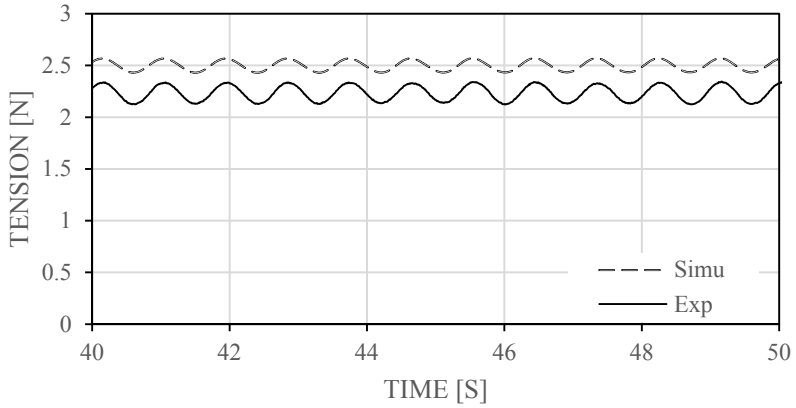

Figure 4-21 Catenary force in time domain, SPAR

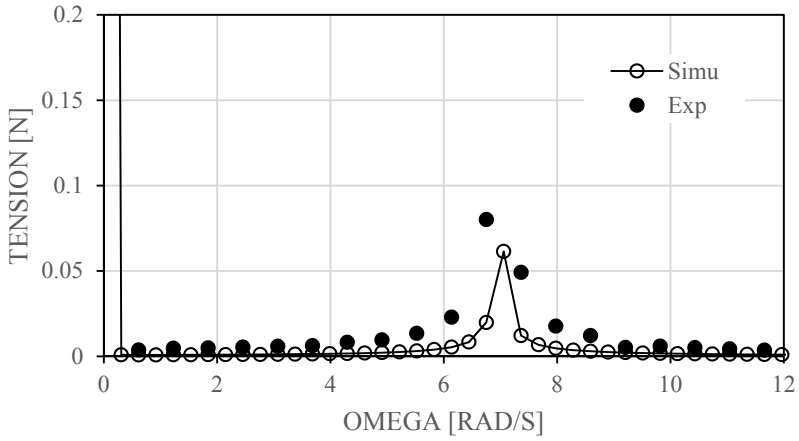

Figure 4-22 Catenary force in frequency domain, SPAR

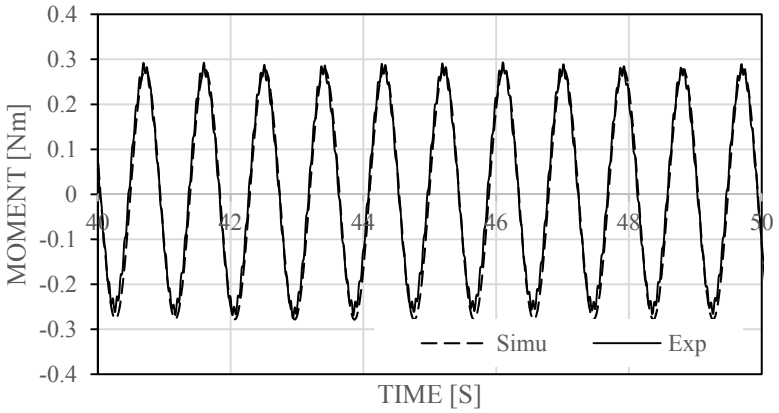

Figure 4-23 Bending moment on the tower in time domain, SPAR

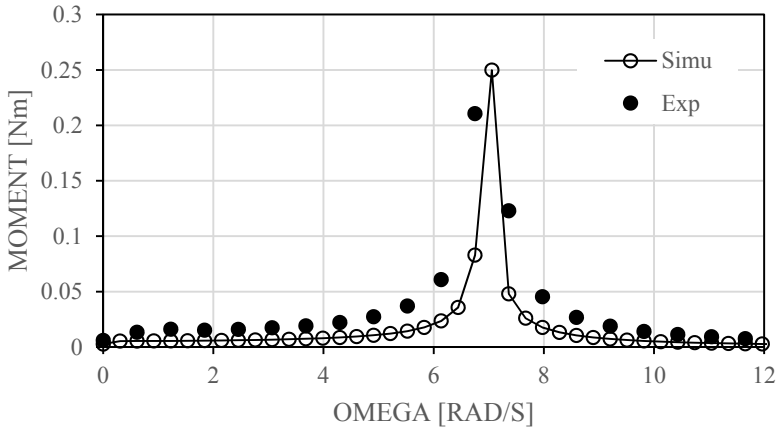

Figure 4-24 Bending moment on the tower in frequency domain, SPAR

4.2.3 Influence of stiffness

The flexibility of the structure was not reflected in the experimental model properly according to Froude's law. The stiffness of the experiment model was much higher than the realistic offshore floating structure. Meanwhile, the simulation for models with increased/decreased stiffness may be performed for comparisons.

To investigate the influence of the flexibility of the structure on the bending moment of the lower hull and mooring tension, another numerical TLP model with lower stiffness on the lower hull is established. The stiffness is selected according to a more realistic offshore floating structure whose stiffness is about 1 percent of that of the experiment model.

Figure 4-25 and Figure 4-26 present the characteristics of mooring tension and bending moment of the lower hull for the model with the lower stiffness. It could be seen that due to the flexibility of the lower hull, the responses of the mooring tension and bending moment are increased. This is because, for the flexible TLP, the natural frequency of the structural system is lowered and the deformation of lower hull has a significant influence when coupling the TLP with the mooring system.

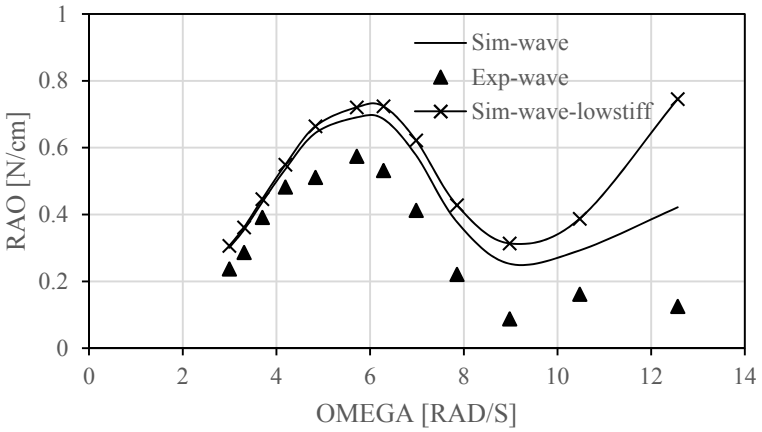

Figure 4-25 Mooring tension of TLP

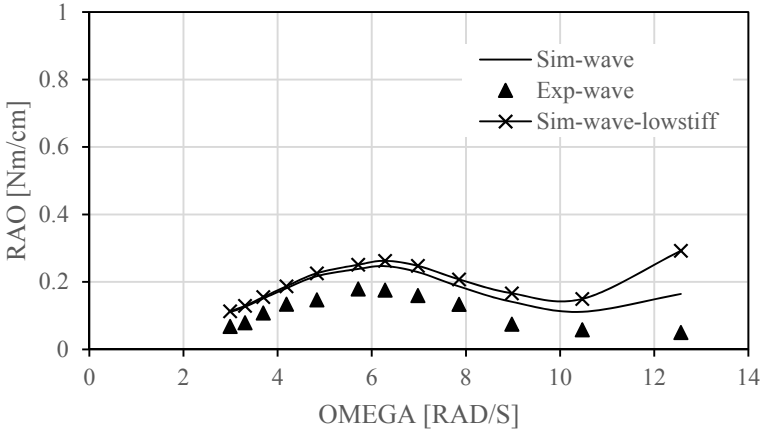

Figure 4-26 Bending moment on the lower hull of TLP

4.3 Conclusions

By comparing the simulation results with experimental results for TLP and SPAR type of FOWT, the accuracy of the simulation is proved. Not only the rigid body motion but also the internal force of structure could be simulated reasonably by the presented numerical model.

It is found out by the simulation and model test that the steady wind thrust has little influence on the dynamic response of FOWT system. The influence of the flexibility on the structure response has been investigated by the simulation. For TLP type of FOWT, smaller stiffness of lower hulls results in an increase of mooring tension and bending moment on the lower hull.

5 BEHAVIOR OF A SYSTEM CONSISTING OF MAIN FLOATER, BUOY AND TETHER

Once the numerical tool is successfully established and validated by the model tests, we should continue the research on the new proposed type of FOWT, OU-Design. To validate the feasibility of the OU-Design, a series of scaled model tests were conducted. The corresponding numerical model consisting of the main floater, buoy and tether is also established based on the time-domain DYNABEAM.

5.1 Scaled Model

5.1.1 Design particulars

A scaled model with a scale ratio 1/100 (See Figure 5-1) was fabricated and employed in a series of tank tests. It is made of GFRP. The principal particulars and weight of the full-scaled model and scaled model are shown in Table 5-1 and Table 5-2 respectively.

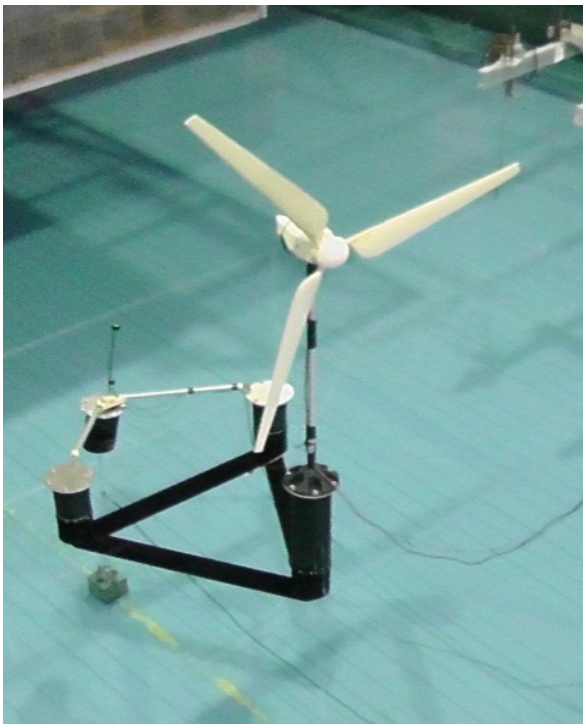

Figure 5-1 Photo of scaled model for OU-Design

Table 5-1 Principal particular of main floater

Item	full scaled model		scaled model	
	Value	Unit	Value	Unit
Mass	13130	t	13130	g
Draft	25	m	250	mm
Distance between columns	75	m	750	mm
Column Dia	11	m	110	mm
Column height	33	m	330	mm
Column height(having tower)	53	m	530	mm
Lower Hull Breadth	6	m	60	mm
Lower Hull Depth	6	m	60	mm
GM	7.13	m	71.3	mm

Table 5-2 Comparison between full-scaled and scaled model

Item	full scaled model		scaled model	
	Weight [kN]	Center of Gravity [m]	Weight [N]	Center of Gravity [mm]
Wind turbine & Tower	16000	117.5	16	1175
Steel & Ballast Weight	115300	12	115.3	120
Total Weight	131300	24.9	131.3	249

Table 5-3 Principal particular of buoy

Item	full scaled model		scaled model	
	Value	Unit	Value	Unit
Mass (Ballast)	1280(500)	t	1280(500)	g
Draft	22.4	m	224	mm
Height	28	m	280	mm
Diameter	11	m	110	mm
Center of Gravity	11	m	110	mm

The principal particulars of buoy in full-scale and model scale are shown in Table 5-3. Initial tension of mooring is shown in Table 5-4.The main floater and the buoy are connected by a rigid yoke in the tank tests.

Table 5-4 Principal particulars of tendon

Item	full scaled model		scaled model	
	Value	Unit	Value	Unit
Length	114.5	m	1145	mm
Initial tension	5880	kN	5.88	N

5.1.2 Scaled model experiment

The experiment was conducted in the Ocean Engineering Basin of Institute of Industrial Science, the University of Tokyo. The dimension of the tank is 50m (length)×10m (width) (See Figure 5-2). The draught was set at 1.5m by adjusting the movable floor. The wave generator, wind generator and current generator are also equipped.

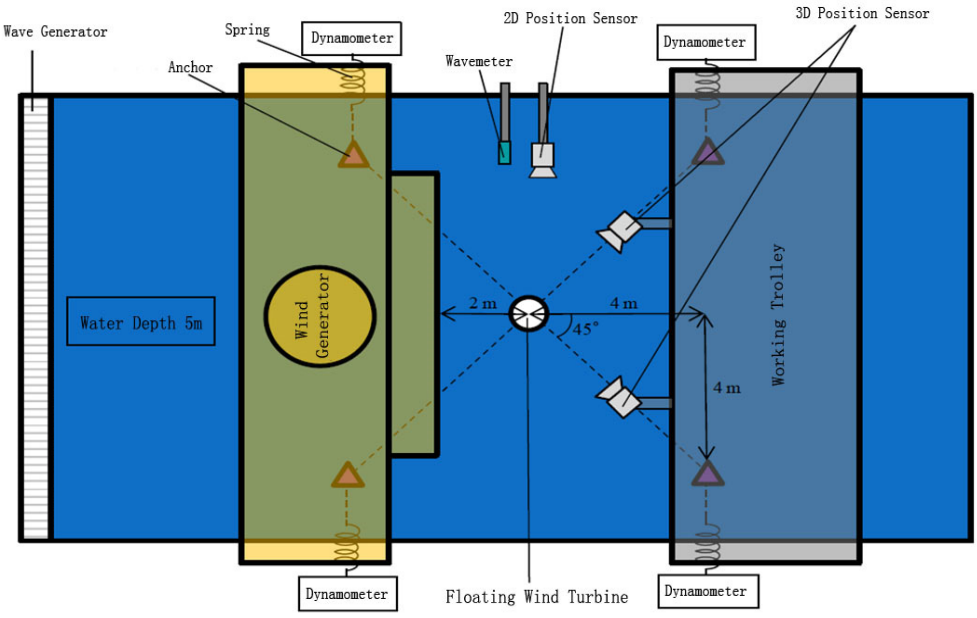

Figure 5-2 The overall arrangement of water tank

a) Measurement

The following items were measured in the tank test.

- The 6 degrees of motion for the platform by 3D camera

- The 3 degrees of motion for buoy by 2D position sensor
- The tension in mooring system
- The rotation speed of the blade
- The wave elevation

b) Experiment conditions

Table 5-5 shows the experimental conditions in terms of blade rotation speed, wave height and wave period. All of these data are taken and translated from the real-sea conditions according to the Froude's law. In addition, to investigate the response behavior at around the natural periods, the relevant tests are also conducted with the wave period set around the natural period of the pitch motion. Only regular wave and steady wind tests are conducted.

Due to the difficulty in keeping the scale law according to the Reynold's number and keeping the quality of the generated wind, both of which may affect the aerodynamic properties, the blade rotation speed at which the prescribed thrust load is stably attained is targeted. To this end, the relation between the wind thrust load and the blade rotation is measured a priori (Figure 5-3). All the tests with winds are targeted at blade rotation 3.0Hz (177rpm). The thrust load of 0.8N is expected correspondingly.

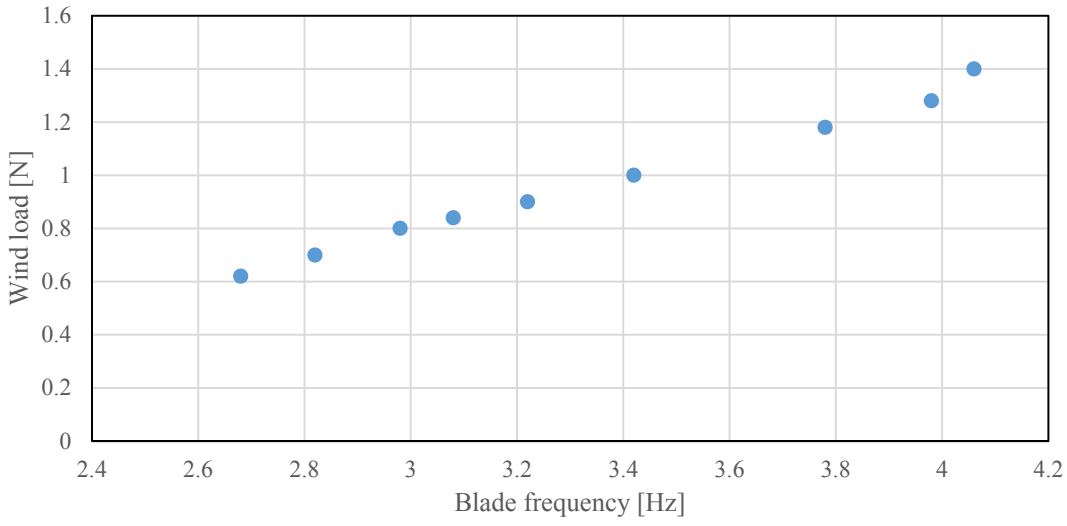

Figure 5-3 Relationship between blade frequency and wind load

Table 5-5 Criteria of the test conditions

Test names	Condition	Number of rotation of the blade [rpm]	Wave height[cm]	Wave period[s]	Test id
Wind tests		163			Exp-no22
		170			Exp-no23
		177	-	-	Exp-no1-1
		177	-	-	Exp-no1-2
		185			Exp-no24
		192			Exp-no25
Wave tests	Regular		4.15	0.70	Exp-no02-1
		-	2.91	0.60	Exp-no03-1
			5.60	0.80	Exp-no04-1
	Middle		5.37	0.85	Exp-no08-1
		-	4.44	0.75	Exp-no09-1
			6.98	0.95	Exp-no10-1
	Cut-out		7.94	1.00	Exp-no14
		-	6.64	0.90	Exp-no15
			7.67	1.10	Exp-no16
	Regular		3.94	0.70	Exp-no02-2
		-	2.60	0.60	Exp-no03-2
			5.37	0.80	Exp-no04-2
	Middle		5.37	0.85	Exp-no08-2
		-	4.15	0.75	Exp-no09-2
			6.88	0.95	Exp-no10-2
Wind and wave tests	Regular		3.85	0.70	Exp-no5-1
		177	3.13	0.60	Exp-no6-1
			6.25	0.80	Exp-no7-1
	Middle		5.53	0.85	Exp-no11-1
		177	3.93	0.75	Exp-no12-1
			6.58	0.95	Exp-no13-1
	Cut-out		7.92	1.00	Exp-no17
		177	6.48	0.90	Exp-no18
			7.33	1.10	Exp-no19
	Regular		3.49	0.70	Exp-no5-2
		177	2.31	0.60	Exp-no6-2
			5.70	0.80	Exp-no7-2
	Middle		5.37	0.85	Exp-no11-2
		177	3.95	0.75	Exp-no12-2
			6.56	0.95	Exp-no13-2

c) Experiment results

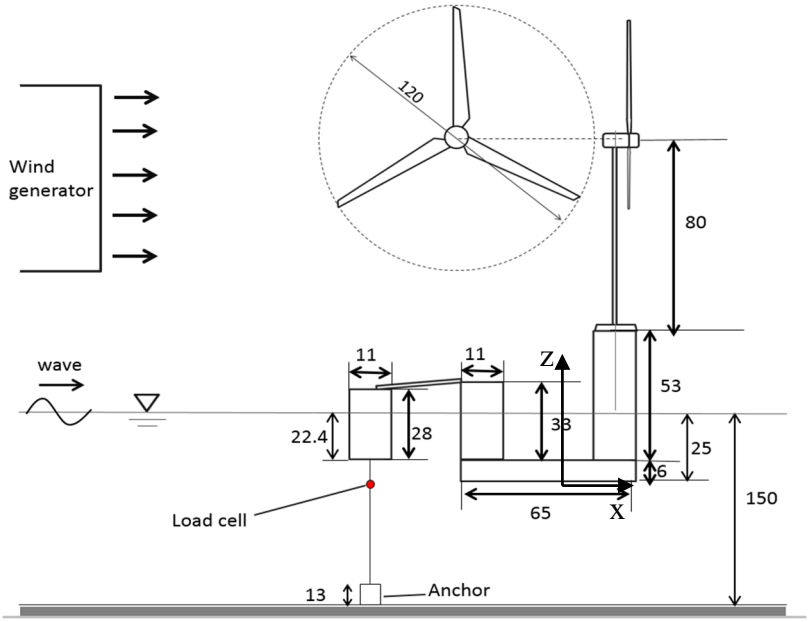

Figure 5-4 The side view of model

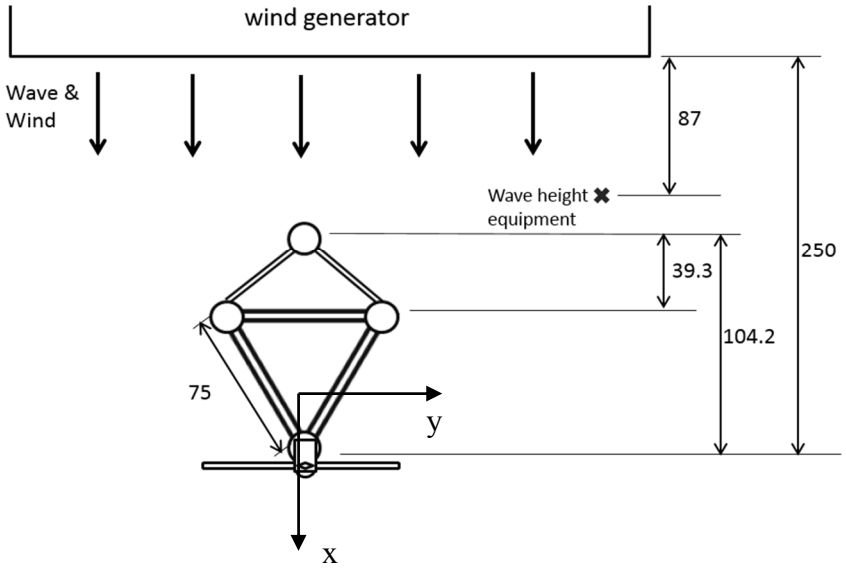

Figure 5-5 The top view of the model

A Cartesian coordinate system is defined as in Figure 5-4 and Figure 5-5. The origin 'o' is the center of gravity of the floater. The x-axis and z-axis are taken parallel to the traveling direction of the waves and positive upwards, respectively. The water depth is set to 1.5m. The data of 6 degrees of freedom are collected by 3D camera per 1/30s.

The power generation efficiency may decrease with the increase of the heel angle of the tower [40]. Figure 5-6 gives the steady drift in surge direction and steady heel of

pitch to the thrust in only-wind condition. If we assume the designing limit criteria on the heel angle is 5degrees, the proposed FOWT has a good performance.

Figure 5-7 shows the time histories of motion in one experiment case of Cut-Out condition (the rotation number of blade: 3.0Hz, design wave height: 7cm, wave period: 1.0s). It is found out that since the direction of wind and wave is identical with the x-axis of structure, the surge, heave and pitch become the main responses and all of these three responses are rather linear. However, a low frequency response with large amplitude can be observed for the sway and yaw. It may be attributed to the low restoring force and moment in these modes.

The DFT ((Direct Fourier Transform) analysis is applied based on 1024 points of data so that the accuracy of the DFT is 20/1024Hz. Figure 5-8 shows the DFT result of surge, heave and pitch for the same case with Figure 5-7.

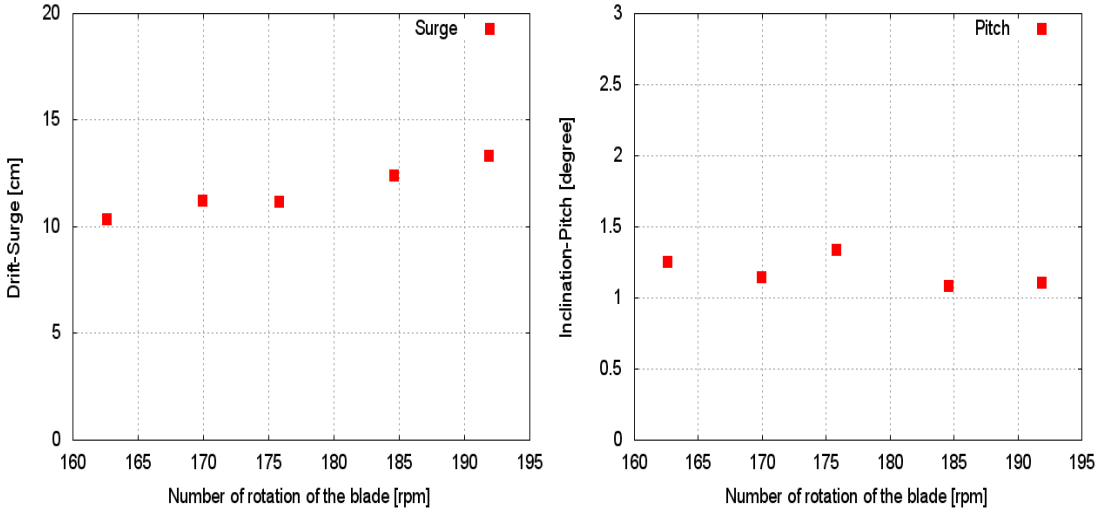

Figure 5-6 The steady drift in surge and heel of pitch to wind

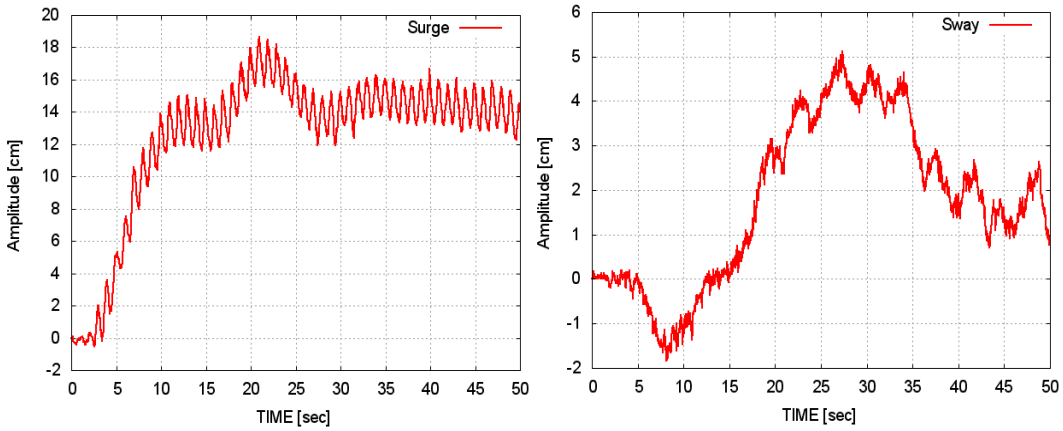

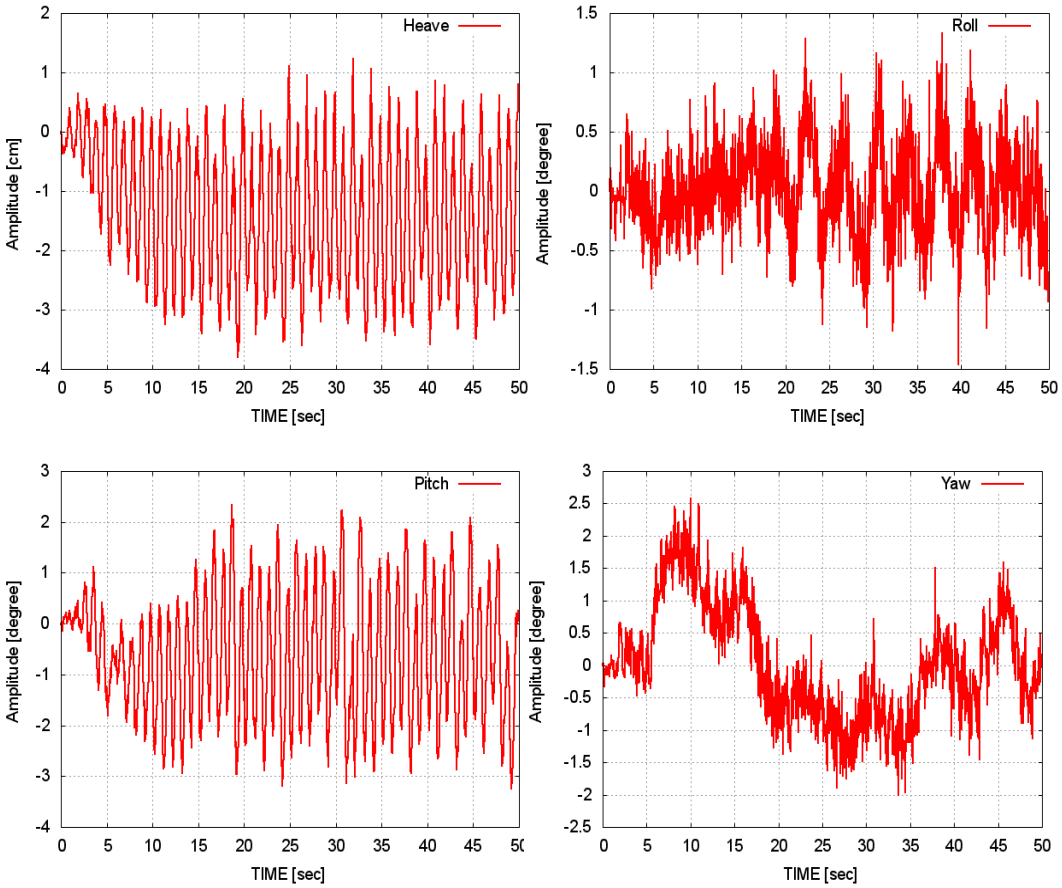

Figure 5-7 The time series of 6 DOF motion

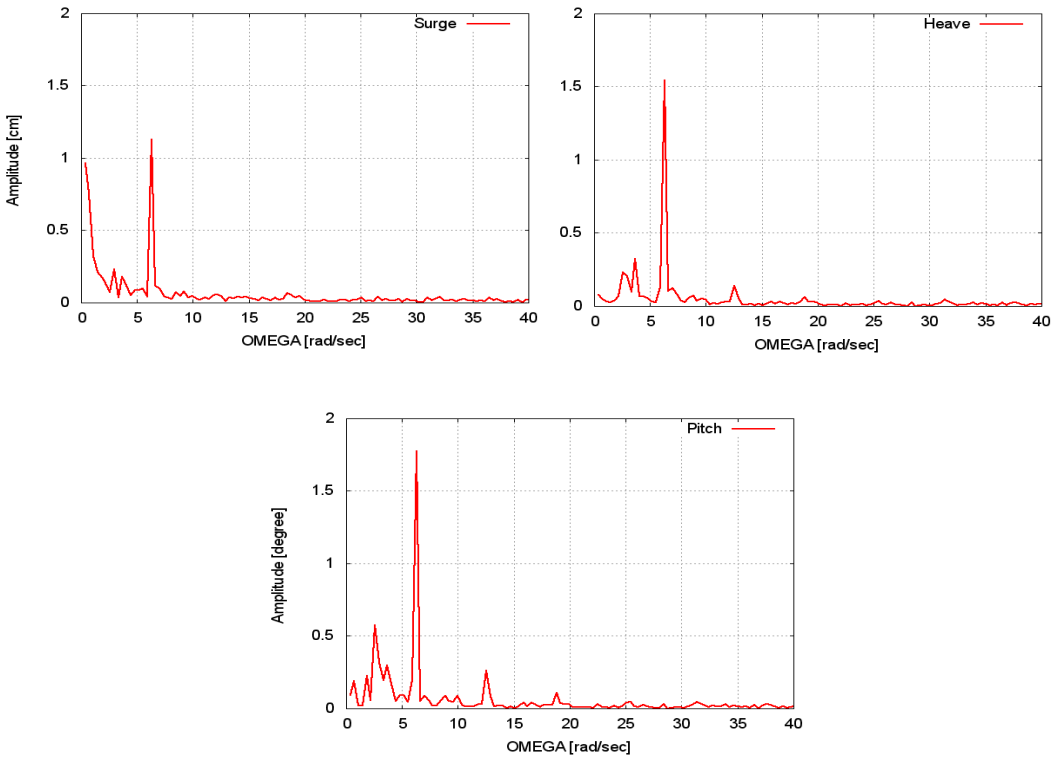

Figure 5-8 The DFT results of surge, heave and pitch

Based on the DFT results, the RAOs for the motion of the main floater can be calculated, which is discussed in following section by comparing with numerical simulation results.
.

5.2 Numerical Models

The relevant theory utilized in simulation has been presented in Chapter 3, based on which the simulation model is established as shown in Figure 5-9.

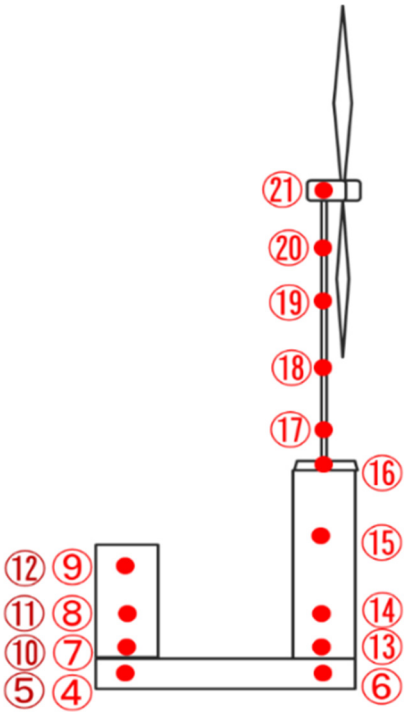

Figure 5-9 Simulation model of main floater

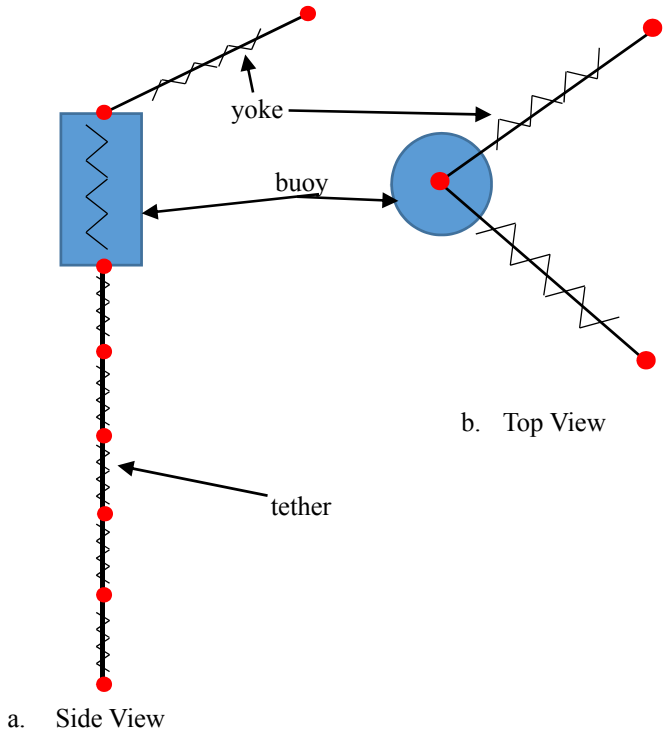

Figure 5-10 Simulation model of mooring system

As the transverse waterplane moment of inertia is small for buoy, it is hard to maintain the initial heel of buoy around zero especially when the measuring instruments are located on the top of the buoy. Even though this initial heel will not affect the external force so much, its influence on the motion of the buoy may be more significant. To reproduce the nonlinear phenomena observed in the scaled model test, it is indispensable to consider this initial heel in simulation. The influence of this initial heel will be discussed in the following uncertain analysis section.

For the FOWT with single-point mooring system, a special attention should be paid on the Yoke-Buoy joint as the restoring force from mooring to main floater is transmitted through this joint. It is necessary to clarify the response of the coupling system if the working condition becomes severer. During experiment, due to the rotation limitation of hinge in Yoke-Buoy joint of the scaled model, it was observed that a “strong contact” between yoke and buoy always occurs in some experimental cases. This “strong contact” behavior is caused by the mistakes during the model manufacture which was not expected in the model-design phase. Even though it may be not allowed in the real offshore structure as it causes some impact load, it has to be taken into account in the simulation in order to reproduce the same behavior of model tests. Figure 5-11 shows the numerical model for the hinge in Yoke-Buoy joint.

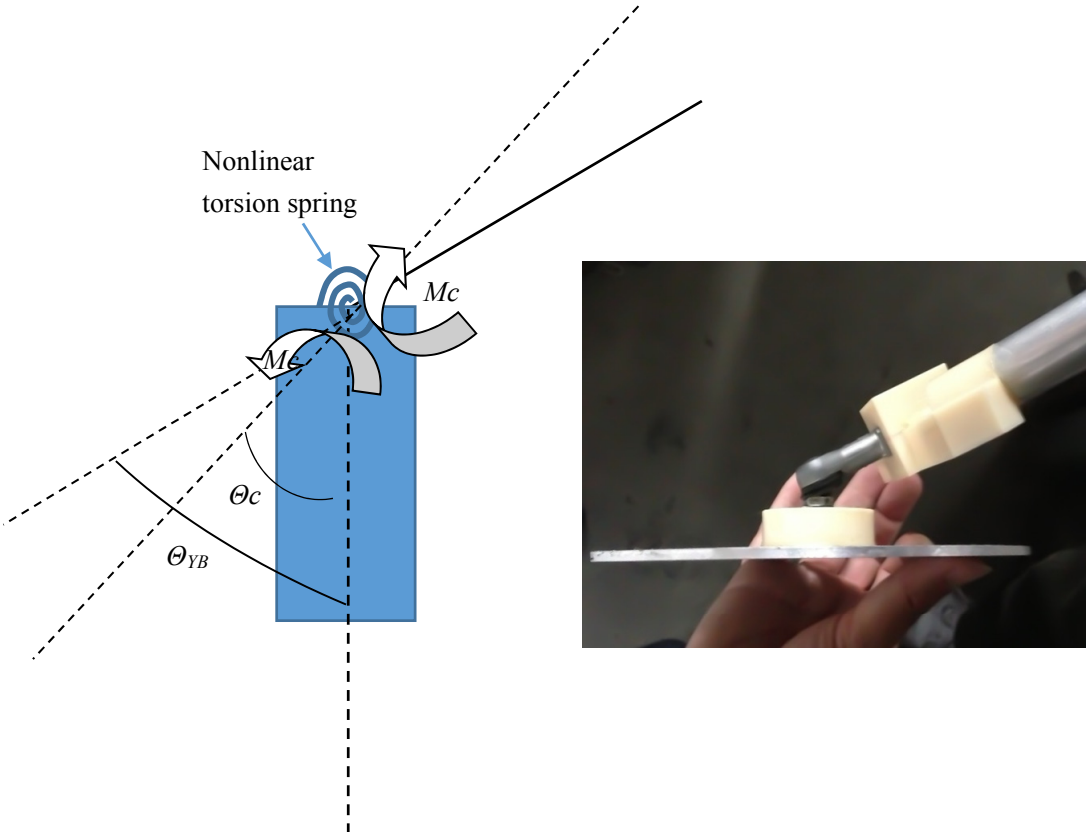

Figure 5-11 The numerical model for the Yoke-Buoy joint

A nonlinear torsion spring with stiffness coefficient K is attached on the hinge joint. The equation for the restoring moment of the spring is shown below:

$$M_c = K(d\Theta) * \Theta_{YB} \qquad \textbf{(5-1)}$$

where:

M_c : the impact moment acting on both of yoke and buoy

$d\Theta = \Theta_{YB} - \Theta_C$

Θ_{YB} : the angle between yoke and axis of buoy

Θ_C : critical value for Θ_{YB}, the contact will happen when $\Theta_{YB} = \Theta_C$

$K(d\Theta) = K_f * (d\Theta)^n$ when $d\Theta<0$

$K(d\Theta) = 0$ when $d\Theta>0$

K_f : the increasing ratio for stiffness K

n: the order of the contact model

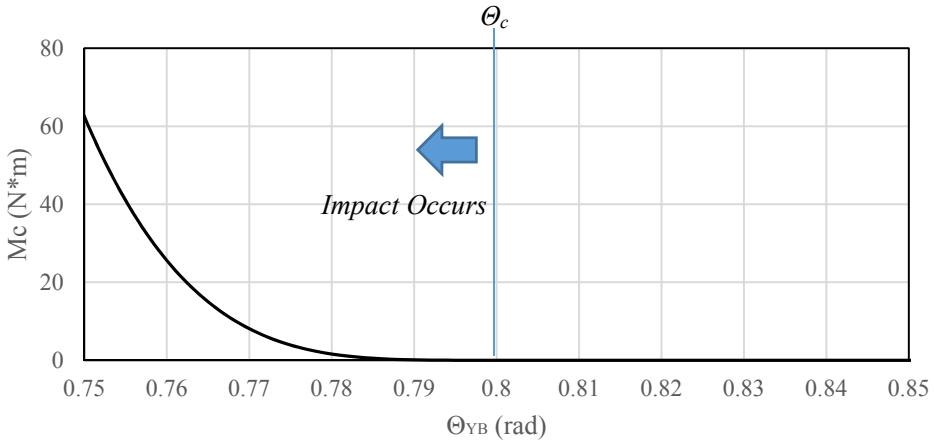

Figure 5-12 **The impact moment** (Θ_c=0.8rad, K_f=1 x10^{7}Nm, n=4)

Θ_c=0.8rad, K_f=1 x10^{7}Nm, n=4 are adopted in the following simulation. The above nonlinear contact model is simply assumed without any detailed consideration of the mechanics, however just for modelling impact moment borne at the joint. The influence of the contact will be discussed in detail in the following section. By checking the experiment data, the impact load caused by the contact mainly occurs in the wind-wave cases as the wind thrust can significantly decrease the angle Θ_{YB}. Therefore, in the following results of only-wave cases, the influence of contact model is not included. Only for the wind-wave cases, the contact influence is discussed.

5.3 Comparison and Discussion

The data of 6 degrees of freedom of motion for the main floater are collected by 3D camera at a rate of 1/30s. The DFT analysis with accuracy of 20/1024Hz is applied for all of the experiment cases and simulation results. As the response of main floater is rather linear, only first order of RAO for the main floater is discussed. However, to check the nonlinearity of mooring system, the comparison for the first and second order of response is presented here.

5.3.1 Response of the main floater

a) Only-wave conditions

Figure 5-13, Figure 5-14 and Figure 5-15 show the comparison of RAOs between experiments data and simulation results for the only-wave cases. The horizontal axis represents the wave circular frequency in model scale. A good agreement is, in general, achieved except for the surge motion in the low frequency region. The magnified figures for the same RAOs with frequency range from 5rad/s to 11rad/s are shown in Figure 5-16, Figure 5-17 and Figure 5-18. To investigate the influence of the mooring system, the comparison for the simulation with and without mooring is also included in all the figures.

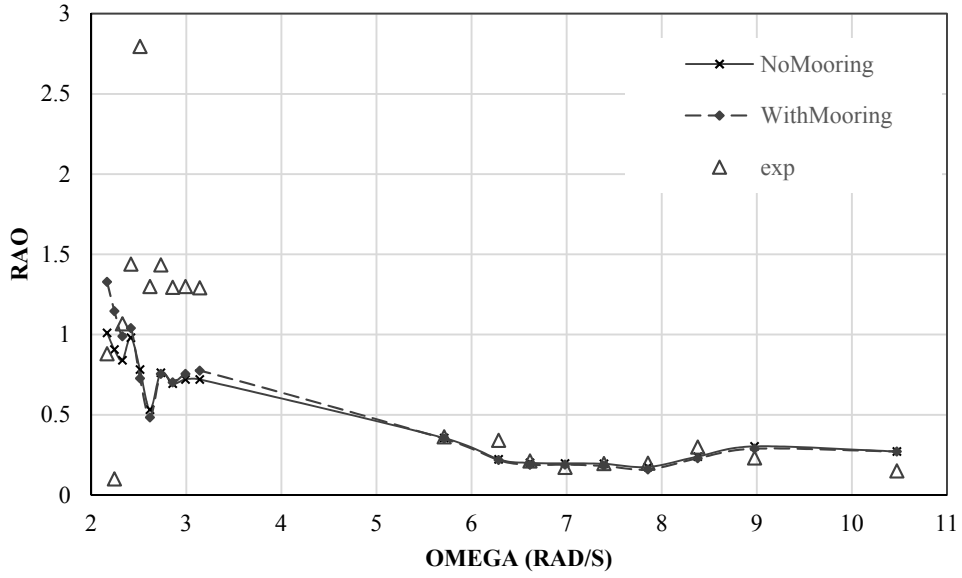

Figure 5-13 Surge of main floater for only-wave cases

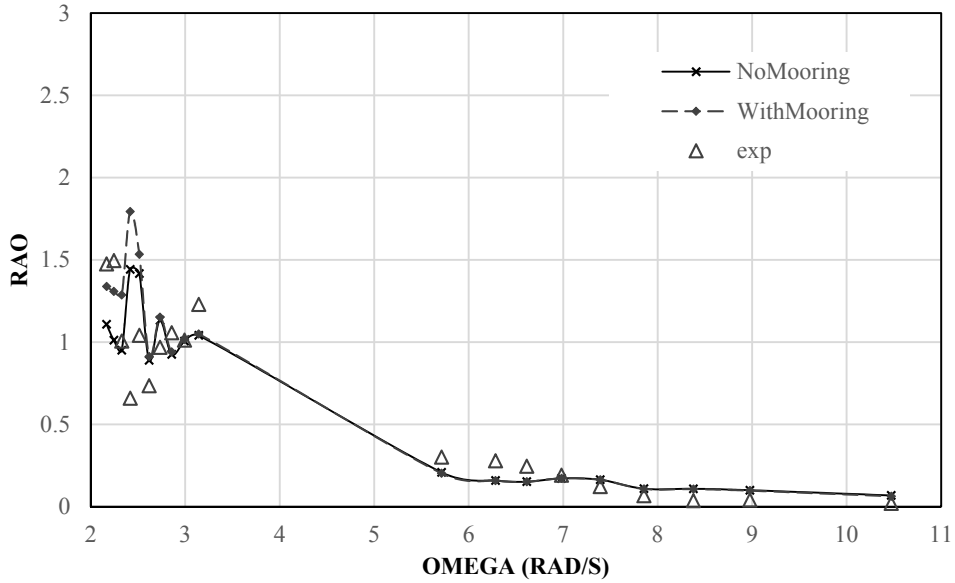

Figure 5-14 Heave of main floater for only-wave cases

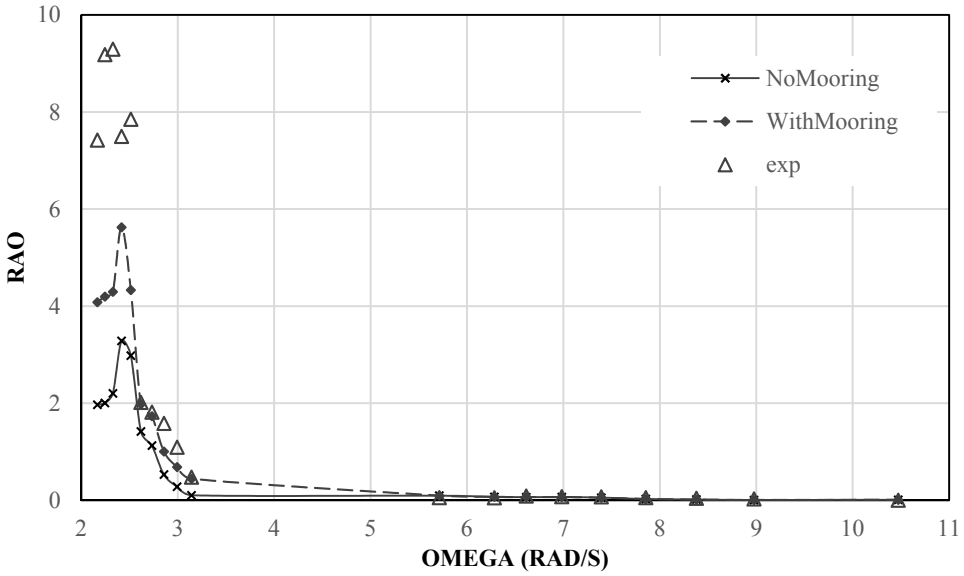

Figure 5-15 Pitch of main floater for only-wave cases

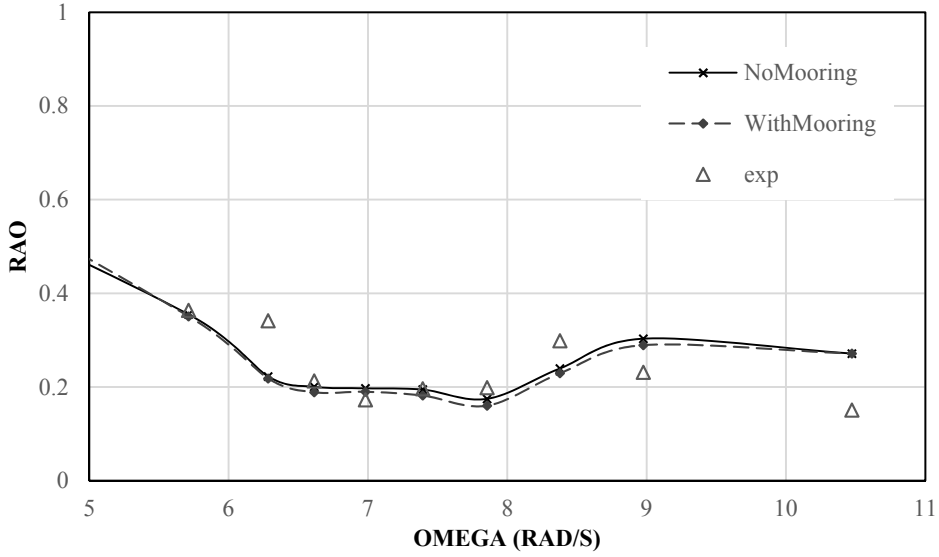

Figure 5-16 Surge of main floater for only-wave cases

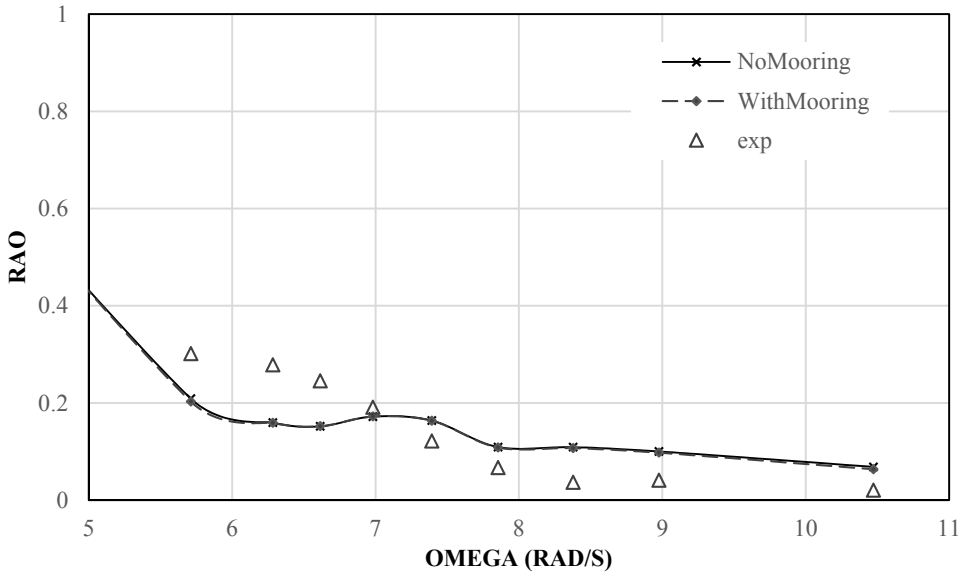

Figure 5-17 Heave of main floater for only-wave cases

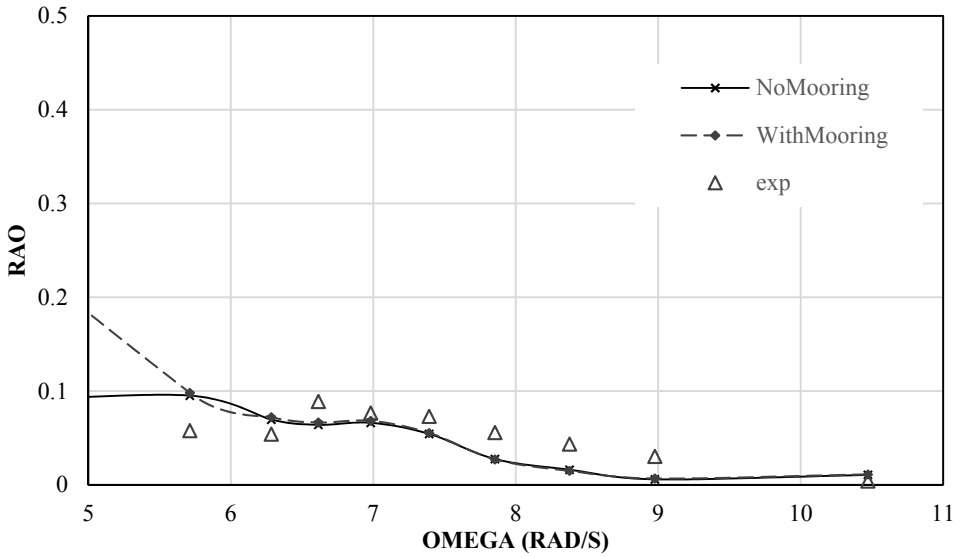

Figure 5-18 Pitch of main floater for only-wave cases

It could be pointed out that the influence of mooring is usually small except for the pitch in the low frequency range (from 2rad/s to 3rad/s or from 2.1s to 3.1s in period) which corresponds to the natural period of pitch (3.4s) for the uncoupled (without mooring) main floater. The reason for this discrepancy is that, due to the influence of mooring, the natural frequency of coupled system becomes larger than the uncoupled system which will result in a larger response in pitch motion.

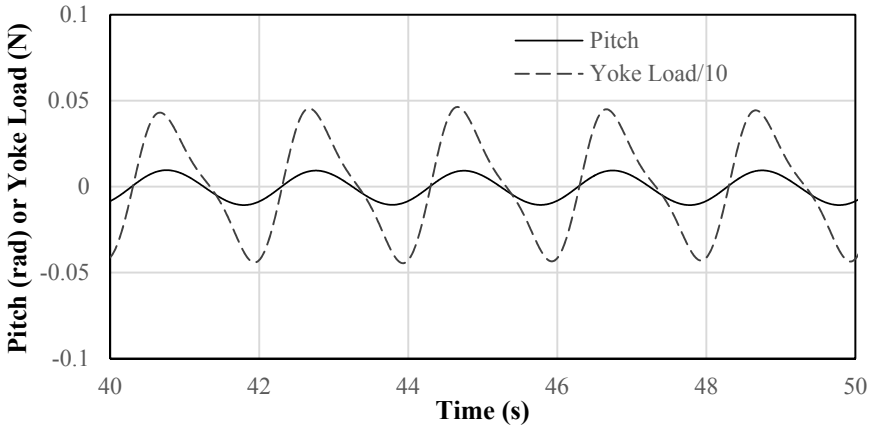

Figure 5-19 The coupling simulation result for pitch and yoke load

Figure 5-19 shows the time histories of the coupling simulation results of pitch motion and yoke load. For the yoke load, the positive value means tension and negative means press. In the Figure, we can find that, the yoke load fluctuates almost in phase with the pitch motion. It means that when the pitch is positive, the yoke will try to pull back the floater and vice versa (see Figure 5-20) which may have resulted in an additional

restoring moment. Therefore, due to the coupling with mooring system, the natural frequency of pitch is increased.

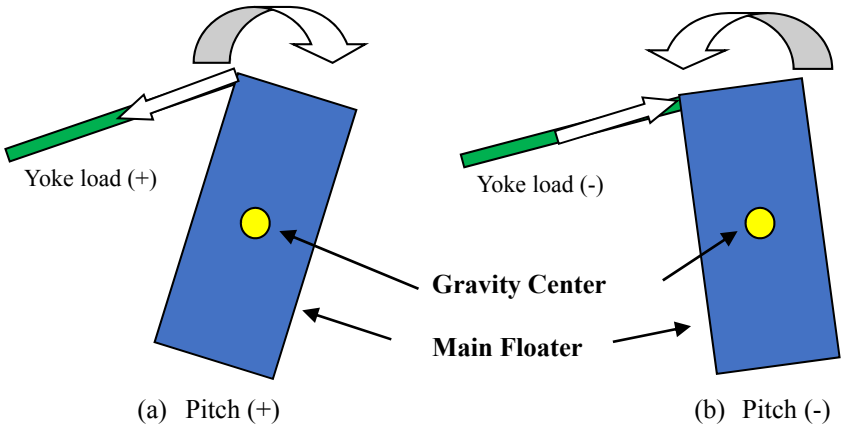

Figure 5-20 Sign convention for yoke load and pitch motion

b) Wind-wave conditions

The comparison for wind-wave cases are shown in Figure 5-21, Figure 5-22 and Figure 5-23. Four series of data, i.e., experiment results, simulation results without mooring, simulation results with considering mooring but no contact, simulation results with considering mooring and contact are presented in the Figures.

In general, the difference between the curves 'NoMoorng' and 'WithMooring-NoContact' is small for all the simulated results. This indicates that the influence of the mooring is small for the motions even under the combined wind and wave loads except at around the natural frequency.

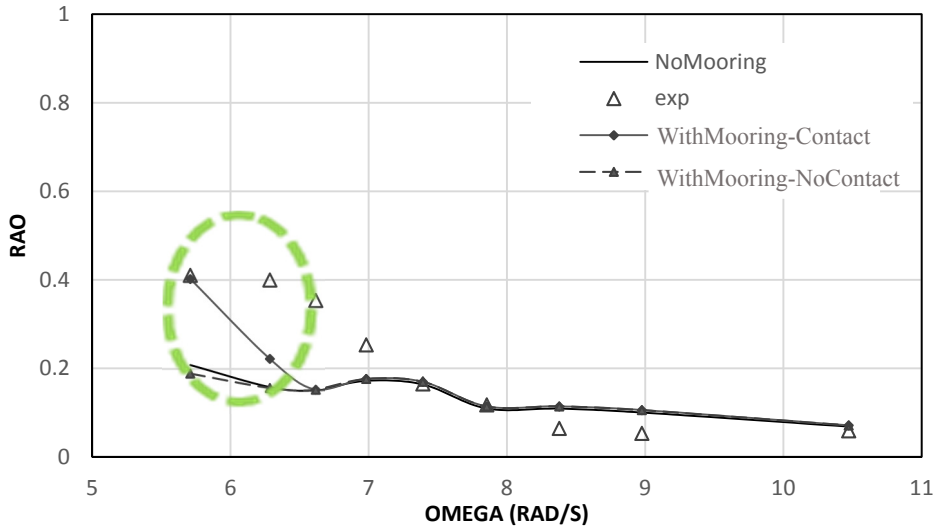

Figure 5-21 Surge of main floater for wind-wave cases

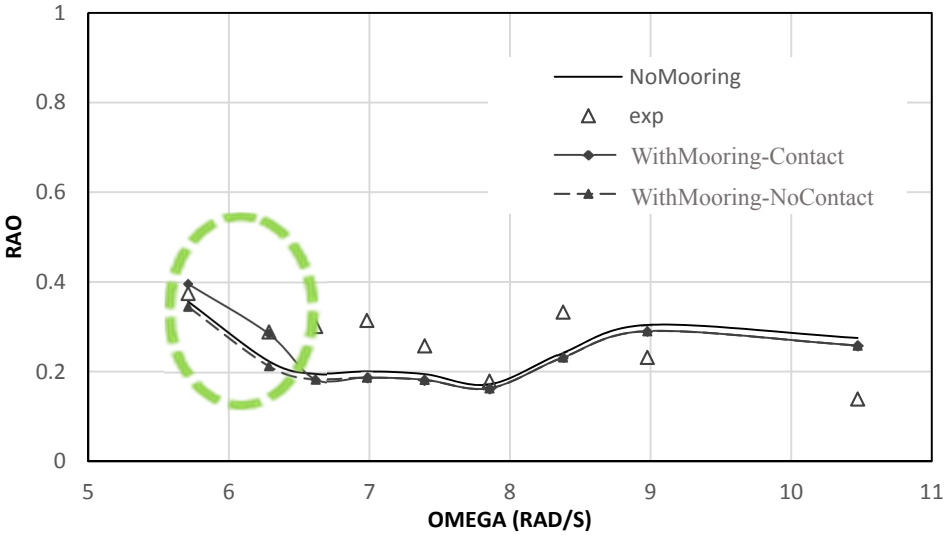

Figure 5-22 Heave of main floater for wind-wave cases

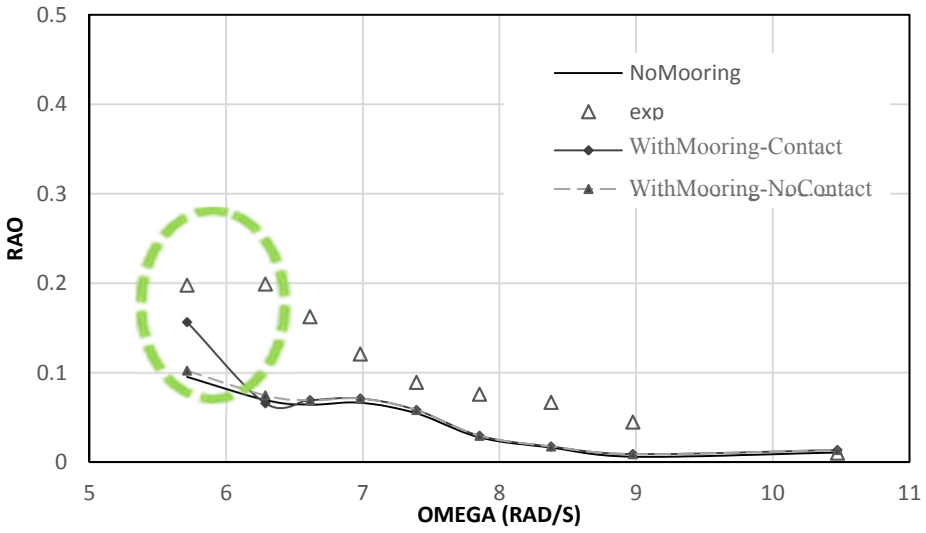

Figure 5-23 Pitch of main floater for wind-wave cases

On the other hand, it could be found out that in the low frequency range (from 5.5rad/s to 6.5 rad/s, or from 0.95s to 1.14s in wave period, circled in the Figure), the experiments data for heave and pitch are always larger than those by the simulation without the contact model 'NoMooring' and 'WithMooring-NoContact'. Introduction of the contact model could partly explain the difference, see the curve 'WithMooring-Contact'. The motion amplitude is increased when the contact load is included.

By observing the time domain experiments data (e.g. Figure 5-30), it could be found that, the contact was always occurring when the wave circular frequency is less than 6.5rad/s, or the wave period is larger than 0.95s. The simulation can also realize this contact load in the same frequency range by utilizing the WithMooring-Contact model.

c) Model uncertainty (contact model)

As we can observe in the Figure 5-23, although considering the influence of contact, the discrepancy between experiment and simulation (WithMooring-Contact) in the wind-wave cases is still significant in the low frequency range. This could be caused partly by the insufficient modeling of the contact load at the joint. The contact model is established based on several uncertain coefficients. All the simulation results for the contact model is calculated with the assumption that $\Theta_c=0.8rad$, $K_f=1$ x10^7Nm, $n=4$. Comparison of the simulation results with the different coefficients Θ_c is shown below. In Figure 5-24, besides the results of experiment and NoContact model, the simulation results of Contact model with various values of Θ_c (0.6rad, 0.8rad, 1.0rad and 1.1rad) are shown.

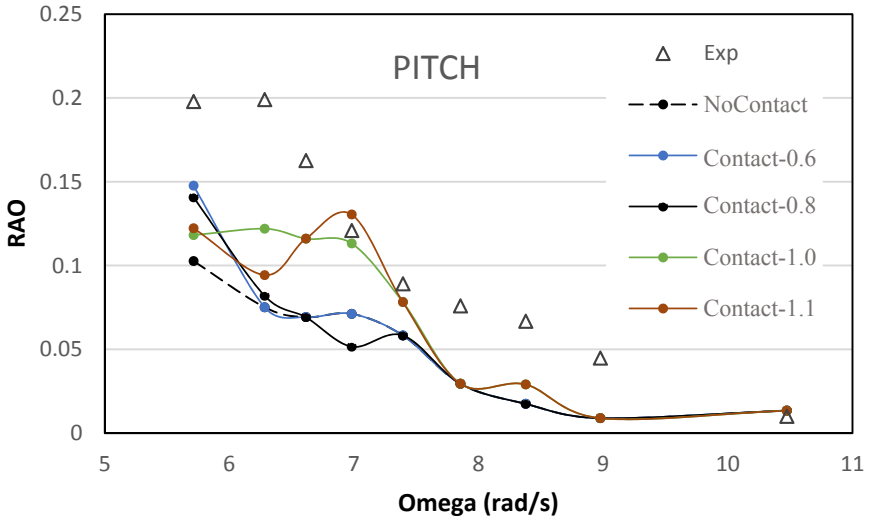

Figure 5-24 Comparison for the pitch motion with different Θ_c

Figure 5-24 shows that, the Θ_c has a significant influence on the pitch motion of the main floater. When the Θ_c becomes larger, the contact can happen more frequently for broader range of frequency.

5.3.2 Response of the mooring system

a) Comparison between simulation and experiment with a focus on nonlinear response

The 1st order and the 2nd order responses of the buoy are discussed in this section. In the following figures, the results for the 1st order and the 2nd order are presented. Both of the 1st order and the 2nd order results are read by the relevant peak value from DFT analysis.

Figure 5-25, Figure 5-26 and Figure 5-27 show the comparison of the 1st and 2nd order quantities between the simulation and experiment under the only-wave conditions. The 2nd order quantity in the plot is obtained simply by dividing the second order value by the wave amplitude or wave slope amplitude. Therefore, the plot does not present RAO any more. However, the expression may be useful to compare the magnitudes directly.

It could be seen that the 2nd order response becomes larger for the lower wave frequency. Comparing with surge and pitch motions, the 2nd order component of heave motion is much more significant. The simulation could basically explain the 1st order and the 2nd order response of experiments. As the relative rotational angle between yoke and axis of buoy hardly reaches the critical angle in the only-wave cases, there is no influence of contact in the simulation results of only-wave cases. So the second order

response is caused by the large displacement/rotation and nonlinear hydrodynamic force.

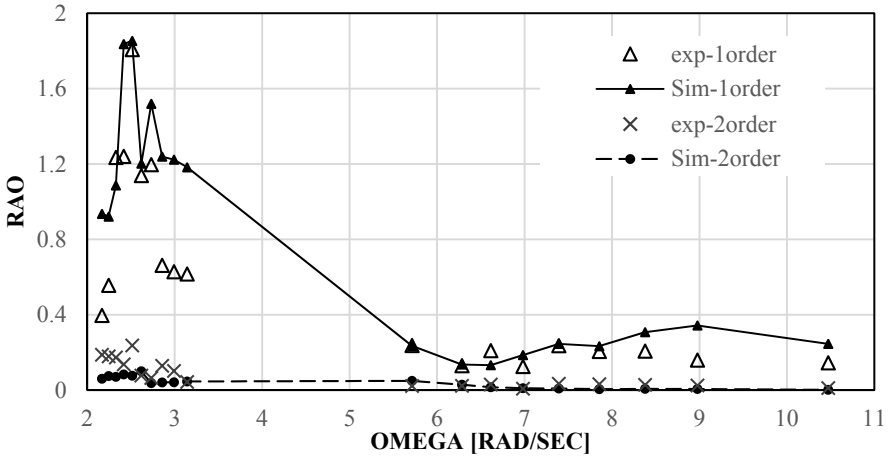

Figure 5-25 Surge of Buoy for only-wave cases

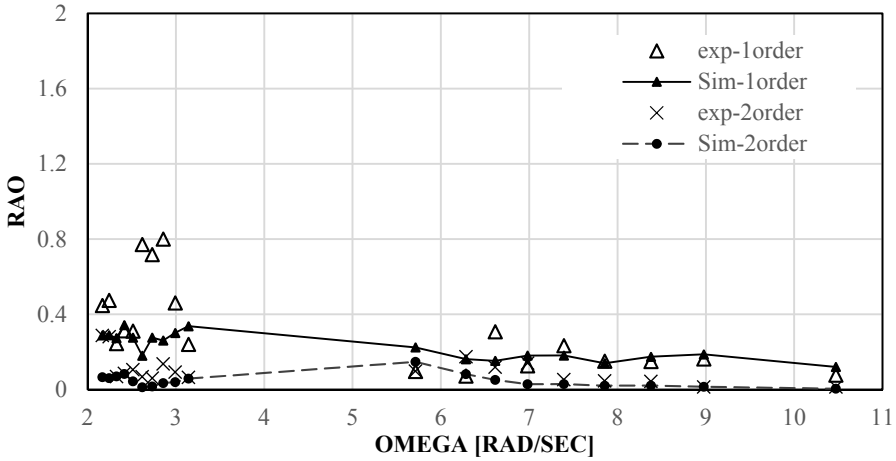

Figure 5-26 **Heave of Buoy for only-wave cases**

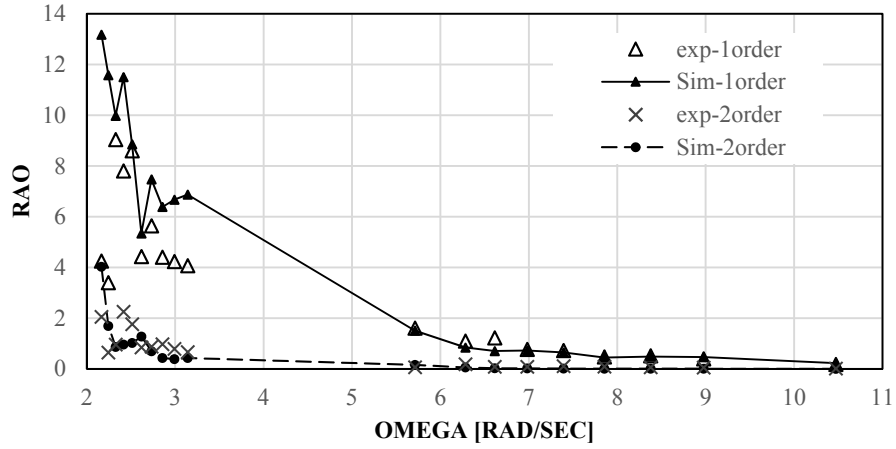

Figure 5-27 **Pitch of Buoy for only-wave cases**

Figure 5-28 shows the ratio of the 2nd order response to the 1st order response of the heave motion. It can be found out that the ratio is usually larger than 10% and the second order response can have almost the same or even larger amplitude in some cases.

Figure 5-29 shows the same comparison, however, under the combined load cases. As the contact may happen for the combined load cases, the results of simulation with and without contact model are compared with the experiment data in Figure 5-29. The present simulation explains the experimental results including the second order quantity well. The nonlinearity could be even larger than those under the only-wave conditions as discussed in the followings.

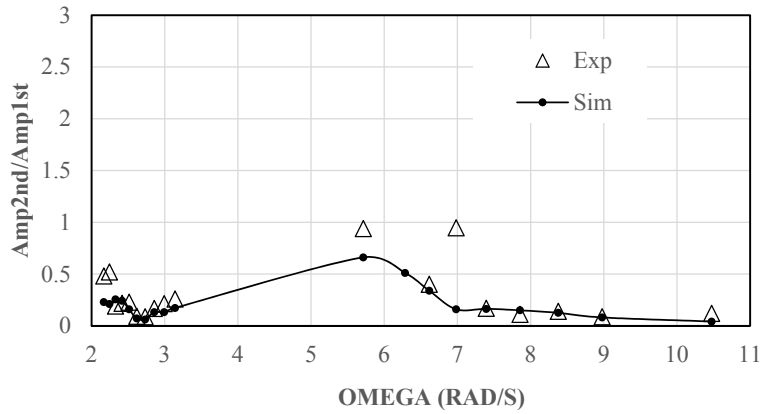

Figure 5-28 The response ratio for heave of buoy for only-wave cases

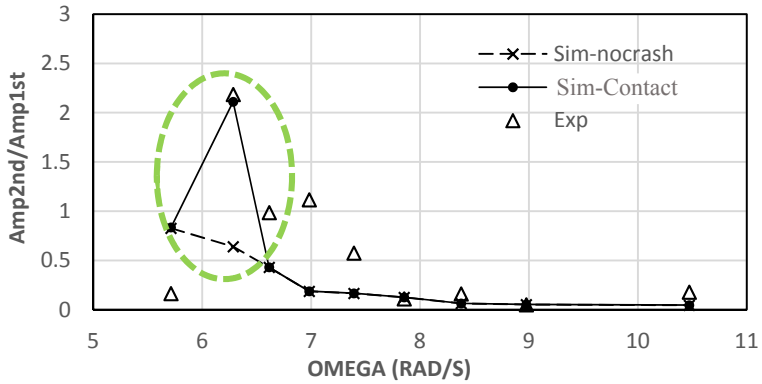

Figure 5-29 The response ratio for heave of buoy for wind-wave cases

By comparing the simulation results with and without contact, we can find that the contact can influence the response to a large extent in the low frequency range which is circled by a green broken line in the plot. In this frequency range, contact occurs frequently. Therefore, the significant nonlinearity of heave for wind-wave cases can be attributed to:

- Nonlinearity of mooring system which includes the nonlinear transformation

matrix caused by the large rotation angle and the nonlinear hydrodynamic force.

- Contact load.

b) Time history of mooring tension when contact happens

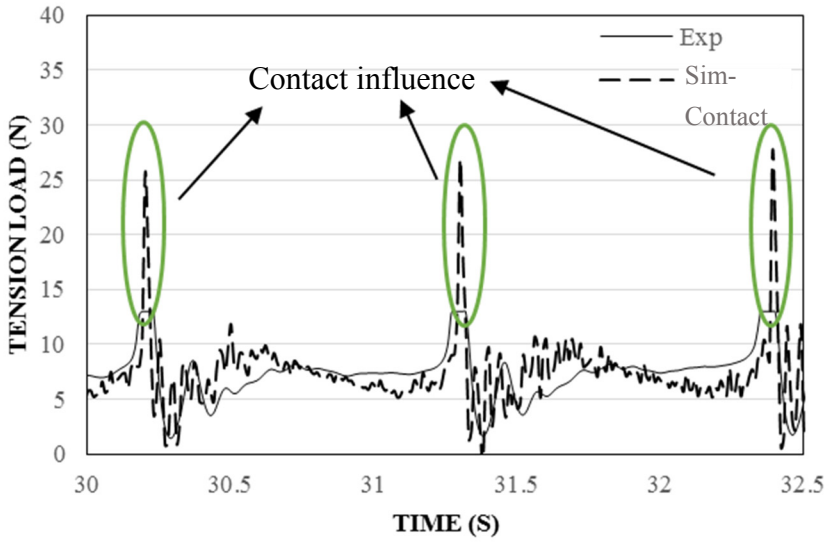

Figure 5-30 Comparison for tension load of tether

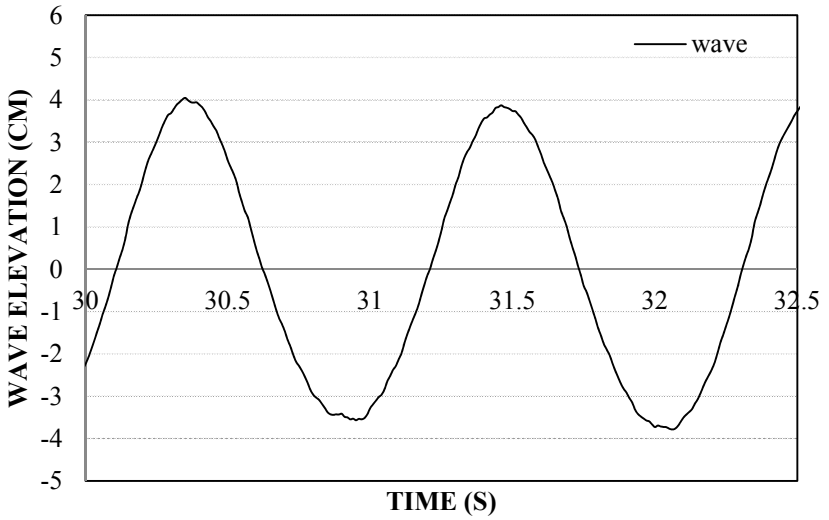

Figure 5-31 Wave condition with wave period 1.1s

As the contact can be easily reflected by the time history of mooring tension, the time domain tension load for one of the test cases (wind-wave, time period 1.1s) is shown in Figure 5-30. Figure 5-31 shows the corresponding regular wave condition measured during the model test. The simulation uses the exact same wave period and wave height according to the model test. Experiment data and simulation results with the contact

model are presented in Figure 5-30. The green circle marks the rapid tension increase caused by the contact. It seems that, due to the upper bound of the load cell, the peak value of load was not captured and thus truncated in the experiment.

c) Model uncertainty (initial heel of buoy)

In order to show the importance of initial heel of the buoy, the comparison between the results of experiment, simulation without initial heel and with different initial heel angle (4 degree, 10 degree and 13 degree) is shown in Figure 5-32.

It can be found that, for the simulation without initial heel (IH-None), the influence of the 2nd order response of heave is significantly overestimated and comparing with the linear response, the 2nd order response becomes dominant which is apparently different from the experiment results. By applying the different value of initial heel angle, we can find that the influence of the 2nd order response decreases with increasing the initial heel angle. As this initial heel is not measured in the experiment, 10 degree of initial heel is assumed in all of the above simulations.

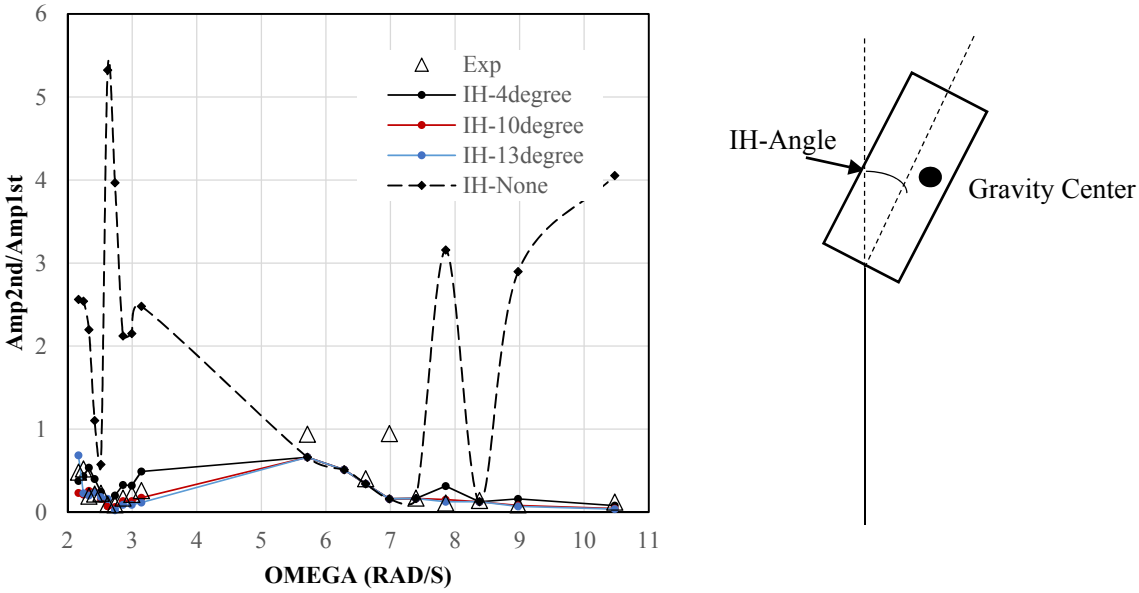

Figure 5-32 Comparison of response ratio of heave for only-wave cases

5.4 Conclusions

A scaled model test was conducted to verify the reasonability of the OU-Design.

The fundamental feasibility of OU-Design in functionality and safety was tested by conducting a scaled model experiment. Both the static heel (less than 1.5 degree) and dynamic heel (less than 2 degree) for pitch motion in the operational conditions were shown to meet the limitation in terms of the power generation efficiency.

The simulation results show that the main floater system is strongly coupled in the motion with the nonlinear mooring system in some particular cases. Through the comparisons between the simulation results and experiments data, the following conclusions can be deduced:

For main floater:

- According to the experiment data, there is a significant difference for pitch between the wave and wind-wave conditions when the wave period is larger than 0.95s. This discrepancy can be interpreted by the coupled simulation with a contact model at the joint.
- For the only-wave cases, based on the simulation results for coupled and uncoupled models, the mooring system has little influence on the motion of main floater under working condition (waves with the wave period 7s-11s in real scale). However, for the low frequency range, the motion of the main floater can be enlarged as a result of change of the natural frequency of the coupled system. The coupling between the floater and the tether is thus requisite for the proposed system.

For mooring system:

- According to the experiment, the second order response can also become large in low frequency range. The present simulation predicts well the tendency.
- The nonlinearity of heave and pitch of the buoy is more significant than that in the surge motion. Specially, the second order heave is usually larger than 10% of corresponding linear response.
- The contact load may have increased the second order response of the buoy under the combined loads.

6 SUB-HARMONIC MOTION

In this chapter, the sub-harmonic response of single-point-mooring (SPM) system is investigated based on the Mathieu instability theory. Simply, the SPM system can be regarded as a buoy connected with a vertical pre-tensioned tether to the sea bed.

A series of scaled model tests have been conducted and a significant nonlinear behavior of the buoy motion, sub-harmonic motion in particular, is observed. Taking account of the influence of time-varying tether tension on the buoy motion, theoretical explanation is made for the sub-harmonic response. The stability of the tethered-buoy system is focused based on the Mathieu instability theory. A strongly coupled numerical model between the buoy motion and the tether behavior is established to clarify the mechanism of the nonlinear motion of the tethered-buoy system. A comparison between the experiment data and simulation results is presented not only for the linear component but also for the sub-harmonic component. Influential factors for the sub-harmonic motion are discussed in detail. It turned out that the sub-harmonic motion is dominated by the nonlinear coupling effect of time-varying tension in the tether with the buoy motion. Finally, the influential factors to the sub-harmonic motion are indicated throughout the comparison between two different buoy models

6.1 Research Background

The tethered-buoy system is found in various marine applications. For example, a buoy system in single-point-mooring (SPM) for Floating, Production, Storage and Offloading systems (FPSOs) is widely adopted. As the SPM system needs less amount of material and less number of anchors than the conventional catenary system does, the lower installation cost can be attained. Also, by introducing the SPM system, the installation space in the sea can be saved significantly compared with the catenary system. The system may be utilized in other applications such as Floating Offshore Wind Turbines (FOWTs). The OU-Design for FOWT system is proposed consisting of a semisubmersible platform and an SPM so that the FOWT can weathervane to the change of the wind, wave and current directions. The weather-vane behavior was verified in a series of scaled model tests for the SPM-FOWT scaled model [26] (see Chapter 2).

Meanwhile, a severe nonlinear response of the tethered buoy was observed which was totally different from the normal harmonic motion. A similar nonlinear response was reported in Otaka and Nihei [41]. A large nonlinear pitch motion occurred during the model test for the FOWT which consists of spar-type platform and single-tension-leg mooring system. It turned out that the severe motion was partly due to sub-harmonic excitation whose motion period is twice as large as the incident wave period which may be interpreted as Mathieu type problem [42].

Many researchers have studied the Mathieu instability of motion of spar platform with catenary mooring system. Amongst others, Haslum and Faltinsen [43] discussed the Mathieu instability problem by taking into account the heave-pitch coupling and instantaneous water-plane area. A similar heave-pitch coupling problem was reported in Rho et al. [44] in which more complicated spar was modeled and studied. He also checked the influence of catenary mooring system on the Mathieu instability of spar by a series of model tests [45]. All of the above researches pointed out that, for the spar platform with catenary mooring system, if the natural frequency (for convenience, all the frequency in this paper means the circular frequency with unit rad/s) for heave is twice the natural frequency for pitch motion, the heave motion can undergo 10 times as large as the incident wave amplitude at resonance and the Mathieu instability problem occurs. Parametric roll of ships is a well-studied Mathieu instability problem. The unsymmetric roll motion occurs even in head seas. Hashimoto and Umeda [46] recently proposed a coupled heave-roll-pitch mathematical model to investigate the coupling influence between roll, pitch and heave when the Mathieu instability occurs. For spar type of platform, a coupled heave-roll-pitch numerical tool was also established by Rodriguez and Neves [47] with considering the influence of nonlinear Froude-Krylov force.

The tethered buoy considered in the present study is connected by one pre-tensioned tether instead of the catenary mooring system. If we assume the axial stiffness of the tether is large enough, the heave motion of the buoy is completely associated with the pitch and surge motions by the tether and it is given in a quadratic and even higher order form of the pitch and surge motions. The heave motion gets the peak value when the surge or pitch motion becomes the largest or the smallest. Thus, the heave motion naturally includes twice the motion frequency of pitch or surge motions, which may cause the Mathieu instability problem as discussed in the above references.

The nonlinear coupling effect of time-varying tether tension may also cause the sub-harmonic motion for the tethered-buoy system. A similar effect is studied for TLP-type platform. Minematsu [48] discussed the Mathieu instability problem for the surge motion of TLP by considering the time-varying tether tension theoretically.

For the pitch motion, however, there is still less research which covers the nonlinear coupling effect of tether tension, especially, for the tethered buoy system. A nonlinear numerical model for the pitch motion of a tethered buoy has been researched by Sao [49] in time domain. He pointed out that, for the tethered buoy system, the sub-harmonic motion occurs and may be mainly caused by the high order hydrodynamic forces under waves with sufficiently large wave amplitude. But he did not discuss it from the viewpoint of the Mathieu instability problem. The clarification of the mechanism of the sub-harmonic motion is yet to be made.

In the present research, besides the test results reported by Otaka and Nihei [41], a series

of model tests are conducted in Osaka University solely on the tethered buoy for various wave conditions to reproduce the sub-harmonic behavior. Both model test results are employed to clarify the mechanism of the sub-harmonic motion. A Mathieu type theoretical model taking account of the coupling between the buoy and the tether is proposed. To simplify the problem and focus on the influence of mooring tension variation, only the coupling between the motions of surge, heave, pitch and mooring tension is taken into account in this paper.

The theoretical model is shown to explain the tank test results qualitatively. Besides, a time-domain DYNABEAM model which accounts for various coupling effects including the one between the buoy motion and the tension variation in the tether, and that between the heave and pitch motions, is also established. A comparison between the experiment and numerical simulation is made. A good qualitative and quantitative correlation is obtained for both linear and nonlinear response components. The numerical model is further utilized to discuss which coupling term contributes the most to the sub-harmonic motion. It turned out that the sub-harmonic motion is dominated by the nonlinear coupling effect of time-varying tension with the buoy motion.

6.2 Analytical Model

6.2.1 Natural frequency and the associated mode

The tethered-buoy system considered in this research consists of a buoy and a pre-tensioned tether which are connected by a pin hinge. The tether is also hinged on the seabed. So, only tension force along the tether acts on the buoy bottom. The wave is assumed to propagate along the x-axis and the tethered-buoy system is assumed to be symmetric along x-axis as well.

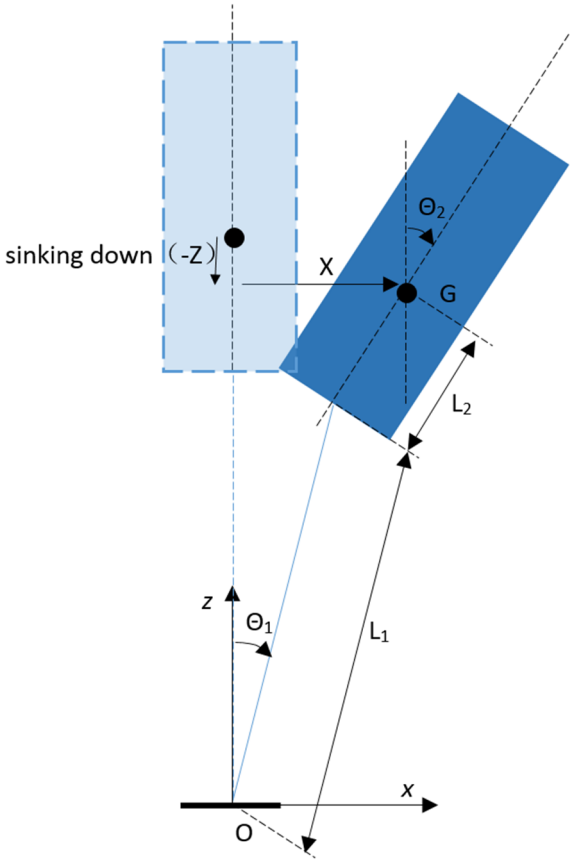

Figure 6-1 Definition of the tethered buoy and coordinate system

If we confine the motions within x-z plane, the equations of motion for the buoy are established for surge, heave and pitch motions as follows (Figure 6-1):

$$
\begin{aligned}
&(m+m_{ax})\ddot{X}+C_x\dot{X}=-T\sin(\theta_1)+F_x \\
&(m+m_{az})\ddot{Z}+C_z\dot{Z}=-mg-T\cos(\theta_1)+F_B+F_z \\
&\left(I+I_a\right)\ddot{\theta}_2+C_\theta\dot{\theta}_2=-TL_2\sin(\theta_2-\theta_1)-F_BGM\sin(\theta_2)+M
\end{aligned}
\qquad \textbf{(6-1)}
$$

where,

X: horizontal displacement of the buoy (surge)

Z: vertical displacement of the buoy (heave)

θ_1: tether angle (angle between the z-axis and the inclined tether)

θ_2: angular displacement of the buoy (pitch)

m: the mass of the buoy

m_{ax}, m_{az}: the added mass for surge (x) and heave (z) motions, respectively

I: the moment of inertia of the buoy for pitch motion

I_a: the added moment of inertia for pitch motion

C_x, C_z, C_Θ: the hydrodynamic damping for surge, heave and pitch motions, respectively

T: tension of tether including the static and dynamic components

L_1: length of tether

L_2: the height of gravity center from the keel of the buoy

GM: the metacentric height measured from the center of gravity

F_B: buoyancy of the buoy

F_x, F_z: hydrodynamic external force in the x-axis and z-axis, respectively

M: hydrodynamic external moment about y-axis

Geometrically, the surge and heave for the buoy are expressed by Eq. (6-2):

$$\begin{aligned} X &= L_1 \sin(\theta_1) + L_2 \sin(\theta_2) \\ Z &= L_1(\cos(\theta_1) - 1) + L_2(\cos(\theta_2) - 1) \end{aligned} \qquad \textbf{(6-2)}$$

By taking up to the second order with respect to the angular displacement θ_1 and θ_2, Eq. (6-2) is simplified to,

$$X = L_1\theta_1 + L_2\theta_2$$
$$Z = -\frac{1}{2}(L_1\theta_1^2 + L_2\theta_2^2) \qquad \textbf{(6-3)}$$

It can be understood from Eq. (6-3) that the heave motion of a quadratic order naturally exists in the tethered-buoy system. The second equation may be approximated as z=0 to the first order. Here, we only discuss the equation of motion in the first order so that the equation of heave motion can be neglected. Also, the varying tension T, the varying buoyancy F_B and the varying metacentric height GM due to the heave motion are replaced by the pre-tension T_0, initial F_{B0} and initial metacentric height GM_0 in Eq. (6-1). In order to discuss the natural mode of tethered-buoy system, all the hydrodynamic external force (or moment) and damping in Eq. (6-1) are neglected. Then, substituting Eq. (6-3) into Eq. (6-1), we obtain Eq. (6-4).

$$(m + m_{ax})L_1\ddot{\theta}_1 + T_0\theta_1 + (m + m_{ax})L_2\ddot{\theta}_2 = 0$$
$$(I + I_a)\ddot{\theta}_2 + (T_0L_2 + F_{B0}GM_0)\theta_2 - T_0L_2\theta_1 = 0 \qquad \textbf{(6-4)}$$

Assuming the angular displacement θ_1, θ_2 of the form $\theta_1 = \phi_1 e^{i\omega t}$, $\theta_2 = \phi_2 e^{i\omega t}$ respectively, Eq. (6-4) can be transformed to the following matrix form:

$$\begin{bmatrix} -\omega^2(m + m_{ax})L_1 + T_0 & -\omega^2(m + m_{ax})L_2 \\ -T_0L_2 & T_0L_2 + F_{B0}GM_0 - \omega^2(I + I_a) \end{bmatrix} \begin{Bmatrix} \phi_1 \\ \phi_2 \end{Bmatrix} = \begin{Bmatrix} 0 \\ 0 \end{Bmatrix} \qquad \textbf{(6-5)}$$

To obtain a nontrivial solution, the determinant of the above matrix has to be set zero:

$$\begin{vmatrix} -\omega^2(m + m_{ax})L_1 + T_0 & -\omega^2(m + m_{ax})L_2 \\ -T_0L_2 & T_0L_2 + F_{B0}GM_0 - \omega^2(I + I_a) \end{vmatrix} = 0 \qquad \textbf{(6-6)}$$

The equation (6-6) is simplified as Eq. (6-7) by introducing the coefficients A, B, C:

$$A\omega^4 - B\omega^2 + C = 0 \qquad \textbf{(6-7)}$$

where,

$$A = (m + m_{ax})(I + I_a)L_1$$
$$B = [(m + m_{ax})(L_2^2 + L_1L_2) + I + I_a]T_0 + (m + m_{ax})GM_0L_1F_{B0}$$
$$C = T_0(T_0L_2 + F_{B0}GM_0)$$

It is easily known that when $C<0$, Eq. (6-7) will have an imaginary root which means that the system becomes unstable. Therefore, for the system to be stable, the initial metacentric height GM_0 has to satisfy the following condition. The stable criteria given by Eq. (6-8) can be also obtained easily by other method (see Appendix C).

$$GM_0 > -\frac{T_0 L_2}{F_{B0}} \qquad \textbf{(6-8)}$$

At last, the two natural frequencies can be obtained as roots of Eq. (6-7) as follows:

$$\omega_1 = \sqrt{\frac{B+\sqrt{B^2-4AC}}{2A}}, \quad \omega_2 = \sqrt{\frac{B-\sqrt{B^2-4AC}}{2A}} \qquad \textbf{(6-9)}$$

where,

$$B^2 - 4AC = \left[\frac{AC}{T_0(I+I_a)} + (m+m_{ax})T_0 L_2{}^2 + T_0(I+I_a)\right]^2 - 4AC$$
$$= \left[\frac{AC}{T_0(I+I_a)} + (m+m_{ax})T_0 L_2{}^2 - T_0(I+I_a)\right]^2 + 4(m+m_{ax})T_0{}^2 L_2{}^2 (I+I_a) > 0$$

Substituting the natural frequency ω into Eq. (6-5), the motion ratio λ which is defined by the ratio of amplitude for θ_1, θ_2 is obtained:

$$\lambda(\omega) = \frac{\phi_1}{\phi_2} = \frac{\omega^2(m+m_{ax})L_2}{-\omega^2(m+m_{ax})L_1 + T_0} \qquad \textbf{(6-10)}$$

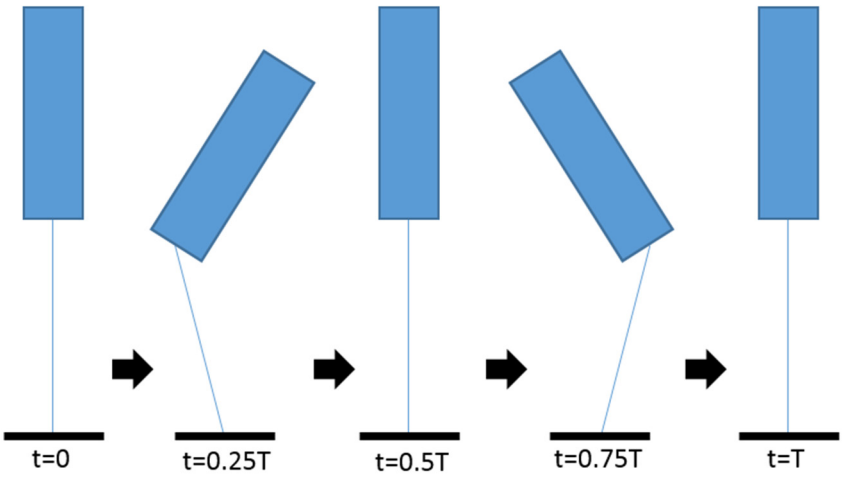

(a) ω_1 (out-phase, T: motion period, pitch dominant mode)

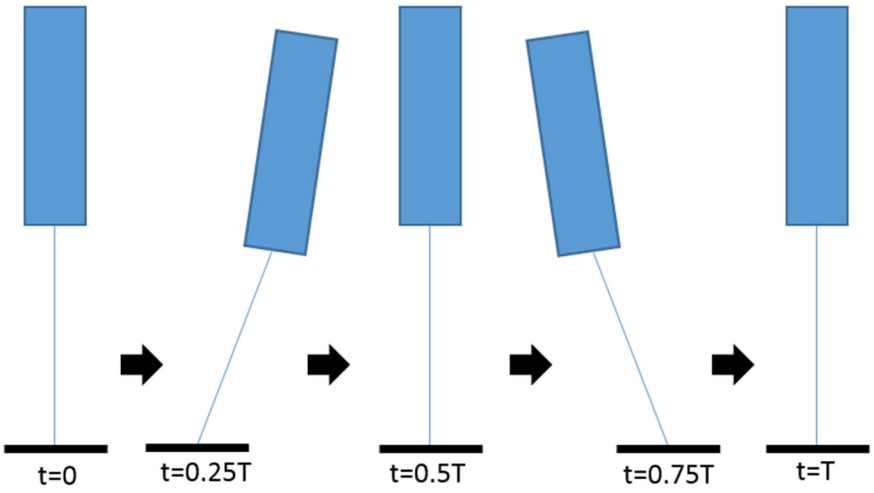

(b) ω_2 (in-phase, T: motion period, surge dominant mode)

Figure 6-2 The motion modes associated with the natural frequency ω1 and ω2

It can be proven that for the natural frequency ω_1, the angular displacement θ_1, and θ_2 have the opposite phase. Meanwhile, they are in-phase for the natural frequency ω_2. The detailed derivation is given in Appendix D. Two different modes associated with the two natural frequencies are shown in Figure 6-2.

Especially for natural frequency ω_1, the motion ratio λ can be easily estimated by Eq. (6-11). See the detail derivation in Appendix E.

$$\lambda(\omega_1) \approx -\frac{L_2}{L_1} \qquad \textbf{(6-11)}$$

If we substitute Eq. (6-11) into the Eq.(6-3), it is known that, the surge motion measured at the gravity center of buoy will be close to zero when the motion mode with the natural frequency ω_1 occurs. If we assume that the heave motion is small enough as well, the natural mode associated with the natural frequency ω_1 is regarded as pitch dominant.

6.2.2 Mathieu instability

When we consider the hydrodynamic external force (or moment) for the tethered-buoy system, the Mathieu instability may occur which is accounted for by the nonlinear component existing in the Eq. (6-1) which includes the varying tension, varying buoyancy and varying metacentric height. Eq. (6-12) rewrites the equation of pitch

motion in Eq. (6-1) by marking out all the time varying components. Tether angle θ_1 is substituted by the motion ratio λ.

$$(I+I_a)\ddot{\theta}_2+C_\theta\dot{\theta}_2+(\rho gA_c(Draft-Z(t))GM(t)+(1-\lambda)L_2T(t))\theta_2=M(t) \qquad \textbf{(6-12)}$$

where,

A_c: waterplane cross-section area

$GM(t)=GM_0-\frac{Z(t)}{2}$: dynamic metacentric height due to heave

The first term, $\rho gA_c \bullet (Draft-Z(t)) \bullet GM(t)$, in restoring stiffness has been discussed in many researches as the coupling effect of heave and pitch. Haslum [43] pointed out that, the dynamic metacentric height plays a dominant role in the coupling behavior and the equation of pitch motion (the influence of tether tension on the body was not considered) can be simplified as a typical form of Mathieu type equation. The system will become unstable when the frequency of heave motion is twice the natural frequency for pitch motion.

The second term, $(1-\lambda)L_2T(t)$, in restoring stiffness represents the nonlinear influence of time-varying tether tension. If we do not consider the heave-pitch coupling and focus on the mechanism of tether influence, the Eq. (6-13) reads:

$$(I+I_a)\ddot{\theta}_2+C_\theta\dot{\theta}_2+(\rho gA_c(Draft)GM_0+(1-\lambda)L_2T(t))\theta_2=M(t) \qquad \textbf{(6-13)}$$

The equation of heave motion can be written as

$$(m+m_{az})\ddot{Z}+C_z\dot{Z}+\rho gA_cZ=F_z(t)-(T(t)-T_0)\cos(\theta_1) \qquad \textbf{(6-14)}$$

The heave motion is regarded as second order as discussed previously. To account for the nonlinear contributions in Eq. (6-13) up to the second order, we may neglect the second and even higher order components in Eq. (6-14) to obtain the following linear approximation.

$$T(t)=T_0+F_z(t) \qquad \textbf{(6-15)}$$

The second term $F_z(t)$ represents the linear contribution of the vertical force on the buoy. For the regular wave with the circular frequency ω, $F_z(t)$ is obtained by applying the

linear potential theory as:

$$F_z(t) = af_z \cos(\omega t) \qquad \textbf{(6-16)}$$

where,

a: the wave amplitude

f_z: the vertical force amplitude per unit wave amplitude

Substituting Eqs. (6-15) and (6-16) into Eq. (6-13), Eq. (6-17) is obtained:

$$(I + I_a)\ddot{\theta}_2 + C_\theta \dot{\theta}_2 + (K_0 + K_1 \cos(\omega t))\theta_2 = M(t) \qquad \textbf{(6-17)}$$

where,

$$K_0 = \rho g A_c (Draft) GM_0 + (1-\lambda) L_2 T_0$$
$$K_1 = a(1-\lambda) L_2 f_z$$

The homogeneous equation of Eq. (6-17) may be rewritten as follows,

$$\ddot{\theta}_2 + n\omega_i \dot{\theta}_2 + (\omega_i^2 + \varepsilon \cos(\omega t))\theta_2 = 0 \qquad \textbf{(6-18)}$$

where,

$$\omega_i = \begin{cases} \omega_1 \\ \omega_2 \end{cases}$$
$$n = \frac{C_\theta}{\omega_i (I + I_a)}$$
$$\varepsilon = \frac{K_1}{I + I_a}$$

If the relationship $\tau = \omega t$ is introduced, Eq. (6-18) may be deduced to the standard Mathieu equation:

$$\frac{d^2}{d\tau^2}\theta_2 + \mu \frac{d}{d\tau}\theta_2 + (\delta + \varepsilon' \cos(\tau))\theta_2 = 0 \qquad \textbf{(6-19)}$$

where

$$\mu = \frac{n\omega_i}{\omega},\quad \delta = \frac{\omega_i^2}{\omega^2},\quad \varepsilon' = \frac{\varepsilon}{\omega^2}$$

The stability for the Mathieu equation has been well studied. Figure 6-3 shows the stability diagram for the damped Mathieu's equation [50] from which it is found that, when the δ=0.25 or 1 (ω=2ωᵢ or ωᵢ), the system becomes unstable. Especially when δ locates around 0.25, the stable criterion can be written in the following inequality [51]:

$$(\delta - \frac{1}{4})^2 - \frac{1}{4}(\varepsilon'^2 - \mu^2) > 0 \qquad \textbf{(6-20)}$$

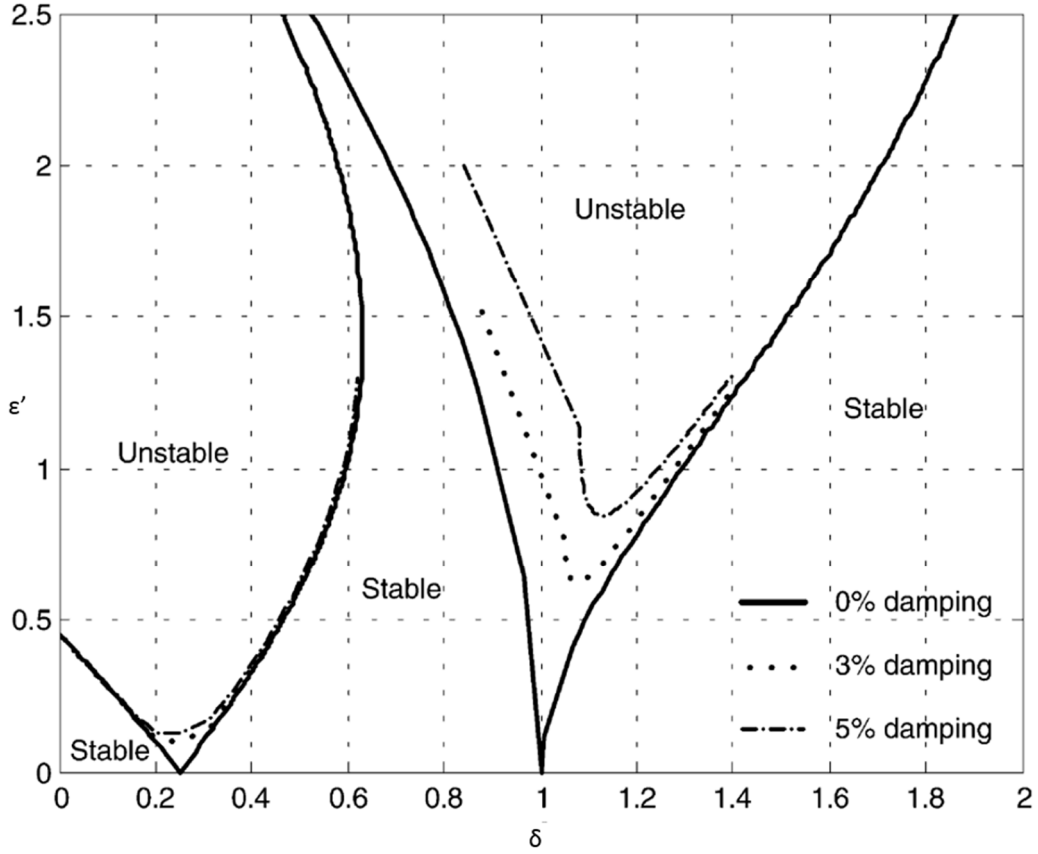

Figure 6-3 Stability diagram for damped Mathieu's equation

Substituting δ, ε', μ in Eq. (6-20) by a, f_z, λ, Eq. (6-20) can be written as a function of wave amplitude and wave frequency as given by Eq. (21).

$$a < \frac{1}{(1-\lambda)L_2 f_z}\sqrt{\frac{(I+I_a)^2(4\omega_i^2-\omega^2)^2}{4} + C_\theta{}^2\omega^2} \qquad \textbf{(6-21)}$$

It can be interpreted that larger vertical hydrodynamic force, larger absolute value of motion ratio (when motion ratio is minus) and smaller gravity height tend to cause the instability of the tethered buoy system for a given amplitude of wave. Also, smaller

damping coefficient C_Θ may cause the instability especially for the waves with wave frequency twice the natural frequency. The influence of pre-tension is reflected in terms of the natural frequency.

6.3 Scaled Model Test

6.3.1 TLSPAR model test

The sub-harmonic behavior was observed in the FOWT model test [41] with the special designed platform model (TLSPAR, Figure 6-4) which consists of SPAR type platform and single pre-tensioned mooring tether (a similar concept may be found in "SWAY" [52]). The principal particulars for the TLSPAR model are shown in Table 6-1. If neglecting the wind influence, the mechanism of TLSPAR motion totally coincides with the tethered-buoy system.

A series of regular only-wave tests (see Table 6-2) were carried out for TLSPAR model in the Ocean Engineering Basin of Institute of Industrial Science, the University of Tokyo. To obtain nonlinear responses, the wave period (0.6s~1.0s) is focused around the half-natural period of pitch motion for TLSPAR model. The experimental setup and the definition of coordinate system for TLSPAR model test is shown in Figure 6-5.

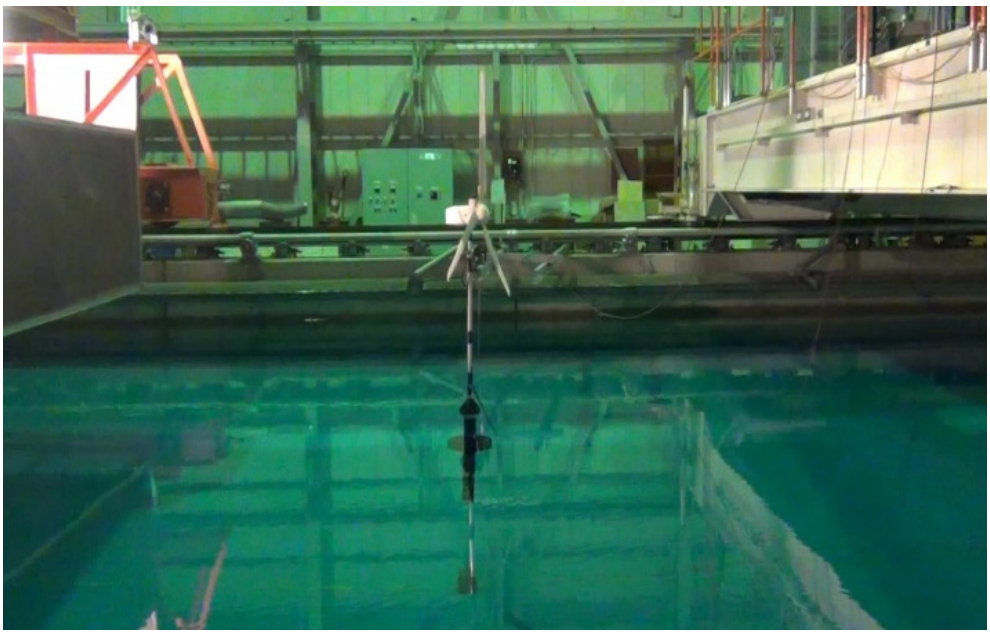

Figure 6-4 Photo of TLSPAR type FOWT

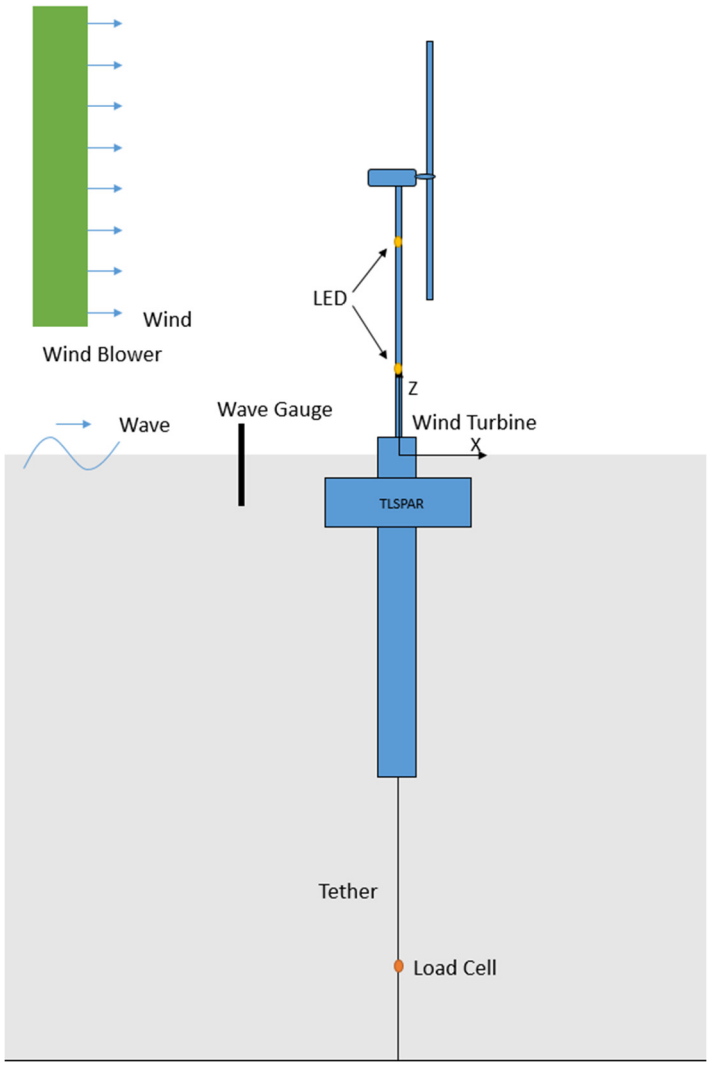

(a) Side-view

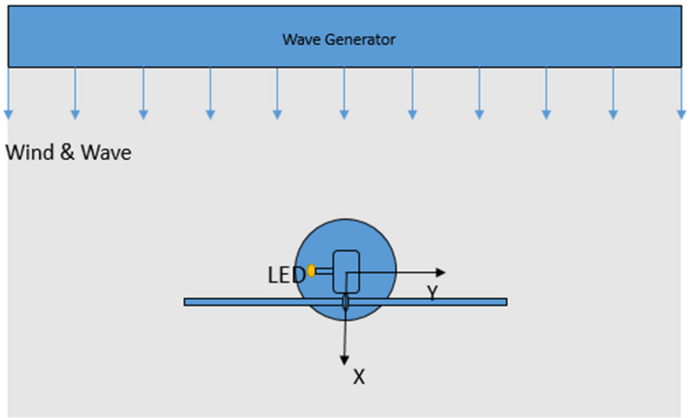

(b) Top-view

Figure 6-5 Arrangement of TLSPAR model test

Table 6-1 Principal particulars of TLSPAR model

Item	Value	Unit
Scale ratio	1/100	-
Mass	7.91	kg
Moment of Inertia (I_{yy})	2.28	kg*m^2
The height of gravity center (L_2)	0.62	m
Height of Tower	0.75	m
Height of Spar	1.19	m
Diameter (minimum)	0.07	m
Diameter (maximum)	0.25	m
Tether Length (L_1)	1.70	m
Draft	1.09	m
Pretension	14.71	N

Table 6-2 Tested wave conditions, TLSPAR

Case ID	Wave Period (s)	Wave Amplitude ζ (cm)	Wave Steepness $k\zeta$	Test Times
TLSPAR_01	0.600	1.215	0.136	1
TLSPAR _02	0.700	1.267	0.104	1
TLSPAR _03	0.800	2.263	0.142	1
TLSPAR _04	0.900	1.817	0.090	1
TLSPAR _05	1.000	2.501	0.101	1
TLSPAR _06	1.100	3.025	0.101	1

6.3.2 SPM model test

In order to better understand the behavior of the tethered-buoy system and reproduce the sub-harmonic response, a series of model tests were conducted in the water tank of Osaka University [53]. A scaled model for the buoy part of the SPM system with the scale ratio 1/200 (See Figure 6-6) was fabricated with GFRP (Glass Fiber Reinforced Polymer). Table 6-3 shows its principal particulars. The model is called SPM model herein.

To clarify the behavior more in an analytical manner, a series of tank tests under regular waves were conducted and the wave condition is given in Table 6-4.

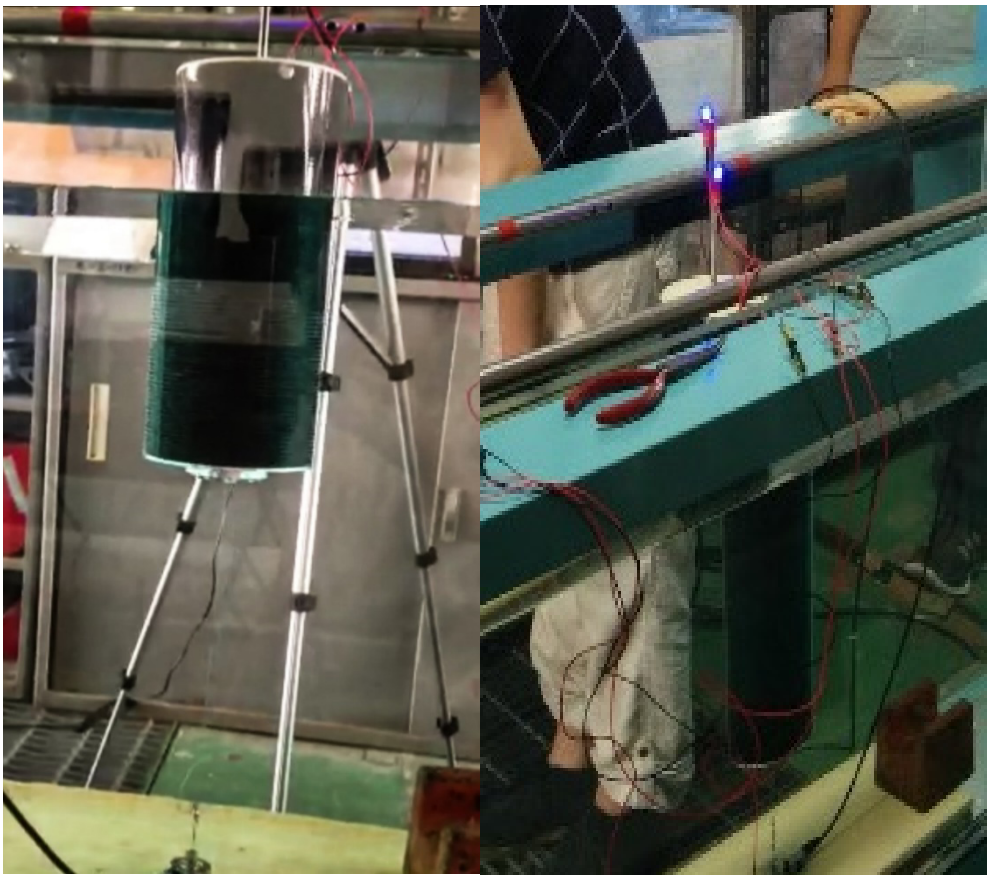

Figure 6-6 Photos of SPM model test

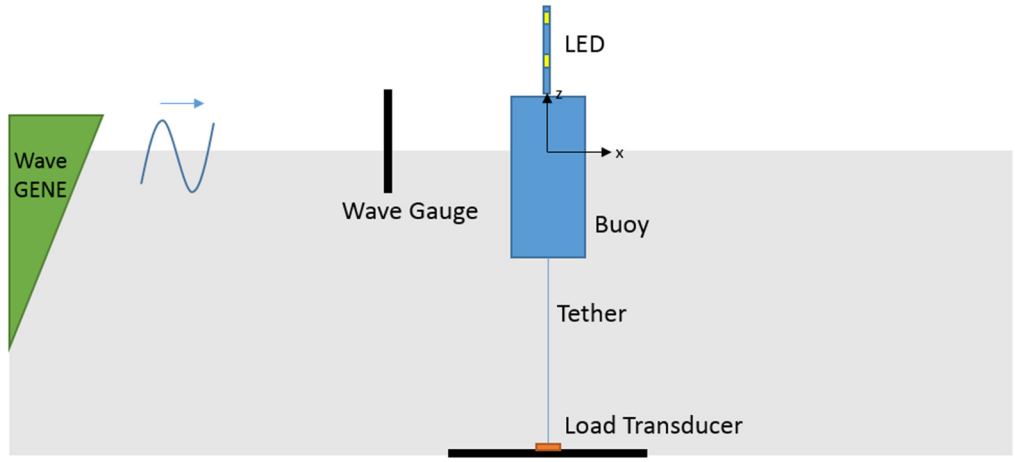

(a) Side-view

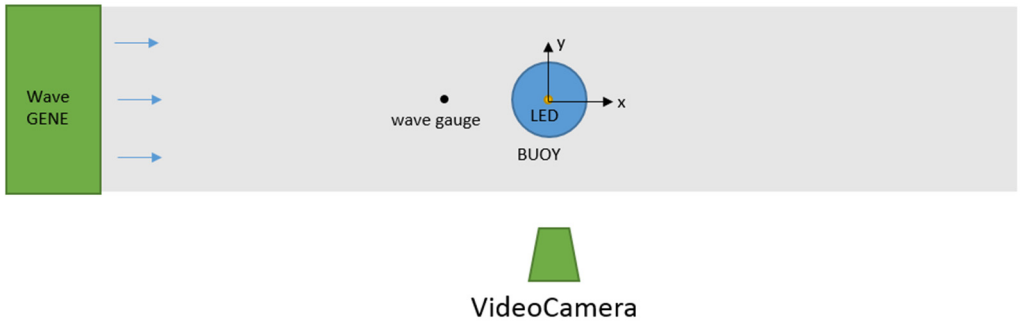

(b) Top-view

Figure 6-7 Arrangement of SPM model test

The side-view and top-view for the arrangement of the model test are shown in Figure 6-7. Two LEDs were attached along the vertical rigid bar on the buoy so that the surge, heave and pitch motions of the buoy can be measured by optical-video-analysis of the motion of the LEDs. The tension of tether was also measured by the load transducer which was located on the bottom.

Table 6-3 Principal particulars of SPM model

Item	Value	Unit
Scale ratio	1/200	
Mass	1.035	kg
Moment of Inertia (I_{yy})	0.00786	kg*m^2
The height of gravity center (L_2)	0.073	m
Height	0.240	m
Diameter	0.100	m
Draft	0.150	m
Tether Length (L_1)	0.270	m
Pretension	1.400	N

Table 6-4 Tested wave conditions, SPM

Case ID	Wave Period (s)	Wave Amplitude ζ (cm)	Wave Steepness $k\zeta$	Test Times
SPM_01	0.500	1.793	0.289	2
SPM_02	0.600	2.219	0.248	2
SPM_03	0.700	3.440	0.283	2
SPM_04	0.800	2.577	0.163	2
SPM_05	0.900	3.169	0.161	2
SPM_06	1.200	3.173	0.100	2
SPM_07	1.300	1.804	0.050	2
SPM_08	1.400	2.717	0.069	2
SPM_09	1.500	1.619	0.037	2

6.4 Numerical Model

In order to simulate the coupling influence between floater (Buoy or SPAR) and mooring tether, two numerical models are established for the floater and the tether, respectively. Then these two models are strongly coupled in the time domain. A more detailed discussion about the simulation can be found in the Chapter 3. The nonlinear influence of coupling between heave-pitch and varying tether tension can be included as discussed in sub-section 3.2.2 and 3.2.3. To verify the nonlinear influence of time-varying tether tension, the linear mooring model is also derived according to sub-section 3.1.2.

6.5 Results and Discussion

6.5.1 TLSPAR model

a) Free decay test

To obtain the natural frequency of pitch for TLSPAR model, a free decay test is carried out and the time domain and frequency domain results are given in Figure 6-8. Besides the higher natural frequency ω_1, the motion mode with lower natural frequency ω_2 is also evidenced as discussed in the theoretical analysis. Table 6-5 shows the natural frequency of TLSPAR model which is obtained by the free decay test, theoretical analysis and numerical simulation. A good correlation exists for the higher natural frequency ω_1. Due to the large damping, the lower natural frequency ω_2 cannot be obtained by the model test so clearly. After IFFT (inverse fast Fourier transform) analysis focusing on the frequency range around natural frequency ω_1, the damping coefficient is obtained which is about 3 percent of critical damping and it is utilized in the following simulation. The free decay test for the motion mode in roll direction was also conducted and the measured natural frequency corresponding to the roll motion locates around 3.4 rad/s.

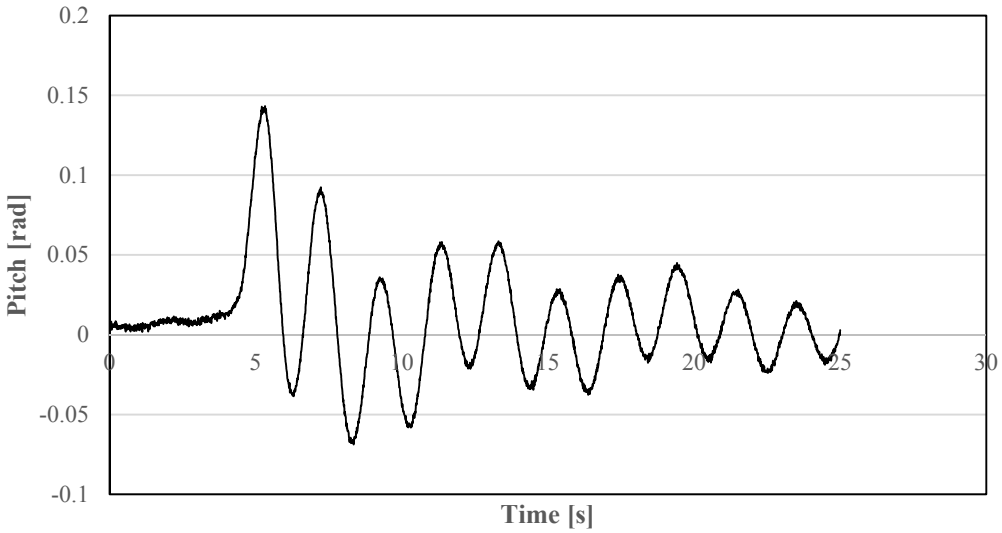

(a) Time domain

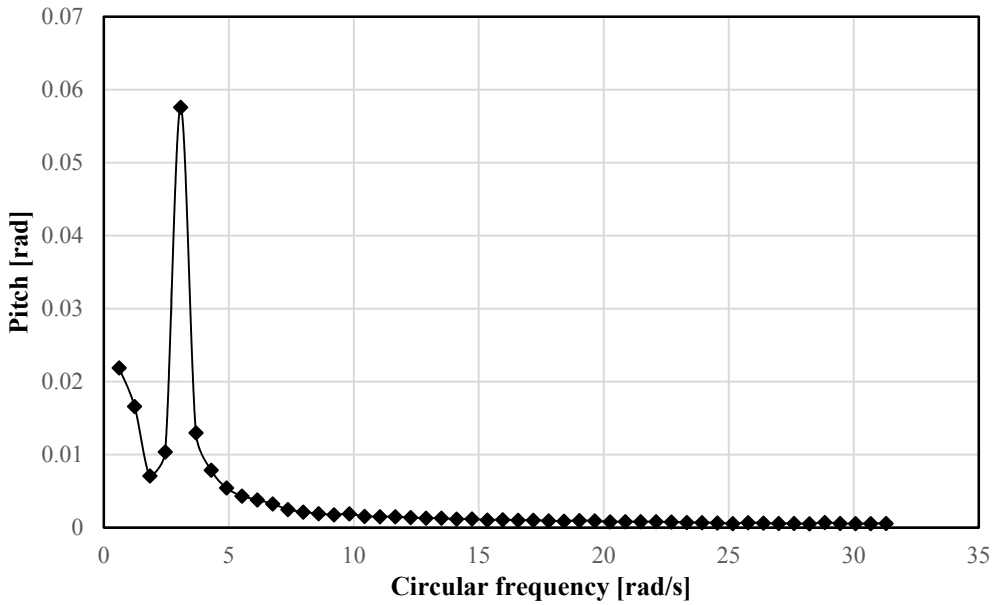

(b) Frequency domain

Figure 6-8 Free decay test results for TLSPAR model

Table 6-5 Comparison of natural frequency among model test, theoretical analysis and numerical simulation for TLSPAR model

Item	Test	Theoretical Analysis	Simulation	Unit
ω_1^*	3.07	3.16	2.92	rad/s
ω_2^{**}	-	0.82	0.79	rad/s

* ω_1 is natural frequency for the pitch dominant mode
** ω_2 is natural frequency for the surge dominant mode

b) RAO comparison

As mentioned previously, the obvious sub-harmonic motion was observed in the tank test for the TLSPAR model. Specially, one typical case with wave period 1.0s is selected and the corresponding pitch motion is shown in Figure 6-9. Figure 6-9(a) shows the time domain results for the pitch motion, in which we can find that the harmonic pitch occurs initially and the pitch motion gradually transforms from harmonic to sub-harmonic response after several cycles. Finally, the pitch motion becomes prominently sub-harmonic. If we conduct the FFT analysis for the time domain data between 25s to 40s, the sub-harmonic response will be more clearly checked, which is shown in Figure 6-9(b).

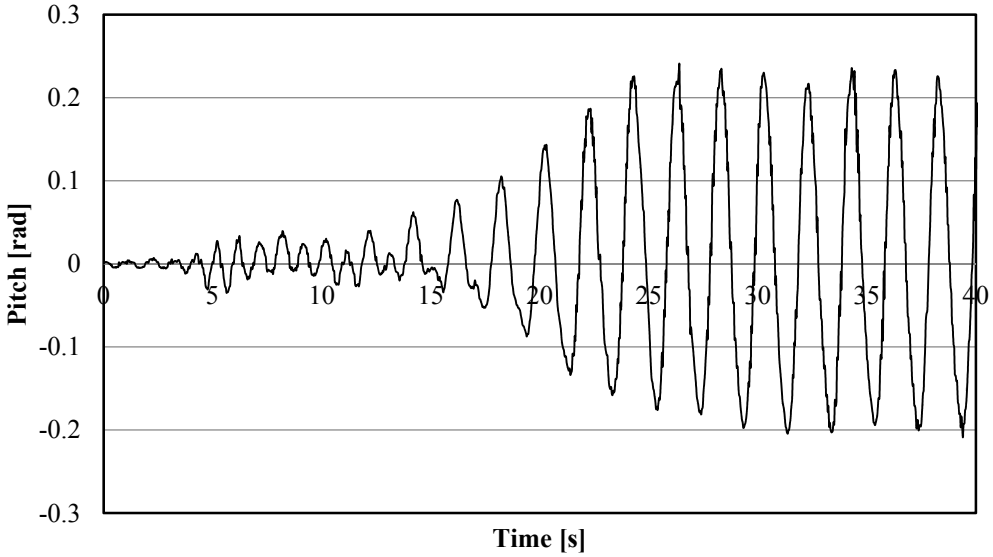

(a) Time domain

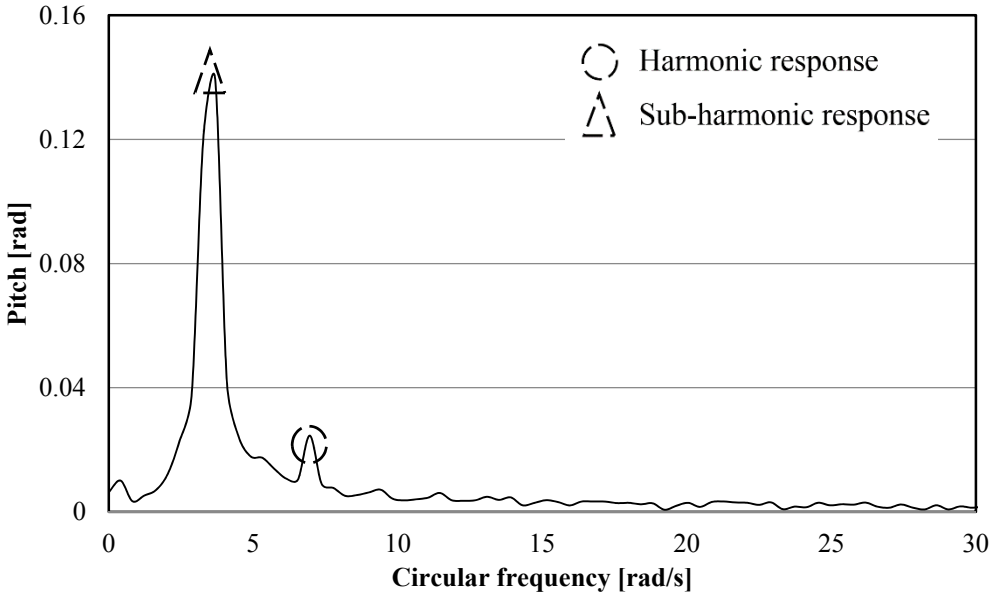

(b) Frequency domain

Figure 6-9 Measured pitch motion of TLSPAR model at wave frequency 6.2 rad/s

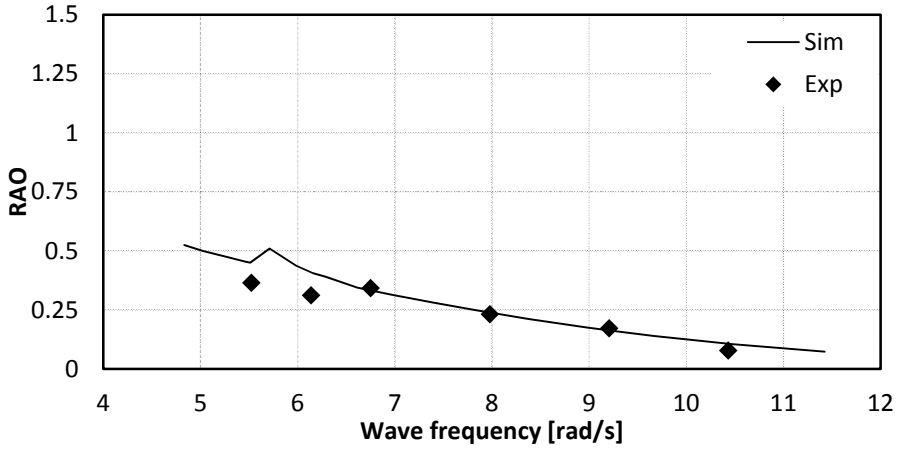

(a) Surge

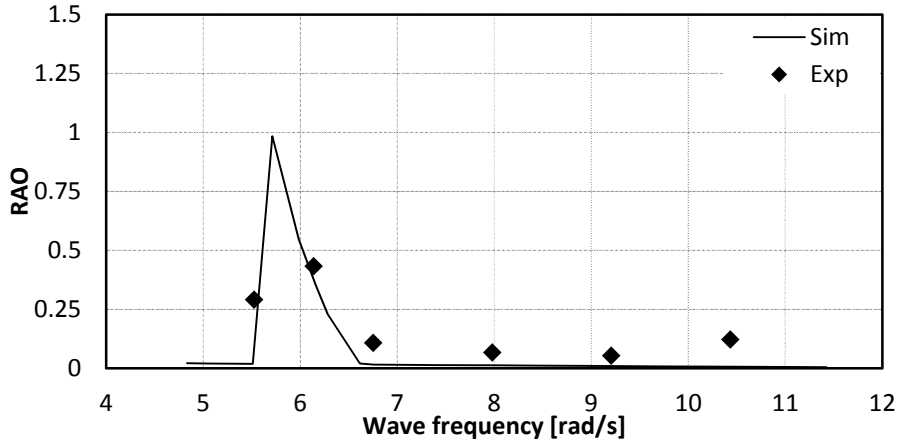

(b) Heave

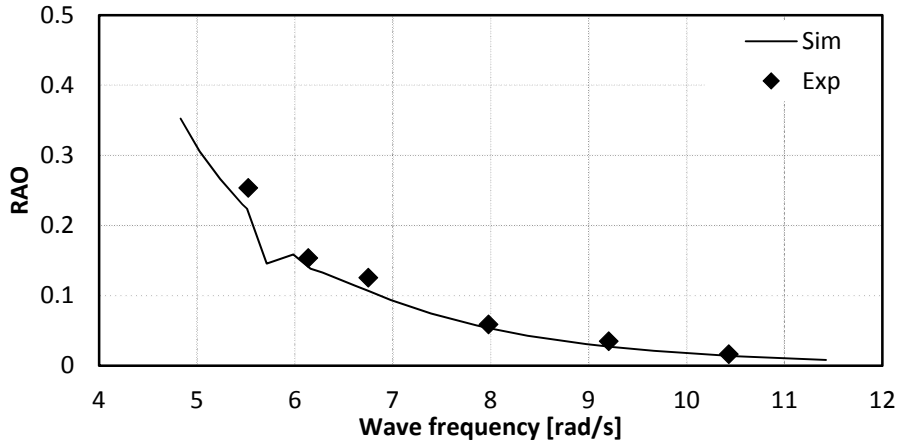

(c) Pitch

Figure 6-10 RAOs of motions of TLSPAR model

Figure 6-10 shows the comparison of RAOs for harmonic response between the model tests and numerical simulations results for surge, heave and pitch. The horizontal axis

shows the incident wave frequency. The value of the vertical axis is obtained by taking the ratio between the amplitude of the first order of the response and the amplitude of the first order of the wave amplitude (for surge) or wave slope (for pitch). It turned out that the simulation can predict the harmonic response of model test with good accuracy. As the natural frequency for the pitch dominant mode locates around 3 rad/s, the surge and pitch increases with the decrease of wave frequency. For heave motion, it has a very limited value for most wave frequency. However, for wave frequency from 5.5 rad/s to 6.5rad/s which is around the twice of the natural frequency, the harmonic component of heave can have a significant value which is caused by the large sub-harmonic response existing in surge and pitch.

Figure 6-11 shows the same results of Figure 6-10 but with the comparison of sub-harmonic response which is marked by suffix ”sub”. For the sub-harmonic response, the horizontal axis means the wave frequency which is same with Figure 6-10. The pseudo-RAO is obtained by non-dimensionalizing the sub-harmonic response (e.g., the triangle in Figure 6-9(b)) by the amplitude of the first order of the wave (amplitude or slope) as well so that the value of harmonic and sub-harmonic response can be compared directly. It can be found that, an obvious sub-harmonic response occurs when the wave frequency are ranged from 5.5 rad/s to 6.5rad/s. It is noted that the amplitude of the sub-harmonic motion is even larger than the maximum amplitude of the linear response.

The correlation between the model tests and simulation results for the sub-harmonic motion is acceptable. For the sub-harmonic heave motion, the measured value is larger than the prediction by the numerical simulation when the wave frequency is equal to 6.74 rad/s. In fact, due to the existence of wind turbine, the moment of inertia for TLSPAR model around x (roll) and y (pitch) is slightly different and the natural frequency for roll is slightly larger than the natural frequency for pitch (see Figure 6-5). Wave frequency 6.74 rad/s is just twice the roll natural frequency and a larger sub-harmonic roll can easily happen even when the wave propagates along x-axis due to the unsymmetrical influence of disturbance. This influence exceeds the scope of this paper and it will not be discussed here.

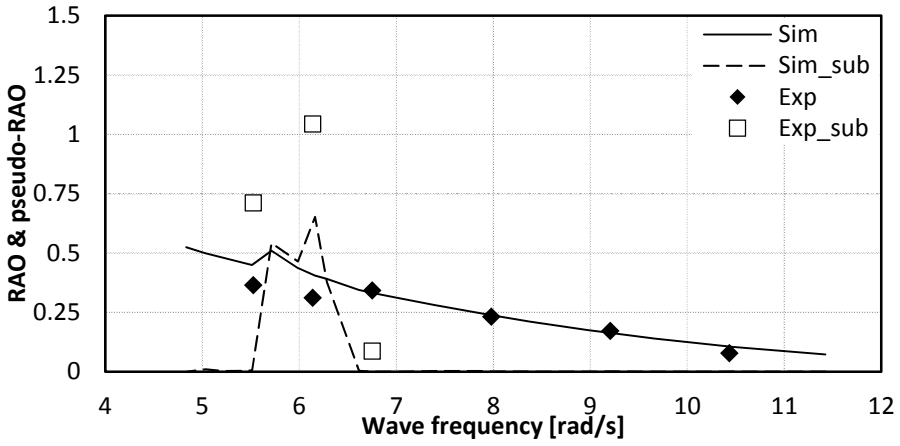

(a) Surge

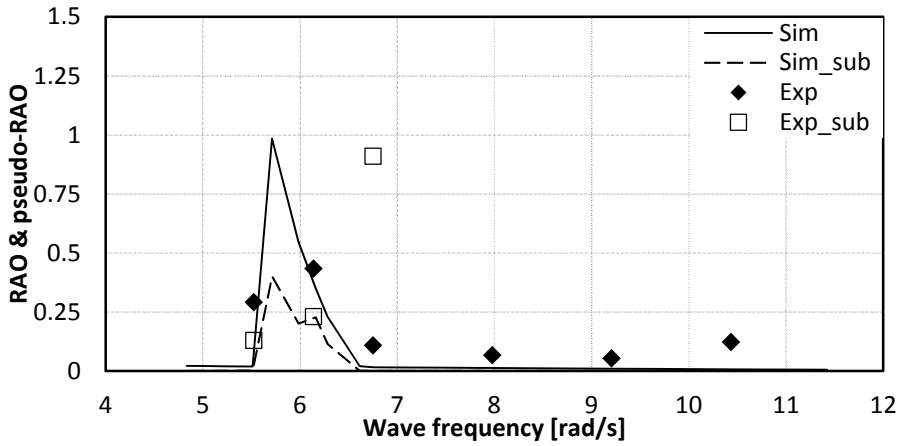

(b) Heave

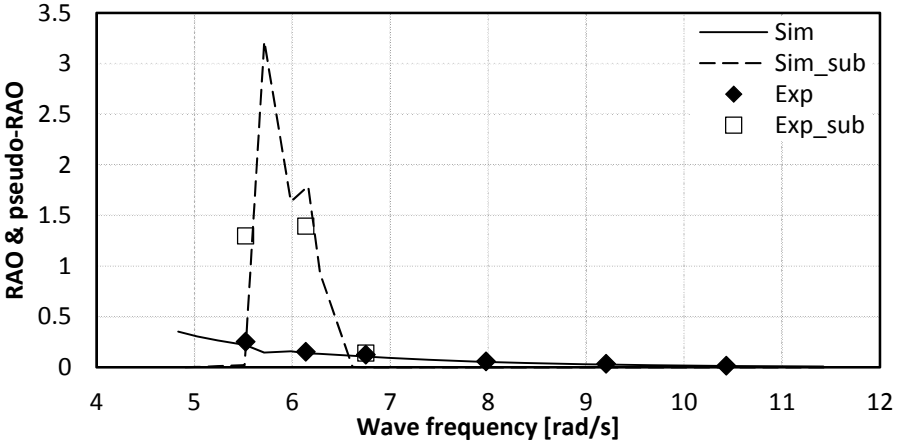

(c) Pitch

Figure 6-11 Comparison between harmonic and sub-harmonic components of motions of TLSPAR model

Figure 6-12 shows the frequency characteristics of the tension variation which includes the RAO for harmonic component and pseudo-RAO for sub-harmonic component. The vertical value of RAO is calculated by taking the ratio between the amplitude of the first order of the tension and the first order of buoyancy variation (ρAgη, ρ: water density, A: cross-section area, g: gravity acceleration, η**:** first order of wave amplitude). The pseudo-RAO for sub-harmonic components is obtained by non-dimensionalizing the corresponding order tension by the first order of buoyancy variation as well. A good agreement for both the harmonic and sub-harmonic components of the mooring tension can be obtained for TLSPAR model. The sub-harmonic response is relatively large when the sub-harmonic motion occurs (wave frequency from 5.5 rad/s to 6.5 rad/s).

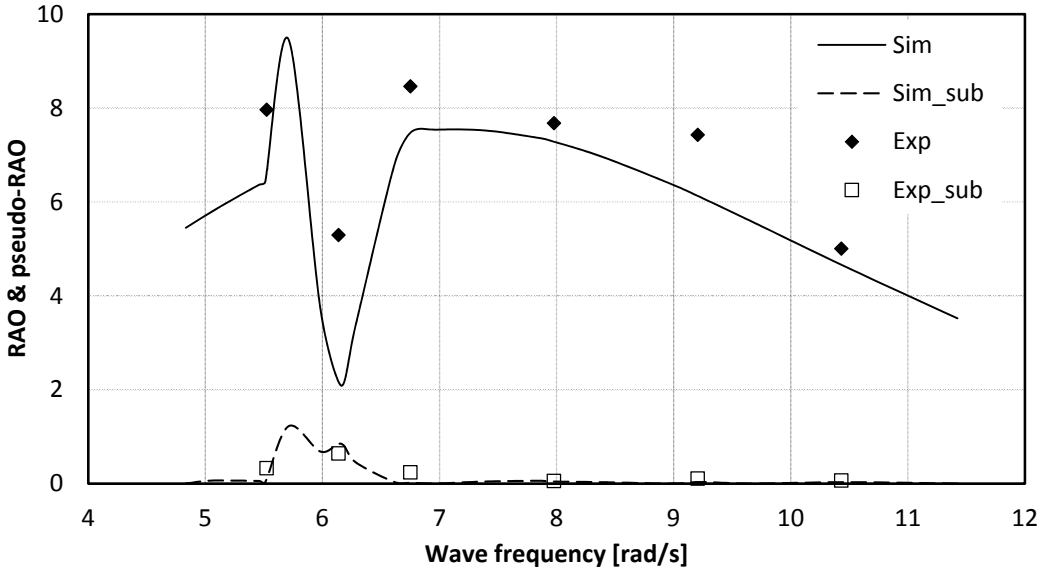

Figure 6-12 Comparison between harmonic and sub-harmonic components of the mooring tension of TLSPAR model

c) Source of sub-harmonic motion

To clarify the mechanism of the nonlinear behavior of the tethered-buoy system, a comparison for sub-harmonic pitch with four different simulation models for TLSPAR is presented in Figure 6-13. With considering the nonlinear influence of tether tension, Sim_sub and Sim(NC)_sub show the simulation results with and without coupling between heave and pitch for TLSPAR model, respectively (see Eq. (6-12)). Sim(LM)_sub and Sim(LMNC)_sub gives the same comparison without all the nonlinear influences of tether. The figure shows that, for the sub-harmonic response, only the models with the coupling effect between the buoy and mooring can reproduce the same behavior when wave frequency is twice as large as the natural frequency of TLSPAR model. It means that, the sub-harmonic behavior is mainly caused by the nonlinear influence of tether tension. Meanwhile, by comparing the model “Sim_sub”

and "Sim(NC)_sub", it can be known, due to the constrained heave motion, that the nonlinear coupling between heave and pitch has very limited influence on the sub-harmonic motion compared with the nonlinear influence of varying tether tension.

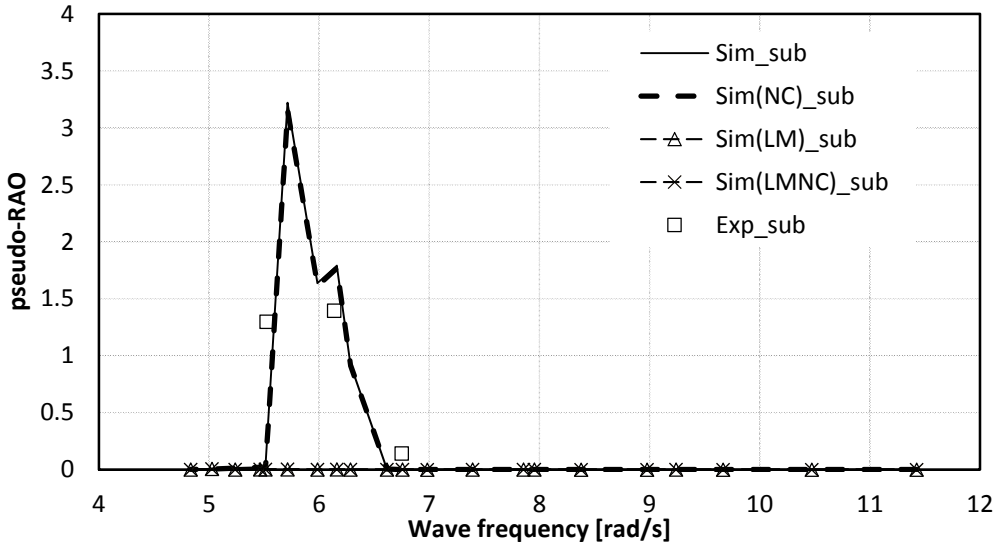

Figure 6-13 Comparison among the sub-harmonic pseudo-RAOs of pitch motion for TLSPAR obtained by using different numerical models

d) Motion ratio between pitch of buoy and tether angle

The motion ratio λ affects the Mathieu instability of tethered-buoy system a lot as it can amplify the influence of the variation of tether tension (see Eq. (6-21)). Two typical cases with TLSPAR model are selected and the time domain results obtained for the cases from model test and simulation are presented in Figure 6-14 and Figure 6-15. They include two series of data, the pitch motion of TLSPAR model (marked by "Pitch") and tether angle (marked by "Tether angle") which is defined by θ_1 in Figure 6-1. It turned out that, for both cases, the simulation can well reproduce the model test not only for the pitch of TLSPAR model but also for the tether angle.

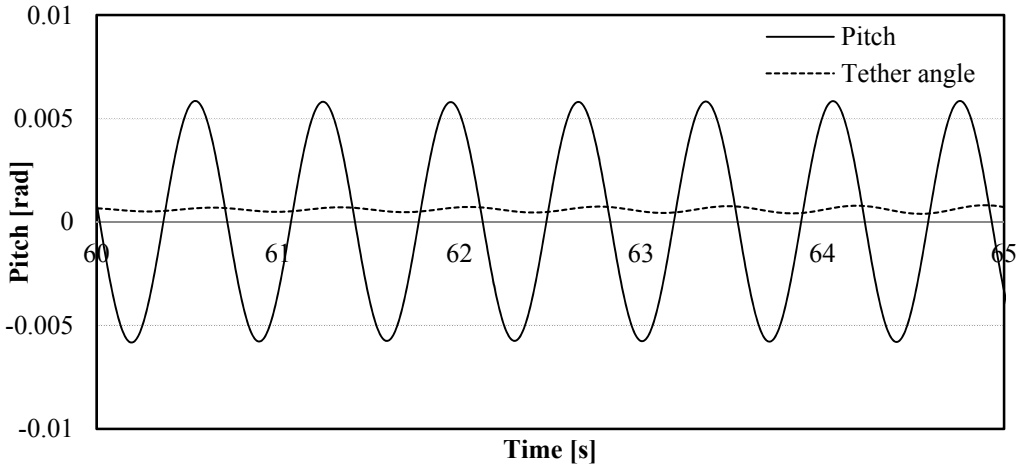

(a) Model Test

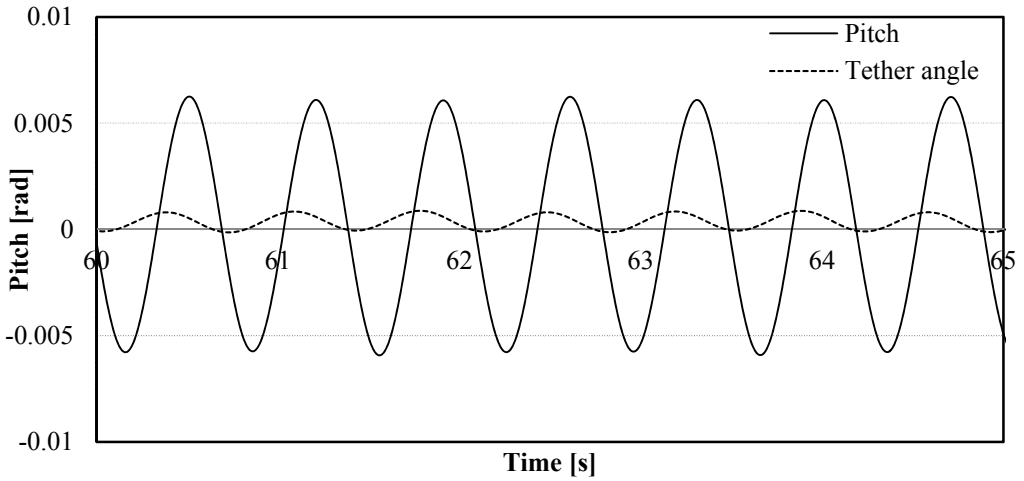

(b) Simulation

Figure 6-14 Time domain results of pitch motion of TLSPAR model at wave frequency 9.0 rad/s

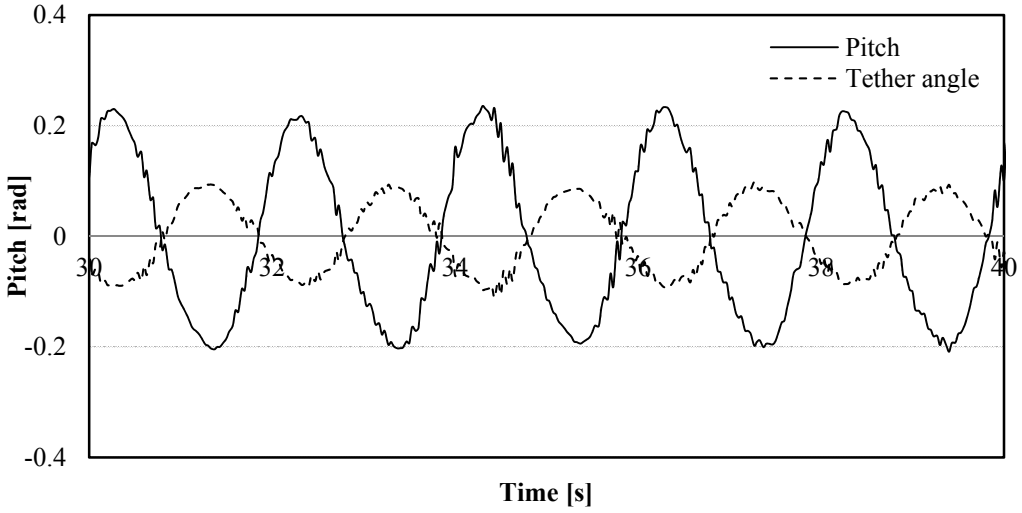

(a) Model Test

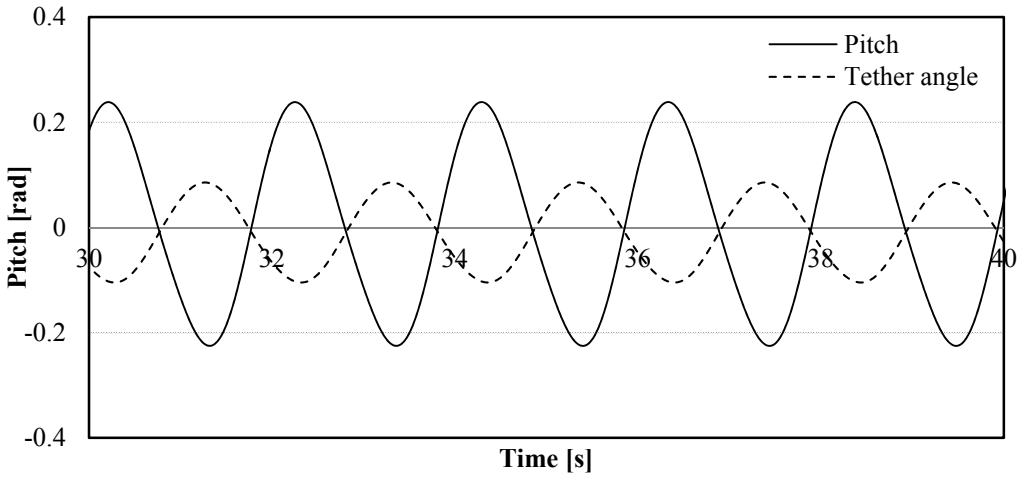

(b) Simulation

Figure 6-15 Time domain results of pitch motion of TLSPAR model at wave frequency 6.2 rad/s

For the case with wave frequency 9.0 rad/s (wave period: 0.7s) when the sub-harmonic motion does not occur, we can find from Figure 6-14 that, the tether angle is relatively small compared with the pitch motion of TLSPAR model. Figure 6-15 shows the case with wave frequency 6.2 rad/s (wave period: 1s) when the sub-harmonic motion occurs. It can be observed that, the tether angle has the opposite phase compared with the pitch of TLSPAR model, which coincides with the theoretical analysis. The motion ratio λ obtained from the model test, theoretical analysis and simulation are listed in Table 6-6. The theoretical analysis turns out to be reasonable by comparing with model test and simulation results.

Table 6-6 Motion ratio for TLSPAR model

Item	Test	Analysis	Simulation
λ	-0.428	-0.394	-0.416

e) Stability diagram

The theoretical analysis has been validated in the previous discussion. Then, by using the theoretical analysis, the stability diagram for the tethered-buoy system can be easily drawn according to the Eq. (6-21) . Added mass and damping coefficients in Eq. (6-21) are estimated by the potential theory. The natural frequency and motion ratio λ can be calculated based on Eq. (6-9) and Eq. (6-10), respectively. Figure 6-16 shows the stability diagram for the TLSPAR. The horizontal axis represents the wave frequency and the vertical axis gives the wave amplitude. The solid line marked by "Mathieu Line" shows the demarcating boundary predicted from Eq. (6-21). "wave break theory" line shows the wave breaking criterion $\left(\frac{H}{\lambda}\right)_{\max} = \frac{1}{7}\tanh(\frac{2\pi d}{\lambda})$ [54]. The figure indicates that when the wave amplitude locates higher than the "Mathieu Line", the system will become unstable.

The wave amplitude observed in the model tests is shown by the closed and open squares marked by "WaveExp". The closed square represents the case in which the sub-harmonic motion occurs according to the experiment and simulation while the open square corresponds to the cases when the harmonic response is prominent. It is found that, for the case with wave frequency from 5.5 rad/s to 6.5 rad/s which is around the twice the natural frequency (3.07rad/s), the sub-harmonic motion occurs and it is well predicted by the "Mathieu Line".

To check the validity of "Mathieu Line" more quantitatively, another series of simulation are conducted by changing the wave amplitude for the cases with wave frequency from 5.5 rad/s to 6.8 rad/s. These cases are also presented in Figure 6-16 with the triangles marked by "WaveRatio". The number indicates the wave amplitude ratio which is defined as the ratio between the simulation wave amplitude and experimental wave amplitude. The closed triangle corresponds to the cases when sub-harmonic motion occurs while the open triangle corresponds to the cases when the harmonic response is prominent. By comparing the case with same wave period but different wave amplitude, the accuracy of prediction of "Mathieu Line" is validated.

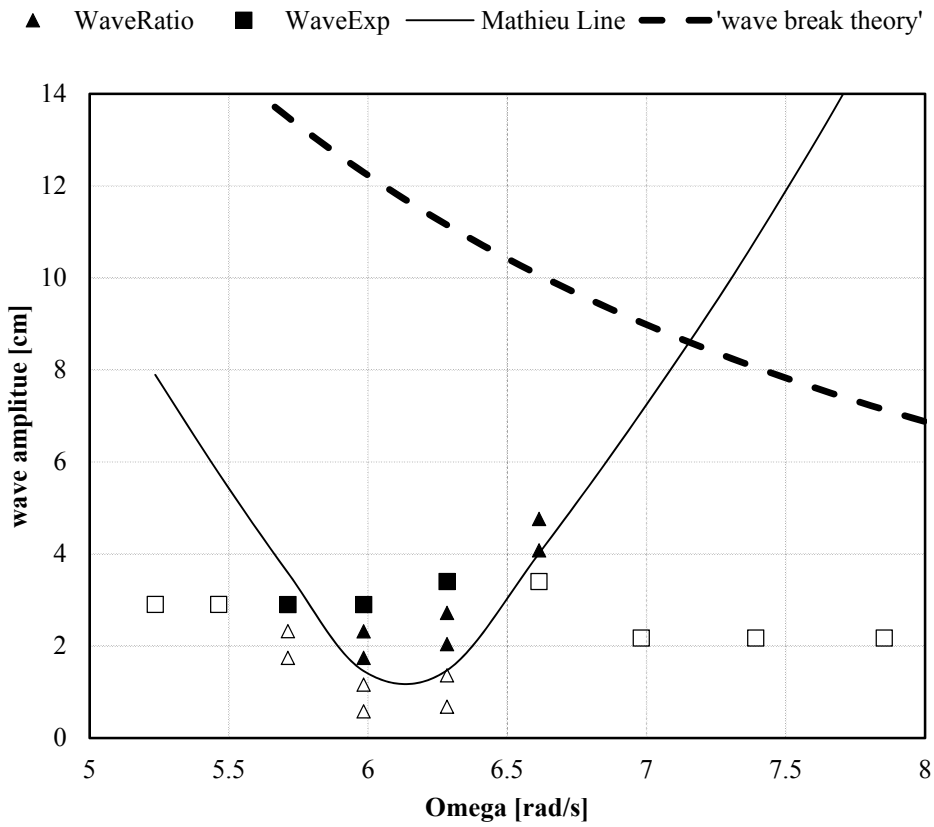

Figure 6-16 Stability diagram for the TLSPAR

The time domain results for the case with wave period 1s (wave frequency 6.2 rad/s) or 10s at full scale are presented in Figure 6-17. Figure 6-17(a) shows three simulation results with different wave amplitude ratio equal to 100%, 80% and 60%. Meanwhile, Figure 6-17(b) shows the simulation results with wave amplitude ratio equal to 100%, 40% and 20%.

It is observed in Figure 6-17(a) that, for cases with 100%, 80% and 60% wave amplitude ratio, the sub-harmonic pitch motion occurs. Meanwhile, Figure 6-17(b) shows that for the case with 40% and 20% wave amplitude ratio, only harmonic response is observed. As the response for the cases with the wave amplitude ratio equal to 40% and 20%, is relatively small, 10% of the response for the case with 100% wave amplitude ratio is shown.

By comparing the cases with wave amplitude ratio equal to 100%, 40% and 20%, it is known that, once the sub-harmonic pitch motion is excited, the amplitude of response is increased tremendously which does not satisfy the linear increasing relationship any more. The relationship between the wave amplitude ratio and pitch amplitude is shown in Figure 6-18. The demarcating boundary between harmonic and sub-harmonic region predicted by Eq. (6-21) is also included in Figure 6-18.

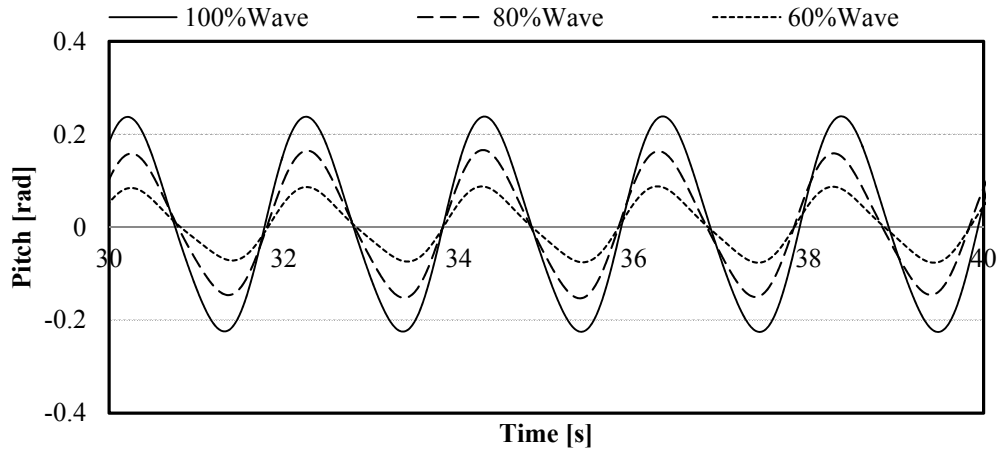

(a) Cases with 100%, 80% and 60% wave amplitude ratio

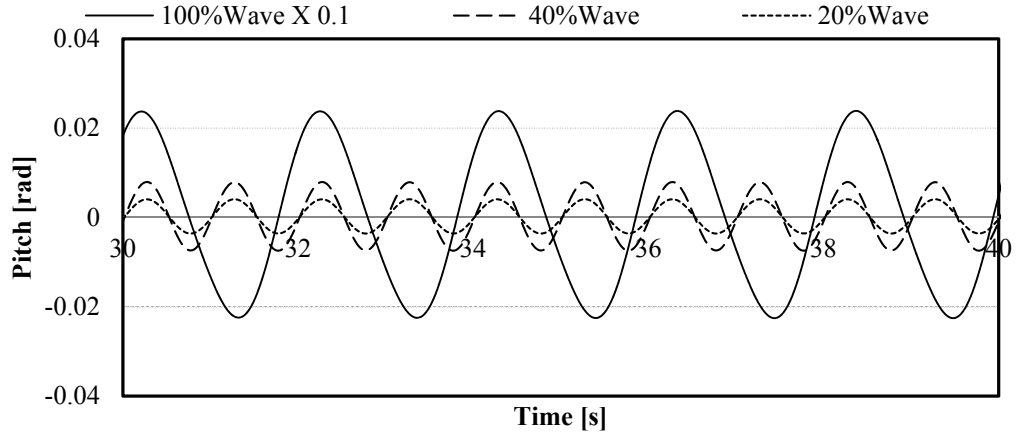

(b) Cases with 100%, 40% and 20% wave amplitude ratio

Figure 6-17 Comparison of time domain pitch motion between different wave amplitude at wave frequency 6.2 rad/s

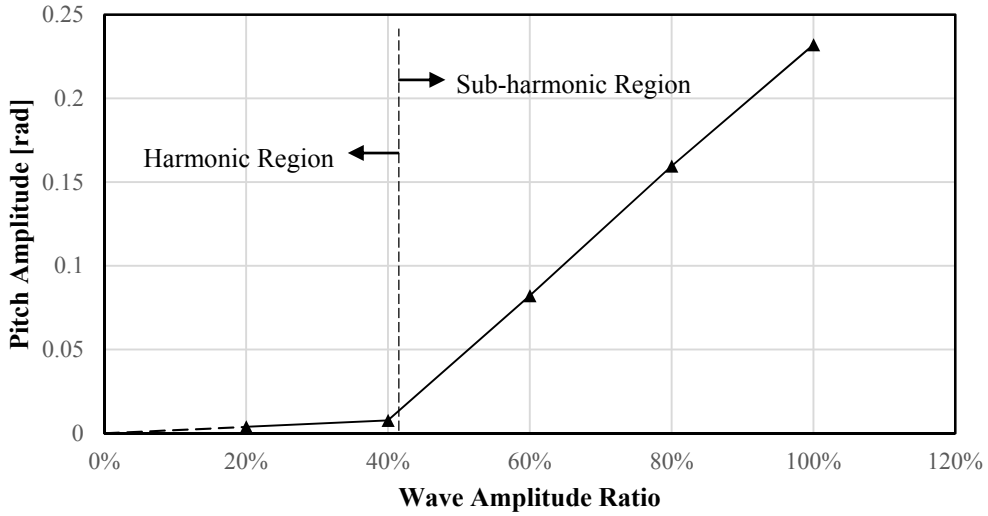

Figure 6-18 Relationship between the wave amplitude ratio and pitch amplitude at wave frequency 6.2 rad/s

6.5.2 SPM model

a) Free decay test

To get the natural frequency of SPM model, a series of free decay tests are conducted. The time domain results and corresponding FFT analysis results in frequency domain are shown in Figure 6-19. Two motion modes are observed as discussed in the theoretical analysis. By picking up the frequency at which the FFT result takes the peak in Figure 6-19(b), the natural frequency is obtained. Table 6-7 gives a comparison of the natural frequency among the decay tests, theoretical analysis, i.e., Eq. (6-9), and numerical simulation. For the higher natural frequency ω_1, the results of theoretical analysis and numerical simulation can explain the test results to some extent. The test value ω_2 may have larger uncertainty due to the small number of measured cycles. But it will give less influence as only the sub-harmonic motion associated with ω_1 is discussed in this paper. To improve the reliability of the decay test, the decay test was carried out by three times and the discrepancy of natural frequency among the multiple tests is less than 5% for the natural frequency ω_1.

The damping coefficient associated with ω_1 is obtained after conducting the IFFT analysis by eliminating the response with the frequency smaller than 1.5 rad/s. The ratio between the damping coefficient and critical damping is between 3%~4% which is utilized in the following simulation.

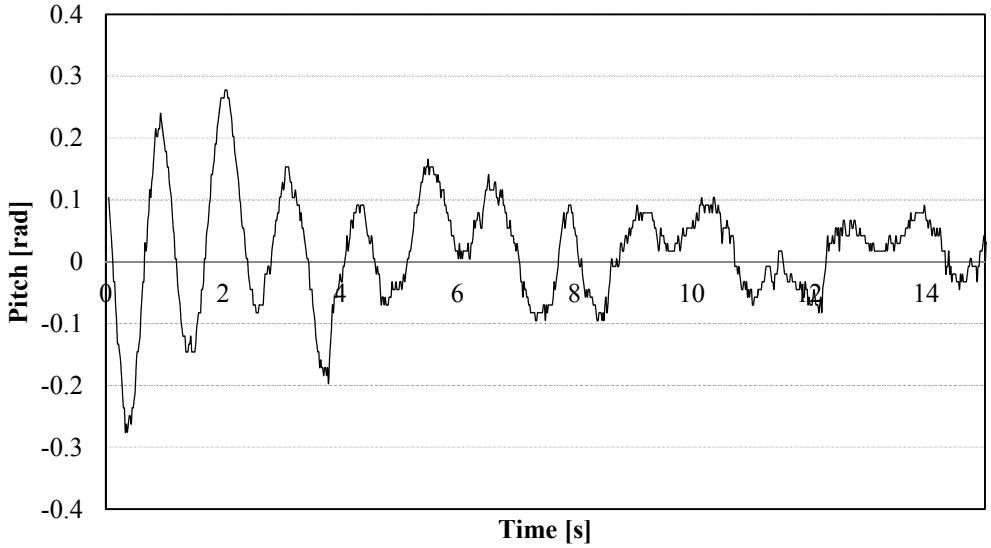

(a) Time domain

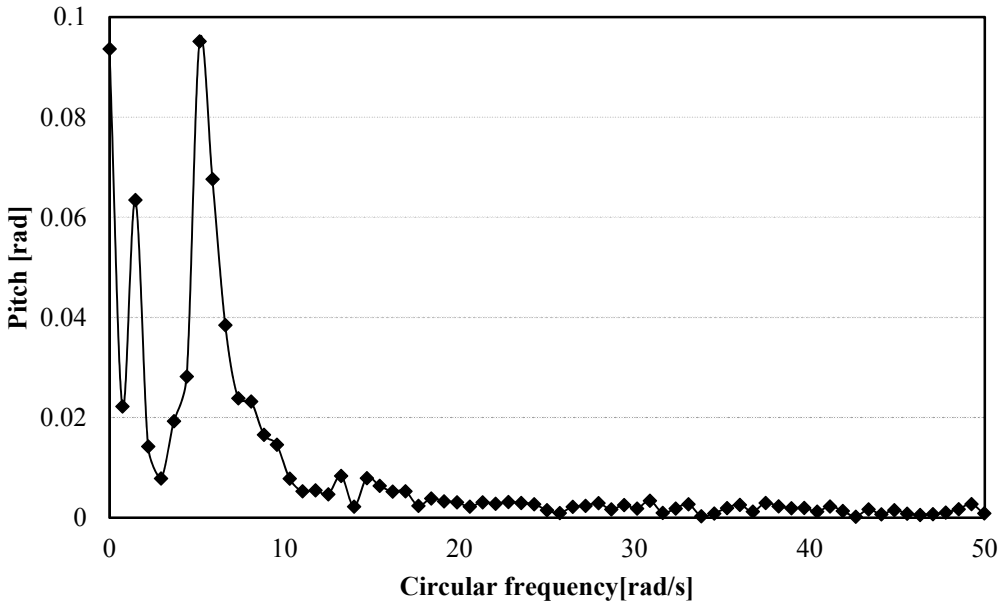

(b) Frequency domain

Figure 6-19 Free decay test results for SPM model

Table 6-7 Comparison of natural frequency among model test, theoretical analysis and numerical simulation for SPM model

Item	Test	Theoretical Analysis	Simulation	Unit
ω_1*	5.14	4.57	4.83	rad/s
ω_2**	1.46	2.0	1.81	rad/s

* ω_1 is natural frequency for the pitch dominant mode

** ω_2 is natural frequency for the surge dominant mode

b) RAO comparison

The tethered-buoy system may have large response or even unstable behavior when the wave frequency is the same as or twice the natural frequency due to the Mathieu instability as discussed for Eq. (6-12). For instance, Figure 6-20 shows a sample of the model test results in the time domain and frequency domain under regular waves with the wave period 0.7s.

From Figure 6-20(a), it can be clearly observed that, the pitch motion is not harmonic any more after 60s. FFT analysis is carried out for the data from 60s to 100s and the results in frequency domain are given by Figure 6-20(b) where two significant peaks are observed. The peak marked by the circle corresponds to the wave period which means the harmonic component and the peak marked by the triangle represents the sub-harmonic component. It is found that, for this case, the amplitude of the sub-harmonic response is even larger than the harmonic response.

Figure 6-21 shows a comparison of harmonic component for the motion of SPM between model test and simulation. The tendency can be reproduced by the simulation except the resonant frequency range around wave frequency 5rad/s. The heave motion is relatively small due to the restriction of tether even in the sub-harmonic frequency range which is different compared with the heave response of TLSPAR. This difference can be explained that for SPM model, the external force in heave direction is relatively small compared with the TLSPAR (see sub-section “Different Mechanism between SPM and TLSPAR Models”).

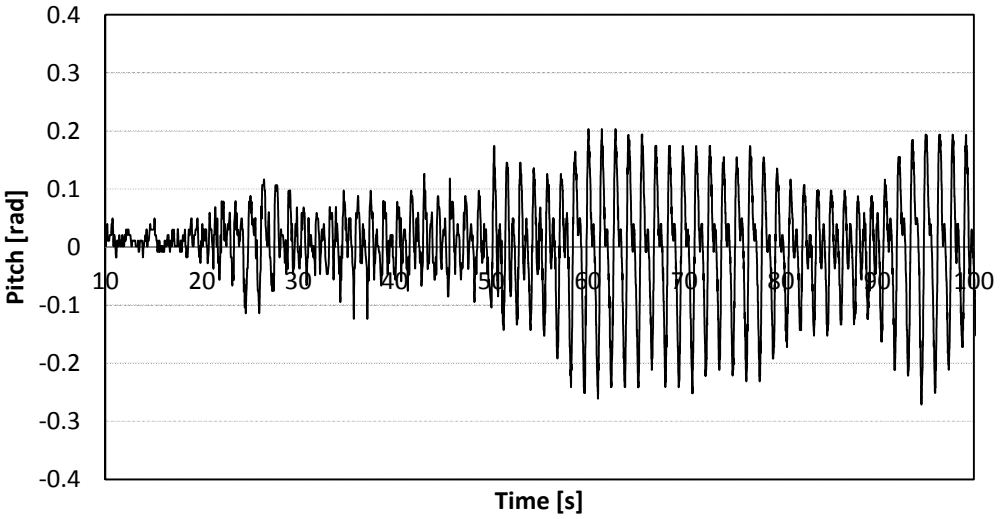

(a) Time domain

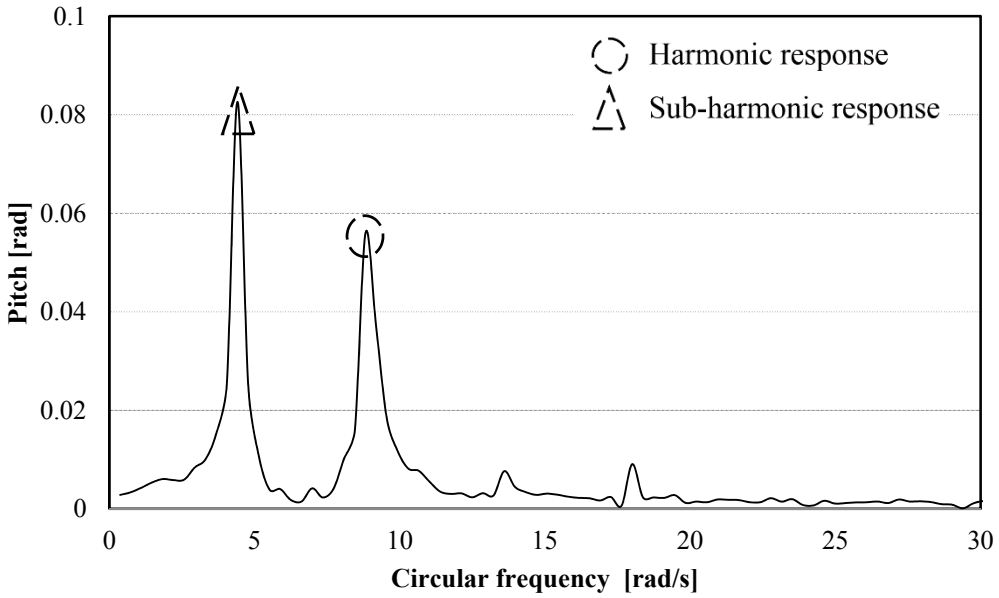

(b) Frequency domain

Figure 6-20 Measured pitch motion of SPM model at wave frequency 9 rad/s

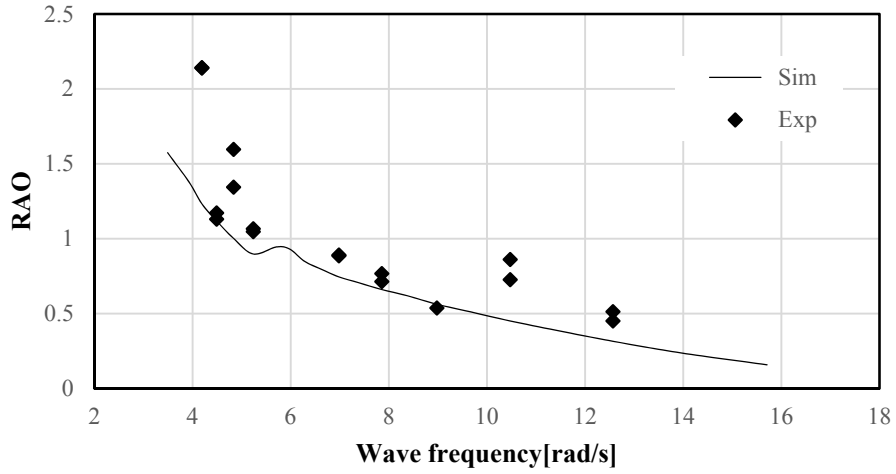

(a) Surge

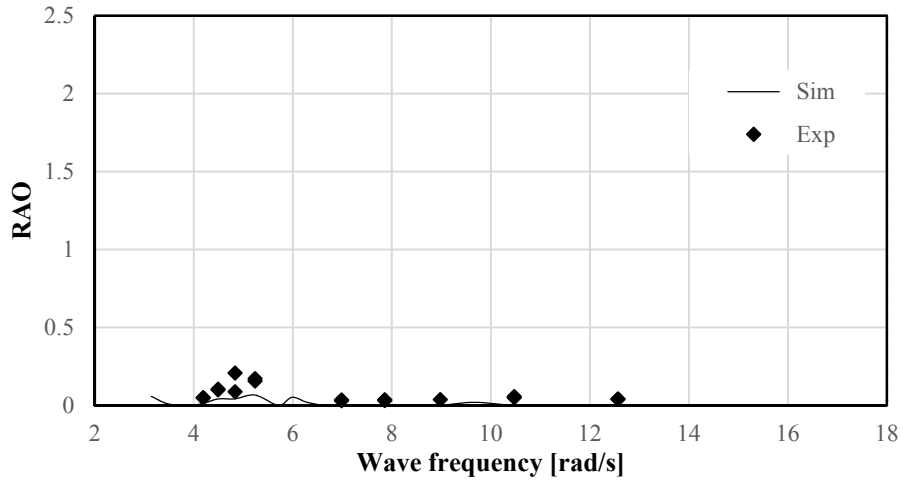

(b) Heave

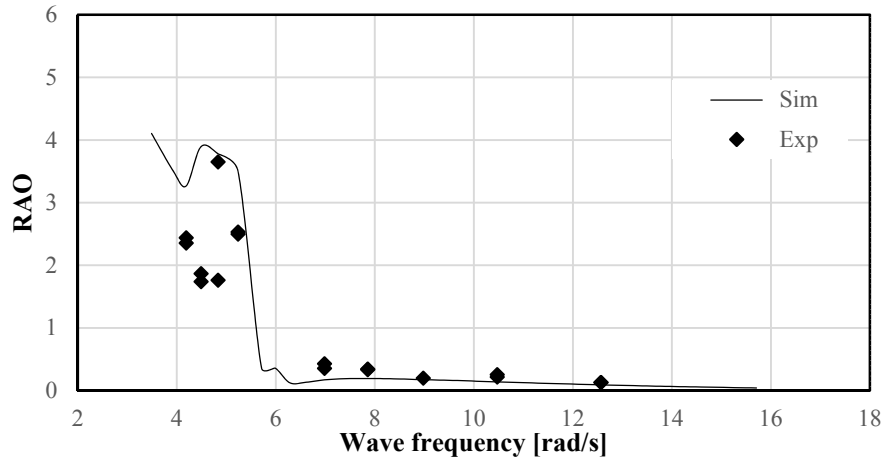

(c) Pitch

Figure 6-21 RAOs of motions of SPM model

A comparison of RAOs and pseudo-RAOs (non-dimensionalized by the amplitude of the first order of the wave, same manner with TLSPAR model) for both harmonic and sub-harmonic response between model test and simulation is given in Figure 6-22. The data name with a suffix ”sub” represents the corresponding sub-harmonic response. The onset of sub-harmonic response is observed from the model tests when the wave frequency is around twice the natural frequency (marked by the circle) and the value of sub-harmonic response is significant compared with the value of harmonic response. A similar behavior can be predicted well by the simulation.

Each of the test cases is repeated twice as indicated in Table 6-4. From the comparison between the two test cases, we can confirm the small scatter except for the resonant frequency range. It is noted that even a slight difference of configuration/installation of the model may induce a large influence on the test results due to the small scale ratio. For example, a difference of 5mm in draft may change the pre-tension value by about 30% which further results in the shift of the natural frequency by about 14%. A careful attention was paid to the installation work.

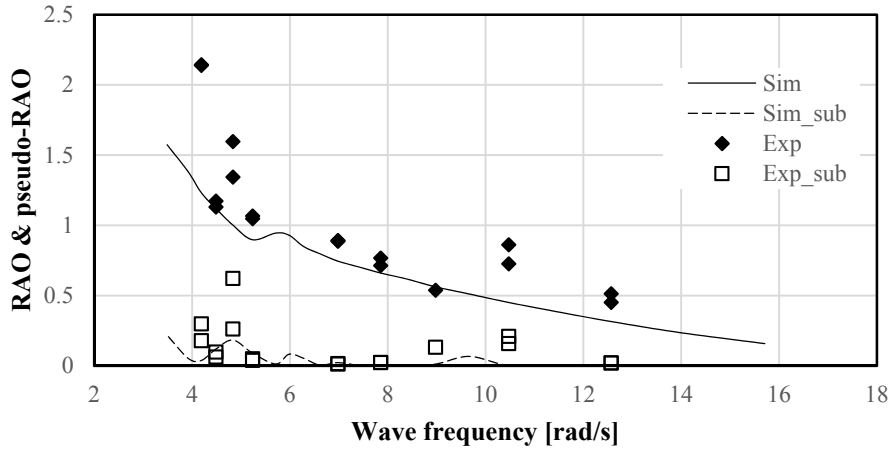

(a) Surge

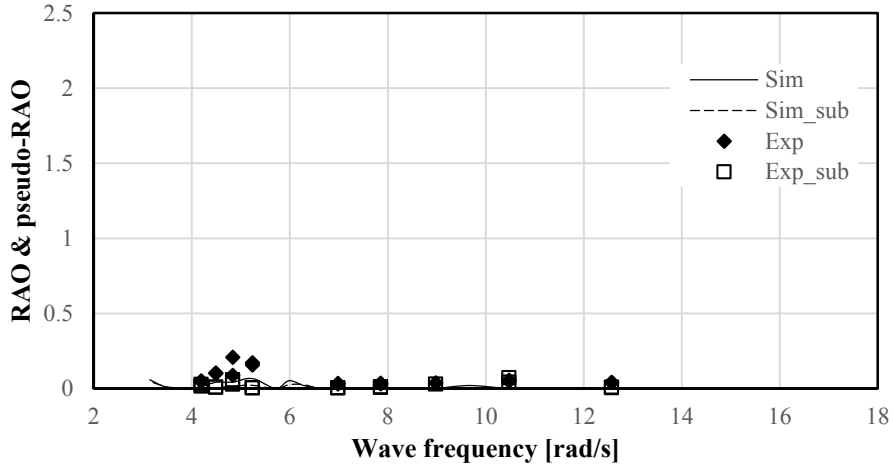

(b) Heave

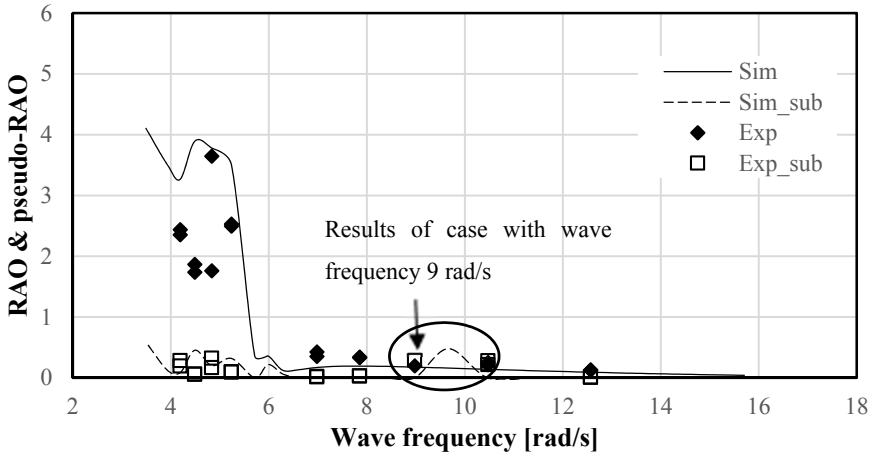

(c) Pitch

Figure 6-22 Comparison between harmonic and sub-harmonic components of motions of SPM model

A comparison for the mooring tension is shown in Figure 6-23. An acceptable correlation between the tests and simulation is obtained for both the RAO and pseudo-RAO. For the harmonic RAO results, a small discrepancy is observed from wave frequency 4.5 rad/s to 5.0 rad/s where the linear resonant response of pitch occurs. The sub-harmonic tension is usually small compared with the harmonic component.

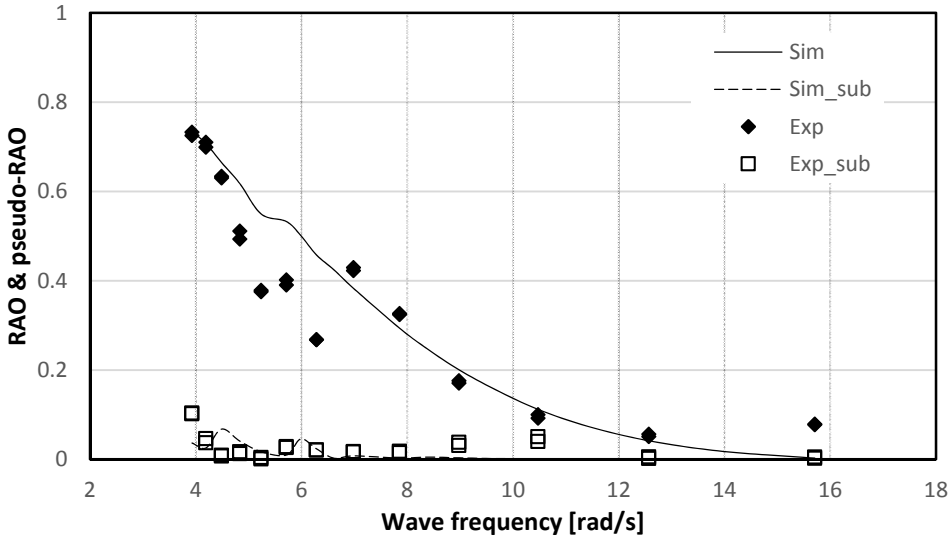

Figure 6-23 Comparison between harmonic and sub-harmonic components of mooring tension of SPM model

6.5.3 Different mechanism between SPM and TLSPAR models

When we revisit the model test results in Figure 6-20a and in Figure 6-9a, it is found out that the SPM and TLSPAR models show slightly different property when the sub-harmonic motion occurs. For SPM model (Figure 6-20a), both harmonic and sub-harmonic pitch exists with slow beating. On the other hand, for TLSPAR model (Figure 6-9a), a more “pure” and “prominent” sub-harmonic pitch motion is observed, which includes much less harmonic response. A similar phenomenon can be also found in the simulation results in Figure 6-24a and Figure 6-24b. Figure 6-24 shows a typical nonlinear response for SPM model (wave frequency 9.6rad/s) and TLSPAR model (wave frequency 6.2rad/s) which is obtained by the simulation.

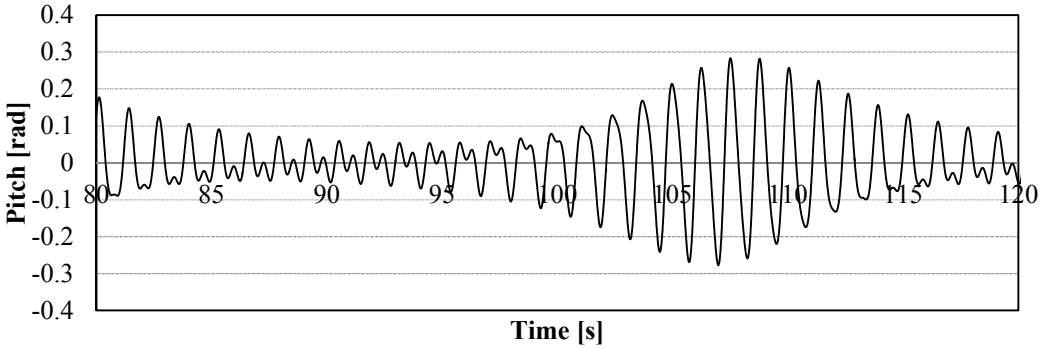

(a) Typical pitch motion of SPM model at wave frequency 9.6rad/s

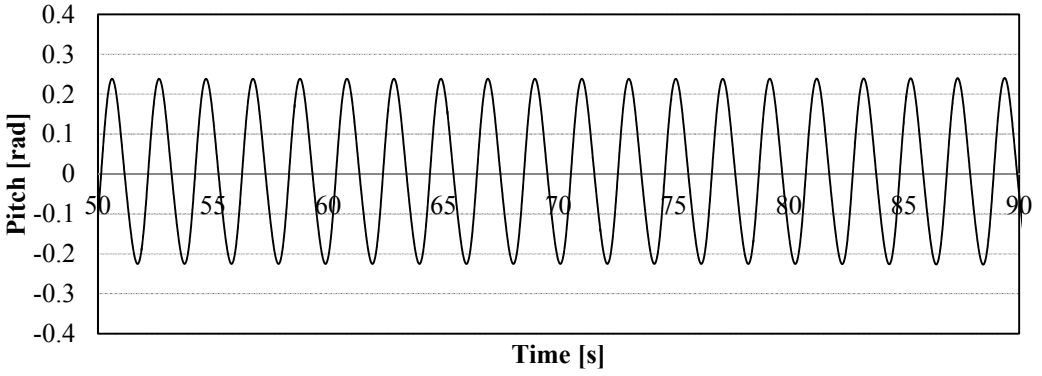

(b) Typical pitch motion of TLSPAR model at wave frequency 6.2rad/s

Figure 6-24 Simulation results for the pitch motion of SPM and TLSPAR models at the frequency when the sub-harmonic motion prominently occurs

These discrepancies can be interpreted by the different hydrodynamic properties. Table 6-8 compares the hydrodynamic forces in terms of the relative acceleration which is non-dimensionalized by the heave acceleration. All the accelerations are obtained by taking the ratio between the respective hydrodynamic force and mass (including added mass). Since the acceleration is obtained by subdividing the force by the mass, the values in the table may be regarded as non-dimensionalized hydrodynamic force. It is known from the table that, for SPM model, the force in surge and pitch are much larger than the TLSPAR model which means that the external force about surge and pitch for SPM model gives more influence on the motion compared with the TLSPAR model. As the external force about surge and pitch can be regarded as the excitation for the harmonic response, the harmonic response of SPM model is more significant than the TLSPAR model. The slow beating is always observed in the Mathieu type problems as a transient behavior [55] and it vanishes after a sufficiently long time depending on the system damping; the slow beating can be suppressed for the large damping.

Table 6-8 Non-dimensional acceleration (a/az)

	SPM	TLSPAR
Surge	5.08	1.19
Heave	1.00	1.00
Pitch	36.48	1.44

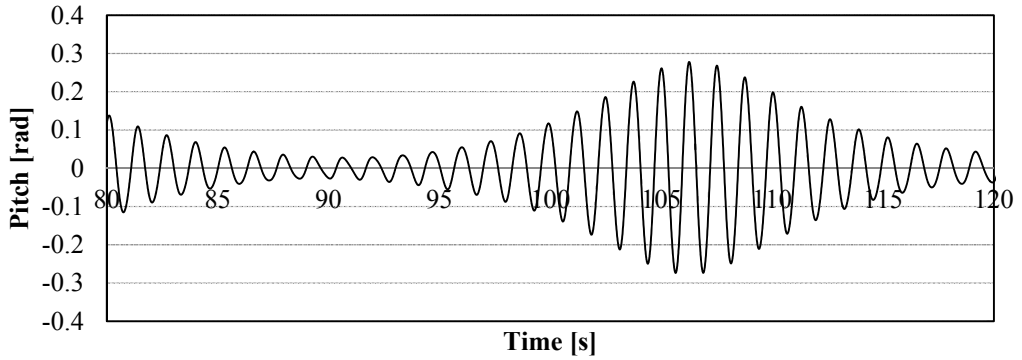

(a) Pitch motion of SPM model with the hydrodynamic external force in surge and pitch decreased to 10% of the original values

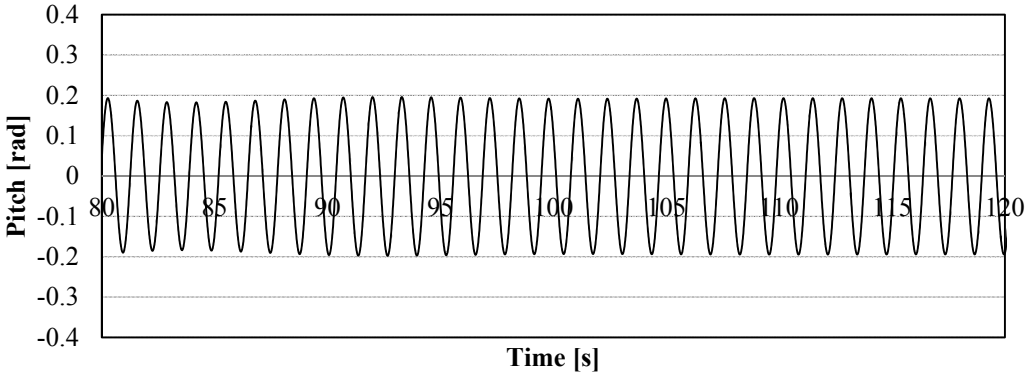

(b) Pitch motion of SPM model with the hydrodynamic external force in surge and pitch decreased to 10% of the original values while increasing the hydrodynamic damping coefficient increased by 1.2 times

Figure 6-25 Simulation results for pitch motion of SPM model with different hydrodynamic coefficients

To show the influence of external force and damping, more simulation for SPM model with same wave condition as Figure 6-24a is conducted with 90% smaller external force about surge-pitch direction and with smaller external force (same with before) and 1.2

times larger damping. The simulation results are shown by Figure 6-25.

It is found from Figure 6-25a that the harmonic response vanishes as the hydrodynamic force in surge and pitch motion decreases. Based on the small force in Figure 6-25a, through manually increasing the damping, the slow beating will also disappear and the response of SPM model can be regarded as same behavior as TLSPAR model.

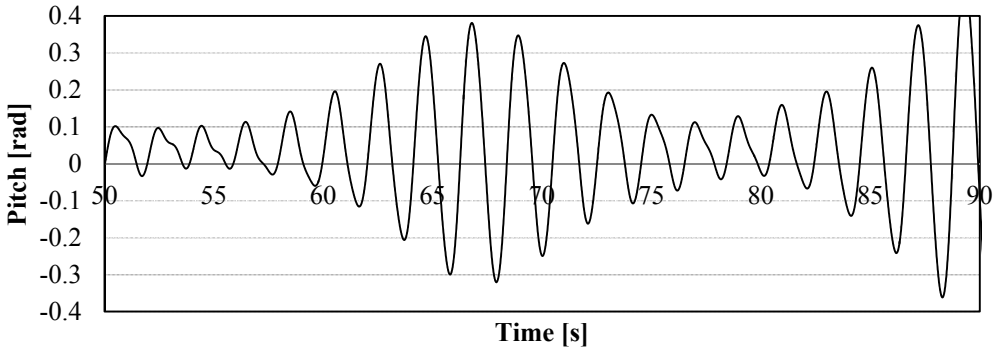

(a) Pitch motion of TLSPAR with the hydrodynamic damping coefficient decreased to 1% of the original value

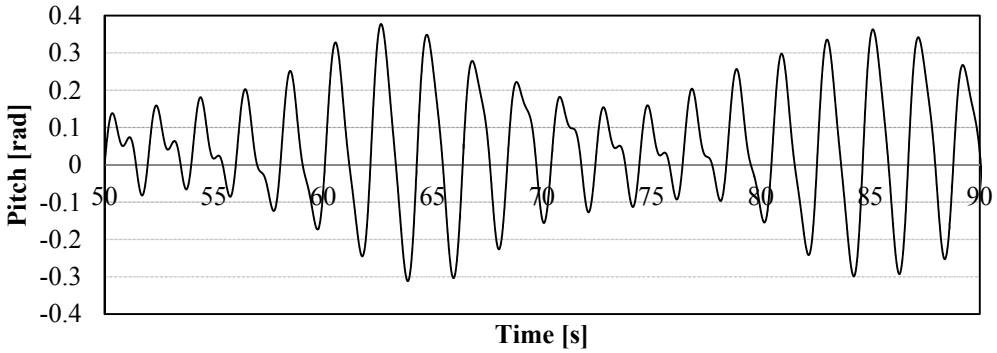

(b) Pitch motion of TLSPAR with the hydrodynamic damping coefficient decreased to 1% of the original value which increasing the hydrodynamic external force in surge and pitch increased by 5 times

Figure 6-26 Simulation results for pitch motion of TLSPAR model with different hydrodynamic coefficients

In the same manner, we can obtain results similar to SPM model for TLSPAR model if we modify the hydrodynamic coefficient by decreasing the damping and increasing the external force in surge and pitch direction. Figure 6-26 shows the simulation pitch motion under same wave condition as Figure 6-24b with 1% of original damping and with smaller damping (same with before) and 5 times larger external force in surge and pitch direction. It is seen that, the conclusion derived from Figure 6-25 can be proven again by Figure 6-26.

The sub-harmonic motion may pose technical challenges in the operability, maintainability, structural safety, etc. of the system. In this regard, it is important to control the sub-harmonic motion. Eq. (6-21) indicates that, in order to get a prominent sub-harmonic motion, the nonlinear influence of varying tether tension should be increased by increasing vertical hydrodynamic force f_z. Increasing the motion ratio λ between L_2 and L_1 in Eq. (6-11) can amplify the influence of vertical hydrodynamic force f_z. Thus, the floater shape such as TLSPAR model is relatively easier to obtain the large sub-harmonic motion.

Meanwhile, we cannot expect a prominent sub-harmonic pitch motion by simply increasing the wave amplitude to obtain the larger hydrodynamic vertical force even when the sub-harmonic frequency of the external force hits the natural frequency. As is the case with SPM model, a combined harmonic and sub-harmonic motion may appear when the hydrodynamic force in horizontal direction and hydrodynamic pitching moment are relatively large. They should be kept sufficiently small to decrease the harmonic response in the background of the sub-harmonic component.

6.6 Conclusions

In this chapter, the mechanism of the nonlinear motion of two tethered-buoy systems has been studied. A theoretical analysis was developed to predict the natural frequency, and hydrostatic and hydrodynamic stability of the tethered-buoy systems. Model test was carried out to observe the nonlinear behavior of buoy motion. Nonlinear numerical model based on time-domain DYNABEAM has been established and validated against the model test in terms of both buoy motions and tether tension variations. The different sub-harmonic behavior between SPM and TLSPAR models has been discussed. We may conclude as follows.

- A sub-harmonic pitch motion is observed for the tethered buoy system. The behavior may be described by Mathieu instability. It occurs when the Mathieu instability condition is satisfied. i.e., the sub-harmonic frequency of the external force is twice the natural frequency of the pitch motion of the buoy.
- The nonlinear influence of time-varying tether tension gives a dominant influence on the sub-harmonic pitch motion of the buoy. The coupling between heave and pitch for the buoy gives only a limited effect to the sub-harmonic motion because of the small heave motion which is constrained by the tether.
- In the design, we can suppress the sub-harmonic motion by decreasing the vertical hydrodynamic force f_z at the frequency where the sub-harmonic motion easily occurs. It can be also mitigated by adopting the smaller motion ratio λ which can be approximated as a ratio of the center of gravity height L_2 to the tether length L_1.
- Large external force in horizontal direction and pitching moment can induce a harmonic motion in a combined manner when the sub-harmonic motion occurs. Then, the slow beating motion is observed with the sub-harmonic motion. It can be decreased or eliminated by increasing the system damping.

The present research results indicate that the Mathieu instability due to floater-mooring coupling may occur even for a catenary-moored floater system when the mooring load undergoes the wave-induced variation and the mooring affects the floater motion. Such an example may be found e.g. in the yaw motion of a floating structure moored by catenaries. The mooring load has a variation with the waves and the tensile load in the mooring lines gives a variable restoring moment around the yaw axis [56]. The discussion made in the present research may hold to such a problem, too.

7 SPH-DYNABEAM COUPLING

As discussed in the previous chapter, a frequency-domain and time-domain numerical tool DYNABEAM has been built, which is designed to deal with hydro-elastic problem with considering the influence of nonlinear structural stiffness, e.g. nonlinear influence of mooring. The hydrodynamic force is mainly calculated based on the linear wave potential theory. Even though some nonlinear components existing in the hydrodynamic force can be included during the time-domain simulation (see Subsection 3.2.2), it is obviously still insufficient to reproduce high nonlinear hydrodynamic behavior such as slamming or sloshing which may contribute a dominate influence when analyzing the collapse of structure. In order to further research the nonlinear structure analysis, it is necessary to apply some mature high order hydrodynamic theory in the time-domain DYNABEAM simulation instead of linear wave potential theory. In this chapter, the smoothed-particle hydrodynamic (SPH) theory is introduced firstly and then numerically coupled with the DYNABEAM model. A simple case for tethered-buoy system (see Chapter 6) is simulated based on the SPH-DYNABEAM model and the calculation results are compared with the normal DYNABEAM model based on potential theory.

7.1 Introduction of SPH Theory

Smoothed-particle hydrodynamics (SPH) is a computational method used for simulating fluid flows. It was developed by Gingold and Monaghan [57] and Lucy [58] initially for astrophysical problems. It has been used in many fields of research, including astrophysics, ballistics, volcanology, and oceanography [59]. As it is a mesh-free Lagrangian method (where the coordinates move with the fluid), and the resolution of the method can easily be adjusted with respect to variables such as the density and the simulation for varying boundary (e.g. free surface) is much easier compared with the usual mesh-based CFD. In this chapter, an open source of SPH, SPHYSICS is coupled with the structural model in DYNABEAM. The relevant theory used in SPHYSICS is briefly introduced below [60] [61] [62].

7.1.1 Interpolation and kernel

In hydrodynamic theory, the following Lagrangian Derivative is the foundation when describing the property of a water particle.

$$\frac{dA}{dt} = \frac{\partial A}{\partial t} + \mathbf{V} \bullet \nabla A \qquad \textbf{(7-1)}$$

where, A denotes some property of a certain water particle such as velocity, density and so on.

In Eq. (7-1), we find spatial derivatives and no matter for what kind of CFD algorithm, how to solve these spatial derivatives based on finite number of ambient points is the key point. In the finite difference methods, the points are the vertices of a mesh. However, in SPH theory, the points are the particles and the spatial derivatives can be solved by some interpolation technique based on some special kernel function as shown in Eq. (7-2).

$$A(\mathbf{r}) = \int A(\mathbf{r}')W(\mathbf{r}-\mathbf{r}', h)d\mathbf{r}' \qquad \textbf{(7-2)}$$

where, $\mathbf{r}$ is the spatial coordinates

h is the kernel smoothing length

W is the kernel function.

The integral in Eq. (7-2) can be written as discrete notation Eq. (7-3) for numerical modeling:

$$A_a = \sum m_b \frac{A_b}{\rho_b} W_{ab} \qquad \textbf{(7-3)}$$

where, $W_{ab} = W(\mathbf{r_a} - \mathbf{r_b}, h)$

m_b and ρ_b are the mass and density for particle b, respectively.

The performance of SPH models highly depends on the choice of the kernel function which should satisfy the positivity, compact support and normalization condition. Of course, the kernel value should decrease with the increasing distance between two particles. Monaghan [60] recommends the following kernel function for the SPH model.

Table 7-1 Kernel function

Kernel	Function	Parameter α (2D)	Parameter α (3D)
Gaussian	$W(r,h)=\alpha\exp(-q^2)$	$\frac{1}{\pi h^2}$	$\frac{1}{(3\pi/2h^3)}$
Quadratic	$W(r,h)=\alpha[\frac{3}{16}q^2-\frac{3}{4}q+\frac{3}{4}] \quad 0\le q\le 2$	$\frac{2}{\pi h^2}$	$\frac{5}{4\pi h^3}$
Cubic	$W(r,h)=\alpha\begin{cases}\frac{3}{4}q^3-\frac{3}{2}q^2+1 & 0\le q\le 1\\ \frac{1}{4}(2-q)^3 & 1\le q\le 2\\ 0 & q\ge 2\end{cases}$	$\frac{10}{7\pi h^2}$	$\frac{1}{\pi h^3}$
Quintic	$W(r,h)=\alpha(1-\frac{q}{2})^4(2q+1) \quad 0\le q\le 2$	$\frac{7}{4\pi h^2}$	$\frac{21}{16\pi h^3}$

where, q is the non-dimensional distance given by q=r/h.

7.1.2 SPH equations

The Euler equations are the equations for the rate of change of velocity, density and position:

$$\frac{d\mathbf{v}}{dt}=-\frac{1}{\rho}\nabla P+\mathbf{g}, \quad \text{momentum equation} \qquad \textbf{(7-4)}$$

$$\frac{d\rho}{dt}=-\rho\nabla\bullet\mathbf{v}, \quad \text{continuity equation} \qquad \textbf{(7-5)}$$

$$\frac{d\mathbf{r}}{dt}=\mathbf{v}, \quad \text{trajectory equation} \qquad \textbf{(7-6)}$$

where, $\mathbf{v}$ is the particle velocity, P is the pressure and $\mathbf{g}$ is the gravity acceleration.

Eq. (7-5) shows that the SPH can deal with the variable density as it is initially designed for the astrophysical problem. Four unknown parameter, $\mathbf{v}$, P, ρ and r existing in three Euler equations and one additional equation is necessary to solve all these four parameters. In general, pressure P can be regarded as a function of density which is addressed in [63] [64]:

$$P = B[(\frac{\rho}{\rho_0})^r - 1] \qquad \textbf{(7-7)}$$

where $\gamma = 7,\ B = c_0{}^2\rho_0 / \gamma,\ \rho_0 = 1000 kgm^{-3}$

$c_0 = c(\rho_0) = \sqrt{\left.\frac{\partial P}{\partial \rho}\right|_{\rho_0}}$ is the speed of sound at the reference density.

During SPH simulation, the spatial derivatives in Eq. (7-4) and (7-5) have to be rewritten in interpolation notation based on the kernel function Eq. (7-2).

a) Momentum equation

The momentum equation can be written as:

$$\begin{aligned}\frac{d\mathbf{v}_a}{dt} &= -\frac{1}{\rho}\nabla P + \mathbf{g} + \Gamma \\ &= -\sum_b m_b(\frac{P_b}{\rho_b^2} + \frac{P_b}{\rho_b^2})\nabla_a W_{ab} + g + \Gamma\end{aligned} \qquad \textbf{(7-8)}$$

where Γ refers to dissipative function which includes two terms: $\Gamma = \Gamma_A + \Gamma_L$.

- Artificial viscosity Γ_A [60]

$$\Gamma_A = -\sum_b m_b \Pi_{ab} \nabla_a W_{ab} \qquad \textbf{(7-9)}$$

where, $\Pi_{ab} = \begin{cases} \dfrac{-\alpha \overline{c_{ab}} \mu_{ab}}{\overline{\rho_{ab}}} & \mathbf{v_{ab}} \cdot \mathbf{r_{ab}} < 0 \\ 0 & \mathbf{v_{ab}} \cdot \mathbf{r_{ab}} > 0 \end{cases}$

$$\mathbf{r_{ab}} = \mathbf{r_a} - \mathbf{r_b},\ \mathbf{v_{ab}} = \mathbf{v_a} - \mathbf{v_b}\ ,\ \mu_{ab} = \frac{h\mathbf{v_{ab}} \cdot \mathbf{r_{ab}}}{\mathbf{r_{ab}}^2 + 0.01h^2}$$

$\overline{c_{ab}} = 0.5(c_a + c_b)$ is the mean sound speed , α is a free parameter depending on the problem.

- Laminar viscosity Γ_L

Laminar viscous strees can be experesed as [65]:

$$\Gamma_L = \sum_b m_b \left(\frac{4\upsilon_0 \mathbf{r}_{ab} \cdot \nabla_a W_{ab}}{(\rho_a + \rho_b)(\mathbf{r}_{ab}^2 + 0.01h^2)}\right)\mathbf{v}_{ab} \qquad \textbf{(7-10)}$$

where, υ_0 is kinetic viscosity.

b) Continuity equation

The change of particle density is calculated by Eq. (7-11) [60]:

$$\frac{d\rho_a}{dt} = \sum_b m_b \mathbf{v_{ab}} \nabla_a W_{ab} \qquad \textbf{(7-11)}$$

7.1.3 Equation modification

To prevent the simulation suffering particle instable problem or large pressure oscillation, some techniques are employed to modify the SPH equation.

a) XSPH variant for stabilize the motion of particle

XSPH variant [66] is proposed to prevent the particle approaching each other too quickly by make the particle speed close to the average value in their neighborhood. Then the trajectory equation can be written as:

$$\frac{d\mathbf{r}_a}{dt} = \mathbf{v}_a + \varepsilon \sum_b \frac{m_b}{0.5(\rho_a + \rho_b)} \mathbf{v}_{ab} W_{ab}$$

where, ε is a free parameter ranging from 0 to 1.

b) Density reinitialization

In SPH, the pressure filed of the particles exhibits large oscillation due to Eq. (7-8) which is 7th order function of density. To overcome this problem, the spatial filter for the particle density is proven to be efficient.

- Shepard Filter [62]
- Moving Least Saquares [67]

c) Kernel correction

Particles near boundaries or the free surface have a truncated kernel which may result in a failure of consistency and normalization. It is possible to solve this problem by correcting the kernel function or its gradient. In SPHYSICS, there are two techniques to avoid these errors from a corrupted interpolating function [61].

- Kernel correction
- Kernel gradient correction

d) Riemann solver formulation

Riemann solver has to be proven with high efficiently to stabilize the CFD simulation [68]. It is also included in the SPH calculation (between each particle pair) to improve the particle pressure fields.

The original purpose of Riemann solver is to solve the discontinuous problem. Figure 7-1 shows a simple case with density discontinuity. When the initial density discontinuity is evolved in time, a shock wave propagates to the right while a rarefaction wave propagates to the left. This can be depicted in an x-t diagram in Figure 7-2. In SPHYSICS, the Riemann solver is used to substitute the discontinues parameter in two particles by the corresponding "Riemann" parameter in the star region.

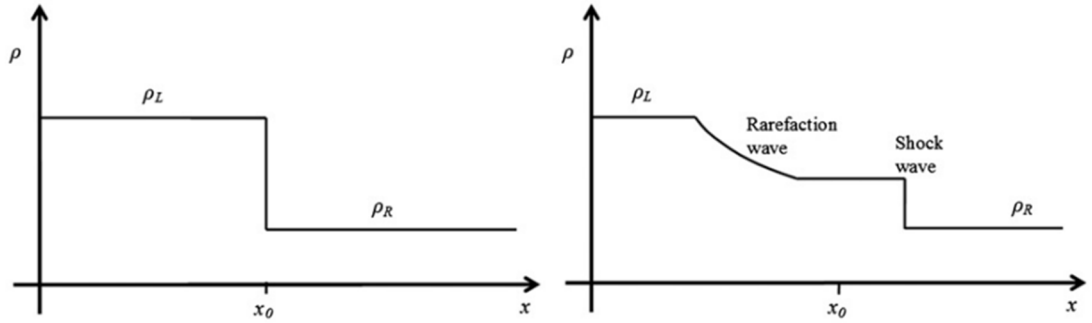

(a) Initial discontinuity in density (b) evolution of discontinuity in density

Figure 7-1 propagation of discontinious density

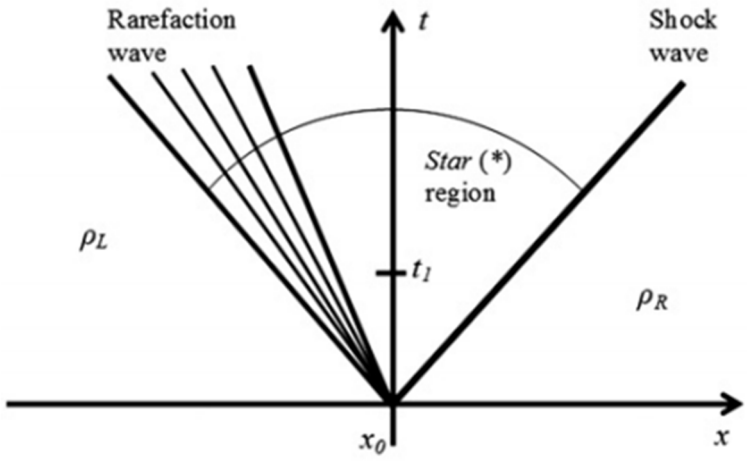

Figure 7-2 Wave solution in x-t diagrams

For example, Eq. (7-8) includes the pressure in two particles, a and b. According to the Riemann solver, the two pressure can be replaced by one pressure corresponding the virtual particle between particle a and b. Then Eq. (7-8) can be rewritten as:

$$\frac{d\mathbf{v}_a}{dt} = -\sum_b m_b 2P_{ab}{}^* (\frac{1}{\rho_b^2} + \frac{1}{\rho_b^2}) \nabla_a W_{ab} + g + \Gamma \qquad \textbf{(7-12)}$$

where, $P_{ab}{}^*$ is the intermediate star value which can be solved by, e.g. acoustic-based solver.

Many different Riemann solvers have been developed and utilized in the SPH simulation, e.g. NCRS [69], CRS [70], HLLC [71]. More information can be referred to the relevant researches.

7.1.4 Boundary condition

In SPH, the boundary is usually escribed by a set of discrete boundary particles (BP). Monghan [60] proposed a repulsive boundary conditions to calculate the force f (Eq. (7-13)) experienced by an fluid particle (FP) acting normal to the wall.

$$f = \mathbf{n} R(\psi) P(\xi) \varepsilon(z, u_\perp) \qquad \textbf{(7-13)}$$

where,

n is the normal vector of the wall.

ψ is the perpendicular distance of the particle from the wall

ξ is the projection of interpolation location onto the chord joining the two adjacent boundary particles

$u_\perp$ is the velocity of FB projected onto the normal vector **n**.

$$R(\psi) = \frac{1}{h} 0.01 c_a^2 \frac{1}{\sqrt{q_n}} (1 - q_n)$$

$$q_n = \frac{\psi}{2h}$$

$$P(\xi) = 0.5(1 + \cos(\frac{2\pi\xi}{\Delta b})) \text{ or } P(\xi) = 1 - \frac{\xi}{\Delta b}$$

Δb is the distance between any two adjacent BPs.

Function $\varepsilon(z, u_\perp)$ is used to adjust the magnitude of the force according to the local water depth and velocity of the FP normal to the boundary [72].

$$\varepsilon(z, u_\perp) = \varepsilon(z) + \varepsilon(u_\perp) \qquad \textbf{(7-14)}$$

where

$$\varepsilon(z) = \begin{cases} 0.02 & z \geq 0 \\ |z / h_0| + 0.02 & -h_0 \leq z \leq 0 \\ 1 & |z / h_0| > 1 \end{cases}$$

and

$$\varepsilon(u_\perp) = \begin{cases} 0 & u_\perp \geq 0 \\ |40 u_\perp| + c_0 & |40 u_\perp| < c_0 \\ 1 & |40 u_\perp| > c_0 \end{cases}$$

z is the elevation above the local still water level h_0.

7.2 GPU Simulation

For CFD simulation, the calculation time is always the critical problem which limit the utilization of CFD in simulation of large scaled model. SPH also meet the some calculation efficiency problem. To overcome this disadvantage, the GPU version of SPH model has been successfully developed which is named as DualSphysics. The accuracy of the GPU calculation has been validated in [73]. It is observed that, based on GPU calculation, DualSphysics provides 10 to 100 times faster calculation than the CPU model. Figure 7-3 shows the comparison of calculation efficiency between the GPU-based and CPU-based SPH model. The relevant specification of GPUs and CPUs are listed in Table 7-2.

Table 7-2 General specifications of GPUs and CPUs

		Number of cores	Processor clock	Memory space
GTX 260	GPU	192	1.24GHz	0.875GB
TESLA M1060	GPU	240	1.36GHz	4GB
GTX 285	GPU	240	1.48GHz	1GB
GTX 480	GPU	480	1.40GHz	1.5GB
Intel i7 940	CPU	4	2.93GHz	-
Intel Xeon X5500	CPU	4	2.67GHz	-
Intel Xeon E5620	CPU	4	2.4GHz	-

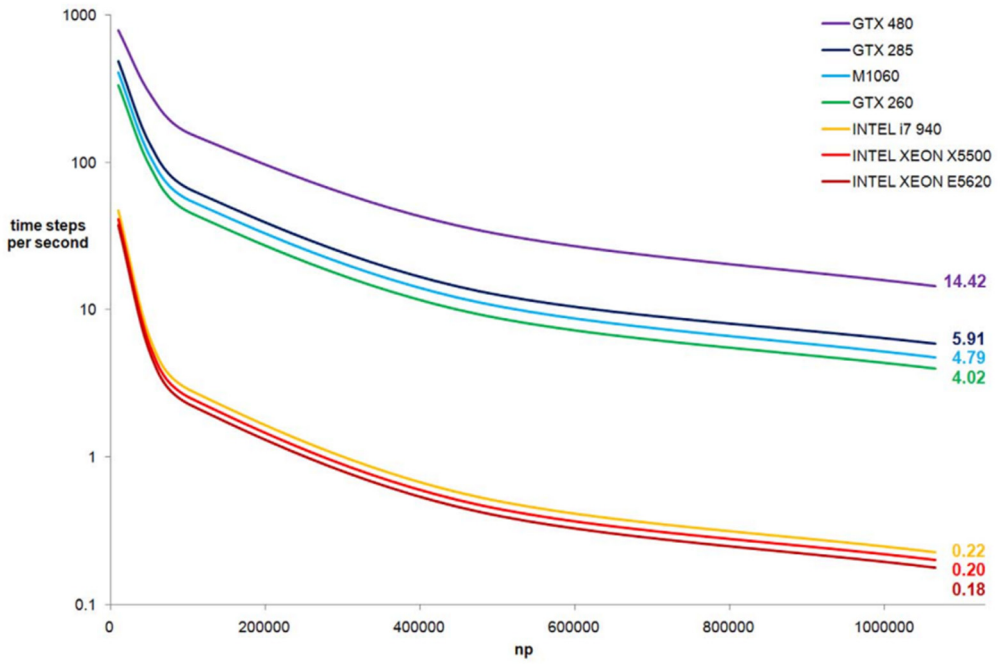

Figure 7-3 Comparison of calculation efficiency between the GPU-based and CPU-based SPH model [CPU-GPU code***]

In Figure 7-3, the x-axis represents the particle numbers in the SPH model, the y-axis means the number of calculation time steps finished in one physical second. It turns out that the GPU of GTX 480 can achieve almost 70 times faster than the fastest CPU, intel i7 940 in terms of calculation speed. The high calculation efficiency becomes clear when the particle number is sufficiently large. By comparing between the different GPU, it is known that the calculation speed mainly depends on the core numbers of GPU. Although the memory space of GPU dominates the maximum number of particles in SPH model, it will give little influence on the calculation speed. In the following simulation, the newest GPU, GTX 780Ti with 2880 cores is used and the calculation speed can be expected as 300 times faster than the intel i7-940-CPU when the particle number is close to or more than 1million.

7.3 SPH-DYNABEAM Coupling Methodology

Here, the DYNABEAM model is the same with what has been introduced in the previous chapter. However, the hydrodynamic estimation for the floater is changed from linear potential theory to SPH theory. The GPU-SPH code, DualSphysics is utilized to couple with the DYNABEAM in time domain. As DualSphysics is written by C++&CUDA and DYNABEAM is written by Fortran90, the mixture-langrage coupling process become more complicated technically. At last, the dynamic link library is used to transfer the data between Fortran-DYNABEAM and GPU-DualSpysics. The coupling flow is shown in the Figure 7-4. It is noted that, predictor-corrector method is introduced into the weakly coupling between the DYNABEAM and DualSpysics. Due to the limitation of weakly coupling, the simulation time step has to be selected as a sufficient small value compared with the natural frequency of the structural model in DYNABEAM. In the following simulation, the permitted largest value for the time step is set as 1 $x10^{-4}$ which automatically decreases when the SPH meets some divergence problem.

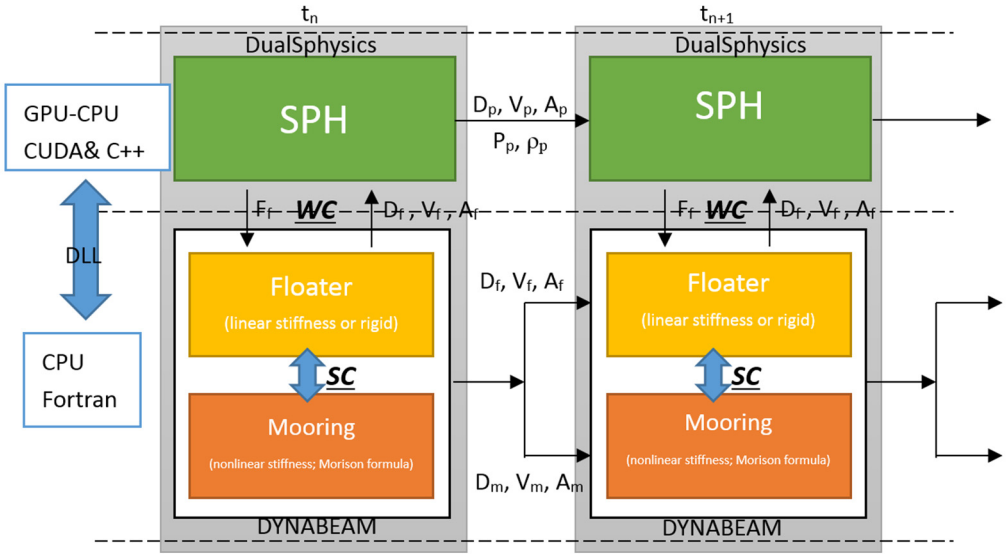

WC: weakly coupling

SC: strongly coupling

D_p, V_p, A_p, P_p, ρ_p: Displacement, Velocity, Acceleration, Pressure and density of fluid particle

D_f, V_f, A_f: Displacement, Velocity, Acceleration of floater

D_m, V_m, A_m: Displacement, Velocity, Acceleration of mooring

F_f: Fluid-induced force

Figure 7-4 coupling flow between SPH and DYNABEAM

7.4 Case Analysis

7.4.1 Regular wave case with small wave amplitude

To verify the reasonability of the coupling model between DYNABEAM and DualSpysics, a series of regular wave simulation for the SPM based on the coupling model are conducted. Then, the simulation results are compared with the simulation under normal DYNABEAM.

Due to the limitation of the boundary condition for the present SPH code, the exact buoyancy cannot be obtained by SPH in which the buoyancy is regarded as the repulsive force between multiple particles. Theoretically, this discrepancy for buoyancy could be decreased by selecting smaller the particle dimension. But as the following simulation case is designed for 3D model, the particle dimension cannot be set too small considering the calculation time problem which means some numerical errors of buoyancy inevitably exist in the SPH simulation. For the SPM model, the pretension of tether may affect a lot on the model response which is equal to the discrepancy between buoyancy and gravity. Even slight error in the estimation of buoyancy will lead to a non-negligible discrepancy in the pretension. For example, considering the test model in Subsection 6.3.2, the corresponding buoyancy in SPH model is overestimated by 12% (12.8N, theoretical: 11.5N) which means that the pretension is overestimated by almost 200% (2.7N, theoretical: 1.4N). In order to get a reasonable value for pretension, the draft of buoy is artificially increased by 6cm so that the pretension in SPH is overestimated by 23% (7.4N, theoretical: 6.1N). The particulars for the modified SPM model is shown in Table 7-3. The particulars for the SPH model is shown in Table 7-4. The coefficient of artificial viscosity is selected as 1 for all the following simulation cases.

Table 7-3 Principal particulars of modified SPM model

Item	Value	Unit
Mass	1.035	kg
Moment of Inertia (I_{yy})	0.00786	kg*m^2
The height of gravity center (L_2)	0.073	m
Height	0.240	m
Diameter	0.100	m
Draft	0.210	m
Tether Length (L_1)	0.240	m
Pretension	6.06	N

Table 7-4 Particulars for the SPH model

Item	Value	Unit
Water Tank Length	6	m
Water Tank Width	0.3	m
Water Depth	0.48	m
Particle Diameter	0.01	m
Particle Number	801066	
Time consuming (s/s)	2100 (1s=35mins)	
GPU (cores)	GTX780Ti (2880)	
CPU (cores)	I7-3930K (3.2GHz, 12)	

Flap type of wave generator is employed in the numerical water tank. 13 regular wave cases are simulated as given in Table 7-5. For each case, simulation period is set as 10s.

Table 7-5 Simulation Cases

Case	Generator Amp	Wave Period	Wave Amplitude
WAVE-Case01.dat	2.5 $x10^{-2}$ m	0.4 s	1.64 $x10^{-2}$ m
WAVE-Case02.dat	2.5 $x10^{-2}$ m	0.5 s	2.47 $x10^{-2}$ m
WAVE-Case03.dat	2.5 $x10^{-2}$ m	0.6 s	2.59 $x10^{-2}$ m
WAVE-Case04.dat	2.5 $x10^{-2}$ m	0.7 s	3.14 $x10^{-2}$ m
WAVE-Case05.dat	2.5 $x10^{-2}$ m	0.8 s	4.32 $x10^{-2}$ m
WAVE-Case06.dat	2.5 $x10^{-2}$ m	0.9 s	3.19 $x10^{-2}$ m
WAVE-Case07.dat	2.5 $x10^{-2}$ m	1.0 s	3.55 $x10^{-2}$ m
WAVE-Case08.dat	2.5 $x10^{-2}$ m	1.1 s	2.91 $x10^{-2}$ m
WAVE-Case09.dat	2.5 $x10^{-2}$ m	1.2 s	2.61 $x10^{-2}$ m
WAVE-Case10.dat	2.5 $x10^{-2}$ m	1.3 s	2.92 $x10^{-2}$ m
WAVE-Case11.dat	2.5 $x10^{-2}$ m	1.4 s	2.26 $x10^{-2}$ m
WAVE-Case12.dat	2.5 $x10^{-2}$ m	1.5 s	2.82 $x10^{-2}$ m
WAVE-Case13.dat	2.5 $x10^{-2}$ m	1.6 s	3.21 $x10^{-2}$ m

The postprocessor for the coupling DYNABEAM and DualSpysics is also developed based on the original postprocessor designed for DualSpysics. Figure 7-5 and Figure 7-6 show the outlook of the postprocessor.

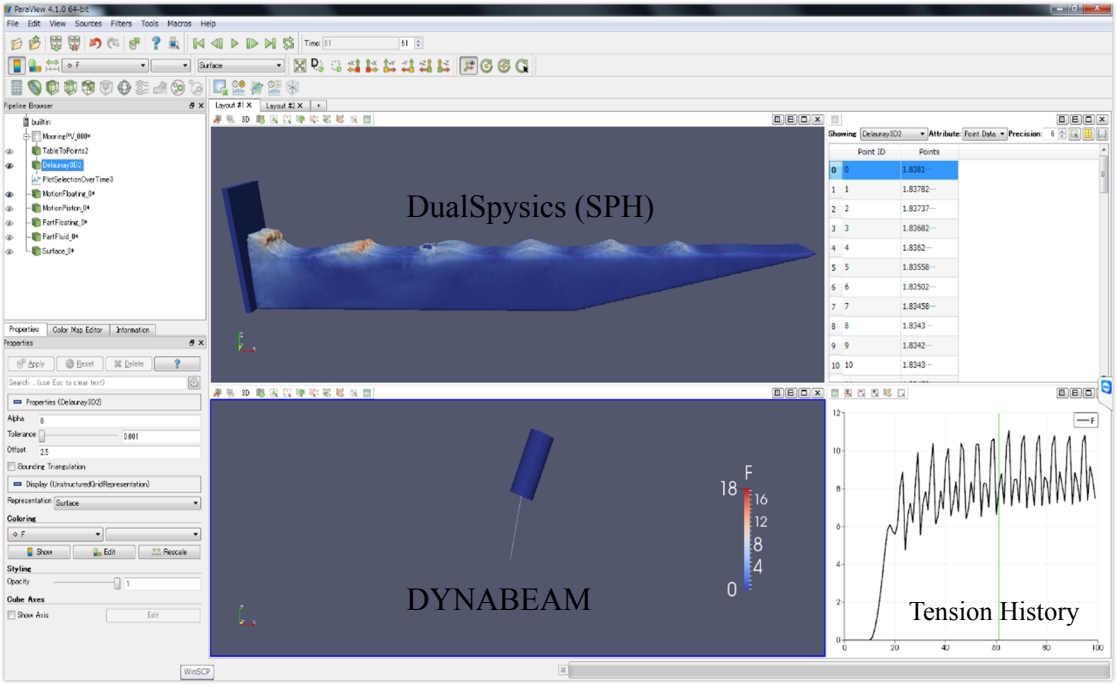

Figure 7-5 Outlook of postprocessor for coupling system (a)

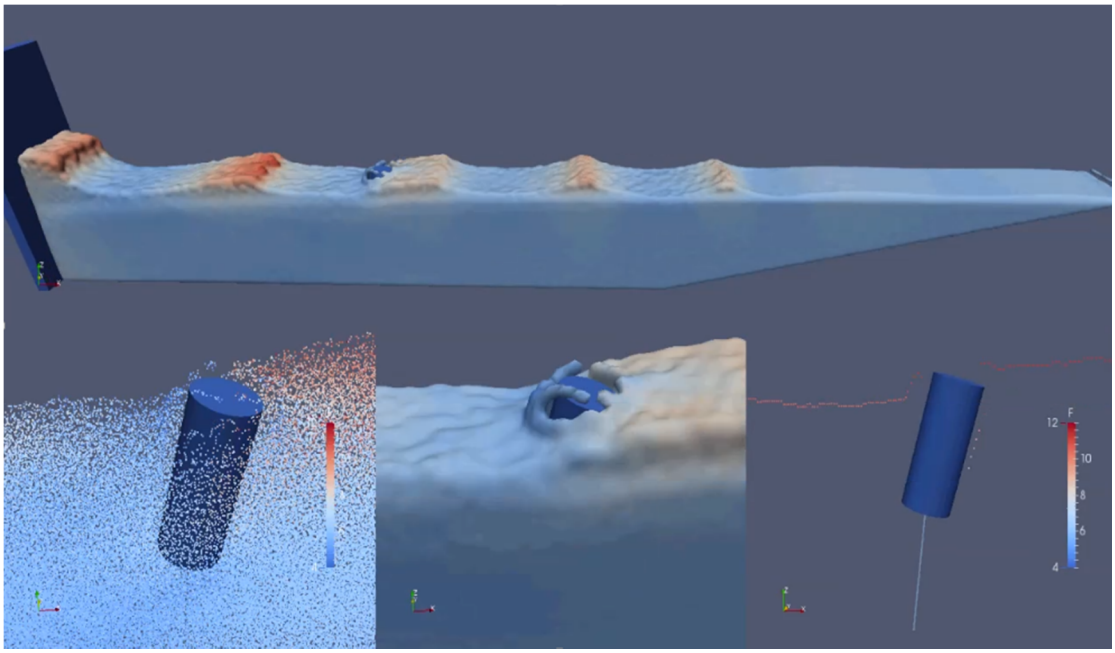

Figure 7-6 Outlook of postprocessor for coupling system (b)

As an example, the time domain results for Case02 are shown from Figure 7-7 to Figure 7-14.

Figure 7-7 shows the generated wave profile. The results of 6 DOF motion of buoy are

given by Figure 7-8 - Figure 7-13. The tether tension is shown in Figure 7-14. In order to avoid impact influence, the external force on buoy which includes gravity, buoyancy and hydrodynamic force are given gradually from 0 to the actual value in period 0s-2s.

As the wave propagates along the x-axis, the motion of sway, roll and yaw are constrained in small degree.

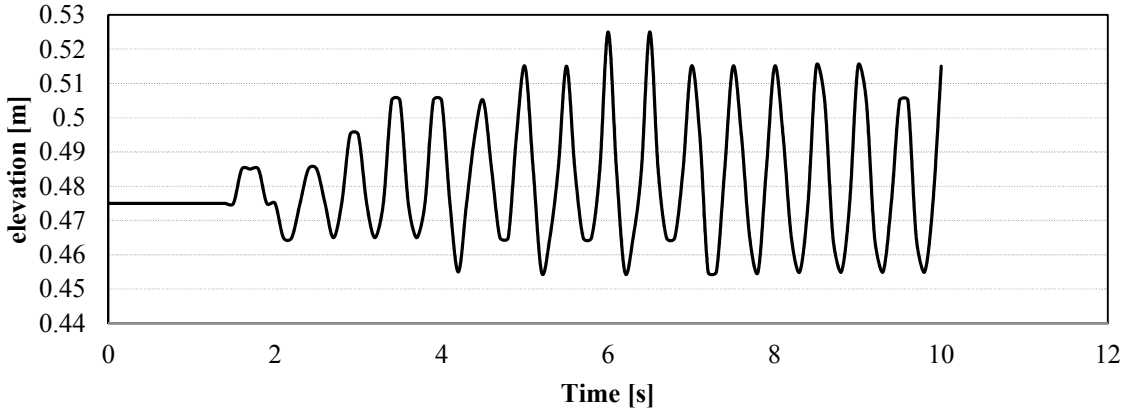

Figure 7-7 Wave elevation (wave period: 0.5s)

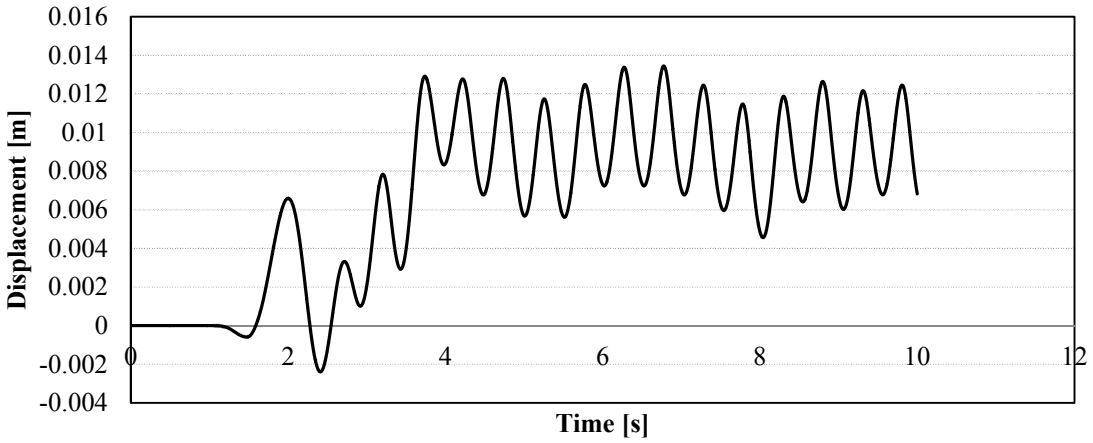

Figure 7-8 Surge (wave period: 0.5s)

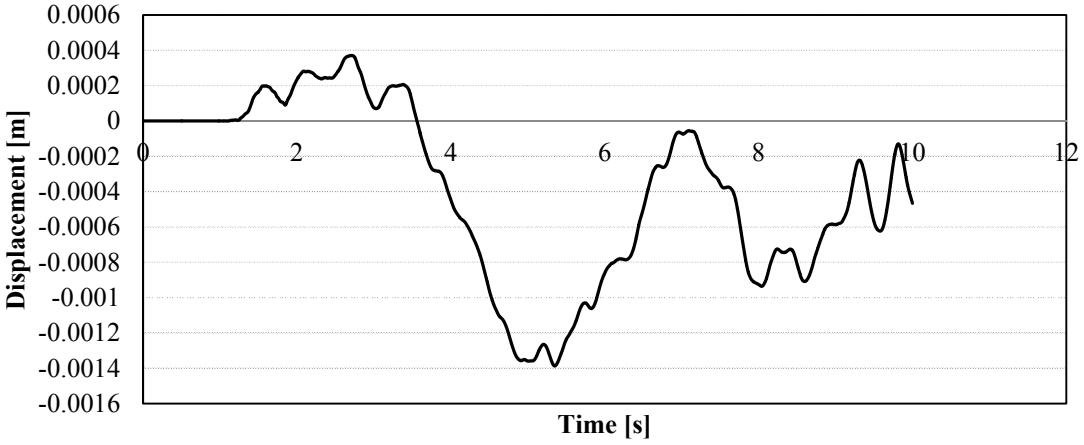

Figure 7-9 Sway (wave period: 0.5s)

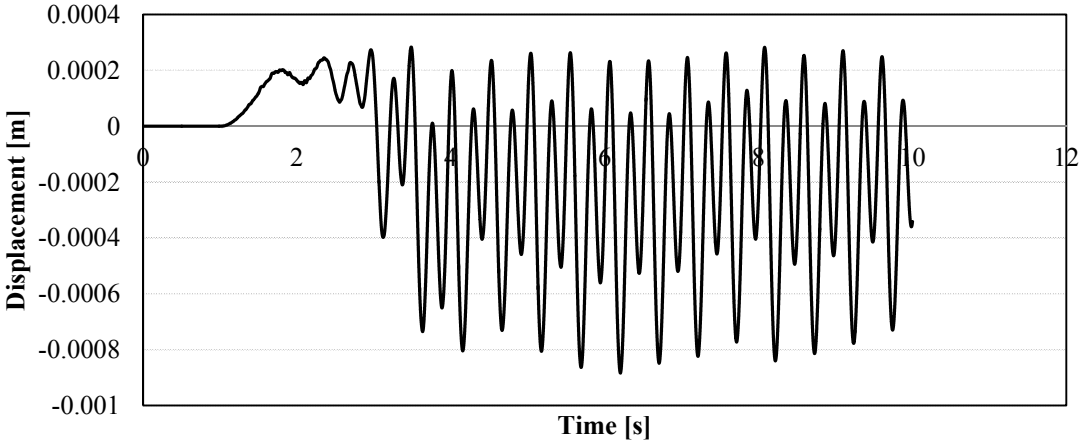

Figure 7-10 Heave (wave period: 0.5s)

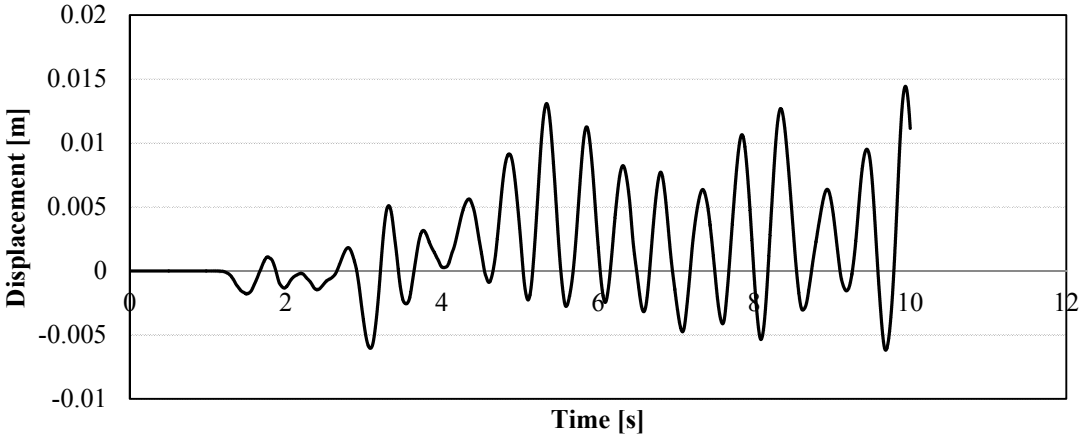

Figure 7-11 Roll (wave period: 0.5s)

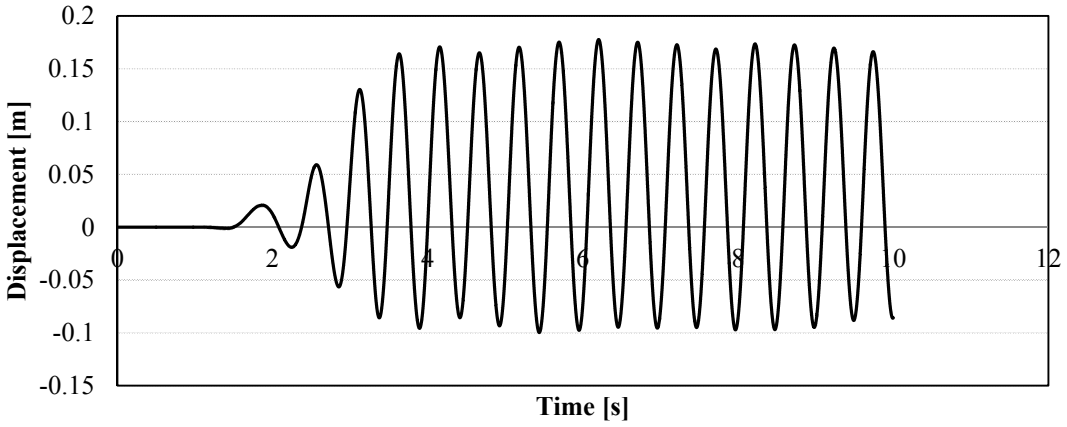

Figure 7-12 Pitch (wave period: 0.5s)

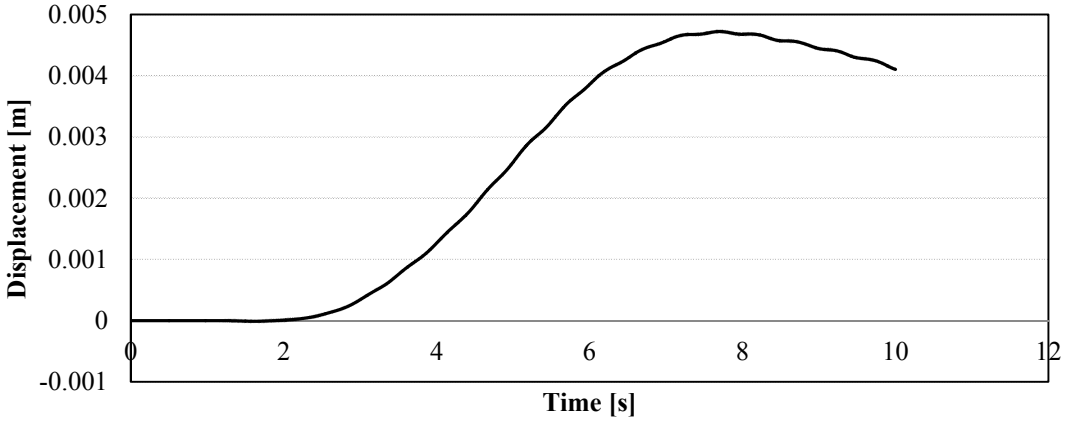

Figure 7-13 Yaw (wave period: 0.5s)

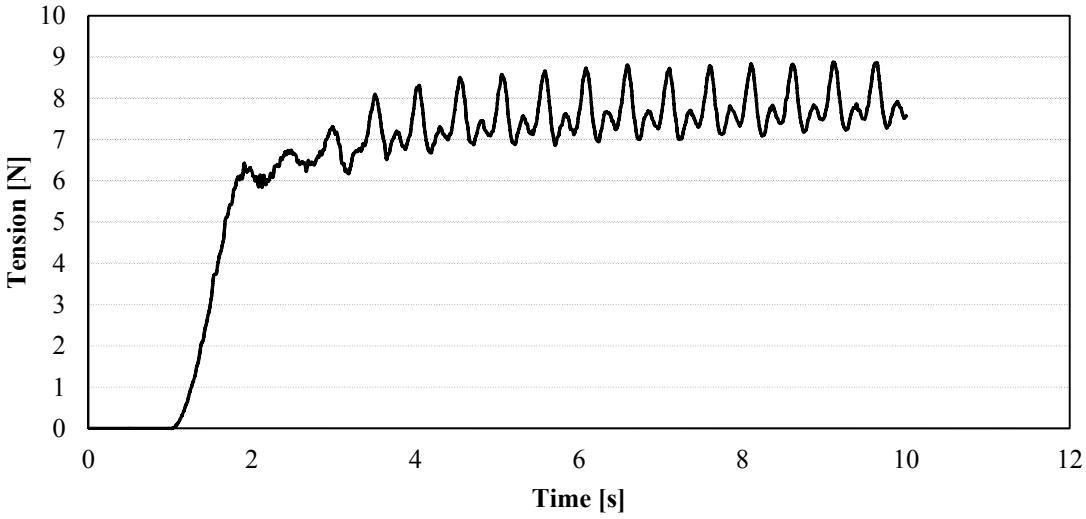

Figure 7-14 Tether tension (wave period: 0.5s)

According to Figure 7-14, it is known that the pretension is overestimated whose theoretical value is 6.1N. It is also observed that, the average value of tension turns to increase slowly with the increasing time. This is caused by the repulsive boundary conditions introduced before in which the convergence problem easily occurs. More research should be done in the future to find the better boundary theory and related coefficients.

The RAOs of simulations results based on SPH model are shown in Figure 7-15, Figure 7-16 and Figure 7-17 for surge, heave and pitch respectively. The x-axis represents the circular wave frequency and the value for y-axis is the non-dimensionalized value by wave amplitude (for surge and heave) or wave slope (for pitch). To validate the SPH simulation results, results of simulation based on potential theory (normal DYNABEAM, noted by Potential) are given in the following figures as well.

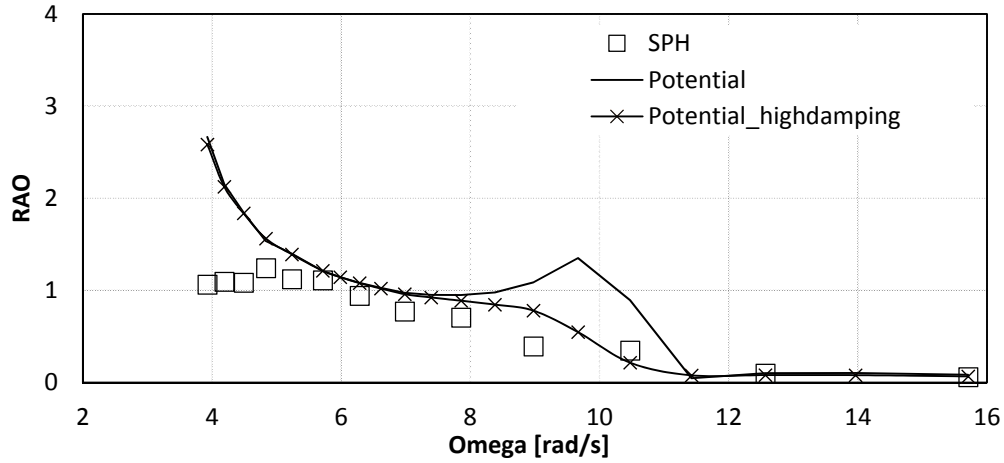

Figure 7-15 Comparison of RAO of surge among different models

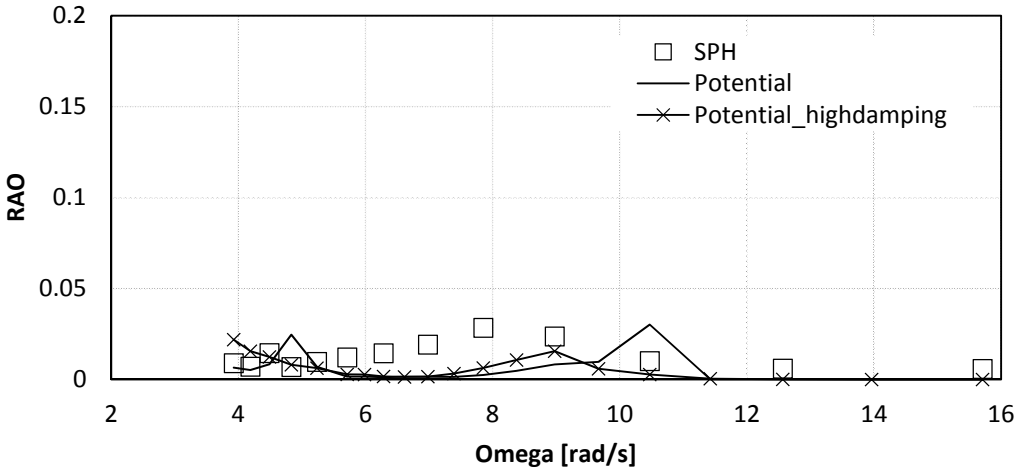

Figure 7-16 Comparison of RAO of heave among different models

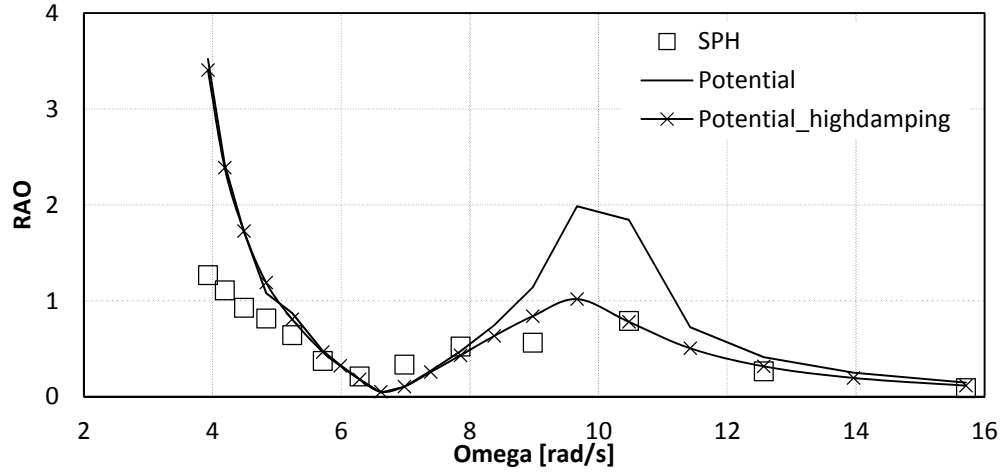

Figure 7-17 Comparison of RAO of pitch among different models

It is found that the tendency between the results based on SPH and potential is basically identical. However, in the frequency range between 9 rad/s to 11 rad/s, the results predicted by the potential theory is greater than that of the SPH theory. This is because that, it is difficult to evaluate a correct damping coefficient by SPH theory. As discussed in the previous section, SPH considers two different viscosities consisting of artificial viscosity and laminar viscosity. To prevent the convergence problem during the SPH simulation, the artificial viscosity is employed which has no physical meaning. How to select an acceptable coefficient for artificial viscosity highly depends on the calculation experience which may affect a lot on the damping of the system. In the following RAO results, the damping evaluated by SPH theory seems larger than the damping based on the potential theory. To prove the discrepancy between the SPH and potential results is caused by the different damping, more potential simulation is carried out with artificially increasing the damping by 10 times and the results are also shown in the RAO comparisons which is marked by "Potential_highdamping". The correlation between the SPH results and potential results with higher damping becomes better.

Same comparison for the tether tension is given in Figure 7-18. Although the tendency is similar between SPH and potential results, the results predicted by SPH is usually larger than that obtained from potential theory. The discrepancy can be decreased by utilizing smaller particles. Optimizing the boundary condition may be also efficient to improve the calculation results. It is known that, the damping contributes small influence on the tension by comparing the results of "Potential" and "Potential_highdamping".

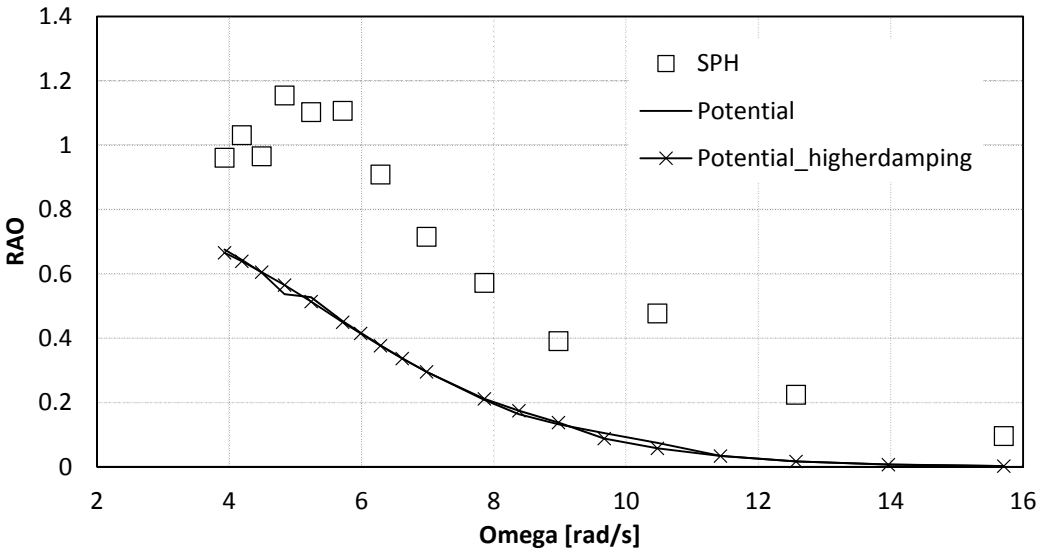

Figure 7-18 Comparison of RAO of tether tension among different models

7.4.2 Green water and slamming test

In this section, large wave is generated to investigate the response of tethered-buoy system. Green water and slamming occurs which cannot be accounted for by the present potential theory based DYNABEAM model.
To observe a severe impact load, the tethered-buoy is redesigned compared with the one used in section 7.4.1. The diameter of buoy is increased while the height and draft is decreased. The principal parameters of the new tethered-buoy system is given in Table 7-6. Same numerical water tank is utilized as described in Table 7-4

Table 7-6 Principal particulars of modified SPM model

Item	Value	Unit
Mass	1.035	kg
Moment of Inertia (I_{yy})	0.00786	kg*m^2
The height of gravity center (L_2)	0.01	m
Height	0.080	m
Diameter	0.200	m
Draft	0.050	m
Tether Length (L_1)	0.400	m
Pretension	5.26	N

Only one wave case is simulated. The generated wave period is set as 1.3s which is same with Case10 in the previous section. However, the amplitude of motion of the wave generator is increased by 8 times (0.2m) to generate a sufficient high wave.

The profile of generated wave is firstly checked without installation of tethered-buoy. The time domain results of the generated wave which are measured at the position where the tethered-buoy will be installed in the next step is shown in Figure 7-19. As the example, the transient wave profile when time is equal to 3.26s is shown in Figure 7-20.

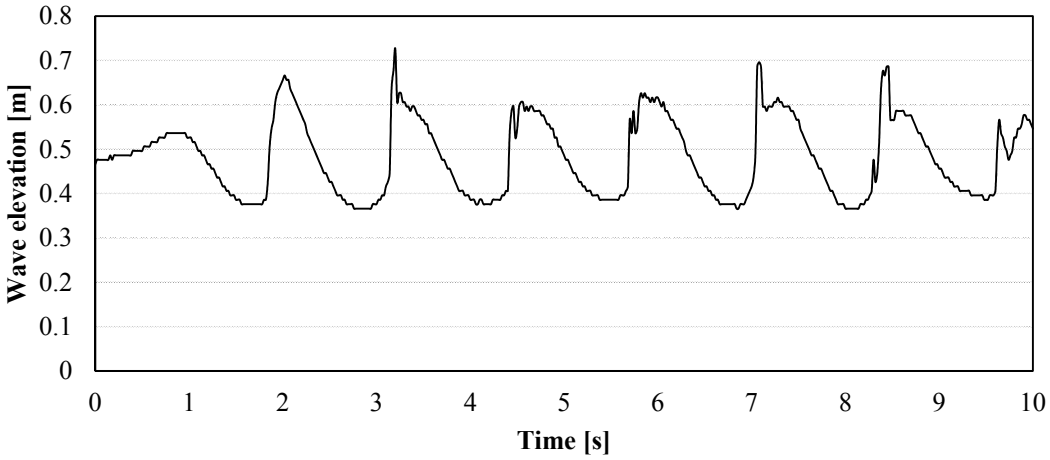

Figure 7-19 Measured wave elevation

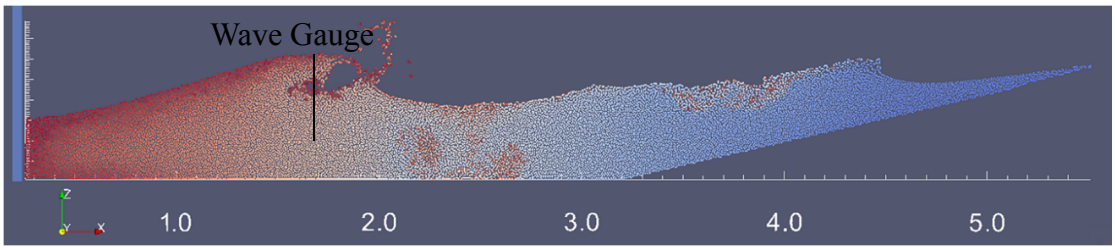

Figure 7-20 Transient wave profile (t=3.26s)

Then the tethered-buoy is installed in the water tank. In order to confirm the influence of the stiffness of the tether, two cases with same wave condition but different stiffness of tether are simulated. Table 7-7 gives the stiffness value and the corresponding natural frequency for the heave mode.

Table 7-7 Stiffness of tether and natural period for heave mode

Case	Stiffness of tether (EA)	Natural period $(2\pi\sqrt{\frac{mL}{EA}})$
Case_H	6.28 x10^3 N	0.051s
Case_L	1.57 x10^3 N	0.102s

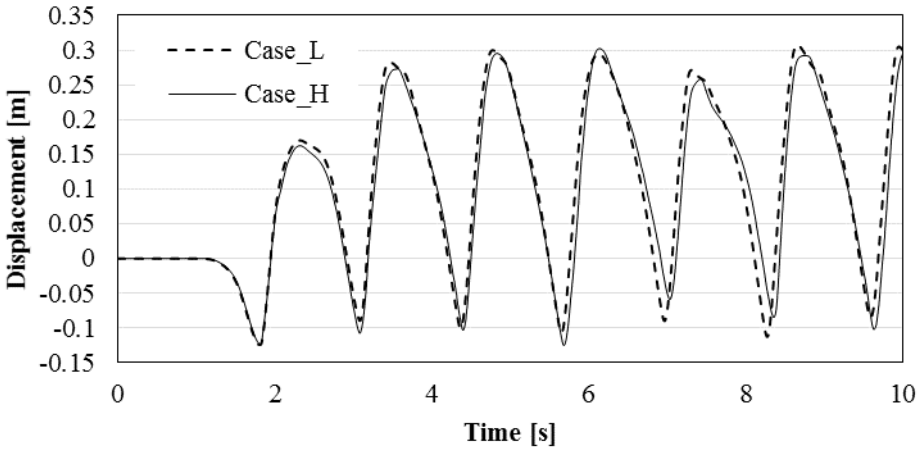

Figure 7-21 Surge motion of buoy

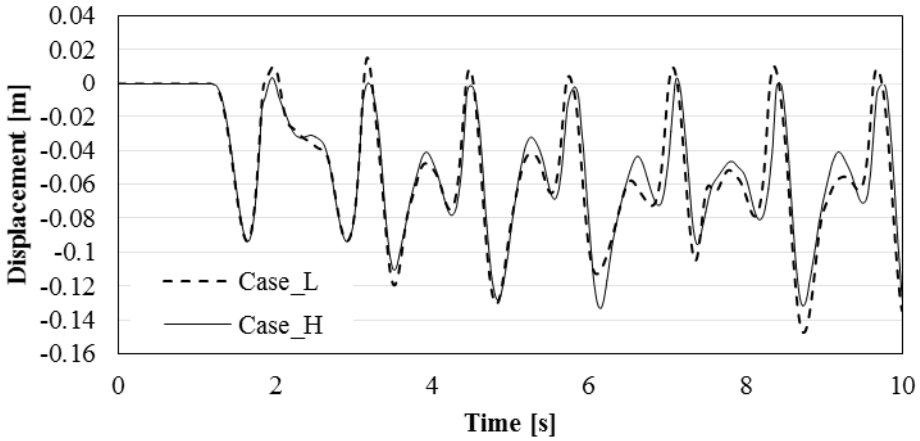

Figure 7-22 Heave motion of buoy

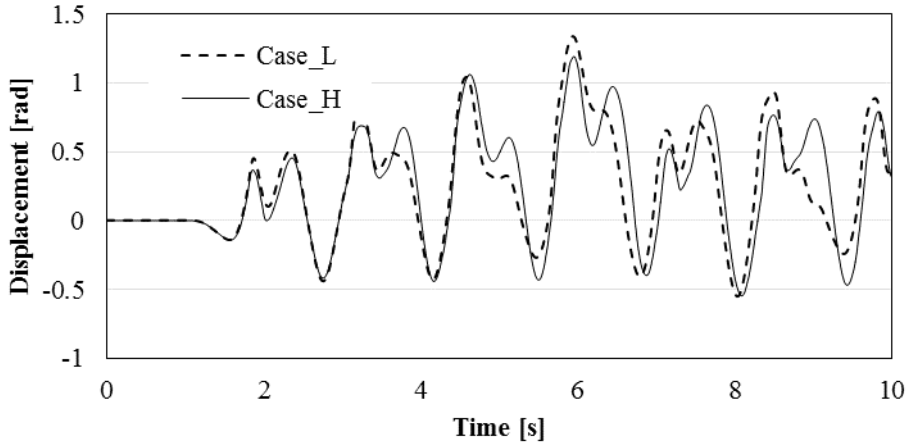

Figure 7-23 Pitch motion of buoy

Figure 7-21, Figure 7-22 and Figure 7-23 present the surge, heave and pitch motions of the buoy for both Case_H and Case_L. Note that all the external forces consisting of gravity and fluid force are added to the tethered-buoy system gradually from 1s to 2s to avoid the initial impact. So the motion of buoy before 1s is zero. It is observed that, the discrepancy of surge for the two stiffness models is relatively small compared with the heave and pitch. The discrepancy of heave can be understood due to the different stiffness of tether. For pitch motion, the large difference is mostly attributed to the coupling influence of different tether tension.

The comparison of tether tension is given in Figure 7-24. The tether tension frequently becomes close to zero as the slack of tether occurs when the wave trough passes the buoy. An obvious discrepancy can be observed as well. To check this discrepancy more clearly, the tether tension in time range 1.6s~2.6s is shown in Figure 7-25. It is found that, when slamming occurs at 1.82s, the tension increases rapidly. The model with high stiffness turns to have severer tension response when the tether becomes tense from slack. Some high frequency response of tension is observed in Figure 7-25. By checking the period of this high frequency response, it is known that this response can be associated with the natural period considering the hydrodynamics damping. So this high frequency response can be regarded as typical ringing behavior. The vertical hydrodynamic force predicted by the SPH is shown in Figure 7-26. The tendency of the vertical hydrodynamic force is same as the tether tension. So, the influence of the structural ringing on the hydrodynamics is clarified.

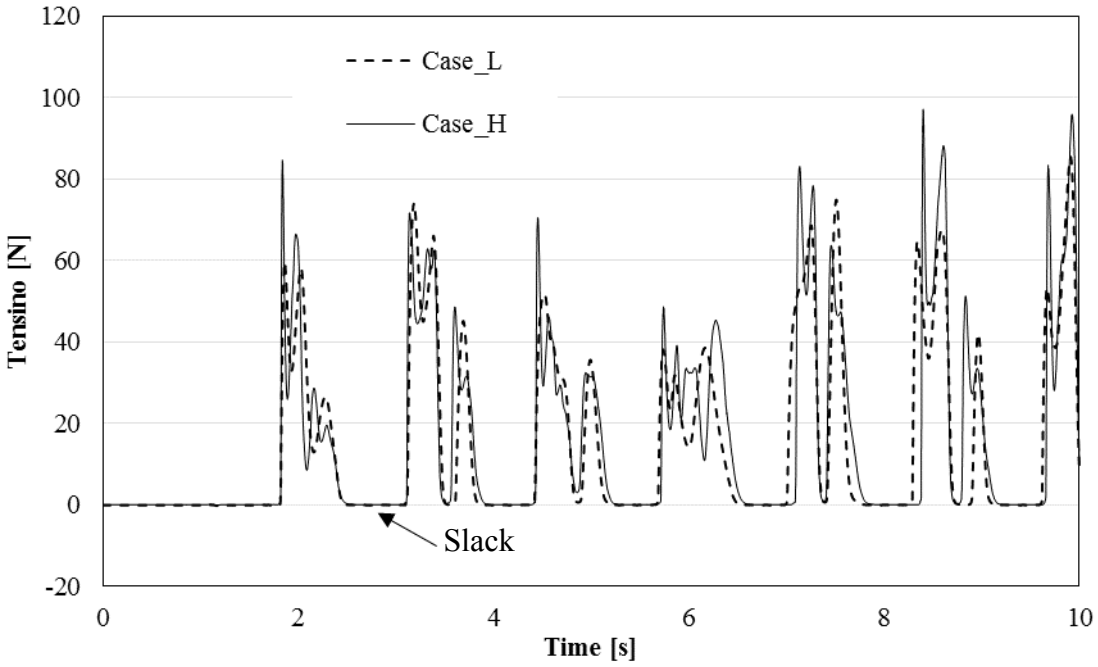

Figure 7-24 Tether Tension

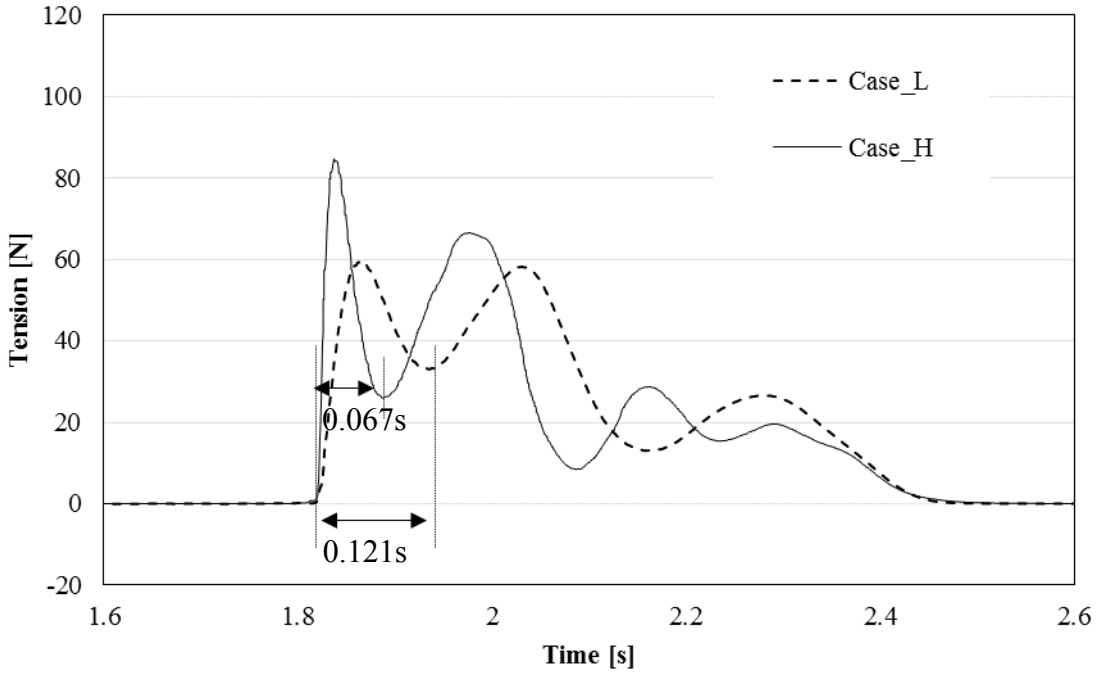

Figure 7-25 Magnification of tether tension (t=1.6s ~ 2.6s)

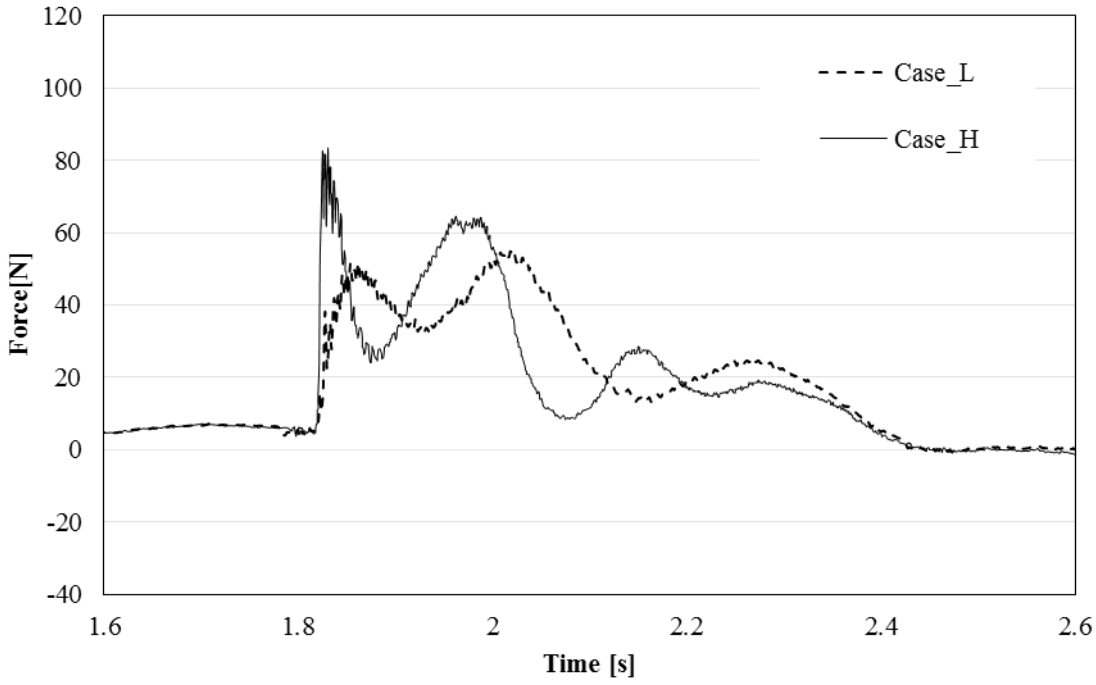

Figure 7-26 Magnification of vertical hydrodynamic force (t=1.6s ~ 2.6s)

Figure 7-27 to Figure 7-36 show the detail simulation results at different time. The left and right figures correspond to the Case_H and Case_L respectively.

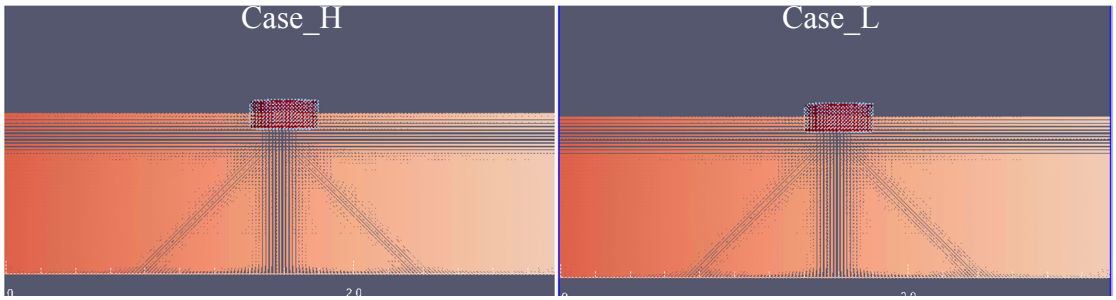

Figure 7-27 Simulation results (t=0s)

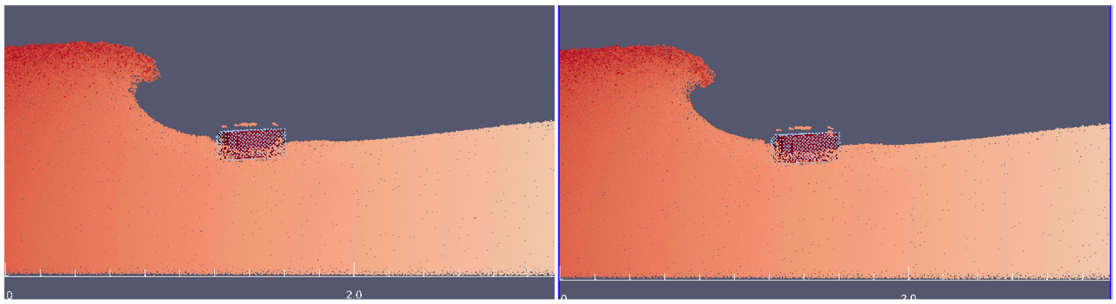

Figure 7-28 Simulation results (t=1.7s)

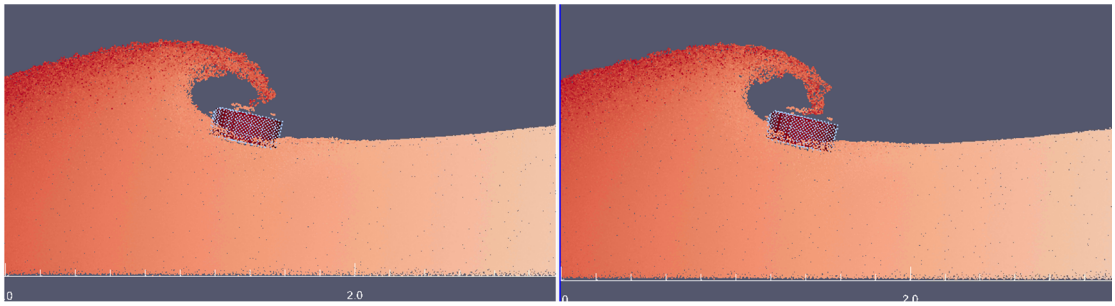

Figure 7-29 Simulation results (t=1.8s)

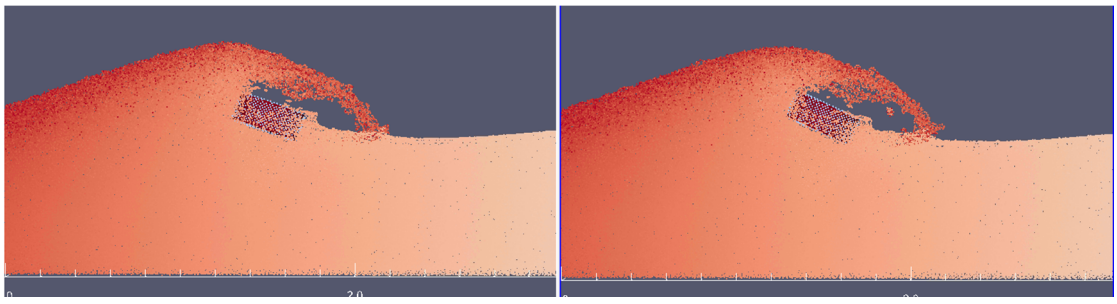

Figure 7-30 Simulation results (t=1.9s)

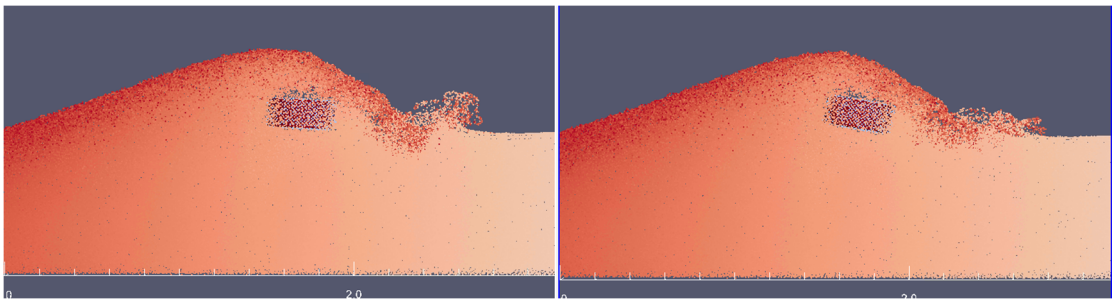

Figure 7-31 Simulation results (t=2.0s)

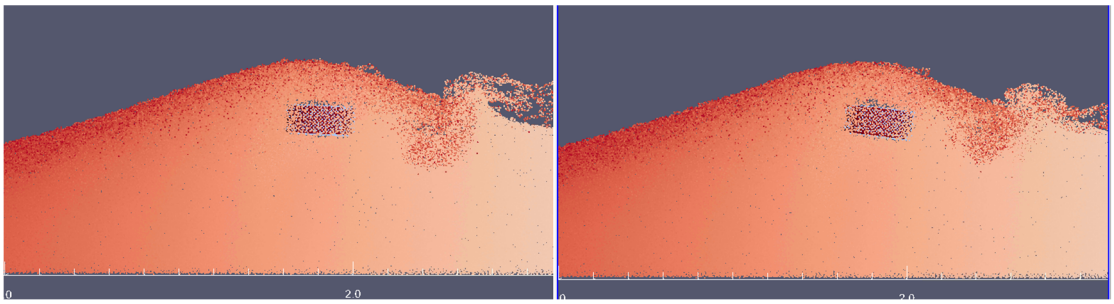

Figure 7-32 Simulation results (t=2.1s)

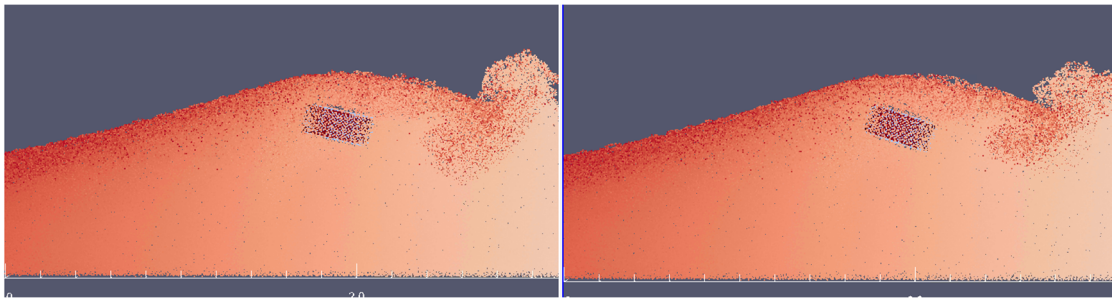

Figure 7-33 Simulation results (t=2.2s)

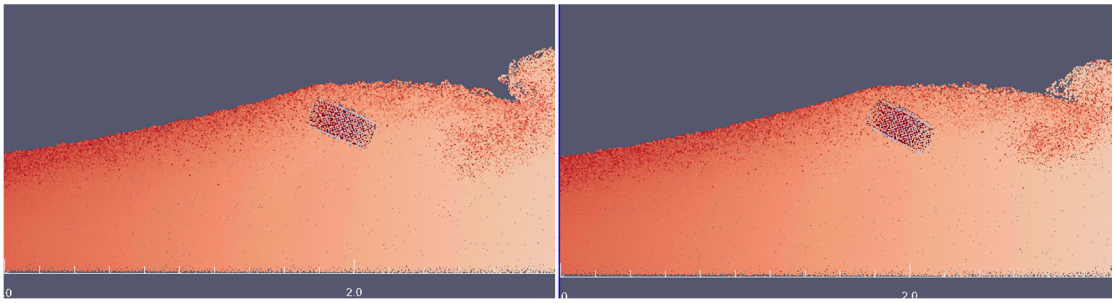

Figure 7-34 Simulation results (t=2.3s)

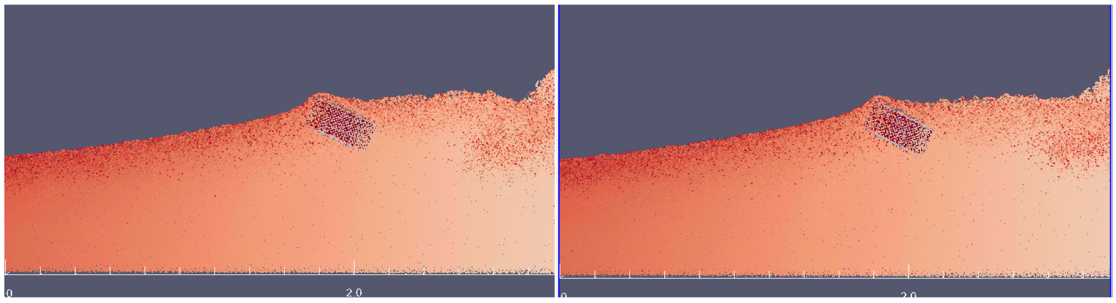

Figure 7-35 Simulation results (t=2.4s)

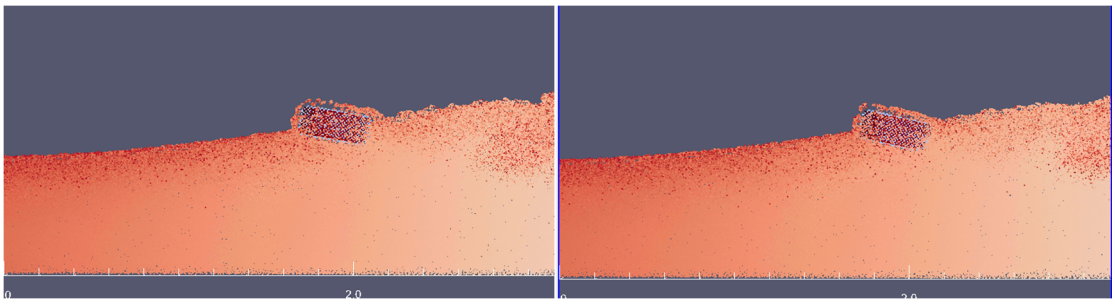

Figure 7-36 Simulation results (t=2.5s)

7.5 Conclusions

In order to further research to high order hydrodynamic problems, the time-domain DYNABEAM is developed to couple with the smoothed-particle hydrodynamics model. A series of regular wave cases are simulated by the new coupling model for tethered buoy system. By comparing the simulation results based on the potential theory, overall agreement in tendency is confirmed. The quantitative difference between them may be attributed to insufficient number of particles model and the artificial viscosity in SPH. Besides, the wave generated in SPH naturally includes nonlinear components which cannot be accounted for by the linear potential theory.

By performing the simulation under the severe wave condition, ringing response of tether after green-water and slamming was observed in SPH model. The interaction between the hydrodynamics and structural ringing was also confirmed. This could be one of strong advantages of SPH model since the potential theory based model cannot explain the nonlinear hydrodynamics in such severe waves.

8 CONCLUSIONS

In this study, an experimental and numerical research on the response of coupled system consisting the main floater, buoy and tether is addressed. This type of system is frequently found in applications such as floating offshore wind turbine (FOWT) system, single-point-moored system, etc. An optimized concept of FOWT system (OU-Design) which consists of semi-submergible (semi-sub) type platform and single-point-mooring (SPM) system proposed in the study is one of such systems.

A nonlinear time-domain code, named as DYNABEAM, is proposed which can capture the strongly coupled behavior among the main floater-mooring buoy and tether. For the mooring part, a formulation based on nonlinear beam element is adopted while the main floater part is modeled as elastic frame structure. The hydrodynamic evaluation for the main floater is made by using linear potential theory, while, the drag force terms and 2^{nd} order incident wave potential are evaluated separately and added to the hydrodynamic model. For mooring tether, the Morison's formula is simply utilized. Strongly coupling methodology is applied to obtain the interaction behavior between the floater and mooring. The coupling process works for not only catenary mooring (low stiffness) but also tensioned tether (high stiffness).

To confirm the validity of the proposed time-domain numerical model, the simulation results are compared against the scaled model test results. Two conventional designs for FOWT, SPAR and TLP types of FOWT, are chosen for comparison as the background mechanics are simpler than the OU-Design. Not only the 6DOF motions of floater but also the mooring tension and structural load on wind tower (SPAR) and lower hull (TLP) are compared between the simulation results and model tests data.

After the validation of the numerical model for the conventional designs, the simulation is further performed on the OU-Design which consists of the main floater, single-buoy and mooring tether. The coupling behavior among the main floater, buoy and tether structures is investigated.

It is found out that, due to the coupling between buoy and tether, the motion of the floater in SPM system may become unstable when the sub-harmonic motion occurs. A similar instability problem has been reported for a scaled model test for TLSPAR type of FOWT. To clarify the behavior, a theoretical analysis method is developed to predict the natural frequency, and hydrostatic - hydrodynamic stability of the tethered-buoy systems. The simulation model is established to reproduce the sub-harmonic behavior observed in the TLSPAR test. Then an independent scaled model test (SPM model) designed for the tethered-buoy system is carried out. A similar instability problem for SPM model is confirmed as predicted by the simulation.

In the last part of the thesis, the discussion is further extended to a nonlinear coupled motion in harsh environment. To this end, a time-domain simulation tool is developed to account for the fully nonlinear hydrodynamic field by introducing the smoothed particle hydrodynamics (SPH) theory.

Finally, the following conclusions in the paper can be derived:

- The proposed numerical model can predict the 6DOF motions, structural load and mooring tension of TLP and SPAR types of FOWT. The floater motion, buoy motion and mooring tension observed in the model test results for the OU-Design can be reproduced well by the proposed simulation model, too. A numerical model accounting for the coupled effects, which is applicable to various types of FOWT is finally established.
- It is found out by the simulation and model test, that the steady wind thrust has little influence on the dynamic response of FOWT system. For TLP type of FOWT, smaller stiffness of lower hulls results in an increase of mooring tension and bending moment on the lower hull due to the coupling influence.
- For OU-Design, the mooring has little influence on the motion of the main floater under designed working condition (wave period 7s-11s). But the influence of mooring becomes larger when the wave frequency approaches the natural frequency of the main floater motion as the natural frequency can be changed by the coupling process. The coupling between the floater and the tether is thus requisite for the proposed system.
- The weakly coupling always meets the convergence problem for the high stiffness model even though the small calculation time step is selected. Meanwhile, the strongly coupling works well not only for the low stiffness structure (e.g. catenary) but also the high stiffness structure (e.g. tension tether).
- A sub-harmonic pitch motion is observed for the tethered buoy system. The behavior may be described by Mathieu instability. It occurs when the Mathieu instability condition is satisfied. i.e., the sub-harmonic frequency of the external force is twice the natural frequency of the pitch motion of the buoy.
- The nonlinear influence of time-varying tether tension gives a dominant influence on the sub-harmonic pitch motion of the buoy. The coupling between heave and pitch for the buoy gives only a limited effect to the sub-harmonic motion as the heave motion is small due to constraint of the tether.
- In the design, we can suppress the sub-harmonic motion by decreasing the vertical hydrodynamic force f_z at the frequency where the sub-harmonic motion easily occurs. It can be also mitigated by adopting the smaller motion ratio λ which can be approximated as a ratio of the center of gravity height L_2 to the tether length L_1.
- Large external force in horizontal direction and pitching moment can induce a harmonic motion in a combined manner when the sub-harmonic motion occurs.
- The slow beating motion is observed with the sub-harmonic motion. It can be decreased or eliminated by increasing the system damping.

- When the results by SPH-DYNABEAM are compared against the DYNABEAM based on potential theory, an overall agreement in tendency is confirmed. The quantitative difference between them may be attributed to insufficient number of particles model and the artificial viscosity in SPH. Besides, the wave generated in SPH naturally includes nonlinear components which cannot be accounted for by the linear potential theory.
- Ringing response of tether after green-water and slamming is observed in SPH model. This could be one of strong advantages of SPH model since the potential theory based model cannot explain the nonlinear hydrodynamics in such severe waves.

Even though the availability of proposed method has been proven for predicting the response of platform and mooring, coupling the present model with aerodynamics is still necessary especially when the dynamic wind load becomes dominant. This coupling work should be finished in the future. Besides, the validation work for the proposed SPH-DYNABEAM model should be performed by conducting some slamming model tests, or potential theory based DYNABEAM with slamming/green-water model implemented in the DYNABEAM model. From the viewpoint of risk evaluation, more complex numerical model for analyzing the structural post-ultimate strength behavior under severe wave condition is also an interesting research topic. An Abaqus-SPH (Abaqus is a commercial nonlinear structural FEM software) coupling numerical model accounting for the collapse behavior is under development now.

ACKNOWLEDGEMENTS

First and foremost, I would like to give my heartfelt thanks to my supervisor, Associate Professor Kazuhiro Iijima for his patience, encouragement, enthusiasm, and of course, vast knowledge which support me during my whole 5-years study life in Osaka University.

I also want to express my deepest gratitude to my professor, Professor Masahiko Fujikubo, for his considerate inspiration and kindness support. By studying under his instruction, I could feel the research sprite and responsibility behind worldwide top researcher, which will guide my life no matter what I will do in the future.

A very special thanks goes out to Professor Masashi Kashiwagi who reviewed and commented my doctoral thesis with one hundred percent sincerity.

I am very grateful to Professor Yasunori Nihei, who provided me so much expert guidance and high-level experimental data without which the validation work cannot be finished.

I want also like to thank the assistant professor, my best friend, Mr. Tatsumi, for his warm help on my study and daily life.

I highly appreciate the consistent assistant from the laboratory secretary, Miss Ohkita. I also wish to acknowledge all the students in laboratory 4 for their help. It's really my honor to study with you.

I would also like to acknowledge all the professors in my department who taught me in class. Without the knowledge I learned, it's impossible for me to complete this thesis.

The financially support from the Japanese Government (MONBUKAGAKUSHO: MEXT) scholarship is gratefully acknowledged.

Last but not the least, I would like to thank my parents and my sister for the support they provided me through my entire life. I must acknowledge my girlfriend, Zhang Lu, you were there for me every step of the way.

BIBLIOGRAPHIES

[1] E. W. E. Association, "Deep water: The next step for offshore wind energy," 2013.

[2] N. Armaroli and V. Balzani, Powering Planet Earth: Energy Solutions for the Future, 2012.

[3] "Offshore Wind Energy," Environmental and Energy Study Institute, 2010.

[4] "http://en.wikipedia.org/wiki/Offshore_wind_power," [Online].

[5] W. Musial, S. Butterfield and A. Boone, "Feasibility of Floating Platform Systems for Wind Turbines," *the 23rd ASME Wind Energy Symposium, Reno, Nevada,* January 5–8, 2004.

[6] C. Watanabe, "http://www.bloomberg.com/news/articles/2012-03-29/floating-windmills-in-japan-help-wind-down-nuclear-power-energy," 2012. [Online].

[7] T. ISHIHARA, "FukushimaFloating OffshoreWind Farm Fukushima Floating Offshore Wind Farm Demonstration Project".

[8] B. Bulder and e. al, "Study to Feasibility of and Boundary Conditions for Floating Offshore," *ECN, MARIN, TNO, TUD, MSC, Lagerway the Windmaster,* 2002.

[9] K. H. Lee, "Responses of Floating Wind Turbines to Wind and Wave Excitation," *MSc Thesis. University of Michigan,* 2005.

[10] E. N. Wayman, P. D. Sclavounos, S. Butterfield, J. Jonkman and W. and Musial, "Coupled Dynamic Modeling of Floating Wind Turbine Systems," *2006 Offshore Technology Conference, 1–4 May 2006, Houston,* May 2006.

[11] E. Wayman, "Coupled Dynamics and Economic Analysis of Floating Wind Turbine Systems," *M.S. Dissertation, Department of Mechanical Engineering, Massachusetts Institute of Technology, Cambridge, MA, USA,* June 2006.

[12] A. Robertson, "Offshore code comparison collaboration continuation within iea wind task 30: phase ii results regarding a floating semisubmersible wind system," *Proceedings of 33th International Conference on Offshore Mechanics and Arctic Engineering OMAE2014,* pp. OMAE2014-24040, 8–13 June 2014.

[13] Y. Bae and M. Kim, "Coupled dynamic analysis of multiple wind turbines on a large single floater," *Ocean Engineering,* 2014.

[14] E. E. Bachynski and T. Moan, "Design considerations for tension leg platform wind turbines," *Marine Structures,* 2012.

[15] T. Ishihara, K. Kagaya and Y. Kikuchi, "Water tank experiment and dynamic analysis of floating offshore wind turbine system considering combined hydrodynamic loadings," *Proceedings of the 35th wind energy symposium,* 2013.

[16] Y. Nihei, M. Matsuura, M. Murai, K. Iijima and T. Ikoma, "New Design Proposal for the TLP Type Offshore Wind Turbines," *OMAE,* 2013.

[17] Y. Nihei, T. Ikoma, M. Kozen, F. Sato, M. Murai and K. Iijima, "Designing Process and Motion Characteristics of Spar Type Offshore Wind Turbines,"

Proceedings of 33th International Conference on Offshore Mechanics and Arctic Engineering, 2013.

[18] K. Iijima, Y. N. Misako Kawai, M. Murai and T. Ikoma, "Conceptual Design of a Single-Point-Moored FOWT and Tank Test for Its Motion Characteristics," *Proceedings of 33th International Conference on Offshore Mechanics and Arctic Engineering,* 2013.

[19] "http://www.fukushima-forward.jp/english/," [Online].

[20] T. Utsunomiya, S. Yoshida, H. Ookubo, I. Sato and S. Ishida, "Dynamic Analysis of a Floating Offshore Wind Turbine Under Extreme Environmental Conditions," *Journal of Offshore Mechanics and Arctic Engineering,* vol. 136, 2014.03..

[21] "http://www.statoil.com/en/Pages/default.aspx," [Online].

[22] "http://www.bluehengineering.com/," [Online].

[23] "http://www.thewindpower.net/windfarm_en_18607_kyushu-university-wind-lens-project.php," [Online].

[24] M. Karimirad and C. Michailides, "V-shaped semisubmersible offshore wind turbine: An alternative concept for offshore wind technology," *Renewable Energy,* vol. 83, pp. 126-143, 2015.

[25] "http://www.principlepowerinc.com/products/windfloat.html," [Online].

[26] C. Ma, M. Kawai, K. Iijima, Y. Nihei, T. Ikoma and M. Murai, "Experimental Study on New Design For FOWT With SPM System," *Proceedings of Annual Spring Meeting of Japanese Society of Naval Architects and Ocean Engineers,* 2013.

[27] K. Iijima, M. Kawai, Y. Nihei, M. Murai and T. Ikoma, "Conceptual design of a single-point-moored fowt and tank test for its motion characteristics," *Proceedings of the 32nd International Conference on Ocean, Offshore and Arctic Engineering,* 2013.

[28] K. Iijima, "Theoretical review of the structural analysis program for the VLFS under waves".

[29] O. M. Faltinsen, "Sea Loads on Ships and Offshore Structures".

[30] H. Suzuki and K. Yoshida, "Nonlinear dynamic analysis method of underwater line structure and its validation," *Journal of Society of Naval Architects of Japan,* vol. 168, pp. 379-387, 1990.

[31] S. Krenk, Non-linear Modeling and Analysis of Solids and Structures, 2010.

[32] H. Hashamdar, Z. Ibrahim and M. Jammel, "Finite element analysis of nonlinear structures with Newmark," *International Journal of the Physical Sciences,* vol. 6(6), pp. 1395-1403, 2011.

[33] O. Faltinsen, Hydrodynamics of High-Speed Marine Vehicles, Cambridge University Press, 2005.

[34] W. Cummins, "The impulse response function and ship motions," *Technical report, Department of the Navy, David Taylor Model Basin,* 1962.

[35] F. Ogilvie, "Recent progress toward the understanding and prediction of ship motions," *Proceedings of the 5th Symposium on Naval Hydrodynamics,* p. 3–128, 1964.

[36] G. Clauss, E. Lehmann and C. Ostergaard, Offshore Structures, Value 1 Conceptual Design and Hydromechanics, 1992.

[37] M. Kozen, "Experimental investigations into the effect of pitch control for FOWTs," *Master thesis of Osaka Prefecture University,* 2014.

[38] Y. Nihei, M. Matsuura, M. Murai, K. Iijima and T. Ikoma, "New Design Process for the TLP Type Offshore Wind Turbines," *Proceedings of OMAE2013, Nantes, France,* pp. OMAE2013-11263, 2013.

[39] C. Ma, K. Iijima and Y. Nihei, "Strongly coupled method for predicting the response of flexible FOWT with mooring and its experimental validation," *Proceedings of the ASME 2014 33rd International Conference on Ocean, Offshore and Arctic Engineering,* Vols. OMAE2014-24625, 2014.

[40] K. Yago, Y. Ohkawa and T. Sawai, "A Basic Study on the Floating Wind Power System, 17th ocean engineering symposium," *The society of Naval Architects of Japan,* pp. 127-134, 2003.

[41] C. Otaka and Y. Nihei, "Studies on the six degrees of freedom motion characteristic of Spar floating offshore wind turbine of single point tension mooring system," *Proceedings of Annual Autumn Meeting 2013 of Japanese Society of Naval Architects and Ocean Engineers,* 2013.

[42] D. W. Jordan and P. Smith, "Nonlinear Ordinary Differential Equations: Problems and Solutions," Oxford University Press, 2007, pp. 417-448.

[43] H. A. Haslum and O. M. Faltinsen, "Alternative shape of spar platforms for use in hostile areas," *Proceedings of the 31st Offshore Technology Conference, Houston,* pp. 217-228, 1999.

[44] J. B. Rho and H. S. Choi, "Heave and Pitch motions of a spar platform with damping plate," *Proceedings of the 12th international offshore and polar engineering conference, Kitakyushu,* pp. 198-201, 2002.

[45] J. B. Rho and H. S. Choi, "An experimental study for mooring effects on the stability of spar platform," *Proceedings of the 13th international offshore and polar engineering conference, Honolulu,* pp. 285-288, 2003.

[46] H. Hashimoto and N. Umeda, "Validation of a numerical simulation model for parametric rolling prediction using PCTC," *Proceedings of the 11th International Conference on Stability of Ships and Ocean Vehicles,* pp. 141-150, 2012.

[47] C. Rodriguez and M. A. S. Neves, "Investigation on parametrically excited motions of spar platforms in wave," *Proceedings of the 11th International Conference on Stability of Ships and Ocean Vehicles,* pp. 509-517, 2012.

[48] H. Minematsu and E. Kajita, "An application of new wave-free columns to the tension leg platform," *Journal of Society of Naval Architects of Japan,* vol. 200,

pp. 85-92, 1986.

[49] K. Sao, T. Numata and S. Kikuno, "Analysis method for single point mooring (report 1)," *Journal of Society of Naval Architects of Japan,* vol. 162, pp. 257-266, 1987.

[50] B. Koo, M. H. Kim and R. E. Randall, "Mathieu instability of a spar platform with mooring and risers," *Ocean Engineering,* vol. 131, pp. 2175-2208, 2004.

[51] J. Li, S. Fan, Y. Li and Z. Guo, "Dynamic stability of parametrically-excited linear resonant beams under periodic axial force," *Chinese Physics B,* vol. 21, 2012.

[52] "SWAY AS website," [Online]. Available: http://www.sway.no/.

[53] C. Ma, K. Iijima and M. Fujikubo, "Coupled response of a tethered buoy in waves," *Proceedings of Annual Autumn Meeting of Japanese Society of Naval Architects and Ocean Engineers,* 2014.

[54] M. Miche, "Movements ondulatoires des mers en profondeur constante ou decroissante," *Annales des Ponts et Chaussees,* pp. 25-78, 131-164, 270–292, 369–406, 1944.

[55] B. Li and J. Ou, "Numerical study on mathieu instability of DDMS platform," *Proceedings of the ASME 2010 29st International Conference on Ocean, Offshore and Arctic Engineering, Shanghai,* 2010.

[56] R. E. Cruz, M. A. S. Neves, L. A. Rivera and P. T. T. Esperanca, "An investigation on the excitation of yaw parametric resonance of a tension leg platform," *Proceedings of the ASME 2012 31st International Conference on Ocean, Offshore and Arctic Engineering, Rio de Janeiro,* 2012.

[57] R. Gingold and J. Monaghan, "Smoothed particle hydrodynamics: theory and application to non-spherical stars," *Mon. Not. R. Astron. Soc.,* vol. 181, p. 375–89, 1977.

[58] L. Lucy, "A numerical approach to the testing of the fission hypothesis," *Astron. J.,* vol. 82, p. 1013–1024, 1977.

[59] "http://en.wikipedia.org/wiki/Smoothed-particle_hydrodynamics," [Online].

[60] J. J. Monaghan, "Smoothed particle hydrodynamics," 2005.

[61] M. Gesteira, B. Rogers, R. Dalrymple, A. Crespo and M. Narayanaswamy, "User Guide for the SPHysics code," 2010.

[62] M. Gesteira, B. D. Rogers, A. J. C. Crespo, R. A. Dalrymple, M. Narayanaswamy and J. M. Dominguez, "SPHysics –developmentofafree-surfacefluidsolver– Part1:Theory and formulations," *Computers & Geosciences,* vol. 48, p. 289–299, 2012.

[63] J. J. Monaghan, R. A. F. Cas., A. M. Kos and M. Hallworth, "Gravity currents descending a ramp in a stratified tank," *Journal of Fluid Mechanics,* vol. 379, p. 39–70, 1999.

[64] G. Batchelor, IntroductiontoFluidDynamics, CambridgeUniversityPress, 1974.

[65] E. Lo and S. Shao, "Simulationofnear-shoresolitarywavemechanicsbyan,"

Applied Ocean Research , vol. 24, p. 275–286, 2002.

[66] J. J. Monaghan, "On the problem of penetration in particle methods," *Journal of Computational Physics,* vol. 82, p. 1–15, 1989.

[67] G. A. Dilts, "Moving-least-squares-particle hydrodynamics–I.Consistency and stability," *International Journal for Numerical Methods in Engineering,* vol. 44, p. 1115–1155, 1999.

[68] E. F. Toro, Shock Capturing Methods for Free Surface Shallow Flows, John Wiley &Sons, 2001.

[69] A. N. Parshikov, "Application of a solution of the Riemann problem to the SPH method," *Computational Mathematics and Mathematical Physics,* vol. 39, 1999.

[70] J. P. Vila, "On particle weighted methods and smooth particle hydrodynamics," *Mathematical Models and Methods in Applied Sciences ,* vol. 9, p. 161–209, 1999.

[71] E. F. Toro, M. Spruce and W. Speares, "Restoration of the contact surface in the HLL-Riemann solver," *Shock Waves,* vol. 4, p. 25–34, 1994.

[72] J. J. Monaghan and A. Kos, "Solitary waves on a Cretan beach," *Journal of Waterway Port, Coastal, and Ocean Engineering,* vol. 125, p. 145–154, 1999.

[73] A. C. Crespo1, J. M. Dominguez, A. Barreiro, M. Gomez-Gesteira and B. D. Rogers, "GPUs, a New Tool of Acceleration in CFD: Efficiency and Reliability on Smoothed Particle Hydrodynamics Methods," *PLOS,* vol. 6, no. 6, 2011.

[74] K. Yoshida and M. Ozaki, "A dynamic response analysis method of tension leg platforms subjected to waves," *Journal of the faculty of engineering, the university of Tokyo,* pp. 885-919, 1984.

APPENDIX A: NEWTON-RAPHSON METHOD

In order to solve the nonlinear equation of motion during the simulation of time-domain DYNABEAM, the Newton-Raphson Method is employed. In this appendix, the solving process of Newton-Raphson Method is introduced.

Based on the assumed relationship among the acceleration, velocity and displacement according to Newmark-beta method, the dynamic equation of motion can be transformed to static problem which is only depended on the displacement (see Chapter 3.2.1c). For static problem, the vector of inner force equals to the vector of external force as shown:

$$Q_t = F_t \qquad \textbf{(A-1)}$$

where, Q_t and F_t represents the inner force and external force at time t respectively.

Assuming Eq. (A-1) is already satisfied and for next time step, $t+\Delta t$, the external force is $F_{t+\Delta t}$ also known, then the inner force in the next time step can be written as:

$$Q_{t+\Delta t} = Q_t + \Delta Q = F_{t+\Delta t} = F_t + \Delta F \qquad \textbf{(A-2)}$$

Eq. (A-2) can be written as incremental form:

$$\Delta Q = \Delta F \qquad \textbf{(A-3)}$$

where

$$\Delta Q = \frac{\partial Q_{t+\Delta t}}{\partial \delta}\Delta\delta = K_{t+\Delta t}\Delta\delta \qquad \textbf{(A-4)}$$

K is the nonlinear stiffness which is a function of the transient displacement δ.

Substituting Eq. (A-4) into Eq. (A-3), a equation for incremental δ can be obtained:

$$K_{t+\Delta t}\Delta\delta = \Delta F \qquad \textbf{(A-5)}$$

Based on Eq. (A-5), the solving iteration based on Newton-Raphson Method can be started by solving set of linear algebraic equations. Initially, Eq. (A-5) can be written as following linear form:

$$K_{t+\Delta t}^{(0)} \Delta\delta^{(1)} = \Delta F \qquad \textbf{(A-6)}$$

where, $K_{t+\Delta t}^{(0)} = K_t$ and K_t is known value. Superscript means the iteration times and initially, it is defined as zero.

After solving $\Delta\delta^{(1)}$, the stiffness $K_{t+\Delta t}^{(1)}$ can be obtained and the residual force is written:

$$\Delta F^{(1)} = \Delta F - K_{t+\Delta t}^{(1)} \Delta\delta^{(1)} \qquad \textbf{(A-7)}$$

Based on the value of $\Delta F^{(1)}$ and $K_{t+\Delta t}^{(1)}$, the incremental displacement can be improved from $\Delta\delta^{(1)}$ to $\Delta\delta^{(2)}$:

$$\Delta\delta^{(2)} = \Delta\delta^{(1)} + \frac{\Delta F^{(1)}}{K_{t+\Delta t}^{(1)}} \qquad \textbf{(A-8)}$$

Then the updated stiffness $K_{t+\Delta t}^{(2)}$ and the residual force $\Delta F^{(2)}$ can be calculated which will be substituted into Eq. (A-8) to improved $\Delta\delta^{(3)}$. This iteration will be looped until the residual force $\Delta F^{(i)}$ smaller than a critical value which represents the solution for Eq. (A-5) $\Delta\delta$ is found. Figure A-1 Shows the process of hunting the accurate solution according to Newton-Raphson method.

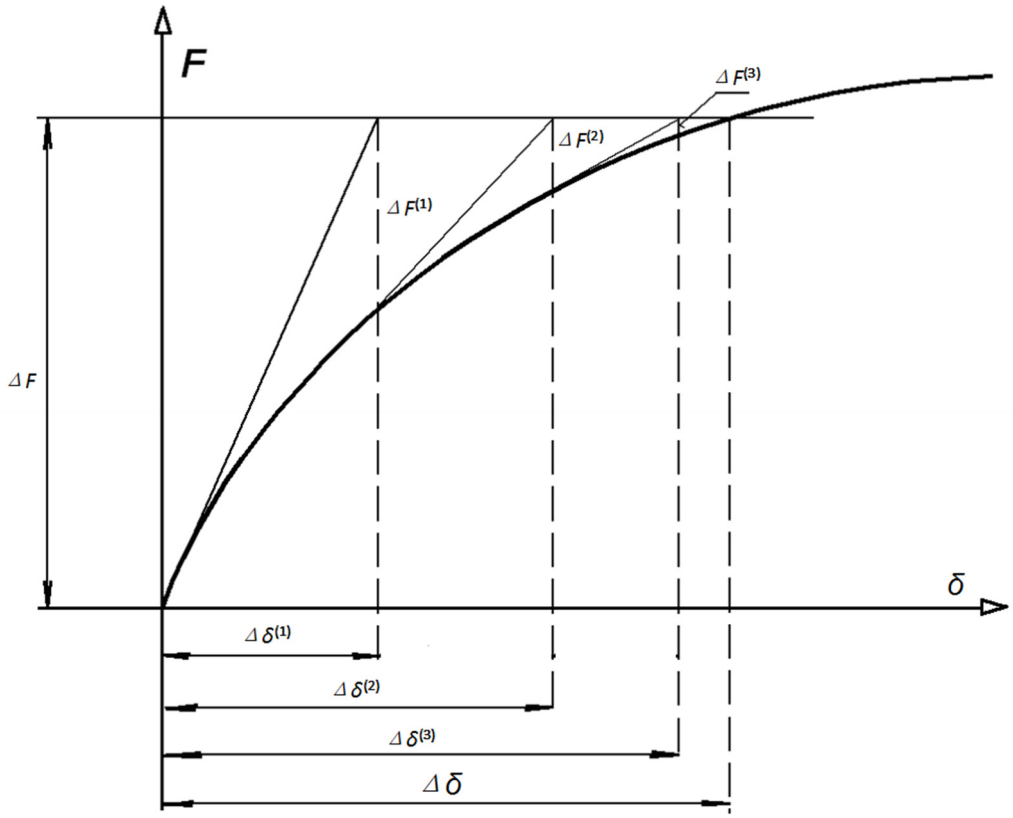

Figure A-1 process of hunting the accurate solution (Newton-Raphson method)

APPENDIX B: THE STATIC CATENARY THEORY

Consider now this cable with an un-stretched length L, at the lower end attached to an anchor point, A, and at the upper end attached to a suspension point, B, in a vertical plane through this cable line. A two-dimensional sketch of this catenary anchor line is shown in Figure B-1.

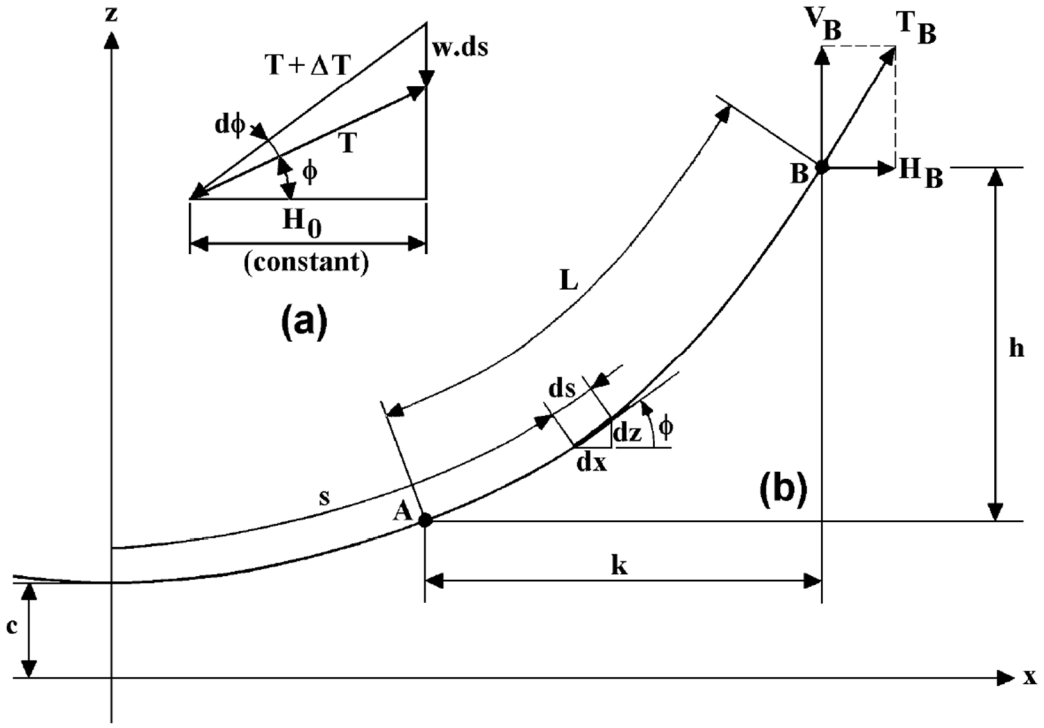

Figure B-1 process of hunting the accurate solution (Newton-Raphson method)

B.1 Inelastic Cable Line

Suppose: the length of the cable, L, is known and the relative positions of two - in principle arbitrary - points A and B on the cable are defined by the distances k and h. The anchor point is defined in (x_A, z_A) and the suspension point on the structure is defined by (x_B, z_B) with:

$$x_B = x_A + k \quad \text{and} \quad z_B = z_A + h$$

The position of the origin of the axis system (x, z) relative to the cable line follows from two unknown coefficients, C_1 and C_2, as will be explained in the following. When defining:

$$u = \frac{dz}{dx} \text{ and } \quad c = \frac{H_0}{w} \qquad \textbf{(B-1)}$$

in which w is the weight per unit length of the cable in water (see Figure B-1), it can be found that:

$$ds = \sqrt{1+u^2} \cdot dx \qquad \textbf{(B-2)}$$

$$du = d(\frac{dz}{dx}) = d(\tan\phi) = \frac{w \cdot ds}{H_0} = \frac{ds}{c} \qquad \textbf{(B-3)}$$

$$du = \frac{\sqrt{1+u^2}}{c} \cdot dx \text{ or } dx = \frac{du}{\sqrt{1+u^2}} \cdot c \qquad \textbf{(B-4)}$$

With this, an integral equation will be obtained:

$$\int dx = c \cdot \int \frac{du}{\sqrt{1+u^2}} \qquad \textbf{(B-5)}$$

Integration of this equation provides:

$$x = c \cdot \ln(u + \sqrt{1+u^2}) + C_1 = \frac{c}{\sinh u} + C_1 \text{ or } u = \sinh(\frac{x}{c} - C_1) \qquad \textbf{(B-6)}$$

Herein, the constant C_1 will be zero because the origin in Figure B-1 is chosen in such a way that the derivative u = dz/dx is zero for x is zero, so:

$$u = \sinh(\frac{x}{c}) \qquad \textbf{(B-7)}$$

Then the equation of the cable curve can be written as:

$$z = \int_0^x u \cdot dx = c \cdot \cosh(\frac{x}{c}) + C_2 \qquad \textbf{(B-8)}$$

The origin in Figure B-1 is chosen in such a way that $C_2 = 0$, thus:

$$z = c \cdot \cosh(\frac{x}{c}) \qquad \textbf{(B-9)}$$

This means that z=c for x=0.

Also, the distance s can be obtained:

$$s = \int_0^x \sqrt{1+u^2} \cdot dx = c \cdot \sinh(\frac{x}{c}) \qquad \textbf{(B-10)}$$

Combining Eq. (B-9) and Eq. (B-10) provides a simple relation between z and s:

$$z^2 - s^2 = c^2 \qquad \textbf{(B-11)}$$

from which after some algebra for the points A and B on the cable line follows:

$$\sqrt{L^2 - h^2} = c\sqrt{2} \cdot \sinh(\frac{k}{2c}) \qquad \textbf{(B-12)}$$

The vales k, h and L are known, and the value of c can be found from this equation in an iterative manner.

Then the relative position of the anchor point can be decided as:

$$x_A = c \cdot \ln(\sqrt{\frac{L+h}{2(L-h)}}) - \frac{k}{2} \qquad x_B = x_A + k$$
$$z_A = c \cdot \cosh(\frac{x_A}{x}) \qquad z_B = z_A + h \qquad \textbf{(B-13)}$$

The tension force can also be obtained as:

$$T = w \cdot z \qquad \textbf{(B-14)}$$

B.2 Elastic Cable Line

In the previous, the elongation of the cable due to the tension force in the cable has not been taken into account. To consider the elongation, the force-strain relationship and the cable characteristics have to be defined. Here, the linear spring model is applied which means that:

$$T = EA \cdot \varepsilon \qquad \textbf{(B-15)}$$

where

E elasticity modulus of the cable

A cross sectional area of the cable

$\varepsilon = \Delta L / L$ specific strain of the cable

The actual length of the cable is given by:

$$L = L_0 + \Delta L_0 \qquad \textbf{(B-16)}$$

In which L_0 is the length of the not-loaded cable and ΔL_0 is the elongation due to the tension force in the cable.

$$\Delta L_0 = \int_0^L \varepsilon(s) ds = \int_0^L \frac{T}{EA} ds \qquad \textbf{(B-17)}$$

To solving the elastic problem, the length given in Eq. (B-12) should be set as the length of the not-loaded cable firstly. This results in a known distribution of the tension forces T in the cable. Then substitute the tension forces T in equation (B-17) to obtain the elongation ΔL_0. Recalculate the cable using the updated length $L = L_0 + \Delta L_0$. Iterate the above process until the $L - (L_0 + \Delta L_0) < \delta$, where δ is the pre-specified error tolerance.

APPENDIX C: PROVE THE CRITERION FOR HYDROSTATIC STABILITY FOR TETHERED-BUOY SYSTEM

The criterion for hydrostatic stability given by Eq. (6-8) could be easily derived as following:

As the gravity and buoyancy should be pure vertical when the tethered-buoy becomes balanced in somewhere, the tether load should be also vertical. Otherwise, there will be no horizontal force to balance the tether load. If we assume the tethered-buoy is not vertically stable so that it should be balanced with some inclination Θ (see Figure C-1).

Assuming the Θ is small, the moment around y axis should be balanced as $(T_0 L_2 + F_B GM)\theta = 0$ (T_0 and F_B increases with the increasing of Θ). So it could be easily known that, $T_0 L_2 + F_B GM$ can be regarded as the restoring stiffness and when $T_0 L_2 + F_B GM > 0$, the tethered-buoy system will be balanced without inclination.

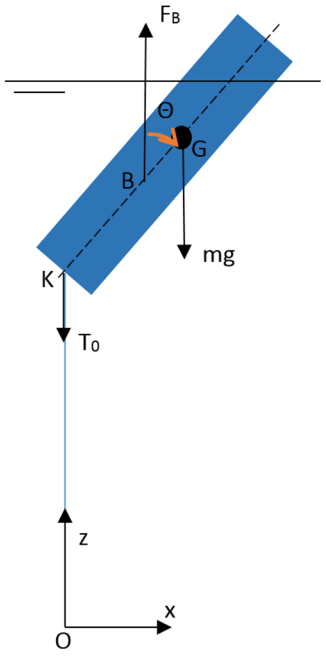

Figure C-1 Balanced tethered-buoy system with initial inclination

APPENDIX D: PHASE OF TWO MODES FOR TETHERED-BUOY SYSTEM

The motion ratio $\lambda(\omega)$ between the amplitude of θ_1, θ_2 is given in Eq. (6-10). In this appendix, it will be proven that the following inequalities hold.

$$\lambda(\omega_1) < 0 \qquad \textbf{(D-1)}$$

$$\lambda(\omega_2) > 0 \qquad \textbf{(D-2)}$$

Inequality Eq. (D-1) can be proved by contradiction.

Firstly, it is assumed that $\lambda(\omega_1) \geq 0$, so we can get (to be convenient, the added mass and added inertia moment are included in the m and I in the following derivation):

$$T_0 \geq \omega_1^2 m L_1 = \frac{\omega_1^2 A}{I} = \frac{\frac{B+\sqrt{B^2-4AC}}{2A} A}{I} = \frac{B+\sqrt{B^2-4AC}}{2I} \qquad \textbf{(D-3)}$$

where, the coefficients A, B, C are defined as Eq. (6-7) which is shown below,

$$A = mIL_1$$
$$B = [m(L_2^2 + L_1 L_2) + I]T_0 + mGM_0 L_1 F_{B0}$$
$$C = T_0(T_0 L_2 + F_{B0} GM_0)$$

Coefficient B can be written as a function as coefficients A and C:

$$B = \frac{A}{I}\frac{C}{T_0} + mT_0 L_2^2 + T_0 I \qquad \textbf{(D-4)}$$

Inequality Eq. (D-3) can be transformed to Eq. (D-5)

$$2T_0 I - B \geq \sqrt{B^2 - 4AC} \qquad \textbf{(D-5)}$$

Take the square value for both sides of Eq. (D-5):

$$\left(2T_0 I - B\right)^2 \geq B^2 - 4AC \qquad \textbf{(D-6)}$$

Substituting the Eq. (D-4) into inequality Eq. (D-6), inequality Eq. (D-7) is derived:

$$mT_0^{\,2} IL_2^{\,2} \leq 0 \qquad \textbf{(D-7)}$$

It is obviously knows that, inequality Eq. (D-7) cannot hold which means that the assumption $\lambda(\omega_1) \geq 0$ is wrong.

Therefore, the inequality Eq. (D-1) is proved.

Inequality Eq. (D-2) can be proved in the same manner.

APPENDIX E: APPROXIMATE ESTIMATION OF MOTION RATIO FOR TETHERED-BUOY SYSTEM

The equation of motion ratio λ Eq. (6-10) can be written in inverse form:

$$\frac{1}{\lambda(\omega)} = \frac{\phi_2}{\phi_1} = -\frac{L_1}{L_2}(1-\frac{1}{\delta}) \qquad \textbf{(E-1)}$$

where

$$\delta = \frac{\omega^2}{{\omega_0}^2} \qquad \textbf{(E-2)}$$

$\omega_0 = \sqrt{\frac{T_0}{mL_1}}$: natural frequency if the buoy is regarded as a mass *m* attached and suspended to a pendulum by the tether with pre-tension T_0.

Substituting the natural frequency ω_1 into Eq. (E-2):

$$\delta = \frac{{\omega_1}^2}{{\omega_0}^2} = \frac{B+\sqrt{B^2-4AC}}{2A} / \frac{T_0}{mL_1} > \frac{B}{2A} / \frac{T_0}{mL_1} > \frac{T_0(I_m+I)}{2mIL_1} / \frac{T_0}{mL_1} = \frac{(I_m+I)}{2I} \qquad \textbf{(E-3)}$$

where

$I_m = m{L_2}^2 + mL_1L_2$: added inertia moment due to the tether influence

It can be known that, with the assumption that the mass is distributed evenly, the inertia moment *I* around the center of gravity is much smaller than I_m. Then, δ is much larger than unity. Finally, we can derive that:

$$\lambda(\omega) \approx -\frac{L_2}{L_1} \qquad \textbf{(E-4)}$$